Quelques aspects de physique des trous noirs, cosmologie et théorie quantique des champs

Flora Moulin

Université Grenoble Alpes

THÈSE

Pour obtenir le grade de

DOCTEUR DE L'UNIVERSITÉ GRENOBLE ALPES

Spécialité : **Physique théorique**

Arrêté ministériel : 25 mai 2016

Présentée par

Flora MOULIN

Thèse dirigée par **Aurélien BARRAU, Professeur, Université Grenoble-Alpes**

préparée au sein du **Laboratoire de Physique Subatomique et Cosmologie (LPSC)**
dans **l'École Doctorale de Physique**

Quelques aspects de physique des trous noirs, cosmologie et théorie quantique des champs

Thèse soutenue publiquement le **16 octobre 2020**
devant le jury composé de :

Pr, Gilles, HENRI
Professeur, Université Grenoble-Alpes (UGA), Président
Dr, Karim, NOUI
Maître de conférences, Université de Tours, Rapporteur
Dr, Julien, GRAIN
Chargé de recherche, Institut d'Astrophysique Spatiale (IAS), Rapporteur
Dr, Frédérique, MARION
Directrice de recherche, Laboratoire d'Annecy de Physique des Particules (LAPP), Membre

Liste des publications

1. Some Clarifications on the Duration of Inflation in Loop Quantum Cosmology, *Class.Quant.Grav. 34 (2017)*, Bolliet, Barrau, Martineau, Moulin

2. Scalar spectra of primordial perturbations in loop quantum cosmology, *Phys.Rev.D 98 (2018)*, Barrau, Jamet, Martineau, Moulin

3. Seeing through the cosmological bounce : Footprints of the contracting phase and luminosity distance in bouncing models, *Phys.Rev.D 96 (2017)*, Barrau, Martineau, Moulin

4. Fast radio bursts and the stochastic lifetime of black holes in quantum gravity, *Phys.Rev.D 96 (2017)*, Barrau, Moulin, Martineau

5. Quantum fields in the background spacetime of a polymeric loop black hole, *Class.Quant.Grav. 36 (2019)*, Moulin, Martineau, Grain, Barrau

6. A status report on the phenomenology of black holes in loop quantum gravity : Evaporation, tunneling to white holes, dark matter and gravitational waves, *Universe 4 (2018)*, Barrau, Martineau, Moulin

7. Quasinormal modes of black holes in a toy-model for cumulative quantum gravity, *Phys.Lett.B 795 (2019)*, Barrau, Martineau, Martinon, Moulin

8. Analytical proof of the isospectrality of quasinormal modes for Schwarzschild-de Sitter and Schwarzschild-Anti de Sitter spacetimes, *General Relativity and Gravitation 52 (2020)*, Moulin, Barrau

9. Dark matter as Planck relics without too exotic hypotheses, *Phys.Rev.D 100 (2019*, Barrau, Martineau, Moulin, Ngono

10. An overview of quasinormal modes in modified and extended gravity, *General Relativity and Gravitation 52 (2020)*, Moulin, Barrau, Martineau

11. Non-trivial effects of sourceless forces for spinors : toward an Aharonov–Bohm gravitational effect ? *Eur.Phys.J.C 79 (2019)*, Fabbri, Moulin, Barrau

12. Cross section for Bhabha and Compton scattering beyond quantum field theory, soumis à *Phys. Lett. B*, Moulin, Fabbri, Barrau

Remerciements

Tout d'abord, j'aimerais remercier Aurélien sans qui rien de tout ça n'aurait été possible. Grâce à toi j'ai eu la chance de passer trois années de ma vie à travailler sur des sujets qui me passionnent. Tu m'as laissée de la liberté dans mon travail tout en étant toujours présent. Ton savoir et ta réflexion m'impressionneront toujours. Travailler avec quelqu'un d'aussi bienveillant que toi fut un plaisir et je pense que tu es le meilleur directeur de thèse que j'aurais pu avoir. Merci pour toutes les connaissances que tu m'as apportées, tes conseils et ton optimisme !

Merci à Luca Fabbri, avec qui j'ai eu l'opportunité de travailler. Tu m'as appris beaucoup de choses et je suis très heureuse de connaître, grâce à toi, les fondements du formalisme polaire.

Ensuite j'aimerais remercier tous mes amis et plus spécialement ceux de Grenoble qui étaient présents au quotidien. Merci à Seb et Ju qui ont toujours été présents pour moi, dans les moments difficiles et dans les moments où tout d'un coup la vie prend un cours totalement différent, inattendu mais plein de bonnes choses. Coeur Love à vous deux ! Merci à Jérem et Léo parce que quand même on forme un trio gagnant. A la grimpe, au ski ou au drak art je me marre toujours autant avec vous. Soirée déjantée à la bobine, pâté en croûte, raclette, montgolfière ou ananas, vous êtes mes bitches pour la vie ! Merci à Mathew pour ces bons moments passés au brugs, au parc ou au roller, à parler de tout et surtout de n'importe quoi. Merci à Kiki toujours là pour blaguer, plein de belles discussions de physique et aussi pas mal de conneries, et aussi le mur de Rome haha. Merci à Rola et Alex, mes amours. Merci à mes colocs, Anto et Jul, auprès de qui j'ai écrit mon manuscrit. Avec quelques circuits training, bons repas, infufus, apéros, karaokés, danses sur les canaps, le confinement c'était pas si pire. Nous avons d'ailleurs quelques souvenirs gravés dans notre fameux "Joural".

Merci à ma famille pour m'avoir toujours soutenue dans mes choix. Et surtout à Fa, car même si on a toujours habité loin l'une de l'autre je peux toujours compter sur toi. Trop fière d'avoir une grande sœur comme toi ! !

Merci à mes potes d'enfance, de lycée et de Lozère car même si on se voit que quelques fois par an on est toujours aussi proches. Merci à Mathilde, mon girafon, venue from Paris. J'étais trop contente de partager ce moment avec toi ! Merci à Estelle, ma toute première amie pour la vie ! C'est pas rien quand même ! Merci à Victoria, colocataire d'internat, avec nos couettes Minnie on étaient mignonnes, non ? Hâte de te voir mon chat et que tu me fasses des crêpes ou des mini-pizzas. Merci aux deux sœurs Gony, Laure et Vio, avec qui nous formons un petit groupe de rap, dont je ne suis pas peu fière, "Les bien braves aux vocalouz" ! Claro que si ! Merci à Johana, hâte qu'on se voit encore plus souvent :) Merci à Lowlow et François le villageois, bandes de hippies ! Merci à Meihdi pour tous nos délires. Tu connais mon histoire mais tu connais pas mon adresse, qu'est-ce tu vas faire ? Hein ? Et merci à Alban, pour tout.

Table des matières

Introduction

Le 20ème siècle marque une période importante pour la physique. La première révolution conceptuelle vient de la relativité restreinte. Cette théorie bouleverse notre perception du temps et de l'espace en remettant en cause les notions de simultanéité et d'espace absolu. Le temps et l'espace deviennent indéfectiblement liés. S'ensuivent des conséquences essentielles parmi lesquelles l'impossibilité d'interactions instantanées à distance, l'équivalence masse-énergie, l'interdiction pour une particule massive d'atteindre la vitesse de la lumière et l'existence de l'antimatière. À la suite de l'établissement de ce nouveau paradigme, deux grandes théories émergent. L'une de façon indépendante, l'autre de façon corrélative.

D'une part, la physique quantique voit le jour. Les particules décrites jusqu'ici seulement par leur aspect corpusculaire, sont désormais décrites également par un aspect ondulatoire. La dualité onde-corpuscule est indispensables dès lors qu'on veut dépeindre les caractéristiques exhaustives d'une particule. Cet aspect ondulatoire donne lieu à des propriétés de délocalisation et à une facette probabiliste. C'est une importante avancée dans notre conception du monde physique. En effet, le principe déterministe ancré dans les lois les plus fondamentales s'en trouve partiellement déconstruit. Et, de façon très remarquable, le phénomène d'intrication quantique – dans lequel les particules enchevêtrées forment un système lié – montre que la théorie est, en un sens, non-locale.

Le formalisme contemporain utilise abondamment la notion de champ et le concept (dont nous verrons qu'il est en réalité non-trivial) de base d'ondes planes. De façon générique, la quantification s'effectue en appliquant des relations de commutation canoniques aux champs considérés et en les promouvant au rang d'opérateurs. La procédure dite de "quantification de Dirac" permet de généraliser la méthode à partir de la structure symplectique de la théorie considérée.

La théorie quantique des champs (TQC) permet de concilier efficacement le principe de la relativité restreinte avec les prescriptions de la mécanique quantique. La dynamique des champs est décrite par des équations différentes qui dépendent de leurs spins. Un champ scalaire, un tenseur de type $(0, 0)$, de spin entier 0, est soumis à l'équation de Klein-Gordon. Un champ électromagnétique, un tenseur de type $(0, 1)$, de spin 1, est soumis aux équations de Maxwell. D'un point de vue théorique, si on associe une particule d'interaction liée à la gravité, cette particule, appelée graviton, serait un tenseur de type $(0, 2)$, de spin 2. Pour compléter ce panel de champs, il existe également le champ fermionique, de spin $1/2$. Ce dernier est non plus décrit par un tenseur mais par un spineur qui se transforme en son opposé sous rotation de 2π. Un champ fermionique est soumis à l'équation de Dirac et une partie de cette thèse y sera consacrée à quelques considérations originales autour des propriétés de ces solutions.

Du point de vue de la physique des particules élémentaires, le formalisme se fonde sur les théories jauge. Celles-ci utilisent des groupes de symétrie locale (groupes de Lie complexes) : U(1), SU(2), SU(3), SU(2)XSU(3), etc. Seule la gravitation fait défaut dans ce paradigme par ailleurs très cohérent, quoique non exempt de difficultés.

D'autre part, en parallèle, la théorie de la relativité générale (RG) s'est imposée. L'espace-temps est courbé par l'énergie. Ainsi, un objet massif va modifier l'écoulement du temps et infléchir les distances à ses alentours. Cela décrit une quatrième force fondamentale conceptuellement très différentes des trois précédentes. En effet, les forces électromagnétiques, faible et forte décrivent la dynamique des particules et pour cela on utilise comme référence l'espace-temps dans lequel elles sont plongées. En gravité, on décrit la dynamique de l'espace-temps lui-même. Il n'y a plus de référence immuable sur laquelle s'appuyer, de structure figée : c'est ce qu'on nomme l'invariance de fond. Mathématiquement, il est possible de décrire la dynamique d'un espace à quatre dimensions en le plongeant dans un espace à cinq dimensions. Mais il est également possible de décrire sa courbure, par exemple, en demeurant dans l'espace-temps lui-même. Pour décrire la propagation des champs du modèle standard des particules en présence de gravitation, on peut utiliser la TQC en espace courbe. Cependant, lorsque l'on veut quantifier l'espace-temps lui même il faut faire appel à la gravité quantique. Il n'existe pas à ce jour une unique théorie de gravité quantique consensuelle. Nous sommes encore à un stade précoce car aucune expérience n'a sondé directement des effets de gravité quantique.

Dans ce manuscrit, nous verrons différents aspects théoriques et phénoménologiques associés à la gravité quantique. Dans un premier temps, nous étudierons la phénoménologie de la cosmologie quantique à boucles (LQC). Ce modèle cosmologique s'inspire des travaux effectués dans le cadre de la gravitation quantique à boucles (LQG). Cette théorie tente de quantifier l'espace-temps de façon invariante de fond. En LQC, le Big-Bang est remplacé par un rebond, précédé d'une phase où l'univers se contracte. Il est alors possible d'étudier les conséquences de cet univers pré-rebond dans l'univers actuel. Nous étudierons ensuite la phénoménologie associée aux trous noirs dans le cadre de la gravité quantique. Nous verrons les éventuels signaux émis par les trous noirs en rebond et les conséquences de la discrétisation de l'espace-temps sur le rayonnement de Hawking. Plusieurs de mes travaux portent sur les modes quasi-normaux (QNMs). Ces derniers décrivent les fréquences propres des ondes gravitationnelles émises lorsqu'un trou noir se trouve dans la phase dite de relaxation. Nous étudierons d'abord les aspects théoriques liés à l'isospectralité, puis nous verrons comment la valeur des QNMs varie en fonction des paramètres de différents modèles au-delà de la RG. Enfin, nous étudierons le formalisme polaire, qui décrit le théorie quantique des spineurs dans une plus grande généralité que la TQC. Dans cette approche, l'unique hypothèse est la validité de l'équation de Dirac. Nous verrons que ce formalisme est apte à décrire l'effet Aharonov-Bohm gravitationnel ainsi que la section efficace de diffusion pour des particules en interaction. Il semble que des effets non-triviaux échappant à la TQC puissent être ainsi décrits.

CHAPITRE 1

La théorie quantique des champs et la relativité générale

Sommaire

Dans ce chapitre, je vais introduire la relativité générale (RG) et la théorie quantique des champs (TQC). La première étend le concept de la relativité restreinte à des espaces-temps courbes. La deuxième permet d'avoir une description relativiste (au sens restreint) de la mécanique quantique. Ainsi avant de présenter ces deux théories, j'énoncerai quelques aspects de la relativité restreinte. Puis je présenterai la gravitation quantique à boucles. Cette théorie tente de quantifier la gravité. Dans ce manuscrit nous utilisons le système d'unités naturelles, mais parfois nous écrirons explicitement la longueur de Planck l_{Pl}. Les vecteurs, et plus généralement les tenseurs, sont notés en gras. Cependant, par abus de langage, on écrit parfois un tenseur avec ses indices sans que l'on fasse référence spécifiquement à une de ses composantes.

1.1 La relativité restreinte

Cette section et la section 1.3 sont inspirées du livre [1].

D'après le principe de relativité, il n'existe pas d'observateur inertiel privilégié. Pour décrire cette propriété, nous introduisons le groupe de Lorentz - le groupe orthogonal O(1, 3). Il est défini par

$$\eta_{ab} = \eta_{cd}\Lambda^{c}{}_{a}\Lambda^{d}{}_{b}, \tag{1.1}$$

avec $\Lambda^{a}{}_{b}$ une transformation de Lorentz

$$x'^a = \Lambda^a{}_b x^b, \tag{1.2}$$

et η_{ab} la métrique de Minkowski, dans la notation index. L'intervalle d'espace-temps

$$ds^2 = \eta_{ab} dx^a dx^b = dt^2 - dx^2 - dy^2 - dz^2. \tag{1.3}$$

est invariant sous transformation de Lorentz. Le sous-groupe orthochrone ($\Lambda^0{}_0 \geq 0$) et propre (det Λ = 1), $SO^+(1,3)$, est appelé le groupe de Lorentz restreint.

Une transformation infinitésimale est décrite par

$$\Lambda^a{}_b = \delta^a_b + \omega^a{}_b. \tag{1.4}$$

L'équation (1.1) montre que ω est antisymétrique, le groupe de Lorentz possède donc six paramètres. Il décrit trois rotations dans l'espace et trois boosts. Les générateurs des rotations sont notés J^i et ceux des boosts K^i. Nous explicitons par leur forme ici, mais l'algèbre de Lie du groupe de Lorentz so(3, 1) s'obtient par commutation des générateurs. L'algèbre de Lorentz s'écrit

$$[J^i, J^j] = \epsilon^{ijk} J^k, \tag{1.5}$$
$$[J^i, K^j] = \epsilon^{ijk} K^k, \tag{1.6}$$
$$[K^i, K^j] = -\epsilon^{ijk} J^k. \tag{1.7}$$

En introduisant $\theta^i = (1/2)\epsilon^{ijk}\omega^{jk}$ et $\eta^i = \eta^{i0}$, les transformations de Lorentz s'écrivent

$$\Lambda = e^{-i\theta_a J^a + i\eta_a K^a}. \tag{1.8}$$

On défini J^{ab} tel que $\Lambda = 1 - i\omega_{ab}J^{ab}/2$ quand $\omega_{ab} \to 0$. On peut montrer que $(J^{ab})^c{}_d = i(\eta^{ac}\delta^b_d - \eta^{bc}\delta^a_d)$. On a $J^{0i} = K^i$ et $J_{ij} = \epsilon_{ijk}J^k$. En notation covariante, l'algèbre de Lorentz se lit

$$[J^{ab}, J^{cd}] = i(-\eta^{ac}J^{bd} - \eta^{bd}J^{ac} + \eta^{bc}J^{ad} + \eta^{ad}J^{bc}), \tag{1.9}$$

et un élément de l'algèbre de Lorentz s'écrit

$$\Lambda = e^{-\frac{i}{2}\omega_{ab}J^{ab}}. \tag{1.10}$$

En définissant

$$\boldsymbol{J}^{\pm} = \frac{\boldsymbol{J} \pm i\boldsymbol{K}}{2}, \tag{1.11}$$

l'algèbre s'écrit

$$[J^{+,i}, J^{+,j}] = i\epsilon^{ijk} J^{+,k}, \tag{1.12}$$
$$[J^{-,i}, J^{-,j}] = i\epsilon^{ijk} J^{-,k}, \tag{1.13}$$
$$[J^{+,i}, J^{-,j}] = 0. \tag{1.14}$$

On a so(3, 1) = su(2) $\bigoplus$ su(2). Les représentations de su(2) $\bigoplus$ su(2) sont étiquetées par deux nombres demi-entiers (j_-, j_+). $(0,0)$ est la représentation scalaire, de dimension 1, $\boldsymbol{J} = 0$, $\boldsymbol{K} = 0$. Les représentations $(1/2, 0)$ et $(0, 1/2)$ sont les représentations spinorielles, de dimension 2. Un spineur dans la représentation $(1/2, 0)$ est appelé spineur de Weyl gauche et est dénoté par ψ_L et un spineur dans

$(0, 1/2)$ est un spineur de Weyl droit ψ_R. Dans la représentation $(1/2, 0)$, $\boldsymbol{J}^-$ est représenté en termes de matrices 2×2 telles que $\boldsymbol{J}^- = \frac{\sigma}{2}$ et $\boldsymbol{J}^+ = 0$. Avec l'équation (1.8), on peut montrer que sous transformations de Lorentz un spineur gauche va se transformer selon :

$$\psi_L \to \Lambda_L \psi_L = \exp\left((-i\boldsymbol{\theta} - \boldsymbol{\eta}) \cdot \frac{\boldsymbol{\sigma}}{2}\right)\psi_L. \tag{1.15}$$

Et dans la représentation $(0, 1/2)$, un spineur droit se transforme selon

$$\psi_R \to \Lambda_R \psi_R = \exp\left((-i\boldsymbol{\theta} + \boldsymbol{\eta}) \cdot \frac{\boldsymbol{\sigma}}{2}\right)\psi_R. \tag{1.16}$$

Les représentations irréductibles $(1/2, 0)$ et $(0, 1/2)$ sont échangées sous parité tel qu'un spineur gauche devient un spineur droit et vice-versa.

Nous définissons un champ de Dirac tel que

$$\psi = \begin{pmatrix} \psi_L \\ \psi_R \end{pmatrix}. \tag{1.17}$$

Il possède quatre composantes complexes et fournit une base pour les transformations de Lorentz et de parité. Il se transforme selon

$$\psi \to \Lambda_D \psi = \begin{pmatrix} \Lambda_L & 0 \\ 0 & \Lambda_R \end{pmatrix}\psi, \tag{1.18}$$

sous transformation de Lorentz. Sous parité, il se tranforme selon $\psi' = \gamma^0 \psi$. Nous renvoyons le lecteur au cours [2] pour plus de détails sur les différentes représentations du groupe de Lorentz.

1.2 La relativité générale

Cette section s'inspire des livres [3, 4].

En relativité restreinte, un observateur libre se déplace selon les géodésiques de la métrique de l'espace-temps qui est plat. En relativité générale (RG), un observateur libre se déplace selon les géodésiques mais cette fois l'espace-temps est courbe.

La relativité est invariante par difféomorphisme (sous une transformation générale de coordonnées). On peut alors procéder de deux façons différentes ce qui va amener à décrire la RG avec différents formalismes [5]. Un premier formalisme consiste à garder les points de la variété fixes mais à changer le système de coordonnées dans l'espace $\mathbb{R}^4$. On fait un changement des vecteurs de base (qui vivent dans $\mathbb{R}^4$) d'un même quadrivecteur (qui vit dans $\mathcal{M}$). C'est le formalisme passif (formalisme de coordonnées). Une autre façon de procéder est de garder la base de $\mathbb{R}^4$ fixe mais de faire bouger les points sur la variété. On change de quadrivecteur mais on garde les même vecteurs de base. C'est le formalisme actif (formalisme des tétrades).

Dans la suite, les indices grecques sont des indices d'espace-temps alors que les indices latins sont des indices de Lorentz, vivant dans l'espace de Minkowski tangent à l'espace-temps. Dans ce manuscrit nous considérons la RG sans torsion.

1.2.1 Les différents formalismes

Le formalisme de coordonnées, passif

L'espace-temps en représenté par la métrique $\boldsymbol{g}$ qui est un tenseur de type (0,2), symétrique et non dégénéré. Une dérivée covariante (ou connexion) est un opérateur d'ordre 1 qui respecte la règle de Leibniz. Soit $\boldsymbol{u}$ un vecteur de l'espace tangent, la dérivée covariante $\boldsymbol{\nabla}$ est définie par

$$\nabla_\mu u^\alpha = \partial_\mu t^\alpha + \Gamma^\alpha_{\mu\beta} u^\beta. \tag{1.19}$$

Soit une courbe C de vecteur tangent $\boldsymbol{u}$, un vecteur $\boldsymbol{v}$ suit le transport parallèle sur C si

$$u^\mu \nabla_\mu v^\alpha = 0. \tag{1.20}$$

Une courbe C est une géodésique si le vecteur vitesse $\boldsymbol{dx/dt}$ suit le transport parallèle, c'est-à-dire

$$\frac{d^2 x^\mu}{dt^2} + \Gamma^\mu_{\alpha\beta} \frac{dx^\alpha}{dt} \frac{dx^\beta}{dt}. \tag{1.21}$$

Une fois la métrique donnée, il existe un choix naturel et unique pour définir la dérivée covariante, provenant du transport parallèle. Si on transporte parallèlement deux vecteurs $\boldsymbol{v}$ et $\boldsymbol{w}$ sur une courbe, il faut que leur produit scalaire reste inchangé, c'est-à-dire

$$u^\mu \nabla_\mu (g_{\alpha\beta} v^\alpha w^\beta) = 0, \tag{1.22}$$

avec $\boldsymbol{v}$ et $\boldsymbol{w}$ satisfaisant l'équation (1.20). La règle de Leibniz nous permet d'obtenir

$$u^\mu v^\alpha w^\beta \nabla_\mu g_{\alpha\beta} = 0. \tag{1.23}$$

Cette équation (1.23) est satisfaite pour toutes les courbes et tous les vecteurs transportés parallèlement si et seulement si

$$\nabla_\mu g_{\alpha\beta} = \partial_\mu g_{\alpha\beta} - g_{\rho\beta}\Gamma^\rho_{\alpha\mu} - g_{\alpha\rho}\Gamma^\rho_{\beta\mu} = 0. \tag{1.24}$$

C'est une condition additionelle, dite condition de métricité, qui permet de définir la dérivée covariante de manière unique [3]. Cette dernière est appelée connexion de Levi-Civita et ses composantes sont les symboles de Christoffel :

$$\Gamma^\mu_{\alpha\beta} = \frac{1}{2} g^{\mu\nu} (\partial_\alpha g_{\beta\nu} + \partial_\beta g_{\alpha\nu} - \partial_\nu g_{\alpha\beta}). \tag{1.25}$$

La RG nous indique que l'espace-temps est courbé lorsqu'il y a un contenu en matière. La courbure F de la connexion de Levi-Civita s'écrit

$$F(\boldsymbol{u}, \boldsymbol{v})\boldsymbol{w} = \nabla_{\boldsymbol{u}} \nabla_{\boldsymbol{v}} \boldsymbol{w} - \nabla_{\boldsymbol{v}} \nabla_{\boldsymbol{u}} \boldsymbol{w} - \nabla_{[\boldsymbol{u},\boldsymbol{v}]} \boldsymbol{w}. \tag{1.26}$$

On peut alors définir le tenseur de Riemann $\boldsymbol{R}$. C'est un tenseur de type (1,3) défini tel que

$$\begin{aligned} R^\rho_{\sigma\mu\nu} &= dx^\rho (F(\partial_\mu, \partial_\nu)\partial_\sigma & (1.27)\\ &= \partial_\mu \Gamma^\rho_{\nu\sigma} - \partial_\nu \Gamma^\rho_{\mu\sigma} + \Gamma^\rho_{\mu\lambda}\Gamma^\lambda_{\nu\sigma} - \Gamma^\rho_{\nu\lambda}\Gamma^\lambda_{\mu\sigma}. & (1.28) \end{aligned}$$

En le contractant on obtient le tenseur de Ricci

$$R_{\sigma\nu} = R^{\rho}{}_{\sigma\rho\nu}. \tag{1.29}$$

Puis une deuxième contraction nous permet de définir le scalaire de Ricci

$$R = R^{\nu}{}_{\nu}. \tag{1.30}$$

Le tenseur de Weyl $\boldsymbol{C}$ est la partie sans trace du tenseur de Riemann. En quatre dimensions on a

$$C_{\rho\sigma\mu\nu} = R_{\rho\sigma\mu\nu} - \tfrac{1}{2}(g_{\rho\mu}R_{\sigma\nu} + g_{\sigma\nu}R_{\rho\mu} - g_{\sigma\mu}R_{\rho\nu} - g_{\rho\nu}R_{\sigma\mu}) + \tfrac{1}{6}(g_{\rho\mu}g_{\sigma\nu} - g_{\rho\nu}g_{\sigma\mu})R. \tag{1.31}$$

La matière courbe l'espace-temps et cette interaction est décrite par l'équation d'Einstein

$$G_{\mu\nu} + \Lambda g_{\mu\nu} = \kappa T_{\mu\nu}, \tag{1.32}$$

avec $G_{\mu\nu} \equiv R_{\mu\nu} - \frac{1}{2}g_{\mu\nu}R$ le tenseur d'Einstein, Λ la constante cosmologique, $T^{\mu\nu}$ le tenseur énergie-impulsion et $\kappa = 8\pi$ en unités naturelles. Cette équation (1.32) peut être retrouvée à partir de l'action donnée par

$$S = \int \left[\frac{1}{2\kappa}(R[g] - 2\Lambda) + \mathcal{L}_{mat}\right] d^4x \sqrt{-\det g}, \tag{1.33}$$

avec $\mathcal{L}_{mat}$ la densité Lagrangienne de la matière et R le scalaire de Ricci. Le tenseur énergie-impulsion est donné par

$$T_{\mu\nu} = -\frac{1}{2\pi}\frac{1}{\sqrt{-\det g}}\frac{\delta S_{mat}}{\delta g^{\mu\nu}} \tag{1.34}$$

La partie gravitationnelle de l'équation (1.33) est appelée action d'Einstein-Hilbert

$$S_{EH} = \frac{1}{2\kappa}\int d^4x \sqrt{-\det g} R[g]. \tag{1.35}$$

Ainsi, l'espace-temps est décrit par une variété Riemannienne, qui se courbe selon le contenu en matière et cela est décrit par l'équation d'Einstein (1.32). Ce formalisme de tenseurs est celui qui est le plus utilisé. Il a l'avantage d'expliciter l'interprétation physique des équations de façon naturelle. Il est notamment utilisé pour décrire la RG sous le formalisme Hamiltonien qui sera utilisé en gravité quantique à boucles (voir la section 1.5). Mais d'autres formalismes sont également utilisés et possèdent d'autres avantages. Les formalismes suivants sont actifs.

Le formalisme des tétrades, actif, réel

Les coefficients de connexion affine $\Gamma^{\mu}{}_{\alpha\beta}$ sont remplacés par des coefficients de connexion de spin $\Omega^{a}{}_{b\mu}$. Dans le formalisme des tétrades, on associe à chaque point de l'espace-temps une base de quatre vecteurs contravariants $e^{a}{}_{\alpha}$. Ces derniers permettent de passer de l'espace-temps à l'espace de Lorentz, ils sont définis tels que

$$g_{\alpha\beta} = e^{a}{}_{\alpha}e^{b}{}_{\beta}\eta_{ab}. \tag{1.36}$$

La matrice inverse e_{a}^{β} est définie par

$$e^a{}_\alpha e_a{}^\beta = \delta^\beta_\alpha \text{ et } e^a{}_\alpha e_b{}^\alpha = \delta^a_b. \tag{1.37}$$

Une transformation de coordonnées est décrite par

$$e^a{}_\mu = e^a{}_\alpha \frac{\partial x^\alpha}{\partial x'^\mu}, \tag{1.38}$$

et une transformation de Lorentz par

$$e^a{}_\mu = e^b{}_\mu \Lambda^a{}_b. \tag{1.39}$$

Dans ce formalisme, la condition de métricité s'écrit

$$\nabla_\mu e^a{}_\rho = \partial_\mu e^a{}_\rho - \Gamma^\beta_{\rho\mu} e^a{}_\beta + \Omega_b{}^a{}_\mu e^b{}_\rho = 0, \tag{1.40}$$

avec $\Omega_b{}^a{}_\mu$ la connexion de spin donnée par $\Omega_b{}^a{}_\mu = e^a{}_\nu \Gamma^\nu{}_{\sigma\mu} e_b{}^\sigma + e^a{}_\nu \partial_\mu e_b{}^\nu$. On peut définir les coefficients de rotation de Ricci

$$\gamma_{abc} = e_a{}^\mu e_{b\mu;\nu} e_c{}^\nu. \tag{1.41}$$

Ils sont antisymétriques par changement des deux premiers indices. Le tenseur de Riemann en indices de Lorentz s'écrit

$$\begin{aligned} R_{abcd} &= R_{\rho\sigma\mu\nu} e_a{}^\rho e_b{}^\sigma e_c{}^\mu e_d{}^\nu & (1.42)\\ &= -\gamma_{abc,d} + \gamma_{abd,c} + \gamma_{baf}[\gamma_c{}^f{}_d - \gamma_d{}^f{}_c] + \gamma_{fac}\gamma_b{}^f{}_d - \gamma_{fad}\gamma_b{}^f{}_c. & (1.43) \end{aligned}$$

Le formalisme de Newman-Penrose, actif, complexe

Le formalisme de Newman-Penrose est un formalisme des tétrades, avec un choix spécifique de vecteurs : $\boldsymbol{l}$ et $\boldsymbol{n}$ sont réels, $\boldsymbol{m}$ et $\overline{\boldsymbol{m}}$ sont complexes conjugués. Les quatre vecteurs sont nuls

$$\boldsymbol{l}.\boldsymbol{l} = \boldsymbol{n}.\boldsymbol{n} = \boldsymbol{m}.\boldsymbol{m} = \overline{\boldsymbol{m}}.\overline{\boldsymbol{m}} = 0. \tag{1.44}$$

Ils satisfont à la condition d'orthogonalité

$$\boldsymbol{l}.\boldsymbol{m} = \boldsymbol{l}.\overline{\boldsymbol{m}} = \boldsymbol{n}.\boldsymbol{m} = \boldsymbol{n}.\overline{\boldsymbol{m}} = 0. \tag{1.45}$$

On impose également la condition de normalisation

$$\boldsymbol{l}.\boldsymbol{n} = 1 \quad \text{et} \quad \boldsymbol{m}.\overline{\boldsymbol{m}} = -1. \tag{1.46}$$

Les dérivées directionnelles sont définies par des symboles spéciaux

$$D = l^\alpha \partial_\alpha; \quad \Delta = n^\alpha \partial_\alpha; \quad \delta = m^\alpha \partial_\alpha; \quad \text{et} \quad \delta^* = \overline{m}^\alpha \partial_\alpha. \tag{1.47}$$

On associe également des symboles à certains coefficients de rotation de Ricci. Ils sont appelés coefficients de spin

$$\kappa = \gamma_{311} \qquad \rho = \gamma_{314} \qquad \epsilon = \frac{1}{2}(\gamma_{211} + \gamma_{341})$$
$$\sigma = \gamma_{313} \qquad \mu = \gamma_{243} \qquad \tau = \frac{1}{2}(\gamma_{212} + \gamma_{342})$$
$$\lambda = \gamma_{244} \qquad \tau = \gamma_{312} \qquad \alpha = \frac{1}{2}(\gamma_{214} + \gamma_{344})$$
$$\nu = \gamma_{242} \qquad \pi = \gamma_{241} \qquad \beta = \frac{1}{2}(\gamma_{213} + \gamma_{343})$$

Dans ce formalisme, les dix composantes indépendantes du tenseur de Weyl sont représentées par cinq scalaires complexes

$$\begin{aligned}
\Psi_0 &= -C_{\alpha\beta\gamma\delta} l^\alpha m^\beta l^\gamma m^\delta &&= C_{1313}, \\
\Psi_1 &= -C_{\alpha\beta\gamma\delta} l^\alpha n^\beta l^\gamma m^\delta &&= C_{1213}, \\
\Psi_2 &= -C_{\alpha\beta\gamma\delta} l^\alpha m^\beta \overline{m}^\gamma n^\delta &&= C_{1342}, \\
\Psi_3 &= -C_{\alpha\beta\gamma\delta} l^\alpha n^\beta \overline{m}^\gamma n^\delta &&= C_{1242}, \\
\Psi_4 &= -C_{\alpha\beta\gamma\delta} n^\alpha \overline{m}^\beta n^\gamma \overline{m}^\delta &&= C_{2424}.
\end{aligned} \tag{1.48}$$

Les équations d'Einstein seront écrites avec les dérivées directionnelles, les coefficients de spin et ces cinq scalaires.

Ce formalisme sera utilisé pour l'article sur la section efficace des trous noirs en LQG (section 3.2) et celui sur l'isospectralité (section 3.3.3).

Le formalisme spinoriel, actif, complexe

Ce formalisme est un cas particulier du formalisme des tétrades. Il est défini avec les quatre matrices 4×4 γ^a, elles vivent dans l'espace de Minkowski et les tétrades permettent de les décrire en espace courbe

$$\gamma^\mu = \gamma^a e^\mu_a. \tag{1.49}$$

Elles obéissent à l'algèbre de Clifford

$$\{\gamma^a, \gamma^b\} = 2\eta^{ab}, \tag{1.50}$$

et en utilisant la propriété (1.36), on a alors

$$\{\gamma^\mu, \gamma^\nu\} = 2g^{\mu\nu}. \tag{1.51}$$

On peut écrire une représentation complexe de l'algèbre de Lorentz

$$\sigma^{ab} = \frac{1}{4}[\gamma^a, \gamma^b]. \tag{1.52}$$

Il est possible de vérifier que ces matrices satisfont effectivement les règles de commutation de l'algèbre de Lorentz. Dans la représentation spinorielle, la transformation de Lorentz s'écrit

$$\Lambda_{\frac{1}{2}} = e^{\frac{1}{2}\omega_{ab}\sigma^{ab}}, \tag{1.53}$$

avec ω_{ab} les six paramètres du groupe de Lorentz. Les matrices γ sont invariantes par rotation simultanée de leur indices vectoriels et spinoriels [6]

$$\Lambda_{\frac{1}{2}}^{-1}\gamma^a\Lambda_{\frac{1}{2}} = \Lambda^a{}_b\gamma^b. \tag{1.54}$$

La connexion spinorielle est définie par

$$\Omega_\mu = \frac{1}{2}\Omega^{ab}{}_\mu\sigma_{ab}, \tag{1.55}$$

et la condition de métricité s'écrit

$$\nabla_\mu\gamma^a = \partial_\mu\gamma^a + \gamma^b\Omega^a_{b\mu} + [\gamma^a, \Omega_\mu] = 0. \tag{1.56}$$

Ce formalisme sera utilisé pour l'article de l'étude des spineurs, dans des potentiels de types hydrogène et oscillateur harmonique, qui décrira également l'effet Aharonov Bohm gravitationnel (section 4.3), ainsi que dans l'article sur la section efficace de la diffusion Compton (section 4.4).

Les équations d'Einstein sont non linéaires et il est très compliqué de trouver des solutions. Grâce aux simplifications dues aux symétries, plusieurs solutions on été trouvées. La première solution est celle de l'univers en expansion. La deuxième solution est celle de trou noir (mais plus généralement c'est une solution de corps sphériques statiques) qui décrit une région de l'espace-temps où la matière ne peut pas s'échapper. Dans les deux cas, la RG prédit une singularité. La gravité quantique pourrait, quant à elle, permettre de résoudre ces singularités.

1.2.2 La cosmologie

On a vu précédemment que la métrique est reliée à la distribution de matière, par les équations d'Einstein (1.32). Pour décrire l'univers comme un tout, ce dernier est supposé homogène et isotrope à très grande échelle. C'est le principe cosmologique, consistant avec les observations. Ces symétries simplifient énormément les équations d'Einstein, et il existe une solution décrite par la métrique de Friedmann-Lemaître-Robertson-Walker (FLRW)

$$ds^2 = -N^2(t)dt^2 + a^2(t)\left[\frac{dr^2}{1-kr^2} + r^2 + r^2\sin^2\theta d\phi\right], \tag{1.57}$$

avec t le temps cosmologique, k le facteur de courbure et a le facteur d'échelle. La fonction lapse $N(t)$ ne joue aucun rôle dynamique, elle correspond un multiplicateur de Lagrange. Elle permet de définir un choix de jauge pour l'évolution de la composante temporelle. L'action est donnée par l'équation (1.33). Pour un univers décrit par l'équation (1.57), le scalaire de Ricci est donné par

$$R = 6\left(\frac{\ddot{a}}{N^2a} + \frac{\dot{a}^2}{N^2a^2} + \frac{k}{a^2} - \frac{\dot{a}\dot{N}}{aN^3}\right), \tag{1.58}$$

et l'action d'Einstein-Hilbert Eq.(1.35) se réduit à

$$S_{EH} = \frac{1}{2\kappa}\int d^4x N a^3\Big(R - 2\Lambda + 2\kappa\mathcal{L}_M\Big). \tag{1.59}$$

avec Λ la constante cosmologique et $\mathcal{L}_M$ le Langrangien qui décrit le contenu en matière de l'univers. La dynamique est dictée par le contenu de l'univers. On suppose que l'univers est rempli d'un fluide parfait, ainsi le tenseur énergie-impulsion s'écrit

$$T_{\mu\nu} = \rho u_\mu u_\nu + p(g_{\mu\nu} + u_\mu u_\nu), \tag{1.60}$$

avec ρ la densité d'énergie, p la pression et u la quadri-vitesse du fluide. Les équations d'Einstein se réduisent alors aux équations de Friedmann

$$H^2 \equiv \left(\frac{\dot{a}}{a}\right)^2 = \frac{\kappa}{3}\rho + \frac{\Lambda}{3} - \frac{k}{a^2}, \tag{1.61}$$

$$\frac{\ddot{a}}{a} = -\frac{\kappa}{6}(\rho + 3p) + \frac{\Lambda}{3}. \tag{1.62}$$

En multipliant l'équation (1.61) par a^2, différenciant cette équation et éliminant $\ddot{a}$ via l'équation (1.62), on obtient

$$\dot{\rho} + 3H(\rho + 3p) = 0. \tag{1.63}$$

On peut alors décrire la densité d'énergie ρ de chaque contenu en fonction de a et du paramètre d'état $\omega \equiv p/\rho$. En supposant ω constant, on a

$$\rho(t) \sim a(t)^{-3(1+\omega)}. \tag{1.64}$$

Le paramètre ω décrit le contenu en matière : $\omega = 1/3$ pour le rayonnement, $\omega = 0$ pour la matière non relativiste et $\omega = -1$ pour une constante cosmologique. Ainsi, pour $\omega \neq -1$, l'expansion de l'univers est décrite selon

$$a(t) \sim t^{\frac{2}{3(1+\omega)}}. \tag{1.65}$$

Le cas $\omega = -1$ décrit un univers dynamique dont la densité d'énergie reste constante au cours du temps. Cela donne lieu à une expansion exponentielle de l'univers, Eq. (1.61). Actuellement nous observons une telle expansion. L'explication standard décrit un univers dominé par l'énergie noire dont les propriétés restent encore incertaines et dont les effets sont décrits par Λ. Une description très rapide du modèle cosmologique serait la suivante : nous avons le Big-Bang, puis l'univers est principalement rempli par le rayonnement, ensuite la matière non relativiste domine (les grandes structures se créent) et enfin nous avons la phase d'expansion accélérée actuelle. Il y a eu une phase d'équilibre entre les photons et les baryons, puis l'expansion de l'univers a permis aux photons de s'échapper de cette interaction et de se propager à travers l'univers. C'est grâce à ce fond diffus cosmologique (dit CMB, pour Cosmic Microway Background), qu'aujourd'hui nous pouvons effectuer des observations des premiers instants de l'univers. Dans ce modèle cosmologique, nous introduisons également l'inflation. Cette dernière décrit une phase d'expansion exponentielle (espace de de Sitter ≡ dS) qui a eu lieu juste après le Big Bang. Ce modèle permet de résoudre les problèmes d'homogénéité, d'isotropie, d'horizon et de platitude. De plus, cette phase d'inflation est importante pour les perturbations primordiales, que

nous verrons dans la section 2.3.1. L'inflation permet également de décrire la création des particules primordiales. En effet, pendant l'inflation on a un vide privilégié associé à l'espace dS, et brutalement, on passe à un autre vide privilégié lorsque l'inflation s'arrête et que l'univers est dominé par le rayonnement. Ainsi la transition est décrite par les transformations de Bogoliubov (1.119, 1.120).

En cosmologie standard, il n'existe aucune prédiction sur la durée de l'inflation. Par contre, il faut qu'elle dure assez longtemps pour permettre de résoudre le problème de l'horizon. Cela signifie que l'inflation doit établir un contact causal entre des régions éloignées du CMB. La durée de l'inflation est exprimée en nombre d'e-folds N défini tel que

$$N = \ln\left(\frac{a_i}{a_f}\right), \tag{1.66}$$

avec a_i et a_f les facteurs d'échelle au début et à la fin de l'inflation, respectivement. Cette phase d'expansion peut être expliquée si l'univers est rempli d'un champ scalaire ϕ. C'est ce modèle ci que nous présentons, cependant il existe un large panel de modèles aptent à générer une phase d'inflation [7].

La dynamique d'un champ scalaire minimalement couplé à la gravité, avec $\Lambda = 0$, est décrit par l'action suivante

$$S = S_{EH} + S_\phi = \int d^4x \sqrt{-g}\left(\frac{1}{2\kappa}R + \frac{1}{2}\partial^\mu\phi\partial_\mu\phi - V(\phi)\right), \tag{1.67}$$

Le tenseur énergie-impulsion correspondant se déduit en dérivant l'action par rapport à $g_{\mu\nu}$ (1.34), on obtient

$$T_{\mu\nu} = -\frac{2}{\sqrt{-\det g}}\frac{\delta S_\phi}{\delta g_{\mu\nu}} = \partial_\mu\phi\partial_\nu\phi - g_{\mu\nu}\left(\frac{1}{2}\partial^\sigma\phi\partial_\sigma\phi + V(\phi)\right). \tag{1.68}$$

On en déduit

$$\rho = \frac{1}{2}\dot\phi^2 + V(\phi) \quad \text{et} \quad P = \frac{1}{2}\dot\phi^2 - V(\phi). \tag{1.69}$$

Ainsi dans un univers homogène et isotrope, l'équation de Klein-Gordon se réduit à

$$\ddot\phi + 3H\dot\phi + \frac{dV}{d\phi} = 0. \tag{1.70}$$

Dans le cas d'un régime de roulement lent (dit "slow-roll"), c'est-à-dire lorsque l'énergie potentielle domine par rapport à l'énergie cinétique, on a une expansion accélérée

$$H^2 \approx \frac{\kappa}{3}V \quad \text{et} \quad \dot\phi \approx -\frac{1}{3H}\frac{dV}{d\phi} \approx \text{constante}. \tag{1.71}$$

Ce modèle décrit une phase d'inflation dans l'univers primordial dictée par la dynamique d'un champ scalaire ϕ.

1.2.3 Les trous noirs

La solution stationnaire, axisymétrique et asymptotiquement plate aux équations d'Einstein dans le vide, la plus générale décrit les trous noirs de masse M, avec une charge Q et un moment cinétique J. Ils sont appelés trous noirs de Kerr-Newman. Ceci est confirmé par le théorème de la calvitie : un trou noir est caractérisé par seulement ces trois paramètres : M, Q et J et ce, peu importe la façon dont il a été formé.

Les trous noirs de Schwarzschild

Les trous noirs de Schwarzschild sont une solution statique à symétrie sphérique des équations d'Einstein dans le vide. D'après les symétries, cet espace-temps peut être décrit par une variété $\mathbb{S}_2 \times \mathbb{U}_2$, avec $\mathbb{S}_2$ la sphère à deux dimensions, dont la métrique s'écrit

$$d\Omega^2 = d\theta^2 + d\varphi^2 \sin^2\theta \tag{1.72}$$

et $\mathbb{U}_2$ une variété à deux dimensions dont la métrique n'est pas définie. Sur $\mathbb{U}_2$, on peut définir des coordonnées u et v telles que les courbes u = constante et v = constante soient de type lumière. La métrique s'écrit alors sous la forme de Kruskal

$$ds^2 = -\frac{32M^3}{r} e^{\frac{r}{2M}} du dv - r^2 d\Omega^2, \tag{1.73}$$

où r est relié à u et v via

$$-uv = \left(1 - \frac{r}{2M}\right) e^{\frac{r}{2M}}. \tag{1.74}$$

On peut ensuite effectuer une transformation conforme pour passer des coordonnées de Krushkal (u, v) aux coordonnées cartésiennes de Penrose $(\tilde{U}, \tilde{V})$

$$u = \tan \tilde{U} \tag{1.75}$$
$$v = \tan \tilde{V} \tag{1.76}$$

L'espace-temps de Schwarzschild peut être alors représenté par un diagramme de Penrose, tracé sur la Figure 1.1. La région I définit l'extérieur du trou noir $r > 2M$ tandis que la région II est l'intérieur du trou noir $r < 2M$. La région IV décrit une solution de trou blanc. Dans les régions I et III, on peut poser

$$\frac{u}{v} = e^{\frac{t}{2M}}, \tag{1.77}$$

et obtenir la métrique de Schwarzschild

$$ds^2 = \left(1 - \frac{2M}{r}\right) dt^2 - \frac{1}{1 - \frac{2M}{r}} dr^2 - r^2 d\Omega^2. \tag{1.78}$$

L'horizon des événements est une hypersurface de rayon $r_h = 2M$, appelé rayon de Schwarzschild.

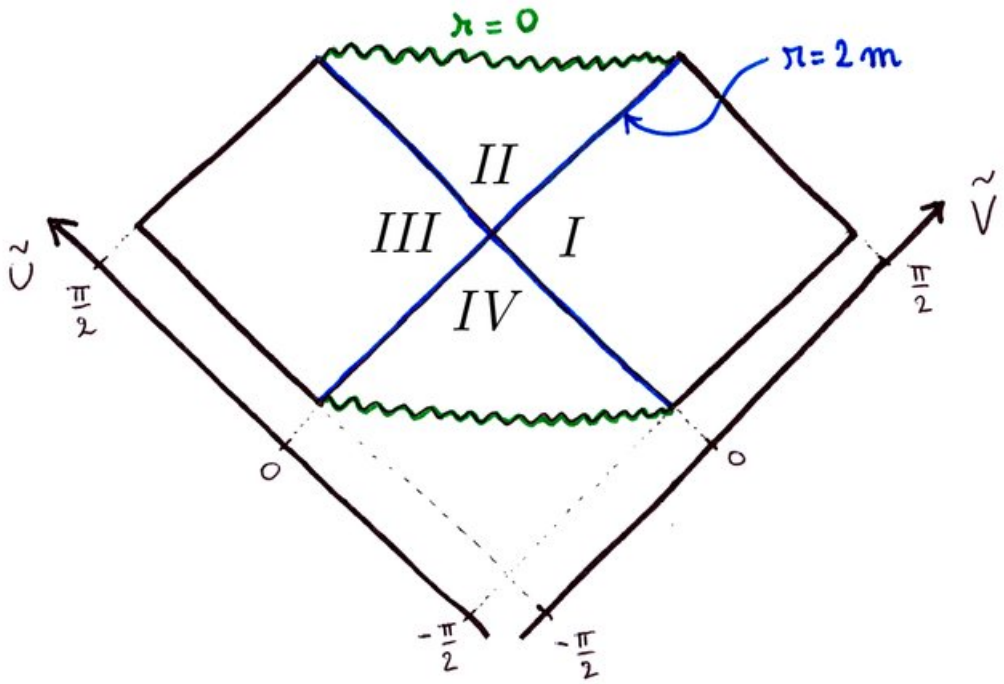

FIGURE 1.1 – Diagramme de Penrose de l'espace temps de Schwarzschild avec $\tilde{U}$ et $\tilde{V}$ les coordonnées cartésiennes de Penrose reliées aux coordonnées de Kruskal par les transformations (1.75) et (1.76) [8].

Les autres solutions et la classification des trous noirs

Le modèle des trous noirs de Schwarzschild est le plus simple étant donné qu'il ne dépend que de la masse. Mais, comme on l'a vu précédemment les trous noirs peuvent dépendre de deux autres paramètres.

Un trou noir de Reissner-Nordström est une solution, à symétrie sphérique, des équations d'Einstein couplées aux équations de Maxwell. Avec Q la charge électrique, la métrique s'écrit

$$ds^2 = \left(1 - \frac{2M}{r} + \frac{Q^2}{r}\right)dt^2 - \frac{1}{1 - \frac{2M}{r} + \frac{Q^2}{r}}dr^2 - r^2 d\Omega^2. \tag{1.79}$$

Ces trous noirs possèdent deux horizons : un horizon des événements, externe, et un horizon de Cauchy, interne.

Les trous noirs en rotation sont décrits par la métrique de Kerr. Avec J le moment cinétique, dans les coordonnées de Boyer-Lindquist, la métrique s'écrit

$$\begin{aligned} ds^2 =& \left(1 - \frac{2Mr}{r^2 + a^2\cos^2\theta}\right)dt^2 + \frac{4Mra\sin^2\theta}{r^2 + a^2\cos^2\theta}dtd\phi - \frac{r^2 + a^2\cos^2\theta}{r^2 - 2Mr + a^2}dr^2 \\ & - (r^2 + a^2\cos^2\theta)d\theta^2 - \left(r^2 + a^2 + \frac{2Mra^2\sin^2\theta}{r^2 + a^2\cos^2\theta}\right)\sin^2\theta d\phi^2, \end{aligned} \tag{1.80}$$

avec $a = J/M$. Cette solution correspond aux trous noirs qu'on observe dans l'univers. En effet, les trous noirs de Reissner-Nordström sont instables car, de part leur charge, ils vont attirer les particules chargées de sorte à devenir neutre.

On classe les trous noirs selon leur intervalle de masse :

- les trous noirs supermassifs qui se trouvent aux centres des galaxies : $M \sim (10^5 - 10^9)M_\odot$,
- les trous noirs intermédiaires $M \sim 10^3 M_\odot$,
- les trous noirs de masses stellaires $M \sim 10 M_\odot$,
- les trous noirs microscopiques.

Dans ce manuscrit, nous aborderons les trous noirs microscopiques, qui sont considérés pour le modèle des trous noirs en rebond (voir la section 3.1). Cependant leur existence n'est pas avérée. En ce qui concerne les ondes gravitationnelles actuellement détectées, elles proviennent de la coalescence de trous noirs stellaires. Les récentes mesures de LIGO vont peut-être chambouler ces catégories en faisant apparaître une sorte de continuum (par exemple avec les trous noirs de 100 masses solaires).

1.3 La théorie quantique des champs

Après avoir introduit la RG pour décrire les espace-temps courbes, nous présentons quelques aspects de théorie quantique des champs. Dans cette section, nous nous plaçons en espace plat puis nous aborderons la description des champs quantiques en espace courbe dans la section suivante. Cette section s'appuie sur les références [1] et [6].

1.3.1 Quantification du champ scalaire

Nous considérons un champ scalaire ϕ réel de masse m. Le Lagrangian d'un tel champ s'écrit

$$\mathcal{L} = \frac{1}{2}(\partial_\mu \phi \partial^\mu \phi - m^2 \phi^2), \tag{1.81}$$

Les équations d'Euler-Lagrange donnent l'équation de Klein-Gordon

$$(\partial_\mu \partial^\mu + m^2)\phi = 0. \tag{1.82}$$

Une onde plane $\phi = A\, exp(ip.x)$ est solution si

$$(p^0)^2 - \boldsymbol{p}^2 = m^2. \tag{1.83}$$

Pour définir une solution plus générale, nous avons besoin d'un produit scalaire

$$\langle \phi_1 | \phi_2 \rangle = -i \int_{\Sigma_t} d^3x \phi_1 \overleftrightarrow{\partial_0} \phi_2, \tag{1.84}$$

avec $f \overleftrightarrow{\partial_\mu} g = f\partial_\mu g - (\partial_\mu f)g$ et Σ_t l'hypersurface spatiale à t constant. Ce produit scalaire est indépendant du temps si les champs ϕ_1 et ϕ_2 sont solutions de l'équation de Klein-Gordon (1.82). Étant donné

$$\langle e^{ik_1^\mu x_\mu} | e^{ik_1^\mu x_\mu} \rangle = (E_{\boldsymbol{k}_1} + E_{\boldsymbol{k}_2}) e^{-i(E_{\boldsymbol{k}_1} - E_{\boldsymbol{k}_2})t} (2\pi)^3 \delta(\boldsymbol{k}_1 - \boldsymbol{k}_2), \tag{1.85}$$

un ensemble de modes orthogonaux est donné par

$$f_{\boldsymbol{k}}(x^\mu) = \frac{e^{ikx}}{\sqrt{E_{\boldsymbol{k}}}(2\pi)^3}. \tag{1.86}$$

Les modes sont dit de fréquence positive (respectivement négative) si

$$\partial_t f_{\boldsymbol{k}} = -iE_{\boldsymbol{k}} f_{\boldsymbol{k}} \quad \text{avec} \quad E_{\boldsymbol{k}} > 0 \tag{1.87}$$

$$(\partial_t f^*_{\boldsymbol{k}} = -iE_{\boldsymbol{k}} f^*_{\boldsymbol{k}} \quad \text{avec} \quad E_{\boldsymbol{k}} < 0 \quad \text{respectivement}) \tag{1.88}$$

Ainsi, une solution générale est la superposition d'ondes planes telle que

$$\phi(x) = \int \frac{d^3p}{(2\pi)^3\sqrt{2E_{\boldsymbol{p}}}}(a_{\boldsymbol{p}}e^{-ipx} + a^*_{\boldsymbol{p}}e^{ipx}) \mid_{p^0=E_{\boldsymbol{p}}}, \tag{1.89}$$

avec $E_{\boldsymbol{p}} = +\sqrt{\boldsymbol{p}^2 + m^2}$.

En TQC, les champs ϕ et leur moment conjugué Π passent au rang d'opérateurs et on impose les relations de commutation suivantes

$$[\phi(t,\boldsymbol{x}), \Pi(t,\boldsymbol{y})] = i\delta^{(3)}(\boldsymbol{x}-\boldsymbol{y}), \tag{1.90}$$

$$[\phi(t,\boldsymbol{x}), \phi(t,\boldsymbol{y})] = [\Pi(t,\boldsymbol{x}), \Pi(t,\boldsymbol{y})] = 0. \tag{1.91}$$

Pour promouvoir le champ ϕ au rang d'opérateur hermitien, on promeut $a_{\boldsymbol{p}}$ en opérateur et $a_{\boldsymbol{p}}*$ en opérateur hermitien conjugué. Ainsi, le champ scalaire s'écrit :

$$\phi(x) = \int \frac{d^3p}{(2\pi)^3\sqrt{2E_{\boldsymbol{p}}}}(a_{\boldsymbol{p}}e^{-ipx} + a^\dagger_{\boldsymbol{p}}e^{ipx}). \tag{1.92}$$

On a alors

$$[a_{\boldsymbol{p}}, a^\dagger_{\boldsymbol{q}}] = (2\pi)^3\delta^{(3)}(\boldsymbol{p}-\boldsymbol{q}), \tag{1.93}$$

$$[a_{\boldsymbol{p}}, a_{\boldsymbol{q}}] = [a^\dagger_{\boldsymbol{p}}, a^\dagger_{\boldsymbol{q}}] = 0. \tag{1.94}$$

Les états de Fock sont décrits par l'action des opérateurs création et annihilation sur le vide. L'état du vide $|0\rangle$ est choisi tel que

$$a_{\boldsymbol{p}}|0\rangle = 0. \tag{1.95}$$

La normalisation relativiste est définie par

$$|\boldsymbol{p}_1...\boldsymbol{p}_n\rangle = \sqrt{2E_{\boldsymbol{p}_1}}...\sqrt{2E_{\boldsymbol{p}_n}}a^\dagger_{\boldsymbol{p}}|0\rangle. \tag{1.96}$$

Elle est choisie ainsi pour avoir

$$\langle \boldsymbol{p}_m|\boldsymbol{p}_n\rangle = 2E_{\boldsymbol{p}_m}(2\pi)^3\delta^{(3)}(\boldsymbol{p}_m - \boldsymbol{p}_n) \tag{1.97}$$

car $2E_{\boldsymbol{p}_m}\delta^{(3)}(\boldsymbol{p}_m - \boldsymbol{p}_n)$ est un invariant de Lorentz. Le nombre de particules est défini par l'opérateur

$$N_{\boldsymbol{k}} = a^\dagger_{\boldsymbol{k}}a_{\boldsymbol{k}}, \tag{1.98}$$

agissant sur l'état du vide.

1.3.2 Quantification du champ de Dirac

Soit un champ de Dirac, son Lagrangien s'écrit

$$\mathcal{L} = \overline{\psi}(i\gamma^\mu \partial_\mu - m)\psi. \tag{1.99}$$

avec γ^μ des matrices à quatre dimensions qui respectent l'algèbre de Clifford (1.50). Les équations d'Euler-Lagrange donnent l'équation de Dirac

$$i\gamma^\mu \partial_\mu \psi - m\psi = 0. \tag{1.100}$$

Dans la représentation chirale donnée par l'équation (1.17), le Lagrangien s'écrit

$$\mathcal{L}_D = i\psi_L^\dagger \overline{\sigma}^\mu \partial_\mu \psi_L + i\psi_R^\dagger \sigma^\mu \partial_\mu \psi_R - m(\psi_L^\dagger \psi_R + \psi_R^\dagger \psi_L). \tag{1.101}$$

Sous parité on a $\psi_L \leftrightarrow \psi_R$ et $\partial_\rho \leftrightarrow -\partial_\rho$ (avec $\rho \, \epsilon \, (1,2,3)$) tels que $\overline{\sigma}^\mu \partial_\mu \leftrightarrow \sigma^\mu \partial_\mu$. La masse apparaît dans le terme qui mélange la partie gauche et la partie droite.

Ici nous avons présenté la représentation chirale des spineurs de Dirac définis par l'équation (1.17). Il est également possible de décrire les spineurs de Dirac dans une autre représentation. On peut définir un nouveau choix de spineur tel $\psi' = U\psi$ avec U une matrice unitaire constante. Dans ce cas on aura $\gamma^{\mu'} = U\gamma^\mu U^\dagger$ et $\overline{\psi}' = (\psi')^\dagger \gamma^0$. Avec la matrice unitaire

$$\frac{1}{\sqrt{2}} \begin{pmatrix} 1 & 1 \\ -1 & 1 \end{pmatrix}, \tag{1.102}$$

le spineur, en représentation standard, s'écrit

$$\psi = \begin{pmatrix} \psi_G \\ \psi_P \end{pmatrix} = \frac{1}{\sqrt{2}} \begin{pmatrix} \psi_R + \psi_L \\ \psi_R - \psi_L \end{pmatrix}, \tag{1.103}$$

avec ψ_G et ψ_P les parties grande et petite du spineur, respectivement. Cette représentation est bien adaptée lorsqu'on veut passer à la limite non relativiste. En effet, dans la représentation de l'impulsion, l'équation de Dirac (1.100) s'écrit

$$p^\mu \partial_\mu \psi - m\psi = 0. \tag{1.104}$$

Ainsi dans le référentiel au repos, dans la limite non relativiste, on a

$$\begin{pmatrix} p_0 \\ 0 \\ 0 \\ 0 \end{pmatrix} = \begin{pmatrix} m \\ 0 \\ 0 \\ 0 \end{pmatrix}. \tag{1.105}$$

Étant donné que la matrice γ^0 s'écrit

$$\begin{pmatrix} \mathbb{I}_2 & 0 \\ 0 & -\mathbb{I}_2 \end{pmatrix}, \tag{1.106}$$

en représentation standard, l'équation (1.104) avec le spineur (1.103) implique que la partie petite du spineur est nulle : $\psi_P = 0$.

Pour quantifier la théorie, on promet ψ et $\psi^\dagger$ au rang d'opérateurs qui satisfont les relations d'anticommutations

$$\{\psi_\alpha(\boldsymbol{x}, t), \psi^\dagger_\beta(\boldsymbol{y}, t)\} = \delta^{(3)}(\boldsymbol{x} - \boldsymbol{y})\delta_{\alpha\beta}, \tag{1.107}$$

avec $\alpha, \beta = 1, 2, 3, 4$ les indices de Dirac, qui indiquent les composantes du spineur. Les crochets $\{.\ ,\ .\}$ indiquent l'anticommutateur. Le champ de Dirac quantifié s'écrit

$$\psi(x) = \int \frac{d^3p}{(2\pi)^3\sqrt{2E_{\boldsymbol{p}}}} \sum_{s=1,2} \left(a_{\boldsymbol{p},s} u^s(p) e^{-ipx} + b^\dagger_{\boldsymbol{p},s} v^s(p) e^{ipx} \right), \tag{1.108}$$

avec $u^s(p)$ et $v^s(p)$ deux spineurs et s indique le spin. Les opérateurs a et $a^\dagger$ sont les opérateurs d'annihilation et de création d'une particule et de même, b et $b^\dagger$, pour les antiparticules. Ils respectent les crochets d'anticommutation :

$$\{a^r_{\boldsymbol{p}}, a^{s\dagger}_{\boldsymbol{q}}\} = \{b^r_{\boldsymbol{p}}, b^{s\dagger}_{\boldsymbol{q}}\} = (2\pi)^3\delta^{(3)}(\boldsymbol{p} - \boldsymbol{q})\delta^{rs}. \tag{1.109}$$

Après avoir vu quelques aspects de TQC en espace plat, nous allons étendre cette théorie à des espace-temps courbe, afin de prendre en compte certains caractéristiques de la RG.

1.4 La théorie quantique des champs en espace courbe

La TQC en espace courbe est une théorie semi-classique. Les champs sont quantifiés et ils se propagent dans un espace courbe qui lui n'est pas quantifié. Dans cette théorie, les états du vides sont différents en fonction de l'observateur. Quel vide correspond à l'état fondamental ? Comment interpréter le concept de particule ?

D'un point de vue heuristique, on passe de la TQC en espace plat à la TQC en espace courbe en remplaçant la dérivée partielle par une dérivée covariante. Par exemple, l'équation de Klein-Gordon (1.82), pour un champ minimalement couplé à la gravité, devient alors

$$\nabla_\mu \nabla^\mu \phi + m^2\phi = 0 \tag{1.110}$$

avec ∇_μ la dérivée covariante. On peut définir un produit scalaire sur une base de solutions ϕ_1 et ϕ_2 de l'équation (1.110). Pour une hypersurface Σ de type espace avec une métrique $\gamma_{\rho\sigma}$ et un vecteur normal n^μ, on définit

$$\langle \phi_1 | \phi_2 \rangle = -i \int_\Sigma d^3x (\phi_1 \nabla_\mu \phi_2^* - \phi_2^* \nabla_\mu \phi_1) n^\mu \sqrt{\det \gamma}. \tag{1.111}$$

Ce produit scalaire est l'analogue de l'équation (1.84) dans le cas d'un espace courbe. Il satisfait

$$\langle \phi_1 | \phi_2 \rangle^* = -\langle \phi_1^* | \phi_2^* \rangle = -\langle \phi_2 | \phi_1 \rangle \quad \text{et} \quad \langle \phi_1 | \phi_1^* \rangle = 0. \tag{1.112}$$

Les relations de commutations s'écrivent

$$[a(\phi_1), a^\dagger(\phi_2)] = \langle \phi_1 | \phi_2 \rangle \,. \tag{1.113}$$

On n'a plus de séparation entre le temps et l'espace comme c'était le cas en espace plat. Le vide et les opérateurs dépendent du choix de base f. Et il n'existe plus un choix de base privilégié. Soit $\{f_i\}$ et $\{g_i\}$ deux ensembles complets de solutions à normes positives, $\{f_i^*\}$ et $\{g_i^*\}$ deux ensembles complets de solutions à normes négatives et $\{f_i, f_i^*\}$ et $\{g_i, g_i^*\}$ deux ensembles complets de solutions à l'équation d'onde (1.110). L'opérateur champ s'écrit alors

$$\phi = \sum_i (a_i f_i + a_i^\dagger f_i^*) = \sum_i (b_i g_i + b_i^\dagger g_i^*). \tag{1.114}$$

Soit $|0_f\rangle$ le vide associé à la base des modes f, on a

$$a_i |0_f\rangle = 0, \quad \forall i \quad \text{et} \quad N_{fi} = a_i^\dagger a_i. \tag{1.115}$$

De même $|0_g\rangle$ est le vide associé à la base des modes g et on a

$$b_i |0_g\rangle = 0, \quad \forall i \quad \text{et} \quad N_{gi} = b_i^\dagger b_i. \tag{1.116}$$

Les modes g_i s'écrivent comme une combinaison linéaire des modes f_i et f_i^* et inversement. On a

$$g_i = \textstyle\sum_j (\alpha_{ij} f_j + \beta_{ij} f_j^*), \tag{1.117}$$
$$f_i = \textstyle\sum_j (\alpha_{ji}^* g_j - \beta_{ji} g_j^*). \tag{1.118}$$

Ainsi on déduit les transformations d'opérateurs

$$b_i = \sum_j (\alpha_{ij}^* a_j - \beta_{ij} a_j^\dagger), \tag{1.119}$$

$$a_i = \sum_j (\alpha_{ji} b_j + \beta_{ji}^* b_j^\dagger). \tag{1.120}$$

Les transformations (1.119) et (1.120) sont appelées transformations de Bogoliubov. Ceci nous permet de calculer la valeur moyenne de l'opérateur nombre de particules vu par un observateur qui utilise les modes g, dans le vide des modes f,

$$\langle 0_f | N_{gi} | 0_f \rangle = \langle 0_f | b_i^\dagger b_i | 0_f \rangle = \sum_j |\beta_{ij}|^2. \tag{1.121}$$

Ainsi, on observe que le nombre de particules est relatif. Ce processus permet d'expliquer l'effet Unruh [9], dont l'effet Hawking [10] est un cas particulier. Ce dernier sera plus amplement discuté dans la section 3.2.

1.5 La gravité quantique à boucles

Quantifier la gravité présente de nombreuses difficultés, la mécanique quantique et la gravité reposent sur des socles très différents. Le point clé est qu'en TQC on quantifie les champs sur un

espace-temps fixe et plat. Or, en gravité quantique, on voudrait quantifier l'espace-temps lui-même. Une des premières tentatives de quantification est celle de Wheeler-De Witt. Cette dernière n'est pas prédictive et utilise des objets mathématiquement mal définis. Une alternative est proposée par la gravité quantique à boucles (LQG). Il existe deux formulations équivalentes de la LQG. Nous présenterons la formulation canonique [5] qui est basée sur le formalisme Hamiltonien de la RG. Dans ce cas la covariance est explicitement brisée mais rétablie par une contrainte. Nous ne présenterons pas la formulation covariante [11], basée sur les mousses de spin, dans ce manuscrit.

1.5.1 Les théories de Yang-Mills

Une théorie de Yang-Mills est une théorie de jauge non abélienne. La relativité générale écrite avec les variables d'Ashtekar, introduites postérieurement, ressemble à une théorie de Yang-Mills. Ainsi, je vais introduire succinctement la construction d'une telle théorie. On a un potentiel vecteur A_μ dont les valeurs sont des éléments de l'algèbre de Lie

$$A_\mu = A_{i\mu} T^i. \tag{1.122}$$

avec T^i les générateurs de l'algèbre qui satisfont

$$[T^j, T^k] = i f^{jkl} T^l, \tag{1.123}$$

avec g la constante de couplage et f^{jkl} les constantes de structure de l'algèbre. La dérivée covariante de Yang-Mills pour décrire les transformations internes dans le groupe s'écrit

$$D_\mu = \partial_\mu + i\frac{g}{2} A_{i\mu} T^i, \tag{1.124}$$

On peut écrire le commutateur de deux dérivées covariantes de Yang-Mills,

$$[D_\mu, D_\nu] = -\frac{g}{2} F^i{}_{\mu\nu} T^i, \tag{1.125}$$

avec

$$F^i{}_{\mu\nu} = \partial_\mu A^i{}_\nu - \partial_\nu A^i{}_\mu + g\epsilon^{ijk} A^j{}_\mu A^k{}_\nu. \tag{1.126}$$

La dynamique est donnée par

$$D_\mu F^{\mu\nu} = 0, \tag{1.127}$$

et le Lagrangien est donné en utilisant la trace

$$L = -\frac{1}{4} \int d^3x F^i_{\mu\nu} F^{i\mu\nu} = 0. \tag{1.128}$$

Pour le groupe de Lie SU(2), dans la représentation fondamentale, les générateurs de l'algèbre su(2) sont les trois matrices de Pauli σ^i et les constantes de structure sont $f^{ijk} = 2\epsilon^{ijk}$.

1.5.2 Le formalisme ADM

La RG décrit un système totalement contraint, ainsi l'Hamiltonien s'écrit comme une combinaison linéaire de contraintes. Le formalisme ADM (Arnowitt, Deser, Misner) est une formulation Hamiltonienne de la RG, qui consiste à séparer l'espace et le temps. La covariance sera rétablie à l'aide d'une contrainte. La variété s'écrit $\mathcal{M} = \mathbb{R} \times \Sigma_t$ avec Σ_t une hypersurface spatiale au temps t. La direction du temps est décrite par le vecteur t^μ dont les trajectoires sont les courbes paramétrées par t et définies sur Σ_t. Soit n^μ un vecteur normal à Σ_t (de type temps) tel que $g_{\mu\nu}n^\mu n^\nu = -1$. Dans la suite, les indices α, β vont de 1 à 3. Avec la convention utilisée, la métrique spatiale est définie par

$$q_{\alpha\beta} = g_{\alpha\beta} - n_\alpha n_\beta. \tag{1.129}$$

Le vecteur t^α est décomposé en une composante tangente et une autre normale à Σ_t

$$t^\alpha = Nn^\alpha + N^\alpha. \tag{1.130}$$

La fonction lapse N définit un choix dans l'évolution de la composante temporelle. Le vecteur shift N^α définit un choix pour l'évolution des composantes spatiales. Ce sont des multiplicateurs de Lagrange. N est associé à la contrainte Hamiltonienne C, qui assure l'invariance de la théorie par reparamétrisation du temps. Les trois multiplicateurs N^α sont associées aux trois contraintes de moments H_α qui assurent l'invariance de la RG sous transformations de coordonnées spatiales à l'instant t donné. Un intervalle d'espace-temps s'écrit

$$ds^2 = N^2dt^2 - q_{\alpha\beta}(N^\alpha dt + dx^\beta)(N^\alpha dt + dx^\beta). \tag{1.131}$$

Ainsi l'action d'Einstein-Hilbert peut s'écrire

$$S = \frac{1}{2\kappa}\int_{\mathbb{R}} dt \int_\Sigma d^3x(P^{\alpha\beta}\dot{q}_{\alpha\beta} - [N^\alpha\mathcal{H}_\alpha + N\mathcal{H}]), \tag{1.132}$$

avec $\dot{q}_{\alpha\beta}$ la dérivée de Lie par rapport au temps telle que

$$\dot{q}_{\alpha\beta} = \mathcal{L}_t q_{\alpha\beta} = N\mathcal{L}_n q_{\alpha\beta} + \mathcal{L}_{N^\gamma} q_{\alpha\beta}, \tag{1.133}$$

et $P_{\alpha\beta}$ le moment conjugué de $q_{\alpha\beta}$, C et $\mathcal{H}_\alpha$ sont les densités de contrainte Hamiltonienne et de moments, respectivement. Dans ce qui suit, nous allons décrire cette théorie avec de nouvelles variables : les variables d'Ashtekar.

1.5.3 Les variables d'Ashtekar

La métrique spatiale peut s'exprimer à l'aide des triades $e^i{}_\alpha$

$$q_{\alpha\beta} = e^i{}_\alpha e^j{}_\beta \delta_{ij}. \tag{1.134}$$

Les triades sont invariantes par rotation, ce qui rajoute trois degrés de liberté supplémentaires. Les cotriades sont des 1-formes à valeur dans su(2). L'extension de l'espace des phases fera ainsi apparaître trois nouvelles contraintes : les contraintes de Gauss G_i. Historiquement, Wheeler et DeWitt ont quantifié la gravité avec la métrique spatiale $q_{\alpha\beta}$ et la courbure extrinsèque de l'hypersurface $K_{\alpha\beta}$.

Néanmoins la théorie est mal définie et ces problèmes sont résolus en LQG grâce à l'introduction des variables d'Ashtekar. La première variable est la densité triade

$$E_i^{\ \alpha} = \sqrt{\det(q)} e_i^{\ \beta}. \tag{1.135}$$

On peut ensuite définir la dérivée covariante D_α, purement spatiale, telle que

$$D_\alpha E_i^{\ \beta} = \partial_\alpha E_i^{\ \beta} + \varepsilon^k_{\ ij} A^k_{\ \alpha} E_k^{\ \beta} \tag{1.136}$$

avec $A^k_{\ \alpha}$ une nouvelle connexion qui dépend de la connexion de spin $\Omega^{ij}_{\ \ \alpha}$ et de $K_{\alpha\beta}$:

$$A^k_{\ \alpha} = \Omega^{ij}_{\ \ \alpha} \varepsilon^k_{\ ij} + \gamma K^k_{\ \alpha}. \tag{1.137}$$

Cette dernière est appelée connexion d'Ashtekar-Barbero et forme avec la densité triade les variables d'Ashtekar. Cette connexion transporte parallèlement des spineurs chiraux. L'espace des phases est le même qu'une théorie de Yang-Mills SU(2). Le paramètre γ est un paramètre libre de la théorie, appelé paramètre de Barbero-Immirzi. Ces deux variables permettent de décrire la RG mais ce qui particulièrement intéressant c'est qu'elles obéissent aux crochets de Poisson

$$\{A^i_{\ \alpha}(\boldsymbol{x}), A^j_{\ \beta}(\boldsymbol{y})\} = \{E_i\ \alpha(\boldsymbol{x}), E_j^{\ \beta}(\boldsymbol{y})\} = 0, \tag{1.138}$$

$$\{A^i_{\ \alpha}(\boldsymbol{x}), E^j_{\ \beta}(\boldsymbol{y})\} = \kappa\gamma \delta^i_j \delta^\beta_\alpha \delta^{(3)}(\boldsymbol{x} - \boldsymbol{y}). \tag{1.139}$$

Ainsi il est possible d'écrire l'action d'Einstein-Hilbert avec ces deux nouvelles variables

$$S = \frac{1}{2\kappa\gamma} \int_{\mathbb{R}} dt \int_\Sigma d^3x \Big(2E_i^{\ \alpha} \dot{A}^i_{\ \alpha} - [\lambda^i \mathcal{G}_i + N^\mu \mathcal{H}_\mu + N\mathcal{H}] \Big). \tag{1.140}$$

et la somme des densités de contrainte du système :

- la densité de contrainte de Gauss

$$\mathcal{G}_i = D_\alpha E_i^{\ \alpha}, \tag{1.141}$$

  qui génère les transformations de jauge SU(2) agissant sur la triade et la connexion.
- la densité de contrainte de moments

$$\mathcal{H}_\alpha = F^i_{\ \alpha\beta} E_i^{\ \alpha}. \tag{1.142}$$

- la densité de contrainte Hamiltonienne

$$\mathcal{H} = \frac{E_i^{\ \alpha} E_j^{\ \beta}}{|\det E_i^{\ \alpha}|} \Big[F^k_{\ \alpha\beta} \varepsilon^{ij}_{\ \ k} - 2(1+\gamma^2) K^{[i}_{\ \alpha} K^{j]}_{\ \beta} \Big], \tag{1.143}$$

  qui génère l'évolution temporelle

avec $F^i_{\ \alpha\beta}$ la forme de courbure (1.126) définie telle que

$$F^i_{\ \alpha\beta} = 2\partial_{[\alpha} A^i_{\beta]} + \varepsilon^i_{\ jk} A^j_{\ \alpha} A^k_{\ \beta}. \tag{1.144}$$

La contrainte de difféomorphisme est définie par une combinaison linéaire de la contrainte de Gauss et de la contrainte de moments

$$\mathcal{D}_\alpha = \mathcal{H}_\alpha - A^i{}_\alpha \mathcal{G}_i. \tag{1.145}$$

Elle génère les difféomorphismes spatiaux. Ainsi l'Hamiltonien total s'écrit comme la somme des contraintes de Gauss, de difféomorphisme et Hamiltonienne : $G[\lambda]$, $D[N^a]$ et $C[N]$.
On a

$$H = \frac{1}{2\kappa\gamma}\int_{\mathbb{R}} dt \int_\Sigma d^3x[\lambda^i \mathcal{G}_i + N^\alpha \mathcal{D}_\alpha + N\mathcal{H}] = G[\lambda] + D[N^a] + C[N]. \tag{1.146}$$

Les équations d'Hamilton donnent lieu aux équations d'Einstein. L'algèbre des contraintes est fermée. En effet, les crochets de Poisson entre deux contraintes sont proportionnelles à une combinaison linéaire des contraintes, elles respectent l'équation (1.123). Les contraintes sont dites alors de première classe. Ainsi, on a l'hypersurface spatiale où les contraintes sont nulles et, étant donné que l'algèbre est fermée, on reste toujours sur cette hypersurface. Ceci nous assure que les solutions physiques restent bien dans l'espace des phases physique au cours de l'évolution temporelle.

La RG écrite avec les variables d'Ashetkar s'écrit telle une théorie de jauge à valeurs dans su(2). Ainsi il serait naturel de travailler dans la représentation des connexions et de considérer la fonction d'onde $\Psi(A^i{}_\alpha)$. Cependant elle diffère d'une théorie de Yang-Mills étant donné qu'elle décrit l'espace-temps. Par conséquent, lorsqu'une distribution de Dirac apparaît, nous ne pouvons pas utiliser les outils de régularisation de la TQC. Nous allons alors passer dans la représentation des boucles où nous travaillons avec les holonomies de la connexion.

1.5.4 La quantification

Dans cette section, nous introduisons l'idée générale de la quantification, sans pour autant en dépeindre les détails techniques. On choisit un espace de Hilbert cinématique $\mathcal{K}_0$ tel que les variables de configuration soient les connexions. Dans la représentation des connexions, on considère un ensemble de fonctionnelles $\Psi[A^i{}_\alpha]$ de carré sommable. Les variables d'Ashtekar sont promues au rang d'opérateur. La connexion est un opérateur multiplicatif

$$\hat{A}^i{}_\alpha \Psi[A] = A^i{}_\alpha \Psi[A], \tag{1.147}$$

et les densités de triades sont des dérivées fonctionnelles

$$\hat{E}_i{}^\alpha \Psi[A] = -i\frac{\delta\Psi[A]}{\delta A^i{}_\alpha}. \tag{1.148}$$

Ces variables vérifient les relations de commutation

$$[A^i{}_\alpha(\boldsymbol{x}), E^j{}_\beta(\boldsymbol{y})] = -i\hbar\kappa\gamma\delta^i_j\delta^\beta_\alpha\delta^{(3)}(\boldsymbol{x}-\boldsymbol{y}). \tag{1.149}$$

Ensuite, il faut promouvoir les contraintes au rang d'opérateurs. La contrainte de Gauss quantique s'écrit

$$\hat{G}_j\Psi = -iD_\alpha\frac{\delta\Psi[A]}{\delta A^j_\alpha} = 0. \tag{1.150}$$

Après avoir appliqué cette contrainte, on a un espace de Hilbert cinématique $\mathcal{K}_1$ qui est invariant de jauge. La contrainte de moments quantique s'écrit

$$\hat{H}_a\Psi = -i\hat{F}^i{}_{\alpha\beta}\frac{\delta\Psi[A]}{\delta A^i{}_\beta} = 0. \tag{1.151}$$

On a alors un espace de Hilbert $\mathcal{K}_2$ invariant sous difféomorphismes spatiaux. Puis la résolution de la contrainte Hamiltonienne permet d'obtenir l'espace de Hilbert $\mathcal{K}_3$ des solutions physiques. Plusieurs difficultés apparaissent lorsqu'on veut promouvoir la contrainte Hamiltonienne au rang d'opérateur. On utilise alors les holonomies des variables d'Ashtekar afin d'avoir un produit scalaire bien défini. D'après le théorème de Giles, les traces d'holonomies constituent une base pour les fonctions de la connexion invariantes de jauge. On peut alors écrire un état sur une base des traces des holonomies tel que

$$\Psi[A] = \sum_\gamma \Psi[\gamma]W_\gamma[A], \tag{1.152}$$

où la somme s'effectue sur toutes les boucles fermées γ possibles et W_γ, dites boucles de Wilson, définies telles que

$$W_\gamma[A] = \mathrm{Tr}\Big(\mathcal{P}\Big[\exp\Big(-\oint_\gamma \dot{\gamma}^\alpha(s)\boldsymbol{A}_\alpha(s)ds\Big)\Big]\Big), \tag{1.153}$$

avec $\mathcal{P}$ l'opérateur d'ordre.

Un des résultats importants de la LQG est que l'aire est quantifié et son spectre est donné par

$$A(j) = 8\pi\gamma l_P^2\sqrt{j(j+1)}, \tag{1.154}$$

avec $j = 1/2, 1, ...$ des demi-entiers. L'aire minimale est $\Delta = 4\sqrt{3}\pi\gamma l_{Pl}^2$.

Dans ce manuscrit, la densité critique cosmologique sera dénotée par ρ_{cr}, elle est définie telle que $\rho_{cr} = 3H^2/\kappa$. La densité critique de la gravité quantique étant la densité maximale qui peut être atteinte sera dénotée par ρ_c. Elle est proche de la densité de Planck mais n'est pas forcément égale à cette dernière.

CHAPITRE 2

La cosmologie quantique à boucles

Sommaire

2.1 La théorie de la cosmologie quantique à boucles

Dans ce chapitre, je vais présenter mes différents travaux sur la cosmologie quantique à boucles (LQC). Tout d'abord, comment le modèle de la LQC est-il construit ? La façon la plus rigoureuse pour décrire un modèle cosmologique qui découlerait de la théorie de la LQG serait de quantifier la théorie fondamentale puis d'appliquer les symétries d'un univers homogène et isotrope à ce système. Cependant, la quantification de la contrainte Hamiltonienne pose encore problème. Il n'est donc pas (encore ?) possible de procéder de la sorte. On peut alors faire l'inverse : appliquer les symétries au système et ensuite effectuer la quantification de ce modèle simplifié. Ces deux façons de procéder ne sont pas toujours équivalentes. Étant donné que la première méthode n'est pas accessible, nous opérons selon la deuxième qui correspond à une approximation de mini-super-espace. La quantification de ce système à symétries réduites, en utilisant les outils de la LQG, amène à un modèle effectif appelé la LQC. La présentation de cette théorie dans les sections suivantes est inspirée, en partie, des travaux suivants : [12, 13, 14].

2.1.1 La théorie classique

Nous considérons un univers plat de sorte que l'hypersurface Σ est de topologie $\mathbb{R}^3$. Étant donné que cet espace n'est pas compact, cela va entraîner des divergences lors de l'intégration sur l'espace. On va alors décrire le système sur une cellule fiducielle homogène puis décrire des résultats qui ne dépendent pas du volume de cette cellule. Le volume comobile de la cellule s'écrit V_0. Pour la quantification, je

vais présenter la façon de quantifier la partie gravitationnelle, tandis que la partie matière est quantifiée de façon usuelle, dans la représentation de Schrödinger. On se place dans la cas d'un univers sans constante cosmologique Λ et rempli d'un champ scalaire sans masse ϕ. La métrique s'écrit

$$ds^2 = -dt^2 + a^2 \mathring{q}_{\mu\nu} dx^\mu dx^\nu, \tag{2.1}$$

avec t le temps propre, a le facteur d'échelle et $\mathring{q}_{\mu\nu}$ la métrique fiducielle de la variété spatiale. Cependant, la théorie est indépendante du fond, donc le temps ne doit pas apparaître. Un des champs est choisi comme horloge interne et la dynamique des autres champs est décrite par rapport à ce dernier. Dans ce cas, le champ scalaire ϕ sera choisi comme horloge. Étant donné qu'il satisfait à l'équation d'onde $\Box\phi = 0$, il est pertinent d'introduire un temps harmonique τ qui satisfait à l'équation d'onde également. Ce choix correspond à avoir une fonction lapse telle que $N = a^3$. La métrique s'écrit alors

$$ds^2 = -a^6 d\tau^2 + a^2(dx_1^2 + dx_2^2 + dx_3^2). \tag{2.2}$$

La métrique spatiale physique est $q_{\mu\nu} = a^2 \mathring{q}_{\mu\nu}$ et le volume physique est $V = a^3 V_0$. Les variables de l'espace des phases gravitationnel sont a et son conjugué $p_a = a\dot{a}$, avec le point qui défini la dérivée par rapport au temps propre. Et les variables de l'espace des phases de matière sont ϕ et $p_\phi = V\dot{\phi}$. Ces variables satisfont

$$\{a, p_a\} = \frac{\kappa}{6V_0} \quad \text{et} \quad \{\phi, p_\phi\} = 1. \tag{2.3}$$

La contrainte Hamiltonienne totale (en prenant en compte la gravité et la matière), dans un univers plat sans constante cosmologique, est donnée par

$$H_{tot} = -\frac{3}{\kappa}\frac{p_a^2 V}{a^4} + \frac{p_\phi^2}{2V}. \tag{2.4}$$

Lorsque cette contrainte est nulle, on retrouve l'équation de Friedmann (1.61). On va réécrire cette contrainte avec les variables d'Ashtekar. Étant donné les symétries, on a

$$A^i{}_\mu = cV_0^{-1/3}\mathring{\omega}^i{}_\mu \quad \text{et} \quad E_i{}^\mu = pV_0^{-2/3}\sqrt{\det \mathring{q}}\,\mathring{e}_i{}^\mu, \tag{2.5}$$

avec c et p la connexion et la triade isotropes, $\mathring{\omega}^i{}_\mu$ et $\mathring{e}_i{}^\mu$ les co-triades et triades fiducielles. On a $c = \gamma V_0^{1/3}\dot{a}/N$ et $|\,p\,| = V_0^{2/3}a^2$. Nous définissons la paire de variables suivantes

$$b = \frac{c}{|p|^{1/2}} \quad \text{et} \quad v = \mathrm{sgn}(p)\frac{|p|^{3/2}}{2\pi}. \tag{2.6}$$

Ces variables satisfont

$$\{b, v\} = 2\gamma, \tag{2.7}$$

et on écrit la contrainte Hamiltonienne sous la forme

$$H_{tot} = -\frac{3}{4\gamma^2}b^2|v| + \frac{p_\phi}{4\pi|v|}. \tag{2.8}$$

Les équations d'Hamilton donnent lieu à une solution d'univers en expansion et une solution d'univers en contraction :

$$\phi = \pm\frac{1}{\sqrt{12\pi}}\ln\frac{v}{v_c} + \phi_c, \tag{2.9}$$

avec v_c et ϕ_c deux constantes d'intégration. Ces solutions classiques possèdent une singularité.

2.1.2 La théorie quantique

Pour passer à un formalisme quantique, il faut promouvoir les variables et la contrainte Hamiltonienne au rang d'opérateurs. Inspirés par la LQG, nous passons aux holonomies. En effet, l'espace de Hilbert cinématique n'admet pas d'opérateur de connexion $\hat{c}$. Par contre, les fonctions exponentielles de la connexion sont bien définies. Pour une connexion à symétrie réduite $A^i{}_\mu$, le long d'un bord droit $\mathring{e}^\mu_k$ avec une longueur fiducielle λ_c, l'holonomie est donnée par

$$h_k^{(\lambda_c)} = \cos\left(\frac{\lambda_c c}{2}\right)\mathbb{I} + 2\sin\left(\frac{\lambda_c c}{2}\right)\tau_k, \tag{2.10}$$

avec $\tau_k = -i\sigma_k/2$, où σ_k sont les matrices de Pauli. Soit $|\mu\rangle$ les états propres de $\hat{p}$, ils satisfont

$$\langle\mu_1|\mu_2\rangle = \delta_{\mu_1\mu_2}. \tag{2.11}$$

Ici, dans le cas des holonomies, on a un delta de Kronecker et non pas un delta de Dirac comme c'est le cas pour la théorie de Wheeler-DeWitt. Les deux théories ont des espaces de Hilbert différents, ainsi les dynamiques cosmologiques associées sont très différentes. Dans la représentation des triades, l'action des opérateurs s'écrit

$$\hat{p}\,|\mu\rangle = \frac{8\pi\gamma l_{Pl}^2}{6}\mu\,|\mu\rangle\,, \tag{2.12}$$

$$\widehat{e^{i\lambda_c c/2}}\,|\mu\rangle = |\mu + \lambda_c\rangle\,. \tag{2.13}$$

La densité de contrainte Hamiltonienne Eq.(1.143) dépend de deux termes. Cependant les deux sont proportionnels pour un espace spatialement plat, homogène et isotrope. Dans ce cas, la contrainte Hamiltonienne s'écrit

$$C = -\frac{1}{\gamma^2}\int d^3x\left(\frac{N}{\sqrt{\det q}}\epsilon^{ij}{}_k E_i^{\ \mu} E_j^{\ \nu}\right)F^k{}_{\mu\nu}. \tag{2.14}$$

Avec les triades homogènes et la fonction lapse telle que $N = a^3$, on a

$$C = \frac{1}{\gamma^2 V_0^{1/3}}\epsilon^{ij}{}_k \mathring{e}_i^{\ \mu}\mathring{e}_j^{\ \nu}|p|^2 F^k{}_{\mu\nu}. \tag{2.15}$$

Le champ de force peut s'écrire classiquement en termes d'une trace des holonomies sur une boucle carrée $\square_{ij}$ sur une face d'une cellule élémentaire dont l'aire $A(\square) = \lambda_c^2$ tends vers zéro. On a

$$\begin{aligned} F^k{}_{\mu\nu} &= -2\lim_{A(\square)\to 0}\mathrm{Tr}\left(\frac{h_{\square_{ij}}^{(\lambda_c)} - \mathbb{I}}{\lambda_c^2}\tau^k\right)\mathring{\omega}^i{}_\mu\mathring{\omega}^j{}_\nu \\ &= \lim_{\lambda_c\to 0}\epsilon^k{}_{ij}\mathring{\omega}^i{}_\mu\mathring{\omega}^j{}_\nu\left(\frac{\sin^2\lambda_c c}{\lambda_c^2}\right), \end{aligned} \tag{2.16}$$

avec $h_{\square_{ij}}^{(\lambda_c)} = h_i^{(\lambda_c)}h_j^{(\lambda_c)}(h_i^{(\lambda_c)})^{-1}(h_j^{(\lambda_c)})^{-1}$. Mais la limite en zéro n'est pas consistante avec l'existence d'une aire minimale Δ donnée par le spectre (1.154) de la LQG. L'aire d'une boucle pour une métrique physique est $\lambda_c^2|p|$, ainsi on demande $\lambda_c = \sqrt{\Delta/|p|}$. La difficulté qui apparaît est que la longueur λ_c dépend de la triade donc l'action de $\exp(i\lambda_c(p)c)$ sur les états propres de la triade est compliquée dans la base $|\mu\rangle$. Par contre, si on passe dans la représentation des volumes $|\nu\rangle$ et qu'on utilise les variables

définies par l'équation (2.6) alors l'opérateur volume et l'opérateur $\widehat{\exp(i\lambda b/2)}$ (avec $\lambda^2 = \Delta$) sont bien définis

$$\hat{V}\,|\nu\rangle = 2\pi l_{Pl}^2 \gamma |\nu|\,|\nu\rangle\,, \tag{2.17}$$

$$\widehat{e^{i\lambda b/2}}\,|\nu\rangle = |\nu + \lambda\rangle\,, \tag{2.18}$$

avec $\nu = v/\gamma\hbar$. La contrainte classique (2.8) écrite en termes d'holonomies est inchangée. Ainsi en utilisant les opérateurs (2.17) et (2.18), on peut trouver les solutions à $\hat{H}_{tot}\Psi(\nu,\phi) = 0$:

$$\begin{aligned}\partial_\phi^2\Psi(\nu,\phi) &= 3\pi\nu\frac{\sin\lambda b}{\lambda}\nu\frac{\sin\lambda b}{\lambda}\Psi(\nu,\phi)\\ &= \frac{3\pi}{4\lambda^2}\nu\Big[(\nu+2\lambda)\Psi(\nu+4\lambda,\phi) - 2\nu\Psi(\nu,\phi) + (\nu-2\lambda)\Psi(\nu-4\lambda,\phi)\Big]\\ &= \Theta\Psi(\nu,\phi),\end{aligned} \tag{2.19}$$

qui peut se réécrire

$$C^+(\nu)\Psi(\nu+4\lambda,\phi) + C^0\Psi(\nu,\phi) + C^-\Psi(\nu-4\lambda,\phi) = \hat{H}_{mat}\Psi(\nu,\phi). \tag{2.20}$$

La forme de la contrainte quantique est similaire à celle de Klein-Gordon avec ϕ analogue au temps et Θ au Laplacien spatial. On choisit les états physiques comme étant les solutions dont les fréquences sont positives

$$-i\partial_\phi\Psi(\nu,\phi) = \sqrt{\Theta}\Psi(\nu,\phi), \tag{2.21}$$

avec le produit scalaire donné par

$$\langle\Psi_1,\Psi_2\rangle = \sum_\nu \overline{\Psi}_1(\nu,\phi_0)|\nu|^{-1}\Psi_2(\nu,\phi_0), \tag{2.22}$$

et ϕ_0 une constante arbitraire. On veut à présent définir des observables. On peut définir l'opérateur $\hat{V}|_{\phi_0}$ qui correspond au volume au "temps" ϕ_0 et l'opérateur $\hat{p}_{\phi_0}$, qui est une constante du mouvement,

$$\hat{V}|_{\phi_0}\Psi(\nu,\phi) = 2\pi\gamma l_{Pl}^2 e^{i\sqrt{\Theta}(\phi-\phi_0)}\Psi(\nu,\phi), \tag{2.23}$$

$$\hat{p}|_{\phi_0}\Psi(\nu,\phi) = \sqrt{\Theta}\Psi(\nu,\phi). \tag{2.24}$$

Le modèle de LQC dans un univers plat avec un champ scalaire sans masse est exactement résoluble en passant dans la représentation b. Étant donné que les fonctions d'ondes $\Psi(\nu,\phi)$ dans la représentation de volume ont un support sur un intervalle discret $\nu = 4n\lambda$ et que b est canoniquement conjugué à ν, leurs transformées de Fourier $\Psi(b,\phi)$ ont un support sur un intervalle continue $(0,\pi/\lambda)$ et on peut résoudre la contrainte quantique [15]. Il est alors possible d'écrire chaque solution en termes d'une partie pour les modes dirigés vers la gauche et une pour les modes dirigés vers la droite et obtenir un produit scalaire. La valeur moyenne de l'opérateur volume, au temps ϕ, s'écrit alors

$$\langle V\rangle_\phi = V_+ e^{\sqrt{12\pi}\phi} + V_- e^{-\sqrt{12\pi}\phi}, \tag{2.25}$$

avec V_+ et V_- deux constantes déterminées par les conditions initiales. Le volume a une valeur minimum :

$$V_{min} = 2(V_+V_-)^{1/2}, \tag{2.26}$$

et le rebond a lieu au temps

$$\phi_b^V = (2\sqrt{12\pi})^{-1} \ln(V_-/V_+). \tag{2.27}$$

Et l'observable densité d'énergie $\hat{\rho}|_{\phi_0}$ est bornée :

$$\langle\hat{\rho}\rangle_\phi \leq \rho_c \quad \text{avec} \quad \rho_c = \frac{3}{8\pi\gamma^2\lambda^2}. \tag{2.28}$$

Pour le choix standard de LQC on a $\rho_c = \sqrt{3}/(32\pi^2\gamma^3)$. Ainsi, on observe qu'en LQC la singularité est résolue.

2.1.3 Le modèle effectif

Lorsque le modèle quantique n'est pas résoluble analytiquement, il est possible de résoudre numériquement l'équation (2.19). Étant donné l'état initial et la fonction d'onde associée le code CHIMERA donne le comportement des fonctions d'ondes à travers le rebond [16]. Il est possible d'écrire un Hamiltonien effectif qui donne de bonnes approximations des valeurs moyennes de ces simulations numériques. Nous présentons de manière très succincte, la construction du Hamiltonien effectif. L'idée générale est de projeter la dynamique quantique de l'espace des phase quantique Γ_Q sur l'espace des phases classique Γ. Pour tout point $\gamma_0 = (q_i^0, p_i^0) \in \Gamma$, on associe un état quantique Ψ_{γ^0}. On défini un sous espace $\overline{\Gamma}_Q \in \Gamma_Q$ en exigeant $q_i^0 = \langle\Psi_{\gamma^0}\hat{q}_i\Psi_{\gamma^0}\rangle$, $p_i^0 = \langle\Psi_{\gamma^0}\hat{p}_i\Psi_{\gamma^0}\rangle$. On exige également que le champ de vecteur Hamiltonien quantique soit approximativement tangent à $\overline{\Gamma}_Q$. Ces conditions permettent de définir un Hamiltonien effectif tel que $H^{\text{eff}}(q_i^0, p_j^0) := \langle\Psi_{\gamma^0}\hat{H}\Psi_{\gamma^0}\rangle$. La contrainte effective s'écrit

$$H_{tot}^{\text{eff}} = -\frac{3}{4\gamma}\nu\frac{\sin^2(\lambda b)}{\lambda^2} + H_{mat}. \tag{2.29}$$

Les équations du mouvement, avec t le temps cosmologique, redonnent les équations classiques, excepté pour l'équation

$$\dot{V} = \frac{3}{\gamma\lambda}\sin(\lambda b)\cos(\lambda b). \tag{2.30}$$

Ce qui amène à une équation de Friedmann modifiée

$$H^2 = \frac{\kappa}{3}\rho\left(1 - \frac{\rho}{\rho_c}\right). \tag{2.31}$$

Ainsi, la LQC décrit un univers en contraction, qui lorsqu'il atteint la densité critique ρ_c va rebondir et décrire un univers en expansion dans lequel nous sommes observateurs.

2.2 Durée de l'inflation en LQC

La cosmologie standard et la LQC prédisent deux équations de Friedmann différentes : Eqs. (1.61) et (2.31) respectivement. Quelles vont être les conséquences de cette différence ? Un premier point concerne la durée de l'inflation.

L'équation de Klein-Gordon (1.70) peut se réécrire comme un système de deux équations différentielles du premier ordre. Au lieu de dériver par rapport au temps cosmologique, il est plus judicieux de dériver par rapport à $\lambda = \ln a$. On a alors

$$\begin{aligned} d\phi/d\lambda &= p/H, \\ dp/d\lambda &= -3p - m^2\phi/H. \end{aligned} \tag{2.32}$$

On introduit les variables sans dimension suivantes

$$x = \frac{m\phi}{\sqrt{2\rho_0}} \quad \text{et} \quad y = \frac{p}{\sqrt{2\rho_0}}. \tag{2.33}$$

Ces variables seront utilisées pour l'analyse numérique de la durée de l'inflation. Ces variables sont usuelles en cosmologie, elles définissent un cercle $x^2 + y^2 = 1$ au moment du rebond.

Dans l'approximation de roulement lent, le nombre d'e-folds N est une fonction du champ scalaire. Il a été montré [17] que pour une température de $T \approx 10^{16}$ GeV au début de la période de rayonnement, l'inflation doit durer au minimum 60 e-folds. La densité de l'univers étant bornée à la densité de Planck, l'inflation peut durer jusqu'à 10^{14} e-folds. Ainsi, la durée de l'inflation dans le modèle standard n'est pratiquement pas contrainte. Cette durée dépend des conditions initiales, x_0 et y_0. On peut montrer que $99,99\%$ de l'espace de phases de ces paramètres entraîne une inflation supérieure à 60 e-folds [18].

Contrairement au modèle standard, la LQC possède un caractère prédictif. En effet, en LQC, la phase d'expansion est précédée d'un rebond, qui lui même est précédé d'une phase de contraction. Ainsi, nous pouvons étudier les conséquences de cette phase. Dans les articles [19] et [20], la phase de contraction est supposée rempli d'un champ scalaire dans un univers homogène et isotrope, dans la branche classique (suffisamment loin du rebond). Ainsi la phase de ce champ est aléatoire et on peut mettre une distribution de probabilité plate sur cette phase. Cette distribution va engendrer une distribution sur les conditions initiales et, par conséquent, sur la durée de l'inflation. Cette distribution de probabilité sur la durée de l'inflation est très piquée (voir l'histogramme rouge de la Figure 3). La plupart des valeurs se trouvent entre 110 et 170 e-folds, avec une valeur moyenne de 145 e-folds environ. Ainsi, non seulement nous avons une prédiction probabiliste sur la durée de l'inflation, mais de plus, cette prédiction se trouve proche de la valeur minimum requise. L'intervalle sur la durée est alors considérablement réduit.

Dans cet article, on compare deux modèles :

— dans le premier cas, on part d'une densité initiale ρ_c puis on applique une dynamique de type RG avec l'équation (1.61), sans constante cosmologique et sans courbure.

— dans le deuxième cas, on part d'une densité initiale ρ_c, étant celle du rebond, puis on applique une dynamique de type LQC avec l'équation (2.31).

Dans les deux cas, les conditions initiales, lorsqu'on a $\rho = \rho_c$, sont données par la distribution de probabilité prédite lorsqu'on considère une distribution de probabilité plate sur la phase du champ dans l'univers en contraction. Ainsi, on a les mêmes conditions dans les deux modèles et on étudie comment la dynamique de fond va influencer la durée d'inflation. Par abus de langage, le premier modèle sera dénoté comme étant le modèle RG. Dans ces deux modèles, on observe trois régimes : (*i*) la phase pré-inflationnaire où ϕ augmente jusqu'à atteindre un maximum, (*ii*) la phase d'inflation qui commence lorsque $\dot{\phi} = 0$ et dure jusqu'à avoir $\phi = 0$ pour la première fois, (*iii*) le champ oscille de façon amortie et se désintègre en particules du modèle standard.

On peut montrer que dans le régime pré-inflationnaire on a

$$x_{RG} \approx x_c + (3/\Gamma)\lambda, \tag{2.34}$$

$$x_{LQC} \approx x_c + (3/\Gamma)\lambda + (\ln 2/\Gamma), \tag{2.35}$$

avec $\Gamma = \sqrt{3\rho_c}/m$ et x_c l'énergie potentielle initiale. Ainsi en LQC la champ scalaire est boosté dans la phase de pré-inflation ce qui amène à avoir une énergie potentielle plus élevée au début de l'inflation. Ceci va engendrer une différence de la durée d'inflation entre les deux modèles. Cette différence est donnée par $\sqrt{8/3}\ln 2\sqrt{N_{RG}}$. On peut donc voir que pour les mêmes conditions initiales, la LQC engendre une inflation qui dure quelques e-folds de plus qu'en RG. On observe donc que la dynamique n'a guère d'importance.

Ainsi, la grande différence de la LQC par rapport à la RG, est non pas dû à la dynamique de fond, car le terme en ρ_c dans l'équation (2.31) est très rapidement négligeable, mais dans sa capacité à prédire de façon probabiliste les conditions initiales.

Cet article a été publié dans *Classical and Quantum Gravity* [21].

Some clarifications on the duration of inflation in loop quantum cosmology

2017 Class. Quantum Grav. 34 145003

(http://iopscience.iop.org/0264-9381/34/14/145003)

IOP Publishing Classical and Quantum Gravity

Class. Quantum Grav. **34** (2017) 145003 (9pp) https://doi.org/10.1088/1361-6382/aa7779

Some clarifications on the duration of inflation in loop quantum cosmology

Boris Bolliet, Aurélien Barrau, Killian Martineau and Flora Moulin

Laboratoire de Physique Subatomique et de Cosmologie, Université Grenoble-Alpes, CNRS/IN2P3 53, avenue des Martyrs, 38026 Grenoble cedex, France

E-mail: boris.bolliet@lpsc.in2p3.fr

Received 12 January 2017, revised 29 May 2017
Accepted for publication 6 June 2017
Published 20 June 2017

Abstract

The prediction of a phase of inflation whose number of e-folds is constrained is an important feature of loop quantum cosmology. This work aims at giving some elementary clarifications on the role of the different hypotheses leading to this conclusion. We show that the duration of inflation does not depend significantly on the modified background dynamics in the quantum regime.

Keywords: loop quantum cosmology, inflation, quantum gravity

(Some figures may appear in colour only in the online journal)

Loop quantum gravity (LQG) is a nonperturbative and background-independent quantization of general relativity (GR). It relies on the Sen–Ashtekar–Barbero variables, that is SU(2) valued connections and conjugate densitized triads. The quantization is obtained using holonomies of the connections and fluxes of the densitized triads. Loop quantum cosmology (LQC) is an effective theory based on a symmetry reduced version of LQG. In LQC, the big bang is believed to be replaced by a bounce due to repulsive quantum geometrical effects (see [1] for a review). For the flat homogeneous and isotropic background cosmology that we consider in this work, the effective LQC-modified Friedmann equation is

$$H^2 = \frac{\rho}{3}\left(1 - \frac{\rho}{\rho_{\rm B}}\right), \tag{1}$$

where $H \equiv (\dot{a}/a)$ is the Hubble parameter, ρ is the total energy density and $\rho_{\rm B}$ is the critical density at the bounce (expected to be of the order of the Planck density). The dot refers to a coordinate time derivative. Throughout all this article we use reduced Planck units: $\sqrt{8\pi G} = 1$. So, in these units, the Planck mass is $m_{\rm Pl} \equiv 1/\sqrt{G} = \sqrt{8\pi}$. We assume that the dominating energy component in the early universe is a scalar field ϕ, with potential $V = \frac{1}{2}m^2\phi^2$. As shown in [2], a massive scalar field is now disfavored by data. This choice however remains interesting so as to compare our study with other results (a quantitative estimate of the effect

of choosing, for example, the Starobinsky potential, used in [3], can be found in [4]). The total energy density can be written as $\rho = \frac{1}{2}\dot{\phi}^2 + V$. As explained in details in [5] it should be made clear that the existence of an inflationary phase is not in itself a consequence of LQC, but of the choice of an appropriate scalar field as the content of the Universe. Based on cosmic microwave background (CMB) measurements and under most reasonable assumptions for the length of *observable inflation* (between horizon exit of the pivot scale and the end of the inflationary phase), one obtains $m \simeq 10^{-6} m_{\rm Pl}$. The equation of motion for the scalar field is

$$\ddot{\phi} + 3H\dot{\phi} + m^2\phi = 0. \tag{2}$$

There are different ways to statistically estimate the duration of inflation in this framework.

At a fixed energy density, ρ_0, one can first ask the following question: for a given number of e-folds N, what is the fraction of trajectories, i.e. solutions to equation (2), that lead to a phase of slow-roll inflation lasting more than N e-folds? It should be noticed that the set of trajectories can be parametrized by $\{a_0, \phi_0\}$. As the energy density has been fixed, the initial time derivative of the scalar field, $\dot{\phi}_0$, is determined in terms of ρ_0 and ϕ_0. This also implies that ϕ_0 can only take values within a finite interval, ranging from $-(\sqrt{2\rho_0}/m)$ to $(\sqrt{2\rho_0}/m)$. In a flat universe, the value of the scale factor has no physical meaning. The number of e-folds of inflation depends on ϕ_0 but not on a_0: $N = N(\phi_0; m, \rho_0)$. So the fraction of trajectories that achieve a phase of inflation lasting more than N e-folds can be written as $\mu = (m\Delta\phi_0)/(2\sqrt{2\rho_0})$, where $\Delta\phi_0$ is the range of initial values of the scalar field that yields the required inflationary phase. It is then necessary to evaluate μ as a function of N. There are two cases in which this can be done analytically: (i) at *low energy*, $\rho_0 \ll m^2$, and (ii) at *high energy* $\rho_0 \gg m^2$. At low energy, the calculation of Gibbons and Turok of the probability for inflation can be used to show that [6]

$$\mu(N) = \mathcal{C} m N^{-\frac{1}{2}} \exp(-3N)\{1 + 1/(6N)\}, \tag{3}$$

where $\mathcal{C}$ is a numerical factor that does not depend on m or ρ_0. For $N \simeq 60$ e-folds, as required to explain the CMB temperature anisotropy, this leads to $\mu(N) \ll 1$. It should be noticed that the conclusions of [6] are to be contrasted with those of [7], which shows the importance of working with well defined probability distribution functions. At high energy, one reaches the opposite conclusion. In this case, one can compute $\Delta\phi_0$ as follows. For a massive quadratic potential the total number of e-folds of inflation can be expressed in terms of the amplitude of the scalar field at the start of the inflationary phase, $\phi_{\rm I}$, as $N \approx (\phi_{\rm I}^2/4)$. In turn, $\phi_{\rm I}$ can be expressed in terms of the initial value of the scalar field as [8]:

$$\phi_{\rm I} = \phi_0 + \mathrm{sgn}(\dot{\phi}_0)\sqrt{(2/3)}\,\mathrm{Arcsinh}\left(\Gamma\sqrt{2/\ln(z)}\right), \tag{4}$$

with $z \equiv 8\Gamma^2 \exp(\sqrt{6}\phi_0)$ and $\Gamma \equiv \sqrt{3\rho_0}/m$. This formula for the amplitude of the scalar field at the start of inflation is valid in LQC, with the modified Friedmann equation given by equation (1). For the standard flat FLRW dynamics, without LQC modifications, the analytical calculations suggest that at the start of inflation the scalar field reaches a maximum value given by (4) minus $(\ln 2/\Gamma)$. In both cases, we find that the range of values of ϕ_0 that do not yield an inflationary phase longer than N e-folds is an interval of size $4\sqrt{N}$ centered on $\phi_0 = 0$. Hence,

$$\mu(N) = 1 - m\sqrt{(2N/\rho_0)}, \tag{5}$$

and $\mu(60) \simeq 0.999\,99$ (for $\rho_0 = 1$) , which means that all but a tiny fraction of the possible trajectories do not go through a long inflationary phase. It might be tempting to interpret μ as a probability measure. This is however not that simple. The phase space of the flat FLRW

universe presents a serious ambiguity: the Liouville measure is proportional to the scale factor and the scale factor can be rescaled arbitrarily. In addition, as explained just before, μ depends on the choice of the surface of initial data. More importantly, the fundamental question to ask is: is there a variable on which a flat (or at least known) probability distribution function (PDF) can be assigned? There is no reason to assume implicitly that the initial values of the field should have a flat PDF.

This work is somehow complementary to what was studied in [9] and sheds a new light on the difference between different predictions made in quantum and classical cosmology.

In [10] it was argued that the two first issues mentioned above can be solved in LQC. It was indeed claimed that the scale factor can be rigorously factored out of the Liouville measure, and that the bounce provides a preferred choice for the surface of initial data. In this study, following [11, 12] we choose a different perspective. We decide, the other way round, to set initial conditions in the remote past of the contracting branch, when the Universe is classical and well understood ($\rho_0 \ll \rho_{\rm B}$). This is not only technically justified but also conceptually necessary if the bounce has to be taken seriously in a causal way. Still, we naturally choose a time which is close enough to the bounce so that it is reasonable to assume a scalar field as the main component of the Universe. The phase of the oscillations of the scalar field in the contracting branch is an obvious variable to which a flat PDF can be assigned [11]. In addition, the key point is that this PDF is preserved over time (as long as one remains in the classical phase when the field oscillates). The numerical analysis of [11] shows that at fixed ρ_0, nearly all possible initial values for the scalar field, ϕ_0, yield an inflationary phase whose number of e-folds is peaked around $N = 142$ e-folds (with $\rho_{\rm B} = 0.41 m_{\rm Pl}^4$).

The procedure to derive this result is simple:

- Consider an initial energy density $\rho_0 = \rho_{\rm Pl}/\alpha^2$, with α large enough so that the evolution starts in the remote past of the contracting phase.
- Choose an initial value for the scalar field and its time derivative by a random sampling of the phase θ_0 between 0 and 2π, where θ_0 is defined such as $\phi_0 = \sqrt{\frac{2}{3}}\frac{\Gamma}{\alpha}\sin\theta_0$.
- Solve the dynamics, across the bounce, until the end of slow-roll inflation in the expanding branch.
- For each θ_0, collect the corresponding number of e-folds.

Finally, one can produce the associated histogram which, in a probabilistic interpretation, is the PDF for the number of e-folds. This is illustrated on the right panel of figure 1 where we also present the PDFs for several initial energy densities corresponding to different values of $\alpha \equiv \sqrt{\rho_{\rm Pl}/\rho_0}$ in order to show that for large values of α the PDF becomes independent of the initial energy density, as explained analytically in [11]. Interestingly, the peakedness of the PDF can be understood as follows. The calculation Gibbons and Turok is often considered controversial in standard cosmology because they somehow set 'initial conditions' for the *final* state. However, in the case of a bouncing Universe it implies that almost none of all the possible trajectories, starting at low energy in the *contracting* branch, have a significant phase of pre-bounce exponential contraction, that is of so-called *deflation*. A trajectory with deflation in the contracting phase leading to $(\phi_{\rm B}, \dot{\phi}_{\rm B})$ can be identified with a trajectory with inflation in the expanding phase with $(\phi_{\rm B}, -\dot{\phi}_{\rm B})$. Equation (4) can be used to calculate the value of the scalar field at the bounce corresponding to the trajectory with no deflation. One simply has to solve equation (4) with respect to $\phi_{\rm B}$ for $\phi_{\rm I} = 0$ and $\dot{\phi}_{\rm B} < 0$. In the limit of large Γ, the solution is well approximated by

$$\phi_{\rm B}^{\rm GT} \equiv \sqrt{(2/3)}\ln\left(2\Gamma/\sqrt{\ln\Gamma}\right). \tag{6}$$

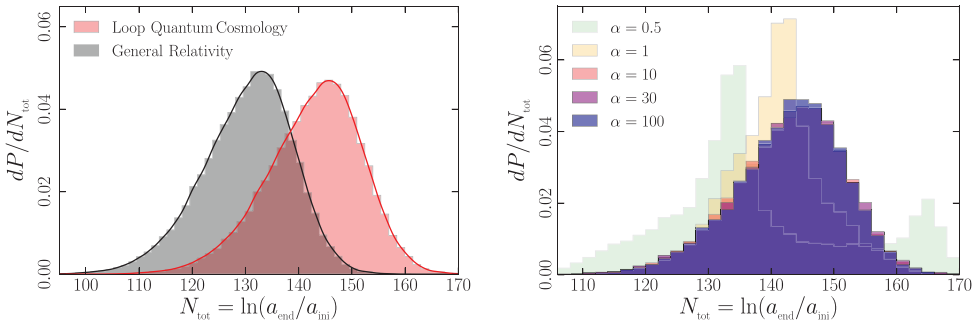

Figure 1. Probability distribution of the number of inflationary e-folds. On the left panel, the black histograms corresponds to a 'GR' like dynamics (using the standard Friedmann equation throughout the evolution). The red histogram is the prediction of loop quantum cosmology. With the standard Friedmann equation the most likely value is $N_{\rm tot} = 133$, while in LQC we find $N_{\rm tot} = 145$. The right panel shows that the probability density function does not depend on the value of the energy density as long as the surface of initial data is set at $\rho \ll \rho_{\rm Pl}$. The different histograms are labeled by $\alpha = \sqrt{\rho_{\rm Pl}/\rho}$. The probability density function converges as soon as α becomes larger than 10.

This can then be inserted back into equation (4), with $\dot{\phi}_{\rm B} > 0$, in order to obtain the value of the field at the start of inflation in the expanding phase and the corresponding number of e-folds of inflation. With the standard values for m and $\rho_{\rm B}$, this calculation yields $N = 142$, in excellent agreement with the numerics (figure 1). Moreover, a closer look at Gibbons and Turok's PDF for the number of e-folds suggests that most trajectories starting in the remote past have less than one e-folds of deflation, see figure 2. This means that nearly all trajectories end up with a value of $\phi_{\rm B}$ that belongs to an interval of size $\Delta\phi_{\rm B} \approx 4$ centered around $\phi_{\rm B}^{\rm GT}$. In terms of number of e-folds this translates into $\Delta N \approx 4\sqrt{N}$, also in agreement with the numerics as can be seen on figure 1.

We shall now investigate to which extent the specific modified dynamics is responsible for the peakedness of the probability density function of the number of e-folds in loop quantum cosmology. The argument we have developed in the previous section did not refer to the modified LQC dynamics. It was essentially based on Gibbons and Turok's analysis combined with the presence of the bounce at Planckian energy density. It can therefore already be guessed that the peakedness does not depend strongly on the LQC modification to the Friedmann equation. To address this question in more details, we consider an artificial bouncing cosmological scenario where the Friedmann equation is left unchanged even at Planckian energy. In this 'GR-like' cosmological scenario, initial conditions for a given trajectory are set in the remote past of the contracting branch at the same energy density and with the same values of ϕ_0 and $\dot{\phi}_0$ than for a trajectory which follows the LQC dynamics (as previously considered). The dynamics is divided into two parts: the contracting branch with a negative Hubble parameter and the expanding branch with a positive Hubble parameter. The evolution, starting in the contracting branch, is artificially stopped when the energy density reaches the LQC critical energy density $\rho_{\rm B}$. The values of $\phi_{\rm B}$ and $\dot{\phi}_{\rm B}$ are collected and used as initial conditions for the dynamics in the expanding branch where the initial Hubble parameter is now positive. At the junction between both phases, the Hubble parameter and therefore $\ddot{\phi}$ are discontinuous but a, ϕ and $\dot{\phi}$ are continuous, as illustrated in figures 3, 4 and 5.

The numerical result for the PDF of the number of e-folds in the GR-like scenario is plotted against the LQC prediction on the left panel of figure 1. The PDF has the same width and shape than in LQC. This confirms that the peakedness does not depend strongly on the specific

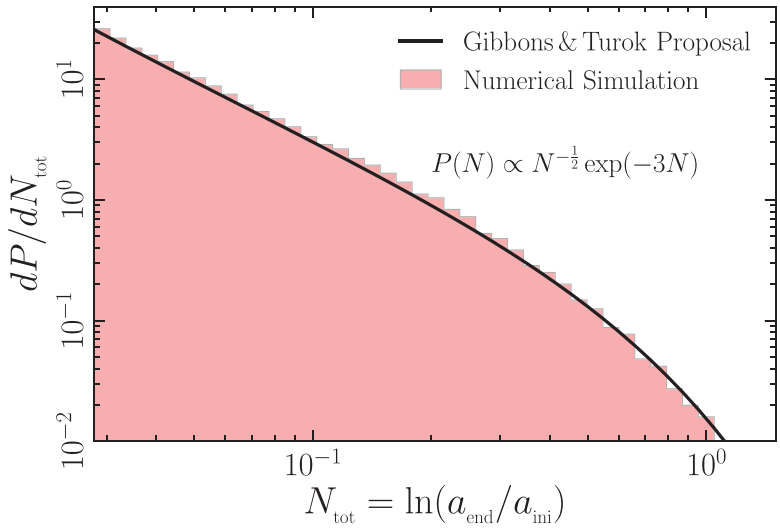

Figure 2. Probability distribution of the number of e-folds, when the surface of initial data is set at low energy density, in a agreement with the result of Gibbons and Turok.

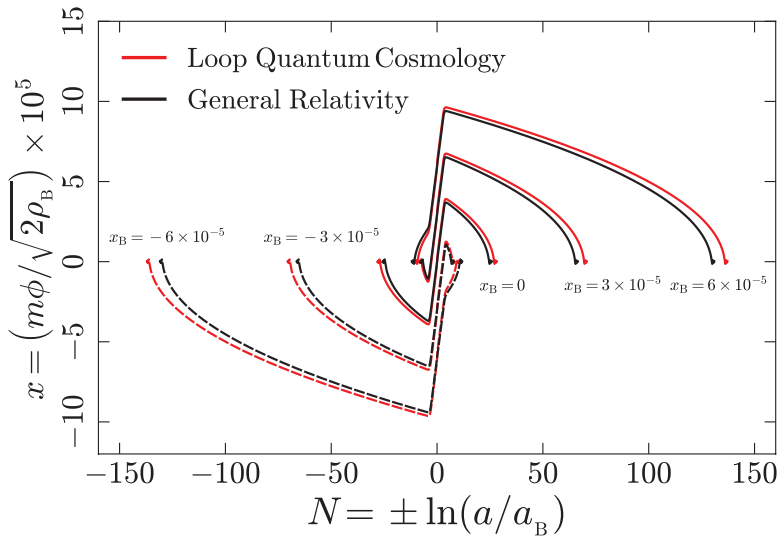

Figure 3. Evolution of the potential energy parameter in the GR-like scenario (black) compared to loop quantum cosmology (red), for different values of $x_{\rm B}$, linearly distributed between -10^{-6} and 10^{-6}. Dashed lines correspond to negative initial values for $x_{\rm B}$.

LQC modified dynamics, and suggests that this feature would remain in case one incorporates additional quantum gravity corrections to the LQC effective equations. Nevertheless, the number of e-folds corresponding to the peak of the PDF is slightly different in the GR-like scenario than in LQC. This can be explained as follows. First, it should be noticed that the difference between the GR-like scenario and LQC becomes significant when $\rho \approx \rho_{\rm Pl}$. Second, as shown in the previous sections, the fraction of trajectories that have a significant phase of deflation in the contracting branch is tiny. This means that at high energy density, the

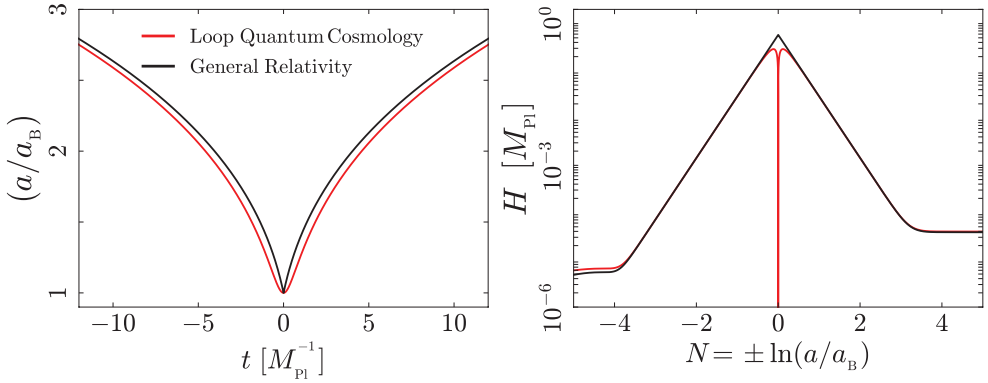

Figure 4. Evolution of the scale factor (left) and the Hubble parameter (right) in loop quantum cosmology (red) and in the GR-like scenario (black).

dynamics of most trajectories is largely kinetic energy dominated. In simplistic terms, deflation can not bring the amplitude of the scalar field to large values because it stops nearly immediately. To inverstigate the difference between the GR-like scenario and LQC, the equation of motion of the scalar field at high energy, and for kinetic energy domination, need to be studied. It is natural to introduce $x \equiv \phi/\sqrt{2\rho_{\rm B}}$ and $y \equiv \dot{\phi}/\sqrt{2\rho_{\rm B}}$, the so-called potential and kinetic energy parameters. As the duration of inflation depends on the scalar field amplitude, it is sufficient to focus on the potential energy parameter. It is easy to show that in the regime compatible with observations

$$x^{\rm GR} \simeq x_{\rm B} + (3/\Gamma)\ln a, \tag{7a}$$

$$x^{\rm LQC} \simeq x_{\rm B} + (3/\Gamma)\ln a + (\ln 2/\Gamma). \tag{7b}$$

In LQC the scalar field is *boosted* by a short phase of super-inflation, $\dot{H} > 0$, during which its amplitude accumulates a surplus of $(\ln 2/\Gamma)$ compared to the standard FLRW dynamics. This yields a difference of $\sqrt{8/3}\ln 2\sqrt{N_{\rm GR}}$ between the number of e-folds in both scenarios. With the standard numerical values of m and $\rho_{\rm B}$, one gets $N_{\rm LQC} - N_{\rm GR} \simeq 13$, in agreement with the numerical results.

Although an exhaustive investigation would in principle be necessary it can be quite safely conjectured that most results derived in this study do not depend on the details of the considered bounce scenario. Actually, the key parameter is the energy density at which the bounce takes place.

One can also study the differences between the primordial power spectra of cosmological perturbations in the GR-like scenario and in LQC (the interested reader can consider [13] for a detailed study in the dressed metric approach and [14] in the deformed algebra approach). As a toy model to focus on the difference between both background dynamics, we set initial conditions for perturbations at an energy density corresponding to the bounce energy density, choosing the Bunch–Davies vacuum as the initial state. The resulting power spectra are shown on figure 6 and compared with the usual slow-roll inflation expectation (dotted lines). Such spectra (and their variants including more subtle LQC effects) are the main observables associated with loop quantum cosmology. Assuming a Bunch Davies state is a valid assumption only for modes with a wavelength small compared to the curvature radius at the bounce, or the Planck length in the 'GR-like' scenario. For such modes, the Bunch Davies state is the 'preferred' vacuum state (selected by the regularity conditions and the symmetry group of flat

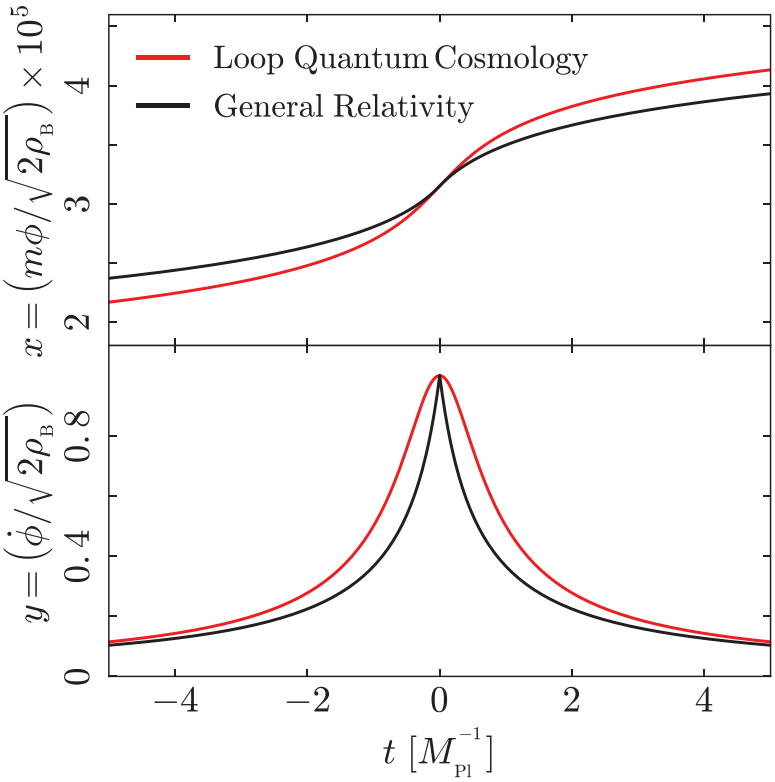

Figure 5. The fraction of potential and kinetic energy in general relativity (black) and loop quantum cosmology (red).

space-time). However, for modes with larger wavelength there is some freedom for the choice of the initial state. Here, our goal is not to discuss the impact of different initial state on the power spectrum, but rather to investigate the effects of two different dynamical models for the background cosmology ('GR-like' and LQC) on the power spectrum resulting from the evolution of modes starting at the same energy density (Planckian) and in the same state.

The duration of inflation is crucial because it determines the location of the window of wavenumbers relevant for the cosmic microwave background anisotropy measurements, with respect to the characteristic LQC scale $k_{\rm LQC} \equiv a_{\rm B}\sqrt{\rho_{\rm B}}$. On infrared scales, the mode functions remain in the Bunch–Davies state with $\mathcal{P}(k) \propto k^2$. We see that in both LQC and the GR-like scenario the power spectra agree with the slow-roll expectations in the ultraviolet regime. Oscillations are present in both scenarios in the range $10^{-3} < k/k_{\rm LQC} < 1$. The amplitude is larger in the GR-like scenario than in LQC, however the period of the oscillations does not seem to be affected by the specific modified LQC dynamics. This shows that oscillations in themselves are a bounce feature but not a specific LQC feature. This motivates the search for complementary probes such as primordial non-gaussianity [15]. For a more detailed comparison of the different kinds of power spectra expected in LQC under different assumptions for the mode propagation, see [16].

The most reliable result of loop quantum cosmology is the modified Friedmann equation describing the background dynamics. It receives a quadratic correction in density which prevents the Universe from collapsing into a singularity. In this article, we have investigated the influence of this modified dynamics on the duration of inflation. The conclusion is that the modification of the Friedmann equation has a very small (but non vanishing) impact on the

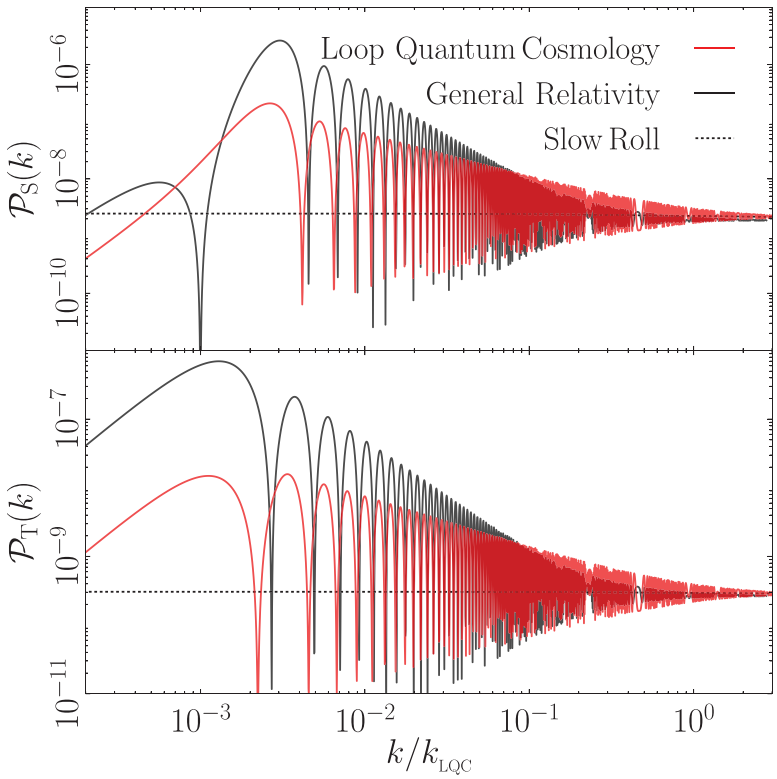

Figure 6. Primordial power spectra of scalar (top) and tensor (bottom) perturbations for the GR-like dynamics in black (standard Friedmann equation, initial condition at the energy density corresponding to the energy density of the LQC bounce) and LQC dynamics in red (initial conditions at the bounce) plotted against the slow-roll expectation (dotted lines). On the x-axis, $k_{\mathrm{LQC}} = a_{\mathrm{B}}\sqrt{\rho_{\mathrm{B}}}$. The spectrum becomes scale invariant in the UV limit.

duration of inflation. The key role played by LQC in 'predicting' inflation—or more precisely the duration of inflation—is not due to the modified dynamics in itself. It is grounded in two different aspects. First, LQC sets the energy scale. This is the fundamental point. As far as the Universe is assumed to be filled by a massive scalar field, inflation happens naturally if the energy scale 'before' inflation is high enough, $\rho \gg m^2$. But whereas starting at the Planck energy density in GR is somehow arbitrary, in LQC the bounce energy density can be calculated (modulo some hypotheses) and derived from the full theory, providing a natural energy scale. This is the first important aspect. Second, LQC selects favored conditions at the bounce, see formula (6), corresponding to a favored duration of inflation $N \simeq 145$, for $\rho_{\mathrm{B}} = 0.41 m_{\mathrm{Pl}}^4$. This is an interesting prediction rooted in the existence of a pre-bounce phase where a natural variable to which a known PDF can be assigned was identified. This cannot be produced in standard cosmology and is specific to bouncing models.

Acknowledgments

The work of BB was supported by a grant from ENS Lyon and a Fulbright Grant from the Franco-American commission.

ORCID

Boris Bolliet https://orcid.org/0000-0003-4922-7401

References

[1] Ashtekar A and Singh P 2011 *Class. Quantum Grav.* **28** 213001
[2] Ade P *et al* 2015 (Planck)
[3] Bonga B and Gupt B 2016 *Gen. Relativ. Gravit.* **48** 71
[4] Martineau K, Barrau A and Schander S 2017 *Phys. Rev.* D **95** 083507
[5] Barrau A and Bolliet B 2016 *Int. J. Mod. Phys.* D **25** 1642008
[6] Gibbons G W and Turok N 2008 *Phys. Rev.* D **77** 063516
[7] Kofman L, Linde A D and Mukhanov V F 2002 *J. High Energy Phys.* JHEP10(2002)057
[8] Bolliet B, Barrau A, Grain J and Schander S 2016 *Phys. Rev.* D **93** 124011
[9] Corichi A and Karami A 2011 *Phys. Rev.* D **83** 104006
[10] Ashtekar A and Sloan D 2011 *Gen. Relativ. Gravit.* **43** 3619
[11] Linsefors L and Barrau A 2013 *Phys. Rev.* D **87** 123509
[12] Linsefors L and Barrau A 2015 *Class. Quantum Grav.* **32** 035010
[13] Agullo I, Ashtekar A and Nelson W 2013 *Class. Quantum Grav.* **30** 085014
[14] Barrau A, Bojowald M, Calcagni G, Grain J and Kagan M 2015 *J. Cosmol. Astropart. Phys.* JCAP05(2015)051
[15] Agullo I 2015 *Phys. Rev.* D **92** 064038
[16] Bolliet B, Grain J, Stahl C, Linsefors L and Barrau A 2015 *Phys. Rev.* D **91** 084035

2.3 Perturbations scalaires en LQC

2.3.1 La théorie des perturbations

La formation des grandes structures actuelles auraient pour origine des perturbations du champ d'inflaton. Durant l'inflation, les fluctuations quantiques de ce champ sont excitées et leur longueur d'onde va croître. Si la longueur d'onde devient plus grande que le rayon de Hubble, le terme de friction devient important et l'amplitude des fluctuations se "gèle". Ces perturbations quantiques ont des conséquences sur la métrique et sont décrites par les équations linéarisées de la RG.

Les perturbations du champ d'inflaton

On considère un champ scalaire sans masse dans un espace de de Sitter, tel que

$$a(t) \propto e^{Ht}, \tag{2.36}$$

avec H constant. Le champ s'écrit

$$\phi + \delta\phi, \tag{2.37}$$

avec ϕ la valeur moyenne du champ et $\delta\phi$ les perturbations qui obéissent à l'équation de Klein-Gordon (1.70). Les modes de Fourier de ces perturbations s'écrivent

$$\delta\phi(\boldsymbol{x}, t) = \int \frac{d^3\boldsymbol{k}}{(2\pi)^{3/2}} e^{i\boldsymbol{k}\cdot\boldsymbol{x}} \delta\phi_{\boldsymbol{k}}(t). \tag{2.38}$$

Leur dynamique est régie par l'équation suivante

$$\frac{d^2}{dt^2}\delta\phi_{\boldsymbol{k}} + 3H\frac{d}{dt}\delta\phi_{\boldsymbol{k}} + \frac{k^2}{a^2}\delta\phi_{\boldsymbol{k}} = 0. \tag{2.39}$$

Pour $\lambda \ll H^{-1}$, on peut négliger le terme de friction $3H(d\delta\phi_{\boldsymbol{k}}/dt)$ et on retrouve l'équation d'un oscillateur harmonique ; les fluctuations oscillent. Pour $\lambda \gg H^{-1}$, on a $k \ll aH$, le dernier terme de l'équation (2.38) est négligeable et les modes deviennent constants.

Les perturbations scalaires de la métrique

Les perturbations du champ scalaire $\delta\phi$ vont modifier le tenseur énergie-impulsion et donc engendrer des perturbations de la métrique. Ainsi, on a

$$g_{\mu\nu} + \delta g_{\mu\nu}, \tag{2.40}$$

avec $g_{\mu\nu}$ la valeur moyenne de la métrique. A priori les deux perturbations doivent être traitées en même temps, cependant à l'ordre linéaire elles peuvent être traitées de façon indépendante. La métrique est décrite par l'équation de Friedmann (1.61) en cosmologie standard et par l'équation modifiée (2.31) dans le cadre de la LQC. Les perturbations de la métrique peuvent être décomposées en des termes scalaires, vecteurs et tenseurs. En effet, à l'ordre linéaire, ces trois types de perturbations sont découplées et peuvent donc être traitées séparément. Ici, nous ne considérons que les perturbations scalaires. L'expression de la métrique perturbée est donnée par

$$ds^2 = a^2(\eta)\Big[-(1+2\varphi)d\eta^2 + 2\partial_\alpha B d\eta dx^\alpha - [(1-2\psi)\delta_{\alpha\beta} + 2\partial_\alpha\partial_\beta E]dx^\alpha dx^\beta \Big], \tag{2.41}$$

avec $\alpha, \beta \epsilon \{1, 2, 3\}$, où nous avons quatre perturbations de champ scalaire φ, B, ψ et E. Ici nous avons utilisé le temps conforme η défini tel que $dt = a(\eta)d\eta$. On peut alors construire des variables invariantes de jauge, ce sont les potentiels de Bardeen [22] :

$$\Phi = \varphi + (B - E')' + H_c(B - E'), \tag{2.42}$$
$$\Psi = \psi - H_c(B - E'). \tag{2.43}$$

avec $H_c = a'/a$ le paramètre de Hubble comobile et le prime désigne la dérivée par rapport au temps conforme. De même, il est possible de définir les quantités invariantes de jauge pour le champ d'inflaton :

$$\delta\phi^{GI} = \delta\phi + \phi(B - E). \tag{2.44}$$

Après avoir introduit ces quantités invariantes, nous avons la liberté de fixer une jauge, on peut ensuite effectuer les calculs et obtenir les quantités physiques. Dans la jauge longitudinale : $E = B = 0$, on a la contrainte suivante : $\varphi = \psi$. Une combinaison linéaire des équations d'Einstein nous permet d'obtenir l'équation du mouvement pour Φ et la partie non diagonale des équations nous impose $\Psi = \Phi$. En définissant

$$z = a\frac{\dot{\phi}}{H} \quad \text{et} \quad v = a\delta\phi^{GI} + z\Psi, \tag{2.45}$$

puis en passant dans l'espace de Fourier, on trouve l'équation de Mukhanov-Sasaki :

$$v'' - \left(k^2 - \frac{z''}{z}\right)v = 0. \tag{2.46}$$

Pour décrire les perturbations en LQC il existe deux approches qui mènent à deux équations du mouvement différentes.

L'approche LQC de la métrique habillée

Cette approche a été développée en 2012 par Agullo, Ashtekhar et Nelson [23, 24, 25]. L'espace de Hilbert total est donné par un produit tensoriel entre l'espace de Hilbert du fond et celui des perturbations. On traite les perturbations dans la représentation de Schrödinger et elles sont quantifiées avec les techniques de TQC en espace courbe mais on n'utilise pas la métrique classique. En effet, le fond, lui, est quantifié à la LQG et ses effets quantiques se retrouvent dans une métrique effective dite métrique habillée

$$\tilde{g} = \tilde{a}^2(-d\tilde{\eta}^2 + \delta_{\mu\nu}dx^\mu dx^\nu), \tag{2.47}$$

avec $\tilde{a}$ et $\tilde{\eta}$ le facteur d'échelle habillé et le temps conforme habillé, respectivement. Le fond est représenté par la fonction d'onde $\Psi[a, \phi]$ et, $\tilde{a}$ et $\tilde{\eta}$ sont obtenus via

$$\tilde{a}^4 = \langle \hat{H}_{FLRW}^{-1/2}\hat{a}^4\hat{H}_{FLRW}^{-1/2}\rangle\langle \hat{H}_{FLRW}^{-1}\rangle^{-1} \quad \text{et} \quad \tilde{\eta} = \tilde{a}^2\langle \hat{H}_{FLRW}^{-1}\rangle d\phi, \tag{2.48}$$

avec $\hat{H}_{FLRW}$ un opérateur associé à la contrainte Hamiltonienne C divisé par 2 pour un fond homogène et isotrope. Les crochets représentent la valeur moyenne par rapport à l'état correspondant à $\Psi[a, \phi]$.

En utilisant le champ scalaire ϕ comme horloge il est possible d'établir les équations du mouvement [23]. On obtient alors l'équation de Mukhanov-Sasaki modifiée, qui s'écrit alors

$$v'' - \left(k^2 - \frac{\bar{z}''}{\bar{z}}\right)v = 0, \tag{2.49}$$

avec $\bar{z}$ une valeur habillée dans une métrique habillée. La variable $\bar{z}$ est initialement définie à partir d'opérateurs, mais les calculs montrent qu'elle se réduit au z usuel et on retrouve l'équation (2.46). Étant donné que les degrés de liberté du fond et les modes d'inhomogénétités sont séparés, cette approche perd la covariance [26]. L'intérêt de cette approche est qu'elle est plus « près » de la théorie mère, car elle tente en effet de traiter les degrés de liberté de façon quantique, mais elle a le défaut de n'avoir pas prouver sa cohérence au sens où il n'est pas évident que l'algèbre résultante soit clause.

L'approche LQC de l'algèbre déformée

L'approche dite de l'algèbre déformée a été initiée par Bojowald en 2006 [27, 28, 29], puis étudié en 2012 avec Cailleteau, Barrau, Mielszarek, et Grain [30, 31, 32, 33]. Dans la section 1.5, on a vu que l'algèbre est fermée sur l'hypersurface des contraintes. Ici on prend en compte la matière, la contrainte Hamiltonienne admet alors un terme en ϕ et p_ϕ et les crochets de Poisson s'écrivent : $\{\,.\,,\,.\,\} = \{\,.\,,\,.\,\}_{b,p} + \{\,.\,,\,.\,\}_{\phi,p_\phi}$. Lorsqu'on intègre la correction d'holonomie dans ces contraintes, on a des anomalies qui apparaissent et l'algèbre n'est plus fermée

$$\{T_i, T_j\} = f_{ij}^k(A,E)T_k + \mathcal{A}_{ij}, \tag{2.50}$$

avec $\mathcal{A}_{ij}$ les termes d'anomalies. Il est possible d'ajouter des termes dans les crochets de Poissons (2.50) qui permettent de retrouver une algèbre fermée. Par exemple, en RG, les crochets de Poisson de la contrainte Hamiltonienne s'écrivent :

$$\{C[N], C[M]\} = -D[S^{\mu\nu}(N\partial_\mu M - M\partial\partial_\nu N)], \tag{2.51}$$

avec $S^\mu_\nu = |detE^\mu_i|E^\mu_i E^i_\nu$. En LQC, si on prend en compte la correction d'holonomie et qu'on supprime les anomalies au second ordre on obtient

$$\{C[N], C[M]\} = \Omega D[S^{\mu\nu}(N\partial_\mu M - M\partial\partial_\nu N)], \tag{2.52}$$

avec

$$\Omega = 1 - 2\frac{\rho}{\rho_c}. \tag{2.53}$$

L'équation de Mukhanov-Sasaki modifiée s'écrit alors

$$v'' - \left(\Omega k^2 - \frac{z''}{z}\right)v = 0. \tag{2.54}$$

Lorsque Ω change de signe, proche du rebond, la structure de l'espace-temps devient Euclidienne [34].

Dans les deux cas

A présent, nous souhaitons définir explicitement le potentiel effectif z''/z. Pour cela on utilise la définition (2.45) et la dynamique de fond. En utilisant les équations (2.31,1.69, 1.70) et leur dérivées, on obtient le potentiel effectif

$$\frac{z''}{z} = a^2\Big[-\partial_\phi^2 V(\phi) + 2H^2 - 2\kappa\Omega\frac{\dot\phi\partial_\phi V(\phi)}{H} - \frac{7}{2}\kappa\Omega\dot\phi^2 + \frac{3\kappa}{\rho_c}\dot\phi^4 + \kappa^2\Omega^2\frac{\dot\phi^4}{2H^2}\Big]. \tag{2.55}$$

Étant donné que cette équation découle de la dynamique de fond, elle est valable pour les deux approches : la métrique habillée et l'algèbre déformée. Le terme Ω n'est pas associé à la seconde approche, il provient de la dérivation de l'équation (2.31).

2.3.2 Le spectre des perturbations scalaires en LQC

Le spectre de puissance des perturbations primordiales est un point clé pour permettre de tester les prédictions de LQC avec les expériences. Actuellement, les inhomogénéités scalaires du CMB sont observables via les variations en température. Dans le futur, les inhomogénéités tensorielles seront accessibles via la détection des modes B (mesure de la polarisation des photons). Dans cet article, nous nous intéressons au spectre des perturbations scalaires prédit par la LQC. On considère un champ scalaire massif avec une inflation à roulement lent. On explore différentes formes de potentiel pour ce champ.

La perturbation de courbure ψ associée à la foliation de l'espace décrit par la métrique ADM (1.131) est définie par

$$e^{6\psi} = \det\left(q_{\mu\nu}/a^2\right), \tag{2.56}$$

avec $q_{\mu\nu}$ la métrique spatiale. Pour un temps conforme η constant dans univers plat, la courbure intrinsèque de l'hypersurface spatiale s'écrit

$${}^{(3)}R = \frac{4}{a^2}\boldsymbol{\nabla}^2\psi. \tag{2.57}$$

On peut alors définir la perturbation de courbure comobile $\mathcal{R}$ telle que

$$\mathcal{R} = \psi + H\frac{\delta\phi}{\dot{\phi}}. \tag{2.58}$$

Elle peut également s'écrire à l'aide des variables de Mukhanov-Sasaki

$$\mathcal{R} = \frac{v}{z}. \tag{2.59}$$

Les modes qui sont plus grands que le rayon de Hubble n'évoluent plus dans le temps. Leur amplitude est figée dés lors qu'ils traversent ce rayon. Puis, après l'inflation, l'échelle de Hubble grandit plus rapidement que les longueurs d'ondes et ces modes re-entrent dans l'horizon de Hubble, pendant la phase dominée par le rayonnement ou la matière. Ainsi les modes sont dé-figés et les perturbations de densité de matière augmentent. Ce processus permet des créer les grandes structures. Au contraire les modes bien plus petits que le rayon de Hubble se comportent comme des ondes planes dans un espace de Minkowski (la courbure est négligeable pour eux). Les fonctions de corrélation à deux points de $\mathcal{R}$ dans l'espace de Fourier définissent le spectre de puissance $P_{\mathcal{R}}$ tel que

$$(2\pi)^3 P_{\mathcal{R}}(k_1)\delta(\boldsymbol{k}_1 + \boldsymbol{k}_2) = \langle \mathcal{R}_{\boldsymbol{k}_1}\mathcal{R}_{\boldsymbol{k}_2}\rangle. \tag{2.60}$$

Dans le cas d'une inflation à roulement lent, le spectre de puissance des perturbations scalaires s'écrit

$$P_S(k) = \frac{k^3}{2\pi^2}P_{\mathcal{R}}(k) = \frac{k^3}{2\pi^2}\left|\frac{v_k}{z}\right|^2 = A_S\left(\frac{k}{k_\star}\right)^{n_s-1}, \tag{2.61}$$

avec $k_\star = 0.05\ \mathrm{Mpc}^{-1}$ l'échelle de pivot.

L'approche de la métrique habillée

Pour commencer, nous nous plaçons dans le formalisme de la métrique habillée et nous considérons un potentiel quadratique. Les conditions initiales sont choisies lorsqu'on se trouve dans un vide de Bunch-Davies, quand le potentiel effectif est négligeable,

$$z''/z \ll k^2, \tag{2.62}$$

pour qu'il n'y est pas d'ambiguïté. En effet, dans ce cas, l'équation de Mukhanov-Sasaki (2.46) a des fréquences indépendantes du temps. Ainsi, les modes ne sont pas affectés par la gravité et se comportent comme dans un espace de Minkowski. On a alors

$$v_k(\eta) = \frac{1}{\sqrt{2k}} e^{-ik\eta}. \tag{2.63}$$

En cosmologie standard, le vide de Bunch-Davies est atteint de façon asymptotique lorsqu'on s'approche du Big-Bang. En LQC, pour les perturbations scalaires, le vide de Bunch-Davies est atteint a différents moments dans la phase de contraction. En effet, on peut voir sur la Figure 3 de l'article, le comportement du potentiel z''/z. On a des oscillations qui s'amplifient à l'approche du rebond. On observe que le potentiel est nul aux temps

$$t_i = 1.46, \times 10^7, \tag{2.64}$$

$$t_i = 1.52 \times 10^7. \tag{2.65}$$

Ces deux instants sont des moments privilégiés pour mettre les conditions initiales. Cependant ces instants sont proches du rebond, où la phase quantique émerge. Ainsi, il faut tout de même, être conscient que ce ne sont pas non plus des conditions idéales mais elles restent préférables à tous les autres choix potentiels étant donné la théorie effective. Dans la Figure 4 de l'article, on observe que pour des conditions initiales choisies aux deux temps qui correspondent au vide de Bunch-Davies (2.64, 2.65), le spectre de puissance est similaire. On peut observer trois comportements : la région ultraviolette où le spectre est proportionnel à $k^{-0.04}$; la région intermédiaire des oscillations et la région infrarouge où le spectre est proportionnel à k^2. Dans la région infrarouge, la condition (2.62) sera moins respectée quand k devient petit. Le choix du vide idéal serait quand $t \to -\infty$ ainsi, le spectre au temps (2.65) doit être légèrement meilleur qu'au temps (2.64). Qu'en est-il de la comptabilité avec les expériences ? Les observations montrent un spectre presque invariant d'échelle. La partie infrarouge ne présente pas cette invariance. La partie intermédiaire n'est pas incompatible car il est possible d'avoir des oscillations qui en moyenne sont invariantes d'échelle. Enfin, la partie ultraviolette est consistante avec les observations. De plus, étant donné qu'une grande partie de l'espace des phases des conditions initiales donne lieu à une durée d'inflation supérieure à 70 e-folds, il est très probable que le spectre observé se trouve dans la région ultraviolette. Ainsi le spectre de puissance de la LQC est compatible avec les expériences.

On a également étudié le spectre pour des formes de potentiel plus générales :

$$V(\phi) = \frac{1}{n} \lambda_n \phi^n. \tag{2.66}$$

Le comportement du potentiel z''/z dépend de la valeur de n, comme le montre la Figure 8. Néanmoins, il existe toujours un nombre fini de points où on est dans les conditions du vide de Bunch-Davies. Les spectres de puissance sont légèrement différents. En fait les lois de puissance dépendent de la valeur de

n. Mais les trois régions disparates sont toujours présentes. La région des ultraviolets est dans tous les cas pratiquement invariante d'échelle.

L'approche de l'algèbre déformée

Dans cette approche, on observe que le spectre de puissance présente une croissance exponentielle dans la région ultraviolette (voir les Figures 12-14). De plus, ce caractère divergeant apparaît peu importe la forme du potentiel du champ scalaire. Ceci n'est pas du tout compatible avec les observations. Cependant, on peut se poser la question de pourquoi un tel comportement apparaît ? Quelle hypothèse fausse-t-elle le résultat ? Un point important, non résolu à ce jour, est le problème transplanckien. En effet, ici on considère la partie du spectre où les longueurs d'ondes sont petites. Ainsi, si on remonte suffisamment loin dans le passé, ces longueurs vont devenir inférieures à la longueur de Planck, et dans ce cas une approche semi-classique n'est pas forcément apte à décrire la physique. Il faudrait considérer un système purement quantique pour traiter le problème.

Cet article a été publié dans *Physical Review D* [35].

Scalar spectra of primordial perturbations in loop quantum cosmology

Aurélien Barrau,[*] Pierre Jamet,[†] Killian Martineau,[‡] and Flora Moulin[§]

Laboratoire de Physique Subatomique et de Cosmologie, Université Grenoble-Alpes, CNRS-IN2P3 53, Avenue des Martyrs, 38026 Grenoble cedex, France

(Received 18 July 2018; published 1 October 2018)

This article is devoted to the study of scalar perturbations in loop quantum cosmology. It aims at clarifying the situation with respect to the way initial conditions are set and to the specific choice of an inflaton potential. Several monomial potentials are studied. Both the dressed metric and deformed algebra approaches are considered. We show that the calculation of the ultraviolet part of the spectrum, which is the physically relevant region for most background trajectories, is reliable, whereas the infrared and intermediate parts do depend on some specific choices that are made explicit.

DOI: 10.1103/PhysRevD.98.086003

I. INTRODUCTION

The calculation of primordial cosmological power spectra is an important way to connect speculative theories of quantum gravity with observations (see [1] for a recent review). Among those theories, loop quantum gravity (LQG) (see, e.g., [2]) has now reached the point where explicit calculations can be performed. At this stage, it remains, however, extremely difficult to derive rigorous cosmological predictions from the full theory. But, in the specific case of loop quantum cosmology (LQC), which can be viewed as the quantization of symmetry reduced general relativity using techniques from LQG (see, e.g., [3,4]), quite a lot of results have already been obtained, beginning with the replacement of the usual big bang by a big bounce. Recently, important improvements were proposed, e.g., in group field theory [5–7], in quantum reduced loop gravity [8–11], in refined coherent state approaches [12], in diffeomorphism invariance derivation [13] or in analogies with a Kasner transition [14], to cite only a few.

Together with hybrid quantization [15,16], two main approaches have been developed in this framework to study inhomogeneities: the dressed metric [17–19] and the deformed algebra [20–23]. The first deals with quantum fields on a quantum background, while the second puts the emphasis on the consistency and covariance of the effective theory. This led to clear predictions about the power spectra [24–29]. Other complementary paths were also considered to investigate perturbations [30–34].

Many works were devoted to tensor perturbations that are easier to handle both for gauge and for anomaly issues. Scalar modes are, however, more important from the observational viewpoint (see, e.g., [24,35–38] for recent works in LQC). This article focuses on scalar spectra and aims at clarifying how previous LQC results obtained for a simple massive scalar field can be generalized to other monomial potentials and to which extent the spectrum is sensitive to initial conditions (i.e., to a vacuum choice) for perturbations. It is essentially impossible to derive fully generic results, so we explicitly investigate different solutions and show the associated numerical computations so that they can be accounted for in future studies.

II. GENERIC FRAMEWORK

We consider here a spatially flat and isotropic FLRW spacetime filled with a minimally coupled scalar field with a monomial potential. We neglect backreaction and trans-Planckian effects.

We first come back to the study developed by some of the authors of this article in [27]. As in this work, we adopt here a causal viewpoint and put the initial conditions, both for the background and the perturbations, as far as possible in the contracting phase preceding the bounce.

The basic ingredients are the following. The Friedmann equation, modified by holonomy corrections, reads as

$$H^2 = \frac{\kappa}{3}\rho\left(1-\frac{\rho}{\rho_c}\right), \tag{2.1}$$

where ρ_c is the critical density (expected to be of the order of the Planck density), and $H = \dot{a}/a$ is the Hubble parameter. The Klein-Gordon equation for the background is given by

$$\ddot{\varphi} = -3H\dot{\varphi} - \partial_\varphi V(\varphi), \tag{2.2}$$

where φ is here used for $\bar{\varphi}$, the average scalar field. The differential system for the background can be summarized as (we choose the convention $a(t_{\rm init}) = 1$)

[*]Aurelien.Barrau@cern.ch
[†]pierre.jamet@vivaldi.net
[‡]martineau@lpsc.in2p3.fr
[§]flora.moulin@lpsc.in2p3.fr

$$\dot{\varphi}(t) = \frac{\partial\varphi}{\partial t}, \tag{2.3}$$

$$\ddot{\varphi}(t) = -3H(t)\dot{\varphi}(t) - \partial_\varphi V(\varphi(t)), \tag{2.4}$$

$$\dot{H}(t) = -\frac{\kappa}{2}\dot{\varphi}^2(t)\left(1 - 2\frac{\dot{\varphi}^2(t)/2 + V(\varphi(t))}{\rho_c}\right), \tag{2.5}$$

$$\dot{a}(t) = H(t)a(t). \tag{2.6}$$

Perturbations are described in the Fourier space by the gauge invariant Mukhanov-Sasaki equation,

$$v_k'' + \left(k^2 - \frac{z''}{z}\right)v_k = 0, \tag{2.7}$$

where $z = \frac{a\dot{\varphi}}{H}$, and the derivation is with respect to the conformal time $d\eta = \frac{1}{a}dt$. One can easily show that

$$\frac{\dddot{z}}{z} = \frac{\dddot{\varphi}}{\dot{\varphi}} + \frac{\ddot{\varphi}}{\dot{\varphi}}\left(2H - 2\frac{\dot{H}}{H}\right) + H^2 - \dot{H} + 2\left(\frac{\dot{H}}{H}\right)^2 - \frac{\ddot{H}}{H}. \tag{2.8}$$

Introducing

$$\Omega = 1 - 2\frac{\rho}{\rho_c}, \tag{2.9}$$

and using

$$\rho = \frac{1}{2}\dot{\varphi}^2 + V(\varphi), \tag{2.10}$$

leads to the final expression,

$$\frac{z''}{z} = a^2\left(-\partial_\varphi^2 V(\varphi) + 2H^2 - 2\kappa\Omega\frac{\dot{\varphi}\partial_\varphi V(\varphi)}{H} - \frac{7}{2}\kappa\Omega\dot{\varphi}^2 + \frac{3\kappa}{\rho_c}\dot{\varphi}^4 + \kappa^2\Omega^2\frac{\dot{\varphi}^4}{2H^2}\right). \tag{2.11}$$

This is the intricate effective potential that has to be dealt with. In the next two sections, we study perturbations as described by the dressed metric approach [17–19], which is very close to the hybrid quantization one as far as phenomenology is concerned [33]. Interestingly, at the effective level, the equation of motion (2.7) is formally the same than in general relativity, even though the value of z''/z is of course heavily modified. We then switch to the deformed algebra approach were an effective change of signature shows up.

III. QUADRATIC POTENTIAL

The resulting typical evolution of the scalar field is shown in Fig. 1: pseudo-oscillations are followed by the bounce and by an inflationary stage. The details obviously depend on the phase of the field during the contracting period but, as shown in [39–41], what is displayed in Fig. 1 is a quite generic behavior. The probability to have, e.g., a phase of deflation is much smaller. All numbers are given in Planck units.

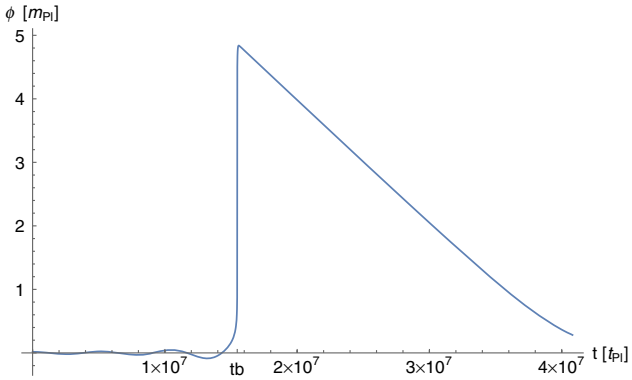

FIG. 1. Temporal evolution of the scalar field, for a mass $m = 1.2 \times 10^{-6}$.

The way to choose initial conditions for the perturbations is more subtle. The usual Minkowski solution,

$$v_k(\eta) = \frac{1}{\sqrt{2k}}e^{-ik\eta}, \tag{3.1}$$

is approached in the so-called Bunch-Davies vacuum. The main requirement to set the vacuum is that the effective potential is negligible so that the equation of motion becomes nearly the one of an harmonic oscillator. In addition, if the causal evolution of the Universe during the bounce is taken seriously and if the word "initial" is taken literally, it makes sense to put initial conditions far away before the bounce, this later constituting in addition the most "quantum" and less controlled moment in the whole cosmic history (see e.g., [42] for a discussion). As it will become clear later, this requirement is actually in tension with the first one (which should be considered as the mandatory one).

The evolution of the absolute value of the effective potential $\frac{z''}{z}$ is shown in Fig. 2 during the full integration time interval. It should be noticed that it increases both in the past and in the future of the bounce (which is located around $t = 1.5 \times 10^7$ on the plot). This raises an issue which is fundamental for bouncing models and should be taken into account with care, as studied later in this article.

Figure 3 shows the effective potential between the beginning of the integration interval and the bounce. The shape is highly complex and very different from what happens either in standard cosmology or in LQC for tensor modes. In the standard cosmological model it vanishes when going backward in time, deep into the de Sitter inflationary phase. This is also true for bouncing models when going far away in the past of the contracting phase, but only for tensor modes. In the considered case, due to the large (negative) value taken by the potential in the remote

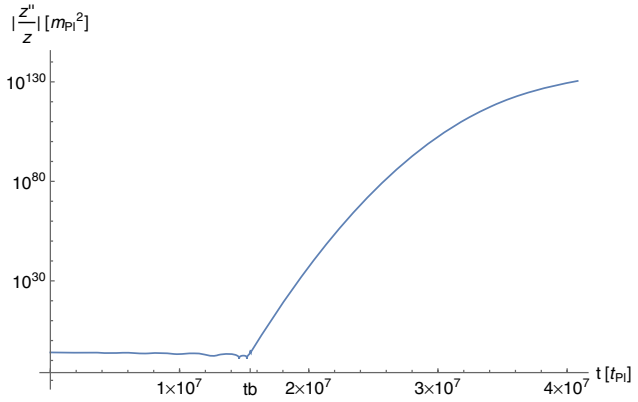

FIG. 2. Temporal evolution of the absolute value of effective potential $\frac{z''}{z}$ over the full integration interval.

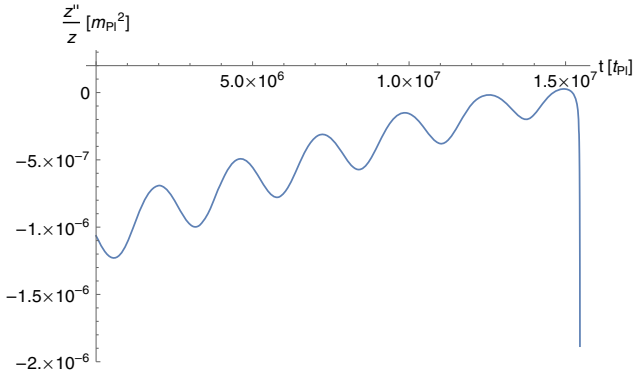

FIG. 3. Temporal evolution of the effective potential $\frac{z''}{z}$ between the beginning of the integration and just before the bounce.

past it is impossible to put stable initial conditions very far from the bounce. Strictly speaking, it might make sense to set initial conditions in this way but the interesting selection criterion associated with the Bunch-Davies vacuum would be lost. If one wants to remain in a framework where a Bunch-Davies–like initial state—which is at least justified to compare with other results—is used, there are two moments which can be chosen such that $\frac{z''}{z}$ vanishes. However, those points are not far from the bounce and the fact that "initial" conditions have to be set at very specific moments is something that deserves to be better understood in the future and should be, at this stage, considered as a weakness (at least at the heuristic level) of those models.

As a first step in a better understanding of the situation, we present in Fig. 4 the primordial power spectra resulting from a full simulation of the evolution of perturbations with initial conditions set both at the first zero, i.e., at $t_i = 1.46 \times 10^7$, corresponding to the earliest time in cosmic history, and at the second zero of the effective potential at $t_i = 1.52 \times 10^7$.

First, it should be emphasized that the ultraviolet (UV) part of the spectrum is the same for both ways of putting

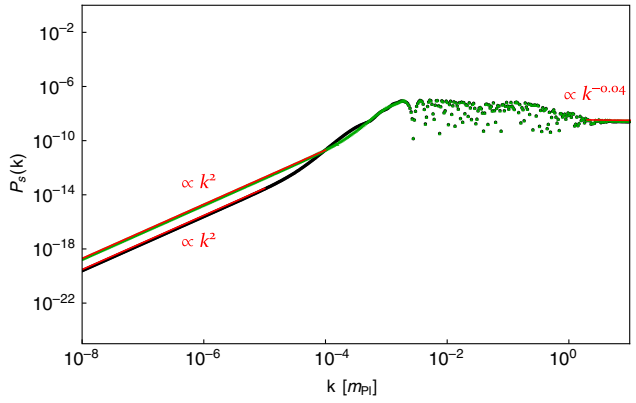

FIG. 4. Primordial scalar power spectra, as a function of the comoving wave number, for a quadratic potential and initial conditions put whether at the first zero of $\frac{z''}{z}$, i.e., $t_i = 1.46 \times 10^7$ (lower plot in the IR, black disks), or at the last zero of $\frac{z''}{z}$, i.e., $t_i = 1.52 \times 10^7$ (upper plot in the IR, green triangles).

initial conditions and is compatible with observations, that is nearly scale invariant with a very slight tilt due to the slow roll of the field during the inflationary stage. This is particularly important as the UV part of the spectrum is most probably the one which is experimentally probed. This last fact entirely depends on the number of e-folds of inflation: the conversion of the comoving wave number into a physical wave number requires the knowledge of the expansion factor of the Universe. Except if the background initial conditions are hyper-fine-tuned, inflation lasts long enough [39–41] so that the observational cosmological microwave background (CMB) window clearly falls in the UV part of the spectrum. In principle, this would require a specific trans-Planckian treatment (see [28,43] for first attempts in this direction) which is not the topic of this study and which is anyway partially accounted for in the dressed metric approach. The oscillations in the intermediate part of the spectra—due to quasi-bound states in the effective Shrödinger equation—are basically the same in both cases, together with the deep infrared (IR) part (throughout all the article we call "infrared" the rising part of the spectrum and "ultraviolet" the scale-invariant one). However, some differences do remain in the junction between the IR and the oscillatory regimes. We have checked that they are not due to numerical issues. Although this is not of high phenomenological significance, this shows that the way initial conditions are set, even around a vanishing effective potential, can influence the resulting power spectrum.

We have also checked that when moving slowly away from the exact point were $\frac{z''}{z} = 0$, the spectrum slowly changes. This is obviously expected but the details of the changes are very hard to guess as the effective potential is very complicated. Basically, the spectrum evolves from a full k^2 to a full k^3 behavior in the IR. Figure 5 presents an intermediate case, and this should be taken into account when interpreting results given in [27].

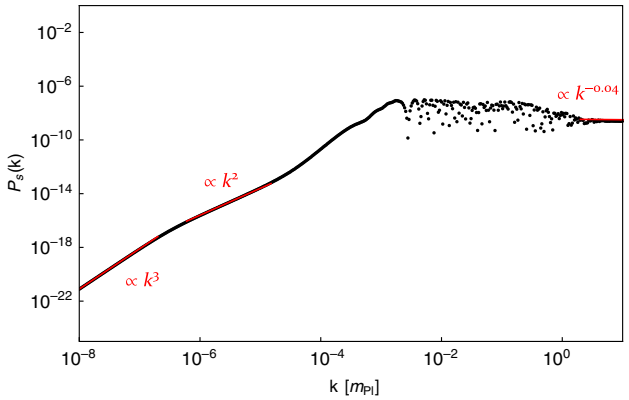

FIG. 5. Primordial scalar power spectrum, as a function of the comoving wave number, for a quadratic potential and initial conditions set $0.6t_{Pl}$ before the Bunch-Davies vacuum at $t_i = 1.46 \times 10^7$.

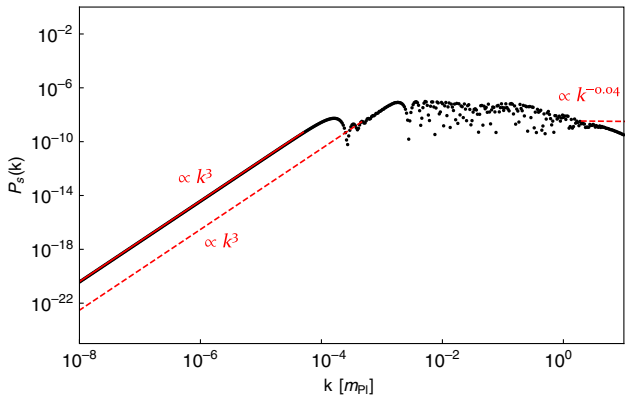

FIG. 6. Primordial scalar power spectrum, as a function of the comoving wave number, for a quadratic potential and initial conditions at local extrema far away from the bounce, at $t_i = 2.00 \times 10^6$. From the dot line to the plain line, one goes deeper in the remote past.

Finally, in Fig. 6, the spectrum is plotted for initial conditions set at a local extremum further away from the bounce, at $t_i = 2.00 \times 10^6$. The plain line corresponds to a point deeper in the past than the dotted line.

This shows that although the global shape of the spectrum is under control—especially in the region of phenomenological significance—the detailed structure is quite sensitive to the way initial conditions are set. In models where the effective potential does not vanish in the remote past, this raises nontrivial issues. This means by no way that those approaches are inconsistent but that some uncertainties associated with the loss of a strong selection criterion on initial conditions have to be included in the analysis.

IV. GENERALIZED POTENTIALS

It is important to investigate whether the scalar spectra obtained hold for other inflaton potential shapes (not to be confused with the effective potential felt by pertubations),

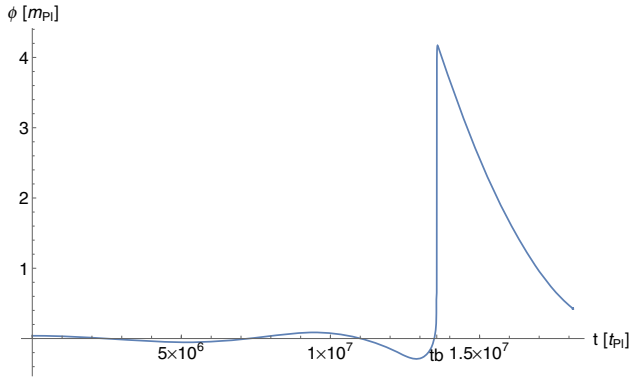

FIG. 7. Evolution of the scalar field for $n = 3$.

beyond the massive scalar field which is not favored by data [44]. The case of plateaulike potentials is very specific in bouncing models (see [41]), so we restrain ourselves to confining monomial potentials of the form:

$$V(\varphi) = \frac{1}{n}\lambda_n \varphi^n. \tag{4.1}$$

No general analytical solution in the deep contracting phase can be found anymore but it is still possible to set initial conditions for the background as done previously. The evolution of the scalar field is qualitatively weakly depending on n. As an example, we show the result for $n = 3$ in Fig. 7.

The situation is more complicated when one considers the details of the effective potential. Figure 8 shows the evolution of z''/z up to the respective bounces for $n = 3$, 4, $4/3$, $5/2$.

Clearly, the shape of the behavior of the effective potential depends on the value of n. The number of points were the potential identically vanishes is finite in each case, leading to a finite number of ways to set a rigorous instantaneous Bunch-Davis vacuum. In all cases, there is also an infinite

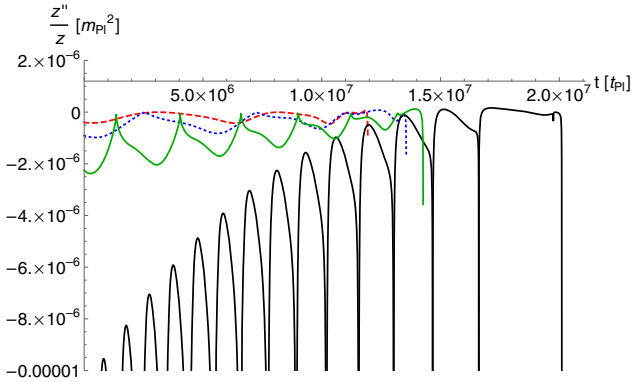

FIG. 8. Evolution of $\frac{z''}{z}$ in the contracting universe up to the respective bounces for $V(\varphi) = \frac{1}{n}\lambda_n\varphi^n$ and $n = 3$ (blue dotted line), $n = 4$ (red dashed line), $n = 4/3$ (black solid line) and $n = 5/2$ (green solid line).

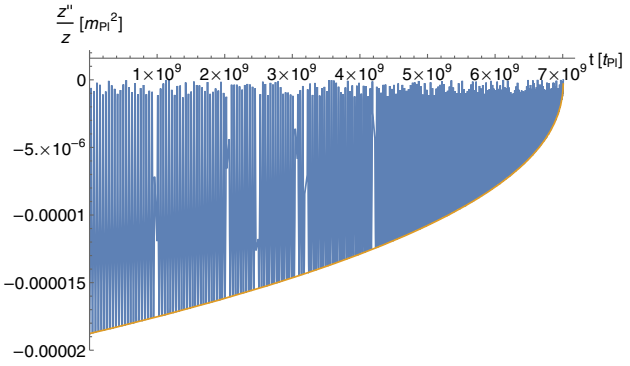

FIG. 9. Evolution of $\frac{z''}{z}$, together with its envelop, in the contracting universe, up to the bounce on a wide time interval.

number of local minima that can be used as approximate vacua, depending on the range of wave numbers relevant for the considered study. We insist once more that the details of the spectrum *do* depend on this choice.

Figure 9 shows the envelope of the effective potential for $n = 3$ when going deeper into the past. It can be empirically fitted by a power law $(t - t_b)^{0.45}$. The oscillations themselves get quite chaotic, reflecting the nonlinearity of the equations. The situation is very different from what happens for the effective potential of tensor modes. It might be that, from the bounce, time flows in two opposite directions. Then it would make sense to put initial conditions at the bounce, as in [17–19]. If, however, the evolution remains globally causal with a unique time direction, the questions raised here cannot be ignored.

As "extreme" examples, we show in Fig. 10 (respectively, Fig. 11) the scalar spectra for $n = 4/3$ (respectively, $n = 5/2$) with initial conditions set close to the bounce and in the deep past. This reinforces the previous conclusions: the "small scales" part of the spectra is nearly scale invariant in all cases (although small differences do exist), making the results compatible with observation for the vast

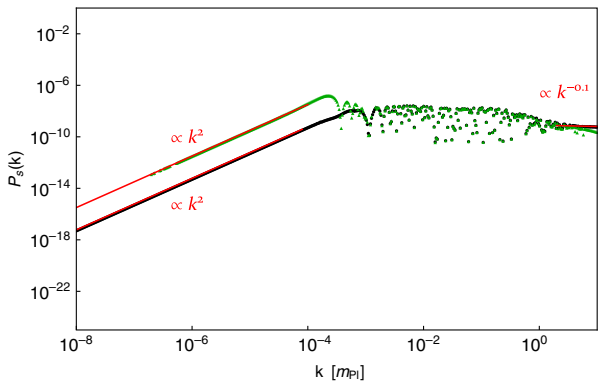

FIG. 10. Spectrum for $n = \frac{4}{3}$ with initial conditions whether close to the bounce, at $t_i = 1.87 \times 10^7 t_{Pl}$ (lower plot in the IR, black disks), or far from it at $t_i = 1.49 \times 10^7$ (upper plot in the IR, green triangles).

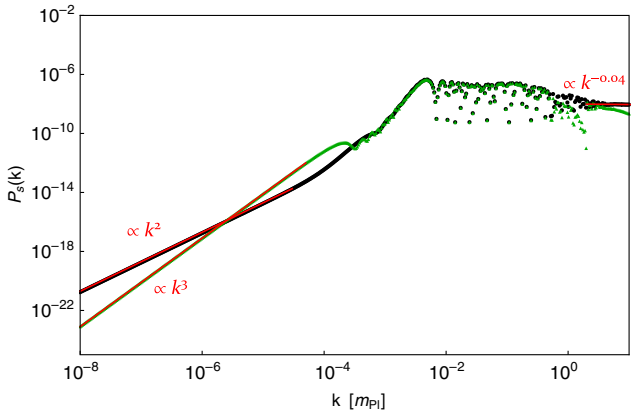

FIG. 11. Spectrum for $n = \frac{5}{2}$ with initial conditions whether close to the bounce, at $t_i = 1.35 \times 10^7$ (k^2 behavior in the IR, black disks), or far from it at $t_i = 1.35 \times 10^6 t_{Pl}$ (k^3 behavior in the IR, green triangles).

majority of the parameter space which leads to an inflationary stage so long that the observable part falls in the deep UV range. However, the IR part and some of the oscillations can sensitive to the details of the inflaton potential shape and to the way initial conditions are set.

V. DEFORMED ALGEBRA

Another approach to LQC, the so-called deformed algebra, relies on a different view of the situation [20–23,45,46]. In this case, the emphasis in put on the consistency of the effective theory. The Poisson brackets are calculated between (holonomy) quantum corrected constraints. Anomalies do appear in general. To ensure covariance, counter-terms with a vanishing classical limit are added to the constraints, so that the system remains "first class" in the Dirac sense. The resulting algebra (including the matter content) is closed and reads as

$$\{D[N_1^a], [N_2^a]\} = 0, \tag{5.1}$$

$$\{H[N], D[N^a]\} = -H[\delta N^a \partial_a \delta N], \tag{5.2}$$

$$\{H[N_1], H[N_2]\} = D\left[\Omega \frac{\bar{N}}{\bar{p}} \partial^a (\delta N_2 - \delta N_1)\right], \tag{5.3}$$

where $D[N^i]$ is the full diffeomorphism constraint and $H[N]$ is the full scalar constraint. The important feature it the $\Omega = (1 - 2\rho/\rho_c)$ term in the last Poisson bracket. It becomes negative close to the bounce and leads to an effective change of signature. The Mukhanov equation of motion in Fourier space reads, in this framework, as

$$\ddot{\mathcal{R}}_k - \left(3H + 2m^2 \frac{\bar{\varphi}}{\dot{\bar{\varphi}}} + 2\frac{\dot{H}}{H}\right)\dot{\mathcal{R}}_k + \Omega \frac{k^2}{a^2}\mathcal{R}_k = 0, \tag{5.4}$$

with

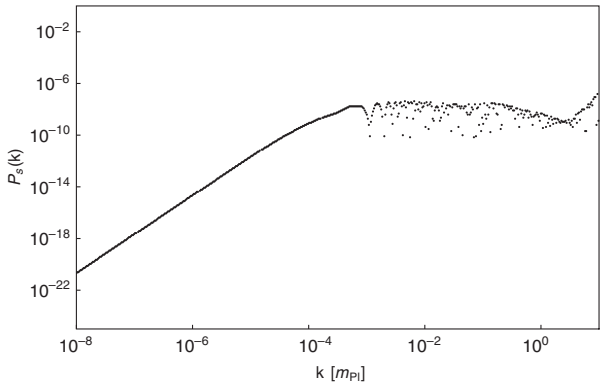

FIG. 12. Spectrum for $n = \frac{4}{3}$ within the deformed algebra approach and initial conditions set at $t_i = 1.87 \times 10^7$.

$$\mathcal{R} := \frac{v}{z}, \tag{5.5}$$

where v is the gauge-invariant perturbation and z is the background variable. Phenomenologically, the main consequence of this model, if a causal view is chosen and a massive scalar field is assumed to fill the Universe, is an exponential growth of the spectrum in the UV [26,27]. It is obviously not compatible with data [29], but this conclusion clearly relies on heavy assumptions that might be radically altered when considering trans-Planckian effects [28] or other ways of setting initial conditions [47,48].

We have readdressed the question of the propagation of scalar perturbations in the deformed algebra framework with new potentials. As can be seen in Figs. 12–14, the UV rise of the spectrum clearly remains present whatever the chosen potential. All the conclusions about the features of this model, therefore, remain valid beyond the massive scalar field approximation. The subtle modifications of the IR shape are actually due to the way the initial vacuum is chosen which is inevitably impacted by the choice of the potential.

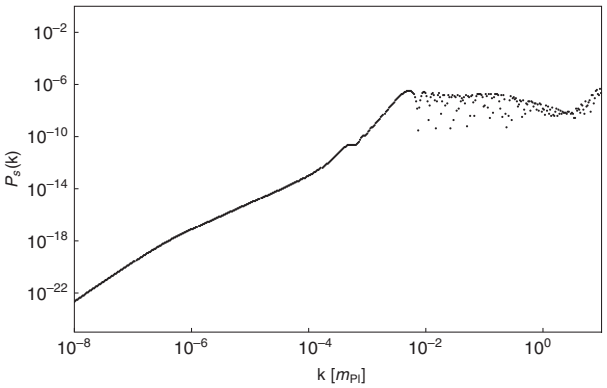

FIG. 13. Spectrum for $n = 3$ within the deformed algebra approach and initial conditions set at $t_i = 1.17 \times 10^7$.

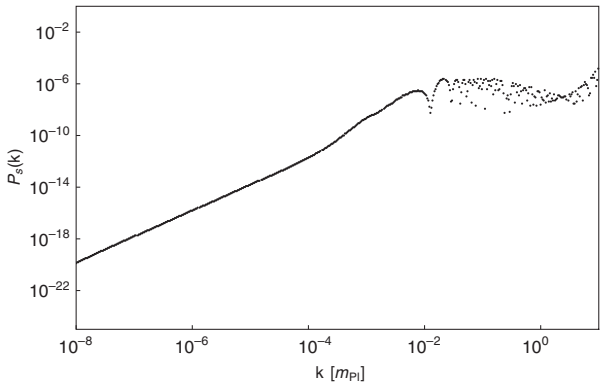

FIG. 14. Spectrum for $n = 4$ within the deformed algebra approach and initial conditions set at $t_i = 1.19 \times 10^7$.

VI. CONCLUSION

In this article, we have addressed the question of the primordial power spectrum of scalar perturbations in a bouncing universe described by loop quantum cosmology by studying the gauge-invariant Mukhanov-Sasaki equation with the appropriate effective potential associated with different inflation potentials. A full numerical simulation was developed. The conclusions are the following:

(i) the temporal behavior of the effective z''/z potential is, in general, highly complicated with a pseudo-periodic structure which depends on the details of the inflaton potential $V(\varphi)$.

(ii) the ultraviolet part of the power spectrum, which is the most relevant one from the observational perspective, is mostly independent of the way initial conditions are set and of the choice of the potential. This makes the main LQC predictions robust.

(iii) the intermediate and infrared parts of the spectrum do depend on the initial conditions and on the inflaton potential. The IR slope varies between k^2 and k^3 depending on the type of vacuum chosen and the amplitude of the oscillations can vary substantially.

This study shows that the main conclusions regarding the compatibility of the spectrum with CMB observations (for most of the parameter space span by initial conditions for the background) in LQC are reliable. However, if the initial values for the inflaton field and its momentum are fine-tuned so that the number of e-folds of inflation is small, the observational window might fall on the intermediate or IR part of the spectrum. In that case, LQC predictions do depend on the way initial conditions (for perturbations) are set and on the choice of the inflaton potential. This should be taken into account in future studies.

ACKNOWLEDGMENTS

K. M. is supported by a grant from the CFM foundation.

[1] A. Barrau, C.R. Phys. **18**, 189 (2017).
[2] C. Rovelli and F. Vidotto, *Covariant Loop Quantum Gravity*, Cambridge Monographs on Mathematical Physics (Cambridge University Press, Cambridge, England, 2014).
[3] A. Ashtekar and P. Singh, Classical Quantum Gravity **28**, 213001 (2011).
[4] A. Ashtekar and A. Barrau, Classical Quantum Gravity **32**, 234001 (2015).
[5] F. Gerhardt, D. Oriti, and E. Wilson-Ewing, arXiv:1805.03099.
[6] D. Oriti, C.R. Phys. **18**, 235 (2017).
[7] D. Oriti, L. Sindoni, and E. Wilson-Ewing, Classical Quantum Gravity **34**, 04LT01 (2017).
[8] E. Alesci, G. Botta, F. Cianfrani, and S. Liberati, Phys. Rev. D **96**, 046008 (2017).
[9] E. Alesci and F. Cianfrani, Int. J. Mod. Phys. D **25**, 1642005 (2016).
[10] E. Alesci and F. Cianfrani, Phys. Rev. D **92**, 084065 (2015).
[11] E. Alesci and F. Cianfrani, Phys. Rev. D **87**, 083521 (2013).
[12] A. Dapor and K. Liegener, Classical Quantum Gravity **35**, 135011 (2018).
[13] J. Engle and I. Vilensky, Phys. Rev. D **98**, 023505 (2018).
[14] E. Wilson-Ewing, Classical Quantum Gravity **35**, 065005 (2018).
[15] M. Fernndez-Mndez, G. A. Mena Marugn, and J. Olmedo, Phys. Rev. D **88**, 044013 (2013).
[16] D. Martín-de Blas, M. Martín-Benito, and G. A. Mena Marugán, Springer Proc. Math. Stat. **60**, 327 (2014).
[17] I. Agullo, A. Ashtekar, and W. Nelson, Classical Quantum Gravity **30**, 085014 (2013).
[18] I. Agullo, A. Ashtekar, and W. Nelson, Phys. Rev. Lett. **109**, 251301 (2012).
[19] I. Agullo, A. Ashtekar, and W. Nelson, Phys. Rev. D **87**, 043507 (2013).
[20] J. Mielczarek, T. Cailleteau, A. Barrau, and J. Grain, Classical Quantum Gravity **29**, 085009 (2012).
[21] T. Cailleteau, J. Mielczarek, A. Barrau, and J. Grain, Classical Quantum Gravity **29**, 095010 (2012).
[22] T. Cailleteau, A. Barrau, J. Grain, and F. Vidotto, Phys. Rev. D **86**, 087301 (2012).
[23] A. Barrau, M. Bojowald, G. Calcagni, J. Grain, and M. Kagan, J. Cosmol. Astropart. Phys. 05 (2015) 051.
[24] I. Agullo and N. A. Morris, Phys. Rev. D **92**, 124040 (2015).
[25] B. Bolliet, J. Grain, C. Stahl, L. Linsefors, and A. Barrau, Phys. Rev. D **91**, 084035 (2015).
[26] L. Linsefors, T. Cailleteau, A. Barrau, and J. Grain, Phys. Rev. D **87**, 107503 (2013).
[27] S. Schander, A. Barrau, B. Bolliet, L. Linsefors, J. Mielczarek, and J. Grain, Phys. Rev. D **93**, 023531 (2016).
[28] K. Martineau, A. Barrau, and J. Grain, Int. J. Mod. Phys. D **27**, 1850067 (2018).
[29] B. Bolliet, A. Barrau, J. Grain, and S. Schander, Phys. Rev. D **93**, 124011 (2016).
[30] E. Wilson-Ewing, Classical Quantum Gravity **29**, 215013 (2012).
[31] S. Gielen and D. Oriti, arXiv:1709.01095.
[32] I. Agullo, Gen. Relativ. Gravit. **50**, 91 (2018).
[33] E. Wilson-Ewing, C.R. Phys. **18**, 207 (2017).
[34] B. Elizaga Navascus, D. Martin de Blas, and G. A. Mena Marugn, Phys. Rev. D **97**, 043523 (2018).
[35] B. Bonga and B. Gupt, Gen. Relativ. Gravit. **48**, 71 (2016).
[36] B. Bonga and B. Gupt, Phys. Rev. D **93**, 063513 (2016).
[37] I. Agullo, A. Ashtekar, and B. Gupt, Classical Quantum Gravity **34**, 074003 (2017).
[38] A. Ashtekar and B. Gupt, Classical Quantum Gravity **34**, 035004 (2017).
[39] L. Linsefors and A. Barrau, Phys. Rev. D **87**, 123509 (2013).
[40] L. Linsefors and A. Barrau, Classical Quantum Gravity **32**, 035010 (2015).
[41] K. Martineau, A. Barrau, and S. Schander, Phys. Rev. D **95**, 083507 (2017).
[42] A. Barrau and B. Bolliet, Int. J. Mod. Phys. D **25**, 1642008 (2016).
[43] A. Espinoza-Garca and E. Torres-Lomas, arXiv:1709.03242.
[44] P. A. R. Ade *et al.* (Planck), Astron. Astrophys. **594**, A20 (2016).
[45] M. Bojowald and G. M. Paily, Phys. Rev. D **86**, 104018 (2012).
[46] T. Cailleteau, L. Linsefors, and A. Barrau, Classical Quantum Gravity **31**, 125011 (2014).
[47] J. Mielczarek, L. Linsefors, and A. Barrau, Int. J. Mod. Phys. D **27**, 1850050 (2018).
[48] M. Bojowald and J. Mielczarek, J. Cosmol. Astropart. Phys. 08 (2015) 052.

2.4 Distance de luminosité dans un univers en contraction

L'émergence d'un univers en contraction précédent la phase d'expansion ouvre de nouvelles perspectives. Ce scénario d'un univers en rebond existe également en dehors de la LQC. Est ce que des observables issues de l'univers pré-rebond pourraient persister dans l'univers actuel ? Dans cet article nous investiguons le comportement de la distance de luminosité dans un univers en contraction. Le flux observé d'une source astrophysique est donné par

$$f = \frac{L}{4\pi D_L^2}, \tag{2.67}$$

avec L la luminosité de la source et D_L la distance de luminosité. Cette dernière permet de décrire la distance parcourue par un signal étant donné que l'univers est dynamique. Dans un univers plat, elle s'écrit

$$D_L = c(1+z)\int_0^z \frac{dz'}{H(z')}, \tag{2.68}$$

avec z le redshift et H le paramètre de Hubble. On peut l'écrire comme une fonction du temps

$$D_L = c\frac{a(t_r)^2}{a(t_e)}\int_{t_e}^{t_r}\frac{dt}{a(t)}. \tag{2.69}$$

avec t_e et t_r le temps cosmologique d'émission et de réception, respectivement. Soit $t = 0$ le temps de rebond et un univers qui se contracte selon $a(-t) = k(-t)^n$. Ici k est une simple constante de proportionnalité, et ne doit pas être confondu avec le facteur de courbure, qui lui est nul. Soit t_e et t_r négatifs, tel que $t_e < t_r$, dans la phase de contraction, alors on a

$$D_L = c\frac{(-t_r)^{2n}}{n-1}\left[\frac{(-t_r)^{1-n}}{(-t_e)^n} - (-t_e)^{1-2n}\right]. \tag{2.70}$$

Il existe trois comportements de la distance de luminosité en fonction de la valeur de n. Ces comportement sont mis en évidence par la Figure 1 de l'article :

1. Pour $n < 1/2$, la limite est donnée par

$$\lim_{t_e\to-\infty} D_L = \infty. \tag{2.71}$$

   La distance de luminosité augmente lorsque l'intervalle de temps augmente.

2. Pour $n = 1/2$, il est intéressant de constater que la limite est donnée par

$$\lim_{t_e\to-\infty} D_L = \frac{2ca(t_r)^2}{k}. \tag{2.72}$$

   Cette valeur de n correspond à un univers dominé par le rayonnement. On observe qu'il existe un régime asymptotique à partir du quel la luminosité observée ne dépend plus du temps d'émission.

3. Pour $n > 1/2$, cette limite est

$$\lim_{t_e\to-\infty} D_L = 0. \tag{2.73}$$

De façon intuitive, la distance de luminosité diminue dès lors que l'univers se contracte plus rapidement que le signal ne se propage. Soit une source observée à $t = t_r$, si elle a été émise peu de temps avant, la distance de luminosité va croitre avec l'intervalle de temps $\Delta t = |t_e - t_r|$. Cependant si cet intervalle continue de croître, alors la distance de luminosité va ensuite diminuer. En effet, le maximum est atteint lorsque

$$-t_e = \left[\frac{2n-1}{n}\right]^{\frac{1}{n-1}}(-t_r). \tag{2.74}$$

Ainsi après ce maximum, une source apparaîtra d'autant plus brillante qu'elle n'a été émise loin de le passé. Cet effet sera évidemment amplifié dans le cas d'un univers en contraction exponentielle.

Dans certains cas, la distance de luminosité diminue ou atteint une valeur asymptotique avec le temps. Cela soulève un paradoxe : un univers infiniment en contraction avec des objets dont la luminosité explose n'est pas viable. En considérant la gravité quantique, la contraction entraîne une croissance de la densité d'énergie jusqu'à atteindre la densité critique ρ_c. Dès lors, les effets quantiques répulsifs vont dominer et on aura le scénario du rebond. Ainsi, cette étude sur la distance de luminosité permet de contraindre le passé asymptotique pour certains types de contenus.

La distance de luminosité n'est pas une observable additive. Un effet intégré engendre qu'une source émise dans la phase de contraction peut voir sa distance de luminosité diminuer autant qu'elle ne sera ensuite augmentée dans la phase d'expansion de sorte qu'elle est la même luminosité à la réception. Évidemment, ici, les effets du rebond sur la propagation du signal ont été omis. Toutefois, en première approximation, on observe que des sources pré-rebond peuvent émettre des signaux qui perdurent dans l'univers post-rebond, de façon non négligeable. C'est le cas des ondes gravitationnelles. En effet leur amplitude est inversement proportionnelle à la distance de luminosité

$$h = \frac{4}{D_L}\left[\frac{G\mathcal{M}}{c^2}\right]^{\frac{5}{3}}\left[\frac{\pi f}{c}\right]^{\frac{2}{3}} g(\tau, \Phi(f)), \tag{2.75}$$

avec $\mathcal{M}$ la "chirp mass", f la fréquence des ondes gravitationnelles,g une fonction qui dépend de la polarisation, τ l'angle du plan orbital et $\Phi(f)$ la phase.

Du point de vue observationel, l'amplitude d'ondes pré-rebond sera fortement atténuée par la phase d'inflation. Cependant, plusieurs modèles à rebond peuvent résoudre les problèmes d'homogénité, d'horizon et de platitude sans avoir recours à l'inflation [36, 37]. Nous nous plaçons dans ce cadre-ci et nous étudions un modèle simplifié. Soit une phase de contraction dominée par le rayonnement, puis une phase stationnaire pour le rebond, suivi d'une phase dominée par le rayonnement, puis la matière. On a considéré des ondes gravitationnelles émises par la coalescence de trous noirs de 10^9 et 10^8 masses solaires (voir la Figure 4). Étant donné, le contenu en rayonnement dans la phase de contraction, la coalescence peut avoir lieu arbitrairement loin avant le rebond. L'amplitude des ondes h est tracée en fonction de la température de l'univers au moment du rebond. On observe que pour des températures raisonnables, l'amplitude est constante et ses valeurs sont d'ordre comparable aux amplitudes prochainement détectables. Évidemment, la formule de l'amplitude est valable seulement en régime perturbatif. Mais pour des températures faibles le régime perturbatif est valide.

Ainsi par cette étude nous avons étudié le comportement de la distance de luminosité dans un univers en contraction. En fonction du contenu elle peut augmenter, mais également stagner ou diminuer. Dans les deux derniers cas, ceci engendre un régime à haute densité d'énergie, où une

description quantique serait de rigueur, qui permet de décrire la phase de rebond. Le comportement de la distance de luminosité permet notamment d'envisager que des ondes gravitationnelles pré-rebond pourraient avoir des amplitudes non négligeables aujourd'hui, selon les modèles. Qu'en est-il de leur fréquences ? Sont-elles dans un intervalle mesurable ? Cela dépend du temps d'émission. Par exemple dans la cas d'un univers parfaitement symétrique au rebond, un signal sera autant "blueshifté" dans la phase en contraction, que "redshifté" dans la phase en expansion. Donc la fréquence observée sera celle émise. Ainsi, on observe d'ores et déjà qu'il existe plusieurs cas possibles où la fréquence se situerait dans l'intervalle des fréquences mesurables mais une étude plus précise serait profitable.

Cet article a été publié dans *Physical Review D* [38].

PHYSICAL REVIEW D **96,** 123520 (2017)

Seeing through the cosmological bounce: Footprints of the contracting phase and luminosity distance in bouncing models

Aurélien Barrau, Killian Martineau, and Flora Moulin

Laboratoire de Physique Subatomique et de Cosmologie, Université Grenoble-Alpes, CNRS/IN2P3 53, avenue des Martyrs, 38026 Grenoble cedex, France

(Received 14 September 2017; published 18 December 2017)

The evolution of the luminosity distance in a contracting universe is studied. It is shown that for quite a lot of natural dynamical evolutions, its behavior is far from trivial and its value can even decrease with an increasing time interval between events. The consequences are investigated and it is underlined that this could both put stringent consistency conditions on bouncing models and open a new observational window on "pre-big bang" physics using standard gravitational waves.

DOI: 10.1103/PhysRevD.96.123520

I. INTRODUCTION

The big bang is a prediction of general relativity (GR) in a regime where the theory is not valid anymore. Singularities are most probably pathologies of the models, not of spacetime itself. It is therefore natural to consider alternatives to the naive big bang image. Importantly, most models replacing the initial singularity by "something else" were not designed to this aim but produce this desirable effect as a consequence of their application to the early universe (see [1,2] and references therein for recent reviews). Among the countless ways to obtain a cosmological bounce, one can mention the null energy condition violation [3], the strong energy condition violation with a positive curvature [4], ghost condensates [5], galileons [6], S-branes [7], quantum fields [8], higher derivative terms [9,10], non-standard couplings [11], supergravity [12], and loop quantum cosmology [13,14]. These are only some examples among a much longer list which also includes, in a way, the ekpyrotic and cyclic scenarios [15,16], together with string gaz cosmology [17]. Bouncing models are natural extensions of the big bang scenario and it comes as no surprise that they arise in many theories beyond GR. (Interestingly, those ideas are also being investigated in the black hole sector, see [18] for a recent review).

All those models are obviously missing an observational confirmation or, at least, strong experimental constraints. As a legitimate step in this direction, many efforts were recently devoted to the calculation of primordial cosmological power spectra. Predictions for the cosmological microwave background (CMB) were made for nearly all the above-mentioned models (as examples for specific settings, explaining the global strategy, one can consider [19,20]).

In this article we follow another path. We investigate the unusual luminosity distance behavior in a contracting universe. We show that it is highly nontrivial. As a consequence, we raise some consistency issues for bouncing cosmological models. We finally suggest possible observational footprints of the contracting phase that could be observed through "usual" gravitational waves.

II. THE LUMINOSITY DISTANCE IN A CONTRACTING UNIVERSE

As far as observations are concerned, an important parameter is the luminosity distance D_L. It is defined by $f = L/(4\pi D_L^2)$, where f is the observed flux from a given astrophysical source and L is its luminosity. Intuitively, the luminosity distance is the "equivalent" distance at which an object of the same luminosity should be in a usual euclidean space to lead to the same observed flux. In a flat expanding universe (in the presence of spatial curvature, the general expression involves trigonometric and hyperbolic functions [21]), it reads as

$$D_L = c(1+z)\int_0^z \frac{dz'}{H(z')}, \tag{1}$$

where H is the Hubble parameter and z is the redshift. For our purpose, it is convenient to rewrite this formula as a function of time:

$$D_L = c(1+z)a(t_r)\int_{t_e}^{t_r} \frac{dt}{a(t)}, \tag{2}$$

where t_e and t_r are the emission and reception cosmic times of the considered signal and $a(t)$ is the scale factor. To study a contracting universe it is even better to get rid of the redshift and write the expression as

$$D_L = c\frac{a(t_r)^2}{a(t_e)}\int_{t_e}^{t_r} \frac{dt}{a(t)}. \tag{3}$$

When one considers the contracting branch of a bouncing scenario, interesting and unusual phenomena can take place. Let us choose $t = 0$ at the bounce time and assume that the universe contracts as $a(t) = k(-t)^n$ before the bounce (with $n = 2/3$ for a matter-dominated phase and $n = 1/2$ for a radiation-dominated phase). The detailed evolution around the bounce could be e.g., given by the loop quantum cosmology modified Friedmann equation [22]

$$H^2 = \frac{\kappa}{3}\rho\left(1 - \frac{\rho}{\rho_c}\right), \tag{4}$$

where ρ_c depends on the details of the model but can be guessed to be close to the Planck density. However we have checked that the observables calculated in this article do not depend on the detailed shape of the modified equation of motion. We therefore approximate the scale factor by a constant function between $-t_B$ and t_B. Let t_e and t_r both be negative—that is in the contracting branch—with $t_e < t_r$. It is then easy to show that:

$$D_L = c\frac{(-t_r)^{2n}}{n-1}\left[\frac{(-t_r)^{1-n}}{(-t_e)^n} - (-t_e)^{1-2n}\right]. \tag{5}$$

When $n < 1/2$, $D_L \to \infty$ when $t_e \to -\infty$. This is in agreement with the intuitive behavior.

However, when $n > 1/2$, $D_L \to 0$ when $t_e \to -\infty$. This is one of the important results we want to stress here. This strange behavior never happens in an expanding universe. It means that, for a fixed reception time t_r, an event that took place earlier in the contracting phase will be seen as *brighter*. Of course, the luminosity distance first increases with higher values of $-t_e$, reaches a maximum, and then decreases. The maximum can be shown (when $n \neq 1$) to be reached when

$$-t_e = \left[\frac{2n-1}{n}\right]^{\frac{1}{n-1}}(-t_r). \tag{6}$$

When $n = 1/2$, $D_L \to 2ca(t_r)^2/k^2$ when $t_e \to -\infty$. This means that events arbitrarily far away in the past will be detected at the same brightness once the asymptotic regime is reached.

Figure 1 shows the luminosity distance evolution for three different values of n. It can be seen that D_L is asymptotically constant in the remote past when $n = 1/2$ and tends to 0 when $n > 2/3$. The numerical values are not relevant and the plot aims at showing the global behavior.

In Fig. 2 we consider the luminosity distance between an event in the contracting phase and the contemporary universe, as a function of the "bounce duration." Figure 2 shows that the detailed value of t_B does not care in the following analysis: the contribution of the bounce phase to the full integral is negligible.

Finally, it is worth considering the cosmological constant case, $a(t) = ke^{-\alpha t}$, where $\alpha = |H| > 0$. The luminosity distance then reads

$$D_L = c\frac{e^{\alpha(t_e - 2t_r)}}{\alpha}\left[e^{\alpha t_r} - e^{\alpha t_e}\right]. \tag{7}$$

Clearly, in this case again, $D_L \to 0$ when $t_e \to -\infty$, as illustrated in Fig. 3. Sources located in the remote past have their flux intensely amplified.

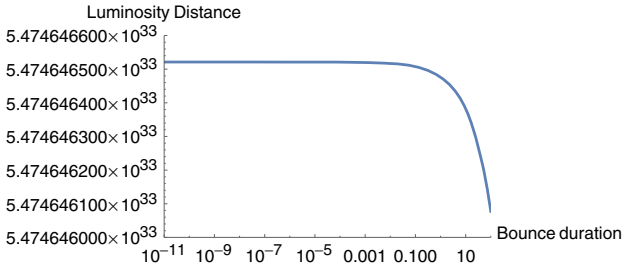

FIG. 2. Luminosity distance (m) as a function of the bounce duration (s) between an event in the contracting phase and the current universe (including radiation dominated and matter dominated phases).

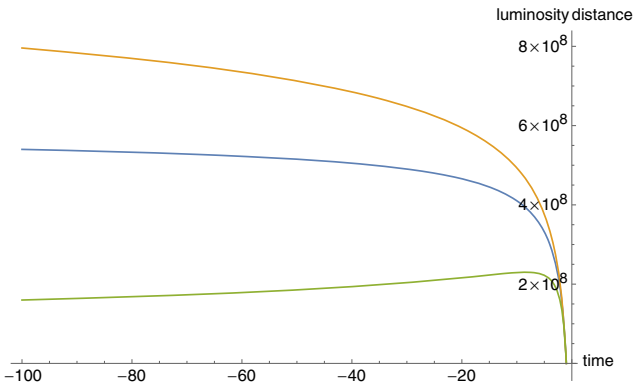

FIG. 1. Luminosity distance (m) as a function of the emission time t_e (s) in the contracting branch for the power law contraction. The reception time t_r has been set to 1 second before the bounce. The lower curve corresponds to $n = 2/3$, the mid curve to $n = 1/2$ and the upper curve to $n = 0.45$.

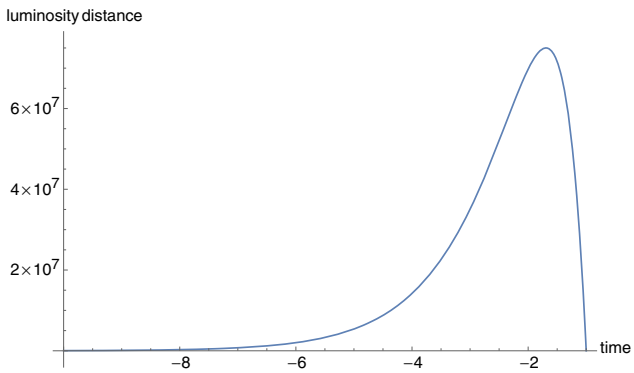

FIG. 3. Luminosity distance (m) as a function of the emission time t_e (s) in the contracting branch for an exponential contraction. The reception time t_r has been set to 1 second before the bounce and α was arbitrarily set to 1 in order to increase the readability.

III. CONSISTENCY CONDITIONS

The results given in the previous section do raise some questions. The case $n > 1/2$ is in no way exotic from the point of view of the equation of state. It actually corresponds to a usual matter dominated universe, as naively expected far away from bounce. The behavior of the luminosity distance is then such that sources that have emitted light in an arbitrary distant past will lead to a measured flux which is arbitrarily amplified by the contraction of the scale factor. This basically means that the energy density will diverge at all points in space, leading to a kind of *new Olbers paradox* worsened by the contraction. In addition the frequency will also become arbitrarily high. As a consequence, the Universe cannot have been forever in a contraction phase with $n > 1/2$ and filled with objects emitting energy. The energy density growth would anyway trigger the bounce—at least in quantum-gravity models where the energy density is bounded from above by quantum geometry repulsive effects. This consistency condition has to be taken into account when building a consistent bouncing universe.

The case $n = 1/2$ is not fundamentally different. The luminosity distance being nearly constant, the energy amount received by each space point would also diverge in a forever-contracting universe. It should be pointed out that even for $n < 1/2$ the space integral of any homogeneous source term will obviously diverge, as this is already the case in a static Minkowski universe.

The exponential contraction case is slightly more subtle. The luminosity distance is rapidly going to zero. The amplification due to the fast contraction of the Universe is thus very intense. However the horizon and physical distances relative evolutions are such that the comoving Hubble radius is shrinking when going backward in time in the contracting branch (as when going forward in time in the expanding branch). The number density of sources causally linked to any space point will therefore also tend to zero and eventually solve the apparent paradox.

IV. SEEING THROUGH THE BOUNCE

Those considerations raise the important question of the possible observation of events having taken place before the bounce. Obviously, most signals or objects possibly existing in the contracting branch will be destroyed of washed out by the huge density reached—in most models—around the bounce time. The only exception could be gravitational waves. This is the only signal coupled weekly enough to matter so that it could propagate through the bounce (the details depend on the specific model considered). This has been investigated in different cases (see, e.g., [23,24]) but focusing only on geometrical aspects—ignoring the aforementioned amplification—and considering consequences on the cosmological microwave background (CMB) spectra.

Let us consider here a different scenario. The hypothesis is that an event emitting intense gravitational waves has taken place before the bounce, e.g., the coalescence of two massive black holes (BHs). Clearly we do not know what the Universe looked like before the bounce. We however assume here that events comparable to what happens in our expanding branch took place in the contracting branch. At the lowest order the wave amplitude produced by a binary system and observed far away can be written [25]:

$$h = \frac{4}{D_L}\left[\frac{G\mathcal{M}}{c^2}\right]^{\frac{5}{3}}\left[\frac{\pi f}{c}\right]^{\frac{2}{3}} g(\tau, \Phi(f)), \tag{8}$$

where $\mathcal{M}$ is the chirp mass, f is the gravitational wave frequency at the observer location, g is a sum and product of trigonometric functions (different for different polarizations) depending on τ, the angle of the orbital plane, and on the phase $\Phi(f)$.

As quite a lot of bouncing models are justified as alternatives to inflation (although bounces are compatible with inflation [26]), it is instructive to focus on a non-inflationary scenario and to study whether a pre-big bounce signal can be detected. (An inflationary phase would obviously dilute the signal to a vanishingly small amplitude.) We consider the following toy model: a contracting radiation-dominated phase, followed by a stationary bouncing phase, followed by the usual radiation-dominated and matter dominated stages. The number of efolds between the bounce and today is of course a relevant parameter that we express through the temperature of the Universe at the bouncing time. On Fig 4, we have plotted the amplitude of gravitational waves emitted by the coalescence of 100 millions and one billion solar masses BHs as a function of the bouncing temperature. Interestingly, for a radiation dominated contracting phase, because the luminosity distance rapidly reaches an asymptotic value, it is not necessary to specify the merging time as long as it is far enough before the bounce. As it can be noticed from the curves, as soon as the temperature is chosen at a reasonable value, the

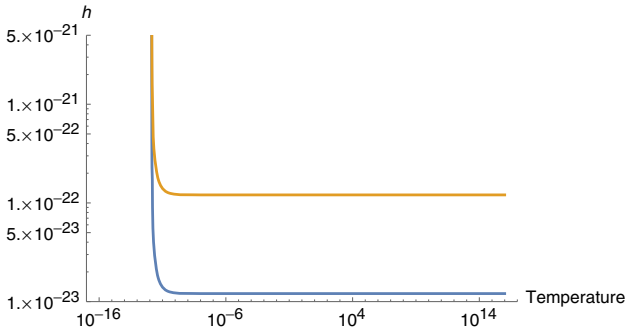

FIG. 4. Gravitational wave amplitude today as a function of the bounce temperature (GeV). The upper curve is for 10^9 solar masses BHs and the lower curve for 10^8 solar masses BHs, both merging in the contracting phase.

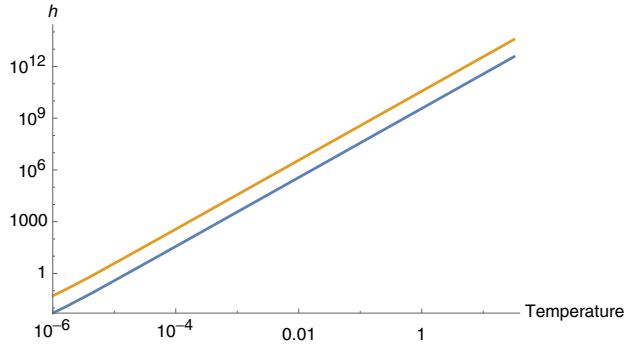

FIG. 5. Gravitational wave amplitude at the bounce time as a function of the bounce temperature (GeV). The upper curve is for 10^9 solar masses BHs and the lower curve for 10^8 solar masses BHs, both merging in the contracting phase.

amplitude is constant and becomes non-negligible and comparable to the sensitivity of current or next-generation experiments. The h asymptotic behavior—which might appear as quite strange at first sight—is just due to the converging property of the integral of $1/a$ which enters the definition of the luminosity distance.

An obvious limitation of this calculation comes from the perturbative treatment. As it can be seen in Fig. 5, as long as the bounce temperature is set much above the nucleosynthesis temperature, the gravitational waves amplitude at the bounce becomes too large to justify a perturbative calculation. This is a limitation to the presented study—which requires a deeper treatment for this case—but not to the presented idea in itself.

However, if the bounce temperature is set to the lowest possible one, the amplitude at the bounce is marginally compatible with a perturbative approach and this study shows—in a consistent way—that, in principle, gravitational waves from events occurring in the contracting phase of bouncing models could be detected in the contemporary universe.

One could also consider a phase of matter domination preceding the radiation dominated era in the contracting branch. If sources are located in this matter dominated phase, the amplitude does depend on the time at which the coalescence takes place. It is then possible to achieve nearly any value by choosing an emission time in the deep past. But the breakdown of the perturbative treatment would them become drastic and the whole result would be questionable. We therefore restrict ourselves to the radiation dominated case.

Another limitation is associated with the homogeneous and isotropic treatment of the bouncing universe. This should be considered as a toy-model approximation. It is however not fully irrelevant. First, it should be pointed out that many bouncing models have been shown to resist the inclusion of anisotropies (see, e.g., [27] for the case of loop gravity) with a quite minor modification of the Friedmann equation [28]. Anisotropic stress on gravitational waves could even be a way to discriminated between models. The homogeneous treatment is harder to justify and should obviously be seen as a first step. Recent calculations [29] have however shown that exact solutions describing a regular lattice of black holes in a cosmological bouncing background do exist.

V. CONCLUSION

In this article we have shown that the luminosity distance in a contracting universe has a highly nontrivial behavior. Because of the "competition" between the expanding wave dilution and the amplification due to the decreasing scale factor, in some cases ($n > 1/2$), the luminosity distance between two events in the contracting branch does *decrease* with an increasing time difference.

As a consequence, some violent events releasing gravitational waves and taking place in the contracting branch of the Universe could be detected today. The question of their frequency is hard to be answered unequivocally as it obviously depends on the precise emission time which, in the case $n = 1/2$, has strictly no impact on the luminosity distance. We leave for a future study the associated statistical analysis, together with the systematic study of the characteristic signatures of "prebounce" signals.

It can already be underlined that several possible ways of discriminating between "prebounce" events and usual "postbounce" events do exist. The most obvious approach is purely statistical: the number of events should simply be higher than expected if sources located before the bounce contribute to the measured events. Beyond this obvious statement, one should also look for the absence of electromagnetic counterparts. Although not demonstrated, electromagnetic signals are usually expected to be associated with merging supermassive BHs. Third, the measured luminosity distances for some events should lie outside of the usual range (either too large or to small). Finally, the measured luminosity distance (inferred from the frequency, the frequency evolution and the amplitude, see e.g., [30] or [31]) might mismatch the real one in a way which is observationally measurable.

ACKNOWLEDGMENTS

K. M is supported by a grant from the CFM foundation.

[1] R. Brandenberger and P. Peter, Found. Phys. **47**, 797 (2017).
[2] D. Battefeld and P. Peter, Phys. Rep. **571**, 1 (2015).
[3] P. Peter and N. Pinto-Neto, Phys. Rev. D **65**, 023513 (2001).
[4] F. T. Falciano, M. Lilley, and P. Peter, Phys. Rev. D **77**, 083513 (2008).
[5] C. Lin, R. H. Brandenberger, and L. Perreault Levasseur, J. Cosmol. Astropart. Phys. 04 (**2011**) 019.
[6] T. Qiu, J. Evslin, Y.-F. Cai, M. Li, and X. Zhang, J. Cosmol. Astropart. Phys. 10 (2011) 036.
[7] C. Kounnas, H. Partouche, and N. Toumbas, Nucl. Phys. **B855**, 280 (2012).
[8] Y.-F. Cai, T. Qiu, Y.-S. Piao, M. Li, and X. Zhang, J. High Energy Phys. 10 (2007) 071.
[9] T. Biswas, A. Mazumdar, and W. Siegel, J. Cosmol. Astropart. Phys. 03 (2006) 009.
[10] T. Biswas, R. Brandenberger, A. Mazumdar, and W. Siegel, J. Cosmol. Astropart. Phys. 12 (2007) 011.
[11] D. Langlois and A. Naruko, Classical Quantum Gravity **30**, 205012 (2013).
[12] M. Koehn, J.-L. Lehners, and B. A. Ovrut, Phys. Rev. D **90**, 025005 (2014).
[13] M. Bojowald, Phys. Rev. Lett. **86**, 5227 (2001).
[14] A. Ashtekar and A. Barrau, Classical Quantum Gravity **32**, 234001 (2015).
[15] J. Khoury, B. A. Ovrut, P. J. Steinhardt, and N. Turok, Phys. Rev. D **64**, 123522 (2001).
[16] P. J. Steinhardt and N. Turok, Phys. Rev. D **65**, 126003 (2002).
[17] T. Battefeld and S. Watson, Rev. Mod. Phys. **78**, 435 (2006).
[18] C. Barcel, R. Carballo-Rubio, and L. J. Garay, J. High Energy Phys. 05 (2017) 054.
[19] P. Peter and J. Martin, hep-th/0402081.
[20] F. Finelli, P. Peter, and N. Pinto-Neto, Phys. Rev. D **77**, 103508 (2008).
[21] D. W. Hogg, astro-ph/9905116.
[22] A. Ashtekar and P. Singh, Classical Quantum Gravity **28**, 213001 (2011).
[23] V. G. Gurzadyan and R. Penrose, Eur. Phys. J. Plus **128**, 22 (2013).
[24] W. Nelson and E. Wilson-Ewing, Phys. Rev. D **84**, 043508 (2011).
[25] M. Maggiore, *Gravitational Waves. Vol. 1: Theory and Experiments*, Oxford Master Series in Physics (Oxford University Press, New York, 2007), ISBN 9780198570745, 9780198520740, URL http://www.oup.com/uk/catalogue/?ci=9780198570745.
[26] A. Barrau, T. Cailleteau, J. Grain, and J. Mielczarek, Classical Quantum Gravity **31**, 053001 (2014).
[27] A. Ashtekar and E. Wilson-Ewing, Phys. Rev. D **79**, 083535 (2009).
[28] L. Linsefors and A. Barrau, Classical Quantum Gravity **31**, 015018 (2014).
[29] T. Clifton, B. Carr, and A. Coley, Classical Quantum Gravity **34**, 135005 (2017).
[30] D. E. Holz and S. A. Hughes, Astrophys. J. **629**, 15 (2005).
[31] B. F. Schutz, ESA SP **420**, 229 (1997).

CHAPITRE 3

Les trous noirs

Sommaire

3.1 Les trous noirs en rebond

Le modèle de cosmologie quantique à boucles décrit un univers en contraction, puis, lorsque la densité critique ρ_c est atteinte, les effets de gravité quantique génèrent une force effective de répulsion qui contrebalance l'attraction gravitationelle et l'univers s'expand. L'idée des trous noirs en rebond est basée sur le même principe [39, 40]. Un trou noir est soumis à l'effondrement gravitationnel, puis, lorsqu'il atteint une certaine densité, l'effondrement est contrebalancé par les effets quantiques. Il transite alors vers une solution de trou blanc par effet tunnel. La singularité est alors évitée. Pour que ce processus puisse exister, il faut qu'il y ait des effets quantiques qui englobent l'horizon. Or, dans cette région la courbure est faible, donc on pourrait penser que les effets quantiques sont négligeables. Cependant, ces effets quantiques peuvent se cumuler dans le temps. Ainsi, proche, mais en dehors, de l'horizon [41], ces effets peuvent peut être devenir importants. En effet, si l'on considère le modèle de désintégration radioactive, un atome d'uranium est stable par unité de temps. Néanmoins, après plusieurs milliards d'années, l'atome finira par se désintégrer par effet tunnel. Le modèle de trou noir en rebond est analogue. La probabilité de transiter vers un trou blanc est faible, mais cumulée dans le temps, le trou noir finira par transiter vers cet état par effet tunnel. Ce modèle a ensuite été amélioré pour corriger les instabilités [42]. Le temps de rebond τ est proportionnel à la masse du trou noir, M, au carré [43] : $\tau = kM^2$ avec k le facteur de proportionnalité (pris de l'ordre de 1). D'autre part, le temps d'évaporation d'un trou noir est proportionnel à sa masse au cube M^3. Ainsi un trou noir va rebondir avant de s'être totalement évaporé et son rayonnement thermique est vu comme un processus dissipatif faible.

Plusieurs études sur la phénoménologie de ce modèle ont été effectuées [44], notamment sur leur capacité à expliquer les sursauts radio rapides (FRBs pour fast radio bursts) [45, 46]. Ces études montrent que les trous noirs en rebond ne peuvent pas être une explication viable. Cependant, dans ces articles, en première approximation, le temps de vie était présumé déterministe. Or, du fait qu'il s'agisse d'un effet tunnel nous devons prendre en compte l'aspect probabiliste. C'est le point clé de l'article ci-joint.

La probabilité qu'un trou noir n'ait pas encore rebondi à l'instant t est donnée par

$$P(t) = \frac{1}{\tau} e^{\frac{-t}{\tau}}, \tag{3.1}$$

comme dans le cas de la désintégration nucléaire. Ainsi le nombre de trous noirs à avoir rebondir après un temps t_H (le temps de Hubble) par unité de temps dt est

$$dN = \frac{N_0}{kM^2} e^{-\frac{t_H}{kM^2}} dt, \tag{3.2}$$

avec N_0 le nombre de trous noirs initiaux. Les trous noirs qui ont le plus de probabilité de rebondir aujourd'hui seraient les trous noirs formés dans l'univers primordial. L'existence de ces trous noirs primordiaux (PBHs pour primordial black holes) n'est pas confirmée à ce jour. Cependant, les contraintes sur ces derniers ont récemment été actualisées [47]. Le spectre de masse des PBHs est noté dN/dM. Le signal des photons émis par un trou noir rebondissant est modélisé par une fonction Gaussienne

$$\frac{dN_\gamma^{BH}}{dE} = Ae^{-\frac{(E-E_0)^2}{2\sigma_E^2}}, \tag{3.3}$$

avec $E_0 = 1/2R_S = 1/4M$. L'amplitude A est fixée de sorte que

$$\int E \frac{dN_\gamma^{BH}}{dE} dE = M. \tag{3.4}$$

Le signal total émis pour une distribution locale de trous noirs en rebond est donnée par

$$\frac{dN_\gamma}{dE} = \int_{M_{Pl}}^{\infty} Ae^{-\frac{(E-E_0)^2}{2\sigma_E^2}} \frac{dN}{dM}(M) \frac{1}{kM^2} e^{-\frac{t_H}{kM^2}}. \tag{3.5}$$

Si les PBHs sont produits par un événement ponctuel, de type transition de phase, alors leur spectre sera piqué, tel que

$$\frac{dN}{dM} \propto e^{-\frac{(M-M_0)^2}{2\sigma_M^2}}. \tag{3.6}$$

Il n'y pas d'a priori sur la masse M_0 autour de laquelle le spectre est piqué. Si cette masse correspond à M_{t_H} (la masse définie telle que le temps de rebond est celui de Hubble), le flux sera plus important. Cependant, étant donné l'aspect probabiliste, pour des masses M_0 supérieures à M_{t_H}, il y aura des trous noirs (dans l'intervalle associé à la queue de la distribution) qui vont rebondir aujourd'hui. Nous pouvons constater par exemple, sur la Figure 1 de l'article, que lorsque la masse centrale vaut $M_0 = 1000 M_{t_H}$, le pic du flux émis se trouve dans l'intervalle d'énergie (10^{-6}eV) correspondant à celui des FRBs.

Dans d'autres modèles, nous avons un spectre large, tel que

$$\frac{dN}{dM} \propto M^{\alpha}. \tag{3.7}$$

Pour une formation de PBH à partir des fluctuations primordiales dans la phase de domination par le rayonnement $\alpha = -5/2$. Mais d'autres processus, comme des transitions de phase, peuvent conduire à des valeurs différentes. La normalisation entre les courbe est choisie telle que la masse totale allant dans les trous noirs est la même :

$$\int_{M_{Pl}}^{\infty} M \frac{dN}{dM} = cte. \tag{3.8}$$

Nous avons également considéré la normalisation telle que le nombre de trous noirs total est le même :

$$\int_{M_{Pl}}^{\infty} \frac{dN}{dM} = cte. \tag{3.9}$$

Ces deux normalisations amènent à des résultats presque identiques. Pour ce type de spectre, la phénoménologie associée est différente. Les prédictions (voir Figure 2) sont un flux qui augmente en loi de puissance avec l'énergie, et la pente varie en fonction de la puissance α du spectre de masse.

Ainsi, on a pu observer, qu'en prenant en compte l'aspect probabiliste de la transition d'un trou noir vers un trou blanc, le signal émit peut se trouver dans l'intervalle de fréquences des FRBs. En fonction de la forme du spectre de masse des PBHs, les prédictions sur la forme du signal sont différentes. Évidemment, les trous noirs en rebond ne sont pas l'explication la plus argumentée pour expliquer la présence des FRBs. D'autres sources astrophysiques peuvent tout aussi bien en être la cause. Cependant, contrairement aux études où le temps de rebond était pris comme déterministe, dans le cas probabiliste l'hypothèse n'est pas écartée. De plus, il est intéressant de noter que les trous noirs en rebond ont une signature différente de celles des sources astrophysiques ou de physique des particules. En effet, plus un trou noir rebondit loin (donc plus son énergie sera "redshiftée"), plus son temps de rebond est petit (donc plus son énergie sera grande). Or il a été montré [48] que ces deux effets se compensent de sorte que le signal ne possède pas beaucoup de dépendance en redshift.

Cet article a été publié dans *Physical Review D* [49].

Fast radio bursts and the stochastic lifetime of black holes in quantum gravity

Aurélien Barrau, Flora Moulin, and Killian Martineau
Laboratoire de Physique Subatomique et de Cosmologie, Université Grenoble-Alpes, CNRS/IN2P3 53, avenue des Martyrs, 38026 Grenoble cedex, France

(Received 4 January 2018; published 22 March 2018)

Nonperturbative quantum gravity effects might allow a black-to-white hole transition. We revisit this increasingly popular hypothesis by taking into account the fundamentally random nature of the bouncing time. We show that if the primordial mass spectrum of black holes is highly peaked, the expected signal can in fact match the wavelength of the observed fast radio bursts. On the other hand, if the primordial mass spectrum is wide and smooth, clear predictions are suggested and the sensitivity to the shape of the spectrum is studied.

DOI: 10.1103/PhysRevD.97.066019

I. INTRODUCTION

Finding observational consequences of quantum gravity is obviously a major challenge. In the last decade most attempts have focused on the early Universe, evaporating black holes, or Lorentz invariance violation (see Ref. [1] for a recent overview). In the last years, the idea that quantum gravity effects could be seen in higher-mass black holes has attracted a lot of interest [2–6]. In particular, it was suggested that the quite mysterious fast radio bursts (FRBs) [7] could be explained by bouncing black holes [8]. There are unquestionably simpler astrophysical explanations that we consider to be more probable, but this hypothesis is worth a deeper look. At the heuristic and intuitive level, this bounce can be understood as a phenomenon quite similar to what is expected to happen to the Universe in loop quantum cosmology [9,10]. In the cosmological framework, the classically contracting branch is linked to the classically expanding one by a quantum tunneling, whereas in the black hole sector the classically collapsing solution is glued to the classically exploding one (on the double cover of the Kruskal map [3]). The usual event horizon is replaced by a trapping horizon [11]. In this brief article we revisit this hypothesis by taking into account the fundamental randomness of the tunneling process that was previously ignored. In Sec. II we assume a peaked mass spectrum for the bouncing black holes and show that the 3 orders of magnitude in energy thought to be missing to explain FRBs can easily be accounted for. In Sec. III we consider a wide mass spectrum and investigate the sensitivity of the signal to the spectral index. We show that the expected emission remains compatible with measurements and make clear predictions.

II. PEAKED MASS SPECTRUM

The heuristic arguments given by Rovelli, Haggard, and Vidotto in the previously mentioned articles suggested that the black hole lifetime could be of the order of M^2 in Planck units (those units are used throughout the rest of the article except otherwise stated). As this is shorter that the Hawking evaporation time (of the order of M^3), this means that black holes might bounce before they evaporate: the Hawking effect would just be a dissipative correction. An exact calculation of this lifetime is in principle possible in loop quantum gravity (see, e.g., Ref. [12]), but it is still hard to perform accurately at this stage [13]. The previous phenomenological works around this hypothesis have focused on gamma-ray bursts [14], FRBs [8], the space-integrated signal [15], and trying to explain the Fermi excess [16]. In all of them the lifetime was taken (as a first approximation) to be deterministic, fixed at the value $\tau = kM^2$ where k was chosen to be of the order of 0.05 (however, in one of the studies [15] its value was varied). We also assume this value in the present article as it the most phenomenologically interesting one (and the smallest one theoretically allowed). However, as the black-to-white hole transformation is to be understood as a tunneling process, the lifetime of a black hole should be considered as a random variable.

The probability that a black hole has not yet bounced after a time t is given by

$$P(t) = \frac{1}{\tau} e^{-\frac{t}{\tau}}. \tag{1}$$

This is the usual "nuclear decay" behavior which comes directly from the fact that the number of bouncing black holes during a time interval dt is proportional to the full number of black holes and to dt. We focus in this study on local effects and neglect the redshift integration as this will play only a minor role in the analysis carried out. The black holes we are interested in can be considered to have been produced in the early Universe, as the range of masses (far below a solar mass) leading to bounces occurring in the

contemporary Universe can only be associated with primordial black holes (PBHs; see Ref. [17] for a rather recent review on the limits on the PBH abundance and references therein for possible formation mechanisms). In general, the number of black holes of a given type bouncing after a time t_H (taken to be the Hubble time as we are considering present-day phenomena) in a time interval dt is

$$dN = \frac{N_0}{kM^2} e^{-\frac{t_H}{kM^2}} dt, \tag{2}$$

where N_0 is the initial abundance. The exponential function entering this calculation comes directly from the random nature of the bounce, as in the previous formula. Let us assume that the initial differential mass spectrum of the considered PBHs is given by dN/dM.

In this study, we focus on the so-called bouncing black hole *low-energy* component as this is the one that is relevant for a possible link with FRBs. This specific component is based on a simple dimensional analysis: photons are assumed to be emitted with a characteristic wavelength that is of the order of the size of the black hole, which is the only length scale of the problem. As in Ref. [16], we model the shape of the signal emitted by a single black hole by a simple Gaussian function:

$$\frac{dN_\gamma^{\mathrm{BH}}}{dE} = Ae^{-\frac{(E-E_0)^2}{2\sigma_E^2}}, \tag{3}$$

where $E_0 = 1/(2R_S) = 1/(4M)$, R_S is the Schwarzschild radius, and M is the mass of the considered black hole. This choice is arbitrary and simply taken as an example. The width is typically fixed to be $\sigma_E = 0.1E_0$, but the results do not critically depend on this value or the detailed shape of the distribution.

The full signal due to a local distribution of bouncing black holes is given by

$$\frac{dN_\gamma}{dE} = \int_{M_{\mathrm{Pl}}}^{\infty} Ae^{-\frac{(E-E_0)^2}{2\sigma_E^2}} \cdot \frac{dN}{dM}(M) \cdot \frac{1}{kM^2} e^{-\frac{t_H}{kM^2}}. \tag{4}$$

The point we want to raise in this study is that the mean energy of the detected signal might *not* be the naively expected one, that is, may *not* be $E \sim 1/(4M_{t_H})$, where M_{t_H} is the mass satisfying $t_H = kM_{t_H}^2$ (this would correspond to black holes having a characteristic lifetime equal to the age of the Universe). The naive expectation $E \sim 1/(4M_{t_H})$ is not in the radio band, but rather 3 orders of magnitude higher in energy, in the infrared band. If the initial mass spectrum is peaked around a value M_0, e.g., according to

$$\frac{dN}{dM} \propto e^{-\frac{(M-M_0)^2}{2\sigma_M^2}}, \tag{5}$$

which can in principle be different than $\sqrt{t_H/k}$, the energy will however be peaked around $1/(4M_0)$ which can differ from $1/(4M_{t_H})$. This is possible precisely because of the distributional nature of the actual bouncing time.

Considering a peaked mass spectrum is not arbitrary and can be justified if PBHs are created, for example, because of a phase transition in the early Universe (see, e.g., Ref. [18]). As the primordial cosmological power spectrum is now clearly known not to be blue [19] (at least on large scales), the naturally expected density contrast is not high enough to produce PBHs [20] and specific post-inflationary phenomena are generically required (see, e.g., Ref. [21]).

In Fig. 1, the expected emitted flux is shown for different values of the central mass M_0 of the initial mass spectrum: M_{t_H}, $10M_{t_H}$, $100M_{t_H}$, and $1000M_{t_H}$. As expected, this shows that the energy of the signal depends on the mass spectrum even if the parameters of the model are fixed. Naturally, when the mass spectrum is peaked at masses well above M_{t_H}, the amplitude of the expected signal decreases as BHs that are exploding today constitute an increasingly smaller fraction of the full population. However, the key point we stress here is that a given mean lifetime $\tau = kM^2$ does not imply a fixed expected energy.

In particular, it was previously emphasized that the expected mean wavelength (obtained by fixing $\tau = t_H$) of the electromagnetic emission associated with bouncing black holes was basically one thousand times smaller than required to explain the FRBs. If the mass spectrum is peaked at masses higher than M_{t_H}, it is however perfectly possible to precisely account for the expected wavelength. The curve on the left in Fig. 1 is peaked around 1.5 GHz, which corresponds to the typical wavelength of FRBs. At this stage, there is no obvious motivation for choosing a specific value for the peak mass. Interesting proposals were recently suggested, for example, in the framework of critical Higgs inflation [22], but (as pointed out in the mentioned reference) the actual peak value could differ from the naively calculated one by several orders of magnitude due to accretion and merging, and many other models do exist that suggest other mass values.

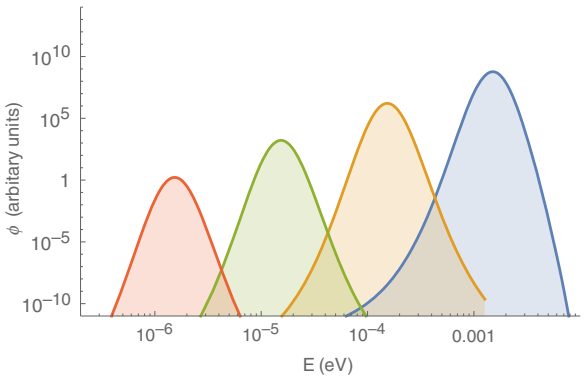

FIG. 1. Differential electromagnetic flux emitted by bouncing PBHs for a central mass M_0 equal (from right to left) to M_{t_H}, $10M_{t_H}$, $100M_{t_H}$, and $1000M_{t_H}$. The normalization is such that the total mass going into PBHs is the same in all cases.

In Fig. 1 the normalization between the different curves is such that the total mass going into black holes is the same:

$$\int_{M_{\rm Pl}}^{\infty} M \frac{dN}{dM} = cte. \tag{6}$$

This is somehow justified if ones tries to account for dark matter with PBHs. The point we want to stress with this remark is simply that the decrease in flux when one moves below the "natural" mass M_{T_H} is not drastic. Accounting for the observed events by shifting the peaked mass to higher values requires a higher density of PBHs. This cannot be done up to arbitrary values, as the upper bounds on the density of PBHs would then be violated. However, orders of magnitude show that the density of PBHs required to account for observed events is very far below the known bounds, and this does not limit the present proposal as the rate of FRBs is actually very small [23]. There is no point in performing a detailed normalization of the expected spectrum at this stage, as the initial mass spectrum normalization is totally unknown and the calculation of any observable would directly depend on it.

We have also considered a second normalization, such that the total number of black holes is the same,

$$\int_{M_{\rm Pl}}^{\infty} \frac{dN}{dM} = cte, \tag{7}$$

and this basically leads to the exact very same results.

Beyond FRBs—which can be explained by astrophysical phenomena—the point raised here is simply the fact that when the probabilistic nature of the bouncing time is accounted for, the mean energy of the emitted signal is also determined by the mass spectrum and not only by the lifetime of the black holes.

III. WIDE MASS SPECTRUM

It is also possible that the mass spectrum of PBHs is quite wide. As a toy model, if it is directly produced by scale-invariant density perturbations in a perfect fluid with equation of state $w = p/\rho$, the mass spectrum can be approximated by [20]

$$\frac{dN}{dM} \propto M^{-1-\frac{1+3w}{1+w}}. \tag{8}$$

In this study, we just consider (as a first approximation) a spectrum

$$\frac{dN}{dM} \propto M^{\alpha}, \tag{9}$$

where α is an unknown parameter. In Fig. 2 we present the expected signal for $\alpha = \{-3, -2, -1, 0\}$ (a spectrum rising with an increasing mass on a wide interval would be rather unphysical). Once again, the shape of the mass spectrum does influence the expected signal as the probabilistic nature of the lifetime is now taken into account: black holes with masses smaller or larger than M_{t_H} do also contribute to the emitted radiation, and changing their relative weights does change the result.

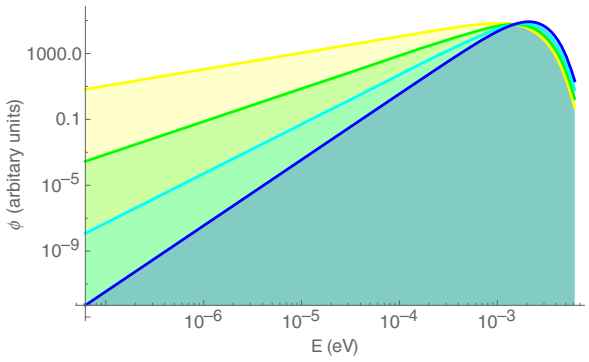

FIG. 2. Signal expected from a wide mass spectrum, with $\alpha = \{-3, -2, -1, 0\}$ from the lower curve to the upper curve at 10^{-6} eV.

This leads to another way of addressing the discrepancy between the "natural" wavelength (around 0.02 cm$\sim 2 \times 10^{-6}$ eV) of bouncing black holes and the observed wavelength (around 20 cm $\sim 2 \times 10^{-3}$ eV) of FRBs. It could indeed be that most bouncing black holes do lead to a signal of wavelength $\sim$0.02 cm and that only the tail (which exists because of the probabilistic nature of the lifetime) of the distribution is observed in the radio band. If the peak is in the infrared—which should occur if the mass spectrum is wide—it might be that it is simply unobserved today. Detectors in the infrared band have proper time constants that are much to high to allow for the measurement of such fast transient phenomena and there are no deep surveys being carried out.

In this case, as shown in Fig. 2, a clear prediction of this model for future observations is that one should expect a higher flux as the energy increases (up to the infrared band). The slope of this increase reflects that of the mass spectrum. This is qualitatively quite independent of the details of the mass spectrum.

IV. CONCLUSION

The possible existence of a black-to-white hole transition through a kind of tunneling process has recently received a lot of attention in quantum gravity. In this brief article we have taken into account the fundamentally random nature of the black hole lifetime in those models. We showed that this can induce a substantial shift with respect to previous studies in which the characteristic lifetime τ [either derived from the full theory (first attempts can be found in Ref. [13]) or inferred by heuristic arguments] was taken as an actual bouncing time.

In a Poisson process, the distribution of time intervals is wide and exponentially decreasing. A bounce can occur after a time which is very different from its characteristic

timescale, with the smallest time being always the most probable one. This should be taken into account (and this was indeed accounted for in Ref. [24]).

Beyond this quite trivial statement, we have shown that, because of this stochastic process, the mean energy of the emitted signal can be different than that previously considered. In particular, if the mass spectrum of PBHs is peaked, it is perfectly possible to match the observed FRBs.

In addition, if the mass spectrum of PBHs is wide and continuous it is still possible to explain the data, and a prediction was suggested for future observations.

The main point of this study was not to revive at any price the hypothesis that FRBs are due to bouncing black holes. Our point was to show that the randomness of the lifetime of black holes in quantum gravity can drastically change the spectral characteristic of the expected signal when the mass spectrum is highly peaked and can lead to interesting predictions in any case.

ACKNOWLEDGMENTS

K. M. is supported by a grant from the CFM Foundation.

[1] A. Barrau, C. R. Phys. **18**, 189 (2017).
[2] C. Rovelli and F. Vidotto, Int. J. Mod. Phys. D **23**, 1442026 (2014).
[3] H. M. Haggard and C. Rovelli, Phys. Rev. D **92**, 104020 (2015).
[4] C. Barcel, R. Carballo-Rubio, and L. J. Garay, J. High Energy Phys. 01 (2016) 157.
[5] C. Barcel, R. Carballo-Rubio, and L. J. Garay, J. High Energy Phys. 05 (2017) 054.
[6] H. M. Haggard and C. Rovelli, Int. J. Mod. Phys. D **25**, 1644021 (2016).
[7] J. I. Katz, Mod. Phys. Lett. A **31**, 1630013 (2016).
[8] A. Barrau, C. Rovelli, and F. Vidotto, Phys. Rev. D **90**, 127503 (2014).
[9] A. Ashtekar and P. Singh, Classical Quantum Gravity **28**, 213001 (2011).
[10] A. Barrau, Scholarpedia **12**, 33321 (2017).
[11] A. Ashtekar and B. Krishnan, Living Rev. Relativity **7**, 10 (2004).
[12] C. Rovelli, *Proc. Sci.*, QGQGS (2011) 003, arXiv:1102.3660.
[13] M. Christodoulou, C. Rovelli, S. Speziale, and I. Vilensky, Phys. Rev. D **94**, 084035 (2016).
[14] A. Barrau and C. Rovelli, Phys. Lett. B **739**, 405 (2014).
[15] A. Barrau, B. Bolliet, F. Vidotto, and C. Weimer, J. Cosmol. Astropart. Phys. 02 (2016) 022.
[16] A. Barrau, B. Bolliet, M. Schutten, and F. Vidotto, Phys. Lett. B **772**, 58 (2017).
[17] B. J. Carr, K. Kohri, Y. Sendouda, and J. Yokoyama, Phys. Rev. D **81**, 104019 (2010).
[18] J. L. G. Sobrinho, P. Augusto, and A. L. Gonalves, Mon. Not. R. Astron. Soc. **463**, 2348 (2016).
[19] P. A. R. Ade *et al.* (Planck Collaboration), Astron. Astrophys. **594**, A13 (2016).
[20] B. J. Carr, Astrophys. J. **201**, 1 (1975).
[21] K. Jedamzik and J. C. Niemeyer, Phys. Rev. D **59**, 124014 (1999).
[22] J. M. Ezquiaga, J. Garcia-Bellido, and E. Ruiz Morales, Phys. Lett. B **776**, 345 (2018).
[23] A. Fialkov and A. Loeb, Astrophys. J. **846**, L27 (2017).
[24] A. Raccanelli, F. Vidotto, and L. Verde, arXiv:1708.02588.

3.2 Propagation de champs quantiques dans un modèle de trous noirs en LQG

Nous avons vu dans la section 1.4 qu'en espace courbe le nombre de particules est relatif à l'état de vide qu'on choisit en tant qu'état fondamental. Ainsi, pour faire ce choix, il faut étudier les symétries afin d'écrire le champ sous forme d'états propres tels que les valeurs propres soit des constantes du mouvement. Ces constantes sont données par les vecteurs de Killing.

Proposition : Soit $\boldsymbol{\zeta}$ un champ de vecteur de Killing et γ une géodésique avec pour vecteur tangent $\boldsymbol{u}$. Alors la quantité $\zeta_\mu u^\mu$ est constante le long de γ.

Ainsi, un choix de vide peut s'effectuer en identifiant les vecteurs de Killing de type temps globalement. On associera alors la coordonnée temporelle au vecteur de Killing et on définira les énergies positives et négatives sur chaque foliation de l'espace à un instant t fixé. Lorsqu'il n'existe pas de vecteur de Killing de type temps global, on peut considérer un vecteur de Killing dans une région. Dans le cas d'un trou noir de Schwarzschild le vecteur de Killing de type temps $\zeta^\mu_{(t)}$ défini tel que $\zeta^\mu_{(t)}\partial_\mu = \partial_t$ permet de définir les fréquences pour un observateur lointain. Pour cet observateur un champ scalaire ϕ quantifié va être défini avec les opérateurs création et annihilation pour les modes entrant et sortant. Lorsque l'on considère l'émission de particules par effet Hawking nous prenons en compte seulement les modes sortants. Les fréquences positives vont être définies par $\partial_t\phi = -i\omega\phi$. Cependant si cet état du vide est choisi comme état fondamental, on observe qu'à l'horizon le tenseur $T_{\mu\nu}$ diverge, alors que ce n'est pas une singularité fondamentale donc il est préférable de choisir un autre état fondamental. Par exemple, il y a les fréquences de l'observateur en chute libre à l'horizon des évènements. Elles sont très différentes des précédentes et ceci est à l'origine de l'effet Hawking que nous allons décrire plus en détails dans la section suivante 3.2.1.

3.2.1 L'effet Hawking

Pour décrire l'effet Hawking nous nous plaçons dans le cadre d'un champ scalaire ϕ décrit dans un espace-temps de Schwarzschild. Nous suivons ici la description décrite dans [50].

Nous avons l'habitude, en TQC en espace plat, de développer l'opérateur champ en modes et ensuite d'associer les opérateurs création $a^\dagger$ et annihilation a à ces modes. Mais en espace courbe il n'existe pas un ensemble naturel de modes en particulier. Comme nous l'avons déjà mentionné, une décomposition en mode permet d'avoir une base dans l'espace des solutions mais ne possède par un caractère fondamental. Ainsi il est possible de procéder différemment et de commencer par une solution de paquet d'onde individuel. Soit f une solution classique complexe de l'équation (dans ce cas, l'équation de Klein Gordon) et ϕ l'opérateur de champ. On peut alors définir l'opérateur annihilation de la façon suivante,

$$a(f) = \langle f|\phi\rangle\,. \tag{3.10}$$

Étant donné que f et ϕ satisfont tout deux à l'équation d'onde, cet opérateur est bien défini et indépendant de la surface où le produit scalaire est évalué. Le caractère hermitien de l'opérateur de

champ ϕ induit

$$a^\dagger(f) = -a(f^*). \tag{3.11}$$

Comme nous venons de le voir, il y a deux notions de fréquences pertinentes :

— les "fréquences de Killing" : infiniment loin, ces fréquences coïncident avec les fréquences vu par un observateur de Minkowski au repos par rapport au trou noir.

— les "fréquences de chute libre" : vues par un observateur en chute libre qui traverse l'horizon.

On considère un trou noir formé par un effondrement gravitationnel avec un état quantique $|\psi\rangle$. Bien longtemps après l'effondrement, on veut définir les observables pour un paquet d'onde P sortant, a fréquences de Killing positives, d'un champ quantique loin du trou noir. Le nombre moyen de particules de ce paquet d'onde sera décrit par :

$$\langle\psi|N(P)|\psi\rangle \quad \text{avec} \quad N(P) = a^\dagger(P)a(P). \tag{3.12}$$

L'opérateur annihilation correspondant au paquet d'onde normalisé P est donné par

$$a(P) = \langle P, \phi\rangle_{\Sigma_f}\,, \tag{3.13}$$

évalué sur Σ_f l'hypersurface spatiale, loin du trou noir. Unruh a montré que [51] l'on peut évaluer la valeur moyenne de $N(P)$ sur Σ_f en utilisant nos connaissances sur Σ_i, une hypersurface assez loin dans le passé de Σ_f mais tout de même bien après la formation du trou noir. Sur Σ_f, on a le paquet d'onde P qui ne contient que des modes sortants. En propageant en arrière ce paquet d'onde via l'équation de Klein Gordon, il se sépare en une partie R réfléchie par la barrière de potentiel du trou noir et une partie T transmise qui se dirige vers l'horizon :

$$P = R + T. \tag{3.14}$$

Le support de R est sur la partie spatiale loin de l'horizon et le support de T est sur une petite région proche, mais en dehors, de l'horizon. Le produit scalaire (3.13) peut être évalué sur Σ_i, car entre les deux hypersurfaces ϕ et P satisfont l'équation de Klein Gordon, donc $a(P)$ ne va pas être modifié. On peut alors séparer l'opérateur annihilation en deux parties

$$a(P) = a(R) + a(T), \tag{3.15}$$

et le nombre moyen de particules (3.12) s'écrit

$$\langle\psi|N(P)|\psi\rangle = \langle\psi|(a^\dagger(R) + a^\dagger(T))(a(R) + a(T))|\psi\rangle\,. \tag{3.16}$$

La métrique du trou noir étant stationnaire, les fréquences de Killing, dans les solutions de l'équation de Klein Gordon, sont conservées. Ainsi R et T ont les mêmes fréquences positives que P. Infiniment loin du trou noir, on a la partie réfléchie et les fréquences positives sont celles d'un espace de Minkowski asymptotiquement. Étant donné qu'il n'y a pas de mode entrant, on a

$$a(R)\,|\psi\rangle = 0, \tag{3.17}$$

on en déduit

$$\langle\psi|N(P)|\psi\rangle = \langle\psi|a^\dagger(T)a(T)|\psi\rangle\,. \tag{3.18}$$

Par contre, l'observateur en chute libre, de temps propre τ, à l'horizon des événements verra des fréquences positives et négatives pour le paquet d'onde T. Au point $\tau = 0$ lorsqu'il traverse l'horizon, l'hypersurface Σ_i intersecte l'horizon. Derrière l'horizon, pour $\tau > 0$, le paquet d'onde T sera nul (car il n'a pas de support). On sait que si une fonction s'annule sur un arc continue du domaine où la fonction est analytique (ici ce sera l'axe réel positive de τ) , alors par prolongement analytique elle est nulle partout dans le domaine. Ainsi n'importe qu'elle fonction a fréquences positives

$$h(\tau) = \int_0^\infty d\omega e^{-i\omega\tau}\tilde{h}(\omega) \tag{3.19}$$

est analytique dans le demi plan de partie imaginaire négative et si $h(\tau) = 0$ pour $\tau > 0$, on aura également $h(\tau) = 0$ pour $\tau < 0$ pour l'observateur en chute libre. On peut alors décomposer le paquet d'onde T en une partie à fréquences positives et une autre à fréquences négatives par rapport à τ

$$T = T^+ + T^- \tag{3.20}$$

et on a également

$$\begin{aligned} a(T) &= a(T^+) + a(T^-) && (3.21)\\ &= a(T^+) - a^\dagger((T^-)^*). && (3.22) \end{aligned}$$

Pour l'observateur, en chute libre, à $\tau < 0$, les paquets d'onde T^+ et $(T^-)^*$ ont des très hautes fréquences. Ainsi, à courte distance, on peut considérer que ces paquets d'onde sont dans leur états fondamentaux et on a

$$\begin{aligned} a(T^+)\,|\psi\rangle &= 0, && (3.23)\\ a((T^-)^*)\,|\psi\rangle &= 0. && (3.24) \end{aligned}$$

En utilisant les équations (1.112),(1.113), (3.22) et (3.24), on obtient que le nombre moyen de particules s'écrit

$$\begin{aligned} \langle\psi|N(P)|\psi\rangle &= \langle\psi|a(T^-)^* a^\dagger((T^-)^*|\psi\rangle && (3.25)\\ &= \langle\psi|[a(T^-)^*, a^\dagger((T^-)^*]|\psi\rangle && (3.26)\\ &= \langle(T^-)^*|(T^-)^*\rangle_{\Sigma_i} && (3.27)\\ &= \langle T^-|T^-\rangle_{\Sigma_i} && (3.28) \end{aligned}$$

Dans le cas d'un trou noir de Schwarzschild, la symétrie sphérique permet de décomposer le champ en harmoniques sphériques. De plus, étant donné que la métrique est statique la dépendance en temps des modes sortants à l'infinie s'écrit $e^{-i\omega t}$ et à l'horizon $e^{-i\omega u}$ avec $u = t - r^*$. La coordonnée u diverge à l'horizon, elle est relié au temps propre de l'observateur en chute libre τ traversant l'horizon. On a

$$\tau \approx -\tau_0 e^{-\frac{u}{4M}}, \tag{3.29}$$

avec τ_0 une constante qui dépend de la vitesse de l'observateur en chute libre et $1/4M$ représente la gravité de surface d'un trou noir de Schwarzschild. On considère le paquet d'onde P longtemps après l'effondrement gravitationnel qui est piqué en la fréquence de Killing ω, puis on le propage en arrière et on regarde la partie T à l'horizon. Sa dépendance en τ pour un observateur en chute libre s'écrit

$$T \sim \exp\Big(i4M\omega \ln(-\tau)\Big), \tag{3.30}$$

pour $\tau < 0$ et s'annule pour $\tau > 0$. On passe alors dans le plan complexe et par continuité analytique l'extension des fréquences positives de $T(\tau)$ pour $\tau > 0$ s'obtient en remplaçant $\ln(-\tau)$ par $\ln\tau + i\pi$: on a alors $T(-\tau)\exp(-4M\pi\omega)$ pour $\tau > 0$. Pour les fréquences négative l'extension avec $\ln\tau - i\pi$ donne $T(-\tau)\exp(4M\pi\omega)$ pour $\tau > 0$. On définie $\tilde{T}$ tel qu'on passe de T à l'extérieur de l'horizon à $\exp(\pm 4M\pi\omega)$ à l'intérieur de l'horizon. Le support de $\tilde{T}$ est défini seulement à l'intérieur de l'horizon où il est constant pour les lignes de lumière sortantes avec $\tilde{T}(\tau) = T(-\tau)$ pour $\tau > 0$. Les paquets d'ondes

$$T^+ = c_+(T + e^{-4M\pi\omega}\tilde{T}), \tag{3.31}$$

$$T^- = c_-(T + e^{+4M\pi\omega}\tilde{T}), \tag{3.32}$$

définissent les fréquences positives et négatives, respectivement, de l'observateur en chute libre. Pour avoir la continuité avec T en dehors de l'horizon, les constantes $c - +$ et c_- s'écrivent

$$c_- = (1 - e^{8M\pi\omega})^{-1}, \tag{3.33}$$

$$c_+ = c_- e^{8M\pi\omega}. \tag{3.34}$$

Étant donné que T et $\tilde{T}$ possèdent deux supports qui ne s'intersectent pas, on a $\langle T|\tilde{T}\rangle = 0$ et $\langle\tilde{T}|\tilde{T}\rangle = -\langle T|T\rangle$. Ainsi on a

$$\langle T^-|T^-\rangle = \frac{\langle T|T\rangle}{(1 - e^{8M\pi\omega})}. \tag{3.35}$$

On obtient alors l'expression pour le nombre de particules

$$\langle\psi|N(P)|\psi\rangle = -\langle T^-|T^-\rangle_{\Sigma_i} \tag{3.36}$$

$$= \frac{\langle T|T\rangle}{e^{8\pi\omega M} - 1}. \tag{3.37}$$

Cette valeur moyenne (3.37) correspond à l'état thermique à la température de Hawking $T_H = 1/8\pi M$ multipliée par le facteur de corps gris :

$$\Gamma = \langle T|T\rangle\,. \tag{3.38}$$

En toute généralité ce facteur de corps gris dépend de la masse du trou noir M, de l'énergie de la particule ω et de son spin s. Il correspond au produit de la section efficace d'émission avec le terme d'espace des phases. Ainsi on peut réécrire le spectre différentiel

$$\frac{dN}{dt} = \frac{\sigma(M, s, \omega)}{e^{\frac{\omega}{T_H}} \pm 1}\frac{d^3k}{(2\pi)^3}. \tag{3.39}$$

La partie thermique ne dépend que de la masse du trou noir et ne nous indique aucune information supplémentaire sur ce dernier. Par contre la section efficace dépend de la forme du potentiel gravitationnel et permet de renseigner sur la géométrie du trou noir. Ainsi, des métriques différentes de trous noirs sont distinguables par le calcul de sections efficaces. Dans l'article suivant, nous avons calculé σ pour un modèle de trou noir provenant de la LQG. Nous présentons ce modèle dans la section suivante.

3.2.2 Le modèle des trous noirs quantiques à boucles

Nous avons vu la quantification polymérique utilisée pour quantifier la LQC. Il existe également un modèle de trous noirs en LQG qui utilise un procédé similaire [52]. On considère les trous noirs de Schwarzschild, écrit avec les variables d'Ashtekar à symétrie sphérique et homogènes. On a un paramètre de polymérisation δ qui définit le pas du réseau et la contrainte Hamiltonienne est exprimée en termes d'holonomie $h^{(\delta)}(A)$. L'homogénéité implique que la contrainte de difféomorphisme est nulle. L'espace-temps considéré est de Kantowski-Sachs : homogène, anisotrope dont la topologie de l'espace est donné par $\mathbb{R} \times \mathbb{S}^2$. Ainsi, la contrainte de Gauss est également nulle. Il faut maintenant imposer que la contrainte Hamiltonienne s'annule et étendre la solution à tout l'espace. La métrique résultante est donnée par

$$ds^2 = G(r)dt^2 - \frac{dr^2}{F(r)} - H(r)d\Omega^2, \tag{3.40}$$

$$G(r) = \frac{(r-r_+)(r-r_-)(r+r_x)^2}{r^4+a_0}, \tag{3.41}$$

$$F(r) = \frac{(r-r_+)(r-r_-)r^4}{(r+r_x)(r^4+a_0^2)}, \tag{3.42}$$

$$H(r) = r^2 + \frac{a_0^2}{r^2}, \tag{3.43}$$

avec $r_+ = 2m$ et $r_- = 2mP^2$ deux horizons, et $r_x = \sqrt{r_+ r_-}$. La fonction polymérique est définie telle que $P = (\sqrt{1+\epsilon} - 1)/(\sqrt{1+\epsilon} + 1)$ avec $\epsilon = \gamma\delta$. Le paramètre a_0 est relié à l'aire minimale du spectre d'aire (1.154), $a_0 = A_{min}/8\pi$. Le paramètre de masse m est relié à la masse ADM $M = m(1+P)^2$. Le modèle décrit un trou noir de Schwarzschild, qui prend en compte la discrétisation de l'espace-temps, avec δ, et l'existence d'une aire minimale, avec a_0. La création de particules par effet Hawking de ce modèle de trous noirs a été étudié [53].

3.2.3 Le rayonnement émis par les trous noirs quantiques à boucles

Le calcul de la section efficace dépend du type de particules considéré car il implique l'équation radiale du mouvement. Nous nous sommes d'abord intéressés au cas d'un champ scalaire puis à celui d'un champ spinoriel. Les résultats sont similaires, ainsi je vais seulement exposer la cas des particules de spin $1/2$.

Pour étudier la propagation des fermions en espace courbe, il est nécessaire d'utiliser un formalisme de tétrades. Le formalisme Newmann-Penrose est particulièrement bien adapté étant donné que l'on considère un trou de type D, dans la classification de Petrov. Les champs fermioniques ψ sont représentés par une paire de spineurs P^A et $\overline{Q}^{A'}$ avec $A, A' = 0, 1$. On écrit alors l'équation de Dirac dans le formalisme de Newman-Penrose. Ceci correspond aux équations $(21-24)$ de l'article. Les symétries du trou noir justifient d'écrire le champ sous la forme : $\Psi(t, r, \theta, \phi) = R(t)S(\theta)e^{i(\omega t + m'\phi)}$ avec ω l'énergie et m' un nombre entier. Une étape clé est de remarquer que les équations sont séparables en une partie radiale et une partie angulaire seulement si on fait l'ansatz suivant :

$$P^0 \propto R_+(r)S_+(\theta), \tag{3.44}$$
$$P^1 \propto R_-(r)S_-(\theta), \tag{3.45}$$
$$\overline{Q}^{0'} \propto R_+(r)S_-(\theta), \tag{3.46}$$
$$\overline{Q}^{1'} \propto R_-(r)S_+(\theta). \tag{3.47}$$

Ainsi les dégrées de liberté des parties radiales et angulaires des particules et anti-particules de spin up et down se mélangent. Une particule de spin up aura la même partie radiale qu'une anti-particule de spin up mais la même partie angulaire qu'une anti-particule de spin down. Cet ansatz permet d'obtenir des équations purement radiales et purement angulaires. Les dernières sont les mêmes que dans le cas d'un trou noir de Schwarzschild. Il en résulte que λ, la constante de séparation, est donnée par $\lambda^2 = (\ell + 1)^2$ avec ℓ le moment angulaire. L'équation radiale pour R_+ pour un fermion sans masse est donnée par

$$\sqrt{HF}\mathcal{D}\Big(\sqrt{HF}\mathcal{D}^\dagger R_+\Big) - \lambda^2 R_+ = 0 \tag{3.48}$$

avec $\mathcal{D}$ un opérateur radial donné par

$$\mathcal{D} = \partial_r + \left(\frac{G'}{8G} - \frac{F'}{8F}\right) + \frac{i\omega}{\sqrt{GF}} \tag{3.49}$$

et $\mathcal{D}^\dagger$ son complexe conjugué.
Nous considérons le rayonnement émis par un trou noir, qui se diffuse sur la barrière de potentiel. Par conséquent, nous cherchons les solutions de l'équation (3.48) qui correspondent aux conditions aux bords suivantes :

— modes entrants et sortants à l'horizon,
— modes sortants à l'infini spatial.

Et nous cherchons le coefficient de transmission. Cependant, par symétrie, ce coefficient sera le même que celui calculé du point de vue d'un champ absorbé avec les conditions :

— modes entrants à l'horizon,
— modes entrants et sortants à l'infini spatial.

Ici nous adoptons le point de vue de l'absorption. On fixe alors les conditions initiales à l'horizon, puis on résout l'équation jusqu'à une distance considérée comme étant l'infini. Puis, à cette distance, on ajuste notre solution numérique avec les conditions à l'infini pour avoir accès au coefficient de transmission. Ce dernier est relié à la section efficace par le théorème optique

$$\sigma(M, s, \omega) = \sum_{\ell=0}^{\infty} \frac{(2j+1)\pi}{\omega^2} \mid A_{\ell,s} \mid^2 . \tag{3.50}$$

Le coefficient de transmission diminue fortement pour les grands ℓ. Dans la pratique, nous avons sommé jusqu'à $\ell = 10$. Les résultats sont dépeins sur les Figures 2 (pour les scalaires) et 3 (pour les fermions) de l'article. On observe que par rapport aux trous noirs de Schwarzschild, les trous noirs quantiques à boucles ont une section efficace plus faible. Plus la valeur du paramètre de discrétisation δ est élevée plus la section efficace diminue. Ainsi plus la discrétisation de l'espace se ressent à grande échelle, moins le flux sera transmis par la barrière de potentiel. Cependant, pour des valeurs raisonnables sur le paramètre δ la différence est très faible.

Cet article a été publié dans *Classical and Quantum Gravity* [54].

PAPER

Quantum fields in the background spacetime of a polymeric loop black hole

IOP Publishing Classical and Quantum Gravity

Class. Quantum Grav. **36** (2019) 125003 (14pp) https://doi.org/10.1088/1361-6382/ab207c

Quantum fields in the background spacetime of a polymeric loop black hole

Flora Moulin[1], Killian Martineau[1], Julien Grain[2] and Aurélien Barrau[1,3]

[1] Laboratoire de Physique Subatomique et de Cosmologie, Université Grenoble-Alpes, CNRS/IN2P3 53 avenue des Martyrs, 38026 Grenoble cedex, France
[2] Institut d'astrophysique spatiale, Université Paris-Sud, CNRS Bâtiments 120 à 121, Université Paris Sud, 91405 ORSAY, France

E-mail: barrau@in2p3.fr

Received 17 December 2018, revised 12 April 2019
Accepted for publication 9 May 2019
Published 28 May 2019

Abstract

The description of black holes in loop quantum gravity is a hard and tricky task. In this article, we focus on a minisuperspace approach based on a polymerization procedure. We consider the resulting effective metric and study the propagation of quantum fields in this background. The cross sections for scalar particles and fermions are explicitly calculated. The Teukolsky–Chandrasekhar procedure used to derived the fermionic radial equation of motion for usual spacetimes is entirely generalized to a much larger class. The resulting radial equation can be used in quite a lot of other contexts.

Keywords: black holes, loop quantum gravity, greybody factors

(Some figures may appear in colour only in the online journal)

Introduction

Loop quantum gravity (LQG) is a mature framework which is mathematically consistent and can be approached by several complementary paths, from canonical quantization to spin-foams (see, e.g. [1–4] and references therein). The ideas of the theory have been successfully applied to the Universe, leading to the loop quantum cosmology (LQC) paradigm (see, e.g. the reviews [5–12], and references therein) and to black holes (BHs) (see, e.g. the reviews [13–17], and references therein).

In this article, we focus on the BH issue and consider the propagation of quantum fields. There are many different attempts to deal with BHs in LQG and to describe their dynamics. In this study, we use an effective corrected metric derived in [18]. This spacetime structure is

[3] Author to whom any correspondence should be addressed.

in no way a final word on the question of the exterior background of an LQG BH. It relies on heavy hypothesis that should be questioned. But it constitutes an interesting phenomenological framework to investigate the questions of cross-sections and greybody factors in an effective quantum gravity-corrected background. Within this spacetime, we investigate in details the scattering of quantum fields. We first draw the general picture used to model BHs in this framework. Then we explain how cross sections are calculated and their meaning. We turn to the explicit computation for scalar particles. Finally, we derive the propagation equation for fermions. Conclusions and perspectives are outlined.

Black holes in loop gravity

BHs are fascinating objects that have been intensively investigated in the framework of LQG [13–17]. To give just one example, the Bekenstein–Hawking entropy is now correctly recovered, although different ways to compute it are still considered (see, e.g. [17]). In microcanonical calculations taking into account only the quantum geometrical degrees of freedom [19] this requires a specific fixing of the Barbero-Immirzi parameter, depending on the details of the state counting [20]. This is not anymore the case in recent holographic models [21–25].

In this study, we use the metric obtained in [18], building on [26]. This framework was precisely set-up to investigate the creation of BHs and their subsequent Hawking evaporation. This question is intimately related to the information paradox which is itself closely linked to the singularity resolution. An interesting approach consists in using the 4-dimensional static model derived in [26] and to make it dynamical. This allows one to reproduce the Hawking calculation of particle creation in a classical BH background and to demonstrate that the whole process is unitary. The spirit of the framework in the line of the long history of 'non-singular' BHs (see, e.g. [27–30], and references therein).

In canonical LQG, the basic variables are the holonomy of the Asktekar connexion and the flux of the densitized triads. In the covariant formulation, space is described by a spin network whose edges are labelled by irreductibles representations of SU(2) and nodes are intertwiners [31]. Intuitively, the edges carry quanta of area and the vertices carry elementary volumes. One of the most important result of LQG is that the area is quantized according to:

$$A(j) = 8\pi\gamma l_{\mathrm{P}}^2\sqrt{j(j+1)}, \tag{1}$$

where γ is the Barbero-Immirzi parameter, l_{P} is the Planck length and j is a half-integer. In [18], several hypotheses were made to describe LQG BHs beginning, as expected, by spherical symmetry which is used to reduce the number of variables. In addition, instead of all *a priori* possible closed graphs, a regular lattice with edges of lengths δ_b and δ_c has been chosen. Details on the structure of lattices possibly used can be found in [32]. The resulting dynamical solution inside the horizon was then analytically continued to the region outside the horizon, showing that it is possible to reduce the two unknown parameters by requiring that the minimum area in the solution is equal to minimum area of LQG (exactly as done in LQC). The remaining free parameter δ_b will now be called δ and referred to as the 'polymeric parameter'. Together with $A_{\mathrm{min}} = A(1/2)$, it determines how 'different' from the usual general relativity (GR) solution the considered BH is.

In practice, the procedure consists in first defining the Hamiltonian constraint by the use of holonomies along the considered fixed graph. It is important to underline that the influence of the choice of a specific graph has not been studied in details and this should be considered as a weakness of the considered approach. Both the diffeomorphism and Gauss constraints are identically vanishing: the first one is zero because of homogeneity and the second one is

zero because the spacetime is of the Kantowski–Sachs form. The Hamiltonian constraint is solved after replacing the connection by the holonomy. Finally, the solution is expanded to the full spacetime, leading to the effective LQG-corrected geodesically complete Schwarzschild metric:

$$\begin{aligned} \mathrm{d}s^2 &= G(r)\mathrm{d}t^2 - \frac{\mathrm{d}r^2}{F(r)} - H(r)\mathrm{d}\Omega^2, \\ G(r) &= \frac{(r-r_+)(r-r_-)(r+r_x)^2}{r^4+a_o^2}, \\ F(r) &= \frac{(r-r_+)(r-r_-)r^4}{(r+r_x)^2(r^4+a_o^2)}, \\ H(r) &= r^2 + \frac{a_o^2}{r^2}, \end{aligned} \tag{2}$$

where $\mathrm{d}\Omega^2 = \mathrm{d}\theta^2 + \sin^2\theta\mathrm{d}\phi^2$, $r_+ = 2m$ and $r_- = 2mP^2$ are the two horizons (being respectively future and past horizons for observers in the two asymptotically flat regions of the associated causal diagram), and $r_x = \sqrt{r_+ r_-} = 2mP$, P being the polymeric function defined by $P = (\sqrt{1+\epsilon^2}-1)/(\sqrt{1+\epsilon^2}+1)$, with $\epsilon = \gamma\delta$, and the area parameter a_o is given by $a_0 = A_{\min}/8\pi$. In principle ϵ is not bounded but the approach is rigorous only when $\epsilon \ll 1$ (at this state no phenomenological bound has been derived on ϵ). The parameter m in the solution is related to the ADM mass M by $M = m(1+P)^2$ (inferred from what is observed at asymptotic infinity). This metric should be considered as a 'toy model' and not taken as a final statement about the spacetime structure around an LGQ BH. It is however very convenient and meaningful for first phenomenological investigations. The associated Penrose digram is given in figure 1. From now, we use only Planck units.

Let us discuss a bit more this solution. The considered spacetime is a particular example of a Kantowski–Sachs spacetime. In the construction, the interior of a spherically symmetric BH is treated as homogeneous, but not explicitly as isotropic. As usual, the connection is replaced by the holonomy in the Hamiltonian constraint and the equation of motion are solved, together with the Hamiltonian constraint. The outcome is an exact solution of a minisuperspace model valid inside the event horizon [26]. Finally, the solution is analytically extended to the whole spacetime. In other words, the metric was assumed to be valid everywhere and it was explicitly proven with a coordinate transformation that the singularities at the two horizons (event horizon and Cauchy internal horizon) were just coordinate singularities. The resulting metric has a simple, geodesically complete, analytic form in the whole spacetime. The weaknesses are the following. First, the metric cannot be considered a rigorous 'full LQG' solution, although it captures some features of LQG as the minimum area and the use of holonomies. Second, this metric builds on the initial version of LQC. In the future it would be interesting to replace the polymeric parameter by a rescaled one, in the same sense than the μ_0 scheme in LQC has been replaced by the $\bar{\mu}$ one (see [6]). Finally, it is assumed that matter couples minimally to the effective metric.

It should me underlined that the model considered in this article is far from being the only possible one within the LQG framework. It is somehow 'unusual' in the sense that it might lead to possible large quantum gravity effects outside the horizon. Although not something fully exotic (this possibility is e.g. advocated on a different grounding in [33]), it is fair to say that this is not a generic prediction. It is however the specific case where quantum gravity might have an impact on observations and this is why we focus here on this specific setting which is anyway quite well justified in its physical motivations.

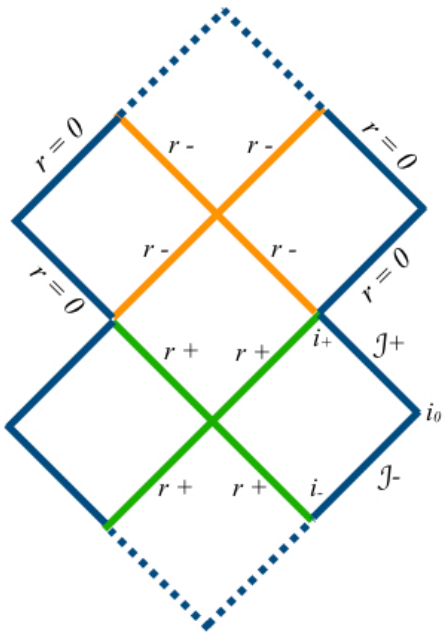

Figure 1. Penrose diagram for the metric considered in this study. The horizons are denoted as r_+ and r_-.

Cross section for evaporating black holes

The Hawking evaporation [34] (as a specific case of the Unruh effect [35]) is one of the most important aspects of BH physics. Although it can be described as semi-classical process in the 'large mass' regime, it requires a quantum gravity treatment near the endpoint. Several attempts to describe it in the framework of LQG were made [36–38]. In this study we focus on another aspect. Basically, the 'naive' Hawking spectrum is described by a blackbody law, in agreement with the Unruh effect which predicts that an accelerated observer sees a bath of thermal particles with temperature $T = a/(2\pi)$. In the case of black holes, the temperature is $T_H = 1/(8\pi M)$: the lighter the BH, the highest its temperature, which makes the whole process very explosive in the last stages (a BH with a mass above the mass of the Moon has a temperature smaller that the one of the cosmological microwave background). However, the real spectrum is slightly more complicated as the emitted particles have to cross a potential barrier before escaping to infinity. This induces a modification, captured by the cross section σ, to the pure blackbody spectrum which is known to encode quite a lot of information on the gravitational theory or spacetime structure considered. The spectrum reads as:

$$\frac{\mathrm{d}N}{\mathrm{d}t} = \frac{1}{\mathrm{e}^{\frac{\omega}{T_H}} \pm 1}\sigma(M, s, \omega)\frac{\mathrm{d}^3k}{(2\pi)^3}, \tag{3}$$

with M the BH mass, s the particle spin, ω its energy and k its momentum.

Cross sections have already been calculated for many metrics, beginning by the pioneering works on Schwarzschild, Kerr, and Reisner–Nordstrom BHs in the case of scalar, fermion and vector fields [39–41]. They have also been investigated for extra-dimensional Schwarzschild–de–Sitter black hole [42], for lovelock gravity [43], for tachyonic fields [44], for scalar fields

in an Einstein–Maxwell background [45], for $f(R)$ gravity minimally coupled to a cloud of strings in $2+1$ dimensions [46], for Einstein–Gauss–Bonnet–de Sitter black holes [47], for black strings [48], for Einstein–Born–Infeld dilaton spacetimes [49], for dRGT massive gravity [50], for Reissner–Nordström–de Sitter black holes [51], for extra-dimensional Kerr black holes [52], for Myers–Perry black holes [53], for dilatonic black holes [54], for rotating charged Goedel black holes [55], to cite only a few remarkable results. In each case the cross section captures some specific and non-trivial characteristics of the considered spacetime. In this article, we calculate the cross sections for a so-called loop BH (LBH), as described by the metric (2), which is static and spherical symmetric. Given those spacetime symmetries, and according to the optical theorem, the cross section reads

$$\sigma(M,s,\omega)=\sum_{l=0}^{\infty}\frac{(2j+1)\pi}{\omega^2}|A_{l,s}|^2, \tag{4}$$

where $A_{l,s}$ is the transmission coefficient of the angular momentum mode l, and $j=l+s$ is the total angular momentum.

Massless scalar field

The dynamics of a massless scalar field minimally coupled to the gravitational field is described by the generalized Klein–Gordon equation:

$$\frac{1}{\sqrt{-g}}\partial_\mu(g^{\mu\nu}\sqrt{-g}\partial_\nu\Phi)=0, \tag{5}$$

where $\boldsymbol{\Phi\equiv\Phi(t,r,\theta,\phi)}$. Since we work within a static and spherically symmetric setting, the scalar field can be written as:

$$\Phi(r,\theta,\phi,t)=R(r)S(\theta)\mathrm{e}^{\mathrm{i}(\omega t+m'\phi)}, \tag{6}$$

where w is the frequency and m' is an integer. When inserting this ansatz in the Klein–Gordon equation (5) with the metric (2), the radial equation reads

$$\frac{\sqrt{GF}}{H}\frac{\partial}{\partial r}\left(H\sqrt{GF}\frac{\partial R(r)}{\partial r}\right)+\left(\omega^2-\frac{G}{H}l(l+1)\right)R(r)=0, \tag{7}$$

with l the orbital quantum number. This result uses the squared angular momentum operator $L^2=-\left[\frac{1}{\sin^2\theta}\frac{\partial^2}{\partial\phi^2}+\frac{1}{\sin\theta}\frac{\partial}{\partial\theta}\left(\sin\theta\frac{\partial}{\partial\theta}\right)\right]$, whose eigenvalues are $l(l+1)$.

As usually done to study this kind of problems, we introduce the tortoise coordinate. Focusing on the two non-trivial coordinates, the metrics (2) reduces to

$$\mathrm{d}s^2=-G(r)\mathrm{d}t^2+\frac{\mathrm{d}r^2}{F(r)}, \tag{8}$$

and the null geodesics are given by $\mathrm{d}s^2=0$, that is $\mathrm{d}t^2=\frac{\mathrm{d}r^2}{GF}\equiv\mathrm{d}r^{*2}$ with r^* the tortoise coordinate. This new coordinate tends to $-\infty$ when r tends to r_+. By introducing a new radial field $\Psi(r)\equiv\sqrt{H}R(r)$ and writing equation (7) with respect to r^*, we obtain:

$$\left(\frac{\partial^2}{\partial r^{*2}}+\omega^2-V(r^*)\right)\Psi(r)=0, \tag{9}$$

$$V(r) = \frac{G}{H} l(l+1) + \frac{1}{2}\sqrt{\frac{GF}{H}}\frac{\partial}{\partial r}\left(\sqrt{\frac{GF}{H}}\frac{\partial H}{\partial r}\right). \tag{10}$$

The potential $V(r)$ vanishes at the horizon r_+ and at spatial infinity.

At the horizon r_+, $\sqrt{H}$ tends to the constant $\sqrt{H(r_p)}$ and the radial part of the wavefunction R is a plane wave with respect to the tortoise coordinate:

$$R(r^*) = A^h_{\text{in}} \mathrm{e}^{\mathrm{i}\omega r^*} + A^h_{\text{out}} \mathrm{e}^{-\mathrm{i}\omega r^*}, \tag{11}$$

with A^h_{in} (respectively A^h_{out}) the probability amplitude for the incoming modes (resp. outgoing modes) at the horizon. For convenience, we choose the absorption point of view. With this convention, there are incoming and outgoing modes infinitely far from the BH and only incoming ones at the horizon. We therefore impose $A^h_{\text{out}} = 0$.

Infinitely far away from the horizon, $\sqrt{H}$ tends to r and the radial wavefunction is a spherical wave with respect to the coordinate r:

$$R(r) = \frac{A^\infty_{\text{in}}}{r}\mathrm{e}^{\mathrm{i}\omega r} + \frac{A^\infty_{\text{out}}}{r}\mathrm{e}^{-\mathrm{i}\omega r}. \tag{12}$$

For a scalar particle, the transmission amplitude for the mode l is given by:

$$|A_l|^2 = r_+^2 \left|\frac{A^h_{\text{in}}}{A^\infty_{\text{in}}}\right|^2 = 1 - \left|\frac{A^\infty_{\text{out}}}{A^\infty_{\text{in}}}\right|^2. \tag{13}$$

The calculation of the cross section relies on the following steps. For each quantum number l, we solve the radial equation (7) so as to determine the transmission coefficients A^∞. Numerical computations must be performed from the horizon (where the radial wavefunction takes the form of equation (11)) until infinity (where the radial wave function takes the form of equation (12)). In practice, the numerical solving begins at $r_{\text{ini}} = r_+ + 10^{-3} r_+$ and stops sufficiently far at $r_{\text{end}} \approx 300/\omega$ which can be considered as infinity at the chosen accuracy.

We decompose the radial wavefunction $R(r)$ into its real part $U(r)$ and its imaginary part $V(r)$. At $r_{\text{ini}} \approx r_+$, the normalization condition $R(r_{\text{ini}}) = 1$ ensures that there are only incoming modes and $\frac{\mathrm{d}R(r_{\text{ini}})}{\mathrm{d}r} = \frac{\mathrm{i}\omega}{\sqrt{G(r_{\text{ini}})F(r_{\text{ini}})}}$. Technical details are given in appendix A.

The radial equation is solved with a fifth order Runge Kutta method until r_{end}. The radial wavefunction is fitted with the function given by equation (12) so as to obtain the coefficients A^∞_{out} and A^∞_{in}. Then the $|A_l|^2$ can be obtained from equation (13). The bigger the l, the smaller the $|A_l|^2$ and numerical investigations have shown that stopping at $l = 10$ is sufficient. Finally, equation (4) is used to evaluate the cross section. The results are presented in figure 2.

The cross section does decrease when ϵ increases. One can also notice a slight energy shift of the pseudo-periodic oscillations toward a lower frequency (in $M\omega$) when ϵ increases. When $\epsilon < 10^{-0.8}$, it is hard to distinguish between the solutions. As far as phenomenology is concerned, it seems that taking into account the quantum corrections does not influence substantially the cross section of a scalar field for reasonable values of ϵ (that is $\epsilon \ll 1$). The main trend is however clear.

Spin $\frac{1}{2}$ field

For spacetimes such that $\mathrm{d}s^2 = f(r)\mathrm{d}t^2 - f^{-1}(r)\mathrm{d}r^2 - r^2\mathrm{d}\Omega^2$, the radial equation is given by the Teukolsky master equation [56]. The metric given by equation (2), without any specified expressions for $G(r)$, $F(r)$ and $H(r)$, is however more general and basically includes

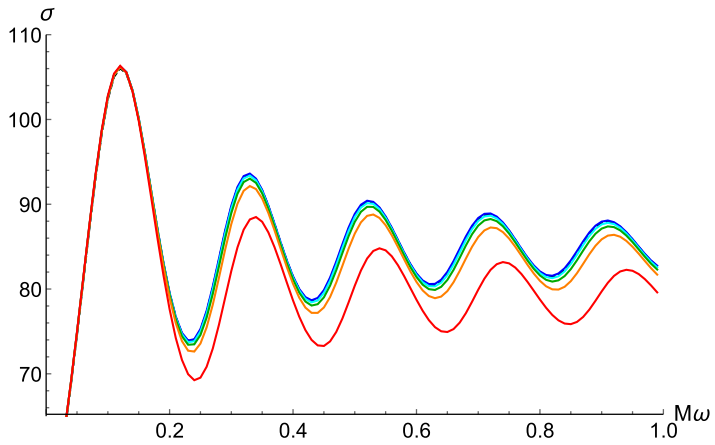

Figure 2. Emission cross section for a scalar field with energy ω in the background spacetime of a LBH of mass M for different values of ϵ ($\epsilon = \gamma\delta$ measures the 'quantumness' of spacetime). From bottom to top: $\epsilon = 10^{\{-0.3,-0.6,-0.8,-1,-3\}}$. The blue line, corresponding to $\epsilon = 10^{-3}$ is superposed with the cross section for a Schwarzschild BH.

all the static and spherical spacetimes. To the best of our knowledge, the fermionic radial equation for such spacetimes has not been explicitly derived. In the following, we derive this equation by generalizing the Teukolsky–Chandrasekhar procedure [57]. This can be used in other contexts.

To this aim, we have used the Newmann–Penrose formalism [58], which is, among other desirable properties, well-suited for spherical BHs. In this formalism, we have chosen a null basis consisting of a pair of real null vectors $\mathbf{l}$ and $\mathbf{n}$ and a pair of complex conjugate null vectors $\mathbf{m}$ and $\overline{\mathbf{m}}$:

$$\mathbf{l}\cdot\mathbf{l} = \mathbf{n}\cdot\mathbf{n} = \mathbf{m}\cdot\mathbf{m} = \overline{\mathbf{m}}\cdot\overline{\mathbf{m}} = 0. \tag{14}$$

The orthoganility conditions are imposed:

$$\mathbf{l}\cdot\mathbf{m} = \mathbf{l}\cdot\overline{\mathbf{m}} = \mathbf{n}\cdot\mathbf{m} = \mathbf{n}\cdot\overline{\mathbf{m}} = 0. \tag{15}$$

We also require the following normalization:

$$\mathbf{l}\cdot\mathbf{n} = 1 \ \text{ and } \ \mathbf{m}\cdot\overline{\mathbf{m}} = -1. \tag{16}$$

This normalization condition is not necessary in the Newmann–Penrose formalism, but it is convenient for our purpose. Any basis with the properties given by equations (14)–(16) can be used. We choose the basis vectors:

$$l^i = \frac{1}{\sqrt{2}}\left(\frac{1}{\sqrt{G}}, -\sqrt{F}, 0, 0\right), \tag{17}$$

$$n^i = \frac{1}{\sqrt{2}}\left(\frac{1}{\sqrt{G}}, \sqrt{F}, 0, 0\right), \tag{18}$$

$$m^i = \frac{1}{\sqrt{2}}\left(0, 0, \frac{1}{\sqrt{H}}, \frac{\mathrm{i}}{\sqrt{H}\sin\theta}\right), \tag{19}$$

$$\overline{m}^i = \frac{1}{\sqrt{2}}\left(0, 0, \frac{1}{\sqrt{H}}, \frac{-\mathrm{i}}{\sqrt{H}\sin\theta}\right). \tag{20}$$

When δ tends to zero and a_0 vanishes, this basis tends to the Carter tetrad, which can be used to describe a Schwarzschild BH [59]. However, usually, the Kinnersley tetrad is preferred for Schwarzschild BHs [57]. Different choices for the tetrads will lead to different spin coefficients and finally to apparently different, but actually *equivalent*, radial equations.

For spin $\frac{1}{2}$ fields, the wavefunction is represented by a pair of spinors, P^A and $\overline{Q}^{A'}$, with $A = 0, 1$ and $A' = 0, 1$. The Dirac equation in the Newmann–Penrose formalism can be written as [57]:

$$(D + \epsilon - \rho)P^0 + (\delta^* + \pi - \alpha)P^1 = \mathrm{i}\mu_* \overline{Q}^{1'}, \tag{21}$$

$$(\Delta + \mu - \gamma)P^1 + (\delta + \beta - \tau)P^0 = -\mathrm{i}\mu_* \overline{Q}^{0'}, \tag{22}$$

$$(D + \epsilon^* - \rho^*)\overline{Q}^{0'} + (\delta + \pi^* - \alpha^*)\overline{Q}^{1'} = -\mathrm{i}\mu_* P^1, \tag{23}$$

$$(\Delta + \mu_* - \gamma^*)\overline{Q}^{1'} + (\delta^* + \beta^* - \tau^*)\overline{Q}^{0'} = \mathrm{i}\mu_* P^0, \tag{24}$$

with

$$D = l^i\partial_i; \quad \Delta = n^i\partial_i; \quad \delta = m^i\partial_i; \quad \delta^* = \overline{m}^i\partial_i \tag{25}$$

μ_* is related to the mass of the fermion m_e by $\mu_*\sqrt{2} = m_e$. The spin-coefficients are derived from the rotation coefficients. In the tetrad formalism (for more details, see, e.g. [57]), the λ-symbols are defined as:

$$\lambda_{abc} = e_{bi,j}[e^i_a e^j_c - e^j_a e^i_c], \tag{26}$$

the a, b et c indices do indicate the vector of the basis, while the i and j indices are the coordinates. The correspondence reads as $\boldsymbol{e_1} = \boldsymbol{l}$, $\boldsymbol{e_2} = \boldsymbol{n}$, $\boldsymbol{e_3} = \boldsymbol{m}$ and $\boldsymbol{e_4} = \overline{\boldsymbol{m}}$ with $\boldsymbol{e^1} = \boldsymbol{e_2}$, $\boldsymbol{e^2} = \boldsymbol{e_1}$, $\boldsymbol{e^3} = -\boldsymbol{e_4}$ and $\boldsymbol{e^4} = -\boldsymbol{e_3}$. For example, $e_{12,3}$ represents the second composant of $\mathbf{l}$, derived with respect to θ. The rotation coefficients are defined as:

$$\gamma_{cab} = e^k_c e_{ak;i} e^i_b. \tag{27}$$

Then, from the λ-symbols, the rotation coefficients are obtained with the relation:

$$\gamma_{cab} = \frac{1}{2}(\lambda_{abc} + \lambda_{cab} - \lambda_{bca}). \tag{28}$$

The λ-symbols (26) and the rotation coefficients (27) should not be confused with the spin coefficients λ and γ. The spin coefficients are defined with the rotation coefficients (see appendix B). So first we have calculated the λ-symbols and then we have deduced the spin coefficients:

$$\kappa = \sigma = \lambda = \nu = \tau = \pi = 0, \tag{29}$$

$$\rho = \mu = \frac{\sqrt{F}H'}{2\sqrt{2}H}, \tag{30}$$

$$\epsilon = \gamma = -\frac{\sqrt{F}G'}{4\sqrt{2}G}, \tag{31}$$

$$\alpha = -\beta = -\frac{cot\theta}{2\sqrt{2H}}. \tag{32}$$

Given the symmetries, the wavefunctions can be written as $\Psi(t, r, \theta, \phi) = R(r)S(\theta)e^{i(\omega t+m'\phi)}$ where, as for scalars, ω is the frequency and m' is an integer. We use the following ansatz:

$$P^0 = \frac{e^{i(\omega t+m'\phi)}}{\sqrt{H(r)}(G(r)F(r))^{\frac{1}{8}}}R_+(r)S_+(\theta), \tag{33}$$

$$P^1 = \frac{e^{i(\omega t+m'\phi)}}{\sqrt{H(r)}(G(r)F(r))^{\frac{1}{8}}}R_-(r)S_-(\theta), \tag{34}$$

$$\overline{Q}^{0'} = -\frac{e^{i(\omega t+m'\phi)}}{\sqrt{H(r)}(G(r)F(r))^{\frac{1}{8}}}R_+(r)S_-(\theta), \tag{35}$$

$$\overline{Q}^{1'} = \frac{e^{i(\omega t+m'\phi)}}{\sqrt{H(r)}(G(r)F(r))^{\frac{1}{8}}}R_-(r)S_+(\theta). \tag{36}$$

This is useful as it makes the system separable into a radial and an angular parts. The normalisation with $1/(\sqrt{H(r)}(G(r)F(r))^{\frac{1}{8}})$ is only chosen for convenience. By inserting the previous expressions in Dirac equation (21), we obtain:

$$-(\sqrt{HF}\mathcal{D}^\dagger R_+ + im_e\sqrt{H}R_-)S_+ + R_-\mathcal{L}S_- = 0, \tag{37}$$

with $\mathcal{D}$ a radial operator

$$\mathcal{D} = \partial_r + \left(\frac{G'}{8G} - \frac{F'}{8F}\right) + \frac{iw}{\sqrt{GF}}, \tag{38}$$

and $\mathcal{L}$ an angular operator

$$\mathcal{L} = \partial_\theta + \frac{m'}{\sin\theta} + \frac{cot\theta}{2}. \tag{39}$$

$\mathcal{D}^\dagger$ is the complex conjugate of $\mathcal{D}$ and $\mathcal{L}^\dagger$ is $-\mathcal{L}$ once replacing θ by $\pi - \theta$.

Equation (37) implies:

$$\mathcal{L}S_- = \lambda_1 S_+, \tag{40}$$

$$\sqrt{HF}\mathcal{D}^\dagger R_+ + im_e\sqrt{H}R_- = \lambda_1 R_-, \tag{41}$$

with λ_1 a constant of separation. Proceeding in the same way with equations (22)–(24), three other constants of separation do appear: respectively denoted λ_2, λ_3 and λ_4. Among the eight equations, there is some redundancy and only four are actually independent. The consistency implies: $\lambda_1 = \lambda_2 = \lambda_3 = \lambda_4 \equiv \lambda$. This separation constant λ is neither a λ-symbol nor a spin coefficient, we simply use the notation of [57].

The Dirac equations finally reduce to the following radial and angular systems:

$$\begin{pmatrix} \sqrt{HF}\mathcal{D} & -(\lambda + im_e\sqrt{H}) \\ -(\lambda - im_e\sqrt{H}) & \sqrt{HF}\mathcal{D}^\dagger \end{pmatrix}\begin{pmatrix} R_- \\ R_+ \end{pmatrix} = 0, \tag{42}$$

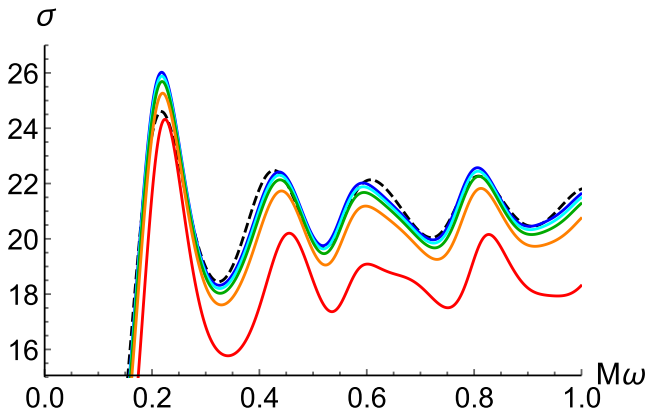

Figure 3. Emission cross section for a fermionic field, with energy ω, in the background spacetime of a LBH of mass M. From bottom to top: $\epsilon = 10^{\{-0.3,-0.6,-0.8,-1,-3\}}$. The dashed dark curve corresponds to the Schwarzschild cross section.

$$\begin{pmatrix} \mathcal{L} & -\lambda \\ \lambda & \mathcal{L}^\dagger \end{pmatrix} \begin{pmatrix} S_- \\ S_+ \end{pmatrix} = 0. \tag{43}$$

By eliminating R_- in equation (42), we obtain the radial equation for R_+:

$$\sqrt{HF}\mathcal{D}\left(\frac{\sqrt{HF}\mathcal{D}^\dagger}{\lambda - \mathrm{i}m_e\sqrt{H}}R_+\right) - (\lambda + \mathrm{i}m_e\sqrt{H})R_+ = 0. \tag{44}$$

The radial equation for R_- is the conjugate of equation (44). This equation generalizes the Teukolsky equation [56]. The separation constant λ is obtained by solving the angular equation, which is the same than in the Schwarzschild case: $\lambda^2 = j(j+1) - s(s-1)$ [60], that is $\lambda^2 = (l+1)^2$ for fermions.

Setting $m_e = 0$ leads to:

$$\sqrt{HF}\mathcal{D}\left(\sqrt{HF}\mathcal{D}^\dagger R_+\right) - \lambda^2 R_+ = 0. \tag{45}$$

This equation of motion can be used to determine the fermionic cross section. We study the asymptotic solutions, near the horizon and at spacial infinity. The function R is splitted into its real part U and its Imaginary part V. Both equations are then solved thanks to equation (44).

For a massless fermionic field, at the horizon, equation (44) tends to:

$$\frac{\partial^2 R_+}{\partial r^2} + \frac{1}{2(r-r_+)}\frac{\partial R_+}{\partial r} + \left(\frac{\omega^2}{C_1} + \mathrm{i}\frac{\omega}{\sqrt{C_1}}\right)\frac{R_+}{(r-r_+)^2} = 0, \tag{46}$$

with $C_1 = \frac{(r_+ - r_-)^2 r_+^4}{(r_+^4 + a_o^2)^2}$. With respect to the tortoise coordinate r^*, equation (46) reads as:

$$\frac{1}{C_1}\frac{\partial^2 R_+}{\partial r^{*2}} - \frac{1}{2\sqrt{C_1}}\frac{\partial R_+}{\partial r^{*2}} + \left(\frac{\omega^2}{C1} + \mathrm{i}\frac{\omega}{\sqrt{C1}}\right)R_+ = 0. \tag{47}$$

The determinant of the characteristic equation of equation (47) is $\det = \frac{1-16\omega(4\omega M+\mathrm{i})}{4C_1}$. There are two roots but, from the absorption point of view, there should be only an incoming

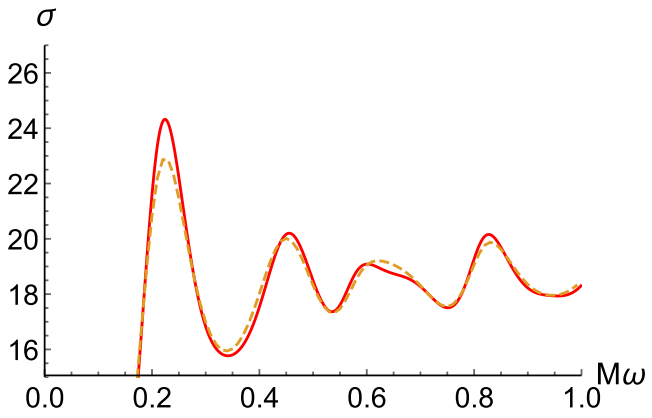

Figure 4. Emission cross section for a fermionic field, with energy ω, in the background spacetime of a LBH of mass M, for $\epsilon = 10^{-0.3}$. The dashed curved corresponds to $a_0 = 0$ and the plain curve to the usual LQG value, $a_0 = A_{\min}/8\pi = \sqrt{3}\gamma/2$.

mode at the horizon. The root x_1 is therefore chosen with a positive imaginary part. Near the horizon, the radial part reads as:

$$R_+(r^*) = A\mathrm{e}^{x_1 r^*}, \tag{48}$$

with A a complex number. As before, we normalize such that $R_+(r_{\mathrm{ini}}) = 1$, which leads to $\frac{\mathrm{d}R_+(r_{\mathrm{ini}})}{\mathrm{d}r} = \frac{x_1}{\sqrt{G(r_{\mathrm{ini}})F(r_{\mathrm{ini}})}}$. At spacial infinity, the solution is a plane wave.

It has been shown in [61] that the transmission coefficient for spin 1/2 fields is given by:

$$|A_l|^2 = \left|\frac{A^h_{\mathrm{in}}}{A^\infty_{\mathrm{in}}}\right|^2. \tag{49}$$

As for the scalar case, we numerically solve equation (44), fit the solution in order to obtain A^∞_{in} for each $l \leqslant 10$, and then obtain the cross section. The result is shown in figure 3. Once again, the general trend is to decrease the cross section when the 'quantumness' increases. As the relative effect is getting bigger with an increasing energy of the emitted particle, this should leave a footprint through a distortion of the instantaneous Hawking spectrum which will exhibit slight suppression of its UV tail.

Finally, in figure 4, we show that the effect of sending to 0 the minimum area a_0 does not have a dramatic effect. However, choosing a non-vanishing a_0 leads to a slight increase of the cross section on the first peak. The cross section itself is of course a continuous function of a_0. This parameter has a clearly different influence than the polymerization parameter.

Conclusion

In this article, we have studied the propagation of quantum fields in the vicinity of a black hole undergoing quantum gravity corrections. It is shown that the effects are generically small but the trend is quite clear. Phenomenologically, large values of the polymerization parameter could be probed by a decreased cross section, together with a slight frequency shift for fermions. In addition, the non-vanishing minimum area leaves a specific footprint on the first peak.

This sets a framework for futures studies, both in LQG or in modified gravity. In the specific case of loop black holes, it would be most interesting to investigate, using the tools developed in this study, the cross sections for recent BH models published in [62] and [63, 64], among others.

As the Hawking evaporation of a black hole is considered to be one of the rare possible probes of quantum gravity, it is mandatory to calculate the cross sections for quantum fields in the associated background spacetime. This article is only a first step in this direction for LQG. It already shows that different quantum corrections—still in the LQG framework—will lead to different effects on the behavior of cross section. This is both useful for accurate calculations of the Hawking spectrum (to refine, e.g. what was done in [65]) and as a probe, in itself, on the intricate spacetime structure.

Acknowledgments

KM is supported by a grant from the CFM foundation.

Appendix A

The initial conditions for solving the radial equation (7) are $R(r_{\rm ini}) = A^h_{\rm in} e^{i\omega r^*} = 1$ and $\frac{dR(r_{\rm ini})}{dr} = \frac{i\omega}{\sqrt{GF}}$. To solve this complex equation, both the real and the imaginary parts have to be solved. Writing $R(r) = U(r) + iV(r)$, the initial conditions are:

$$\begin{aligned} U(r_{\rm ini}) &= 1, \qquad V(r_{\rm ini}) = 0, \\ \frac{dU(r_{\rm ini})}{dr} &= 0, \qquad \frac{dV(r_{\rm ini})}{dr} = \frac{\omega}{\sqrt{GF}}. \end{aligned} \tag{A.1}$$

Far from the BH, we have:

$$U(r) = \frac{a_1}{r}\cos(\omega r) + \frac{b_1}{r}\sin(\omega r), \tag{A.2}$$

$$V(r) = \frac{a_2}{r}\cos(\omega r) + \frac{b_2}{r}\sin(\omega r), \tag{A.3}$$

with $a_1 = \Re(A^\infty_{\rm in}) + \Re(A^\infty_{\rm out})$, $b_1 = \Im(A^\infty_{\rm out}) - \Im(A^\infty_{\rm in})$, $a_2 = \Im(A^\infty_{\rm in}) + \Im(A^\infty_{\rm out})$ and $b_2 = \Re(A^\infty_{\rm in}) - \Re(A^\infty_{\rm out})$. With a fifth order Runge Kutta method, we solve the real and imaginary parts of equation (44) with the initial conditions given by equation (A.1). At $r_{\rm end}$, we fit the solutions of U and V with functions given in equations (A.2) and (A.3) to obtain the coefficients a_1, b_1, a_2, and b_2 so as to deduce $A^\infty_{\rm in}$ and $A^\infty_{\rm out}$.

Appendix B

The spin coefficients defined with the rotation coefficient are given by:

$$\begin{aligned} \kappa &= \gamma_{311} \quad \rho = \gamma_{314} \quad \epsilon = \frac{1}{2}(\gamma_{211} + \gamma_{341}) \\ \sigma &= \gamma_{313} \quad \mu = \gamma_{243} \quad \gamma = \frac{1}{2}(\gamma_{212} + \gamma_{342}) \\ \lambda &= \gamma_{244} \quad \tau = \gamma_{312} \quad \alpha = \frac{1}{2}(\gamma_{214} + \gamma_{344}) \\ \nu &= \gamma_{242} \quad \pi = \gamma_{241} \quad \beta = \frac{1}{2}(\gamma_{213} + \gamma_{343}). \end{aligned}$$

ORCID iDs

Aurélien Barrau https://orcid.org/0000-0003-1670-2966

References

[1] Rovelli C 2004 *Quantum Gravity* (*Cambridge Monographs on Mathematical Physics*) (Cambridge: Cambridge University Press)
[2] Thiemann T 2008 *Modern Canonical Quantum General Relativity* (Cambridge: Cambridge University Press)
[3] Rovelli C and Vidotto F 2014 *Covariant Loop Quantum Gravity* (*Cambridge Monographs on Mathematical Physics*) (Cambridge: Cambridge University Press)
[4] Ashtekar A and Pullin J (ed) 2017 *Loop Quantum Gravity* (*100 Years of General Relativity* vol 4) (Singapore: World Scientific)
[5] Bojowald M 2008 *Living Rev. Relativ.* **11** 4
[6] Ashtekar A and Singh P 2011 *Class. Quantum Grav.* **28** 213001
[7] Barrau A, Cailleteau T, Grain J and Mielczarek J 2014 *Class. Quantum Grav.* **31** 053001
[8] Ashtekar A and Barrau A 2015 *Class. Quantum Grav.* **32** 234001
[9] Agullo I and Corichi A 2014 *Springer Handbook of Spacetime* ed A Ashtekar and V Petkov (Berlin: Springer) pp 809–39
[10] Wilson-Ewing E 2017 *C. R. Phys.* **18** 207
[11] Agullo I and Singh P 2017 *Loop Quantum Gravity: the First 30 Years* ed A Ashtekar and J Pullin (Singapore: World Scientific Publishing) pp 183–240
[12] Barrau A and Bolliet B 2016 *Int. J. Mod. Phys.* D **25** 1642008
[13] Ashtekar A, Baez J C and Krasnov K 2000 *Adv. Theor. Math. Phys.* **4** 1
[14] Gürsel H and Sakallı I 2018 *Adv. High Energy Phys.* **2018** 8504894
[15] Barbero G J F and Perez A 2017 *Loop Quantum Gravity: the First 30 Years* ed A Ashtekar and J Pullin (Singapore: World Scientific Publishing) pp 241–79
[16] Olmedo J 2016 *Universe* **2** 12
[17] Perez A 2017 *Rep. Prog. Phys.* **80** 126901
[18] Alesci E and Modesto L 2014 *Gen. Relativ. Gravit.* **46** 1656
[19] Rovelli C 1996 *Phys. Rev. Lett.* **77** 3288
[20] Agullo I, Fernando Barbero G J, Borja E F, Diaz-Polo J and Villasenor E J S 2009 *Phys. Rev.* D **80** 084006
[21] Ghosh A, Noui K and Perez A 2014 *Phys. Rev.* D **89** 084069
[22] Frodden E, Geiller M, Noui K and Perez A 2014 *Europhys. Lett.* **107** 10005
[23] Ben Achour J, Mouchet A and Noui K 2015 *J. High Energy Phys.* JHEP06(2015)145
[24] Asin O, Ben Achour J, Geiller M, Noui K and Perez A 2015 *Phys. Rev.* D **91** 084005
[25] Ben Achour J and Noui K 2016 *PoS* **FFP14** 158
[26] Modesto L 2010 *Int. J. Theor. Phys.* **49** 1649
[27] Frolov V P, Markov M A and Mukhanov V F 1989 *Phys. Lett.* B **216** 272
Frolov V P, Markov M A and Mukhanov V F 1990 *Phys. Lett.* B **216** 52
[28] Balbinot R, Brady P R, Israel W and Poisson E 1991 *Phys. Lett.* A **161** 223
[29] Hayward S A 2006 *Phys. Rev. Lett.* **96** 031103
[30] Spallucci E, Smailagic A and Nicolini P 2009 *Phys. Lett.* B **670** 449
[31] Rovelli C 2011 *PoS* **QGQGS2011** 003
[32] Alesci E and Cianfrani F 2015 *Phys. Rev.* D **92** 084065
[33] Haggard H M and Rovelli C 2016 *Int. J. Mod. Phys.* D **25** 1644021
[34] Hawking S 1975 *Commun. Math. Phys.* **43** 199
[35] Unruh W G 1976 *Phys. Rev.* D **14** 870
[36] Ashtekar A and Bojowald M 2005 *Class. Quantum Grav.* **22** 3349
[37] Barrau A, Cailleteau T, Cao X, Diaz-Polo J and Grain J 2011 *Phys. Rev. Lett.* **107** 251301
[38] Gambini R and Pullin J 2014 *Class. Quantum Grav.* **31** 115003
[39] Page D N 1976 *Phys. Rev.* D **13** 198
[40] Page D N 1976 *Phys. Rev.* D **14** 1509
[41] Page D N 1977 *Phys. Rev.* D **16** 2402

[42] Kanti P, Grain J and Barrau A 2005 *Phys. Rev.* D **71** 104002
[43] Grain J, Barrau A and Kanti P 2005 *Phys. Rev.* D **72** 104016
[44] Gursel H and Sakall I 2018 (arXiv:1806.03446)
[45] Panotopoulos G and Rincón A 2018 *Phys. Rev.* D **97** 085014
[46] Ovgün A and Jusufi K 2018 *Ann. Phys.* **395** 138
[47] Zhang C-Y, Li P-C and Chen B 2018 *Phys. Rev.* D **97** 044013
[48] Ahmed J and Saifullah K 2017 *Eur. Phys. J.* C **77** 885
[49] Panotopoulos G and Rincón A 2017 *Phys. Rev.* D **96** 025009
[50] Boonserm P, Ngampitipan T and Wongjun P 2018 *Eur. Phys. J.* C **78** 492
[51] Ahmed J and Saifullah K 2018 *Eur. Phys. J.* C **78** 316
[52] Jorge R, de Oliveira E S and Rocha J V 2015 *Class. Quantum Grav.* **32** 065008
[53] Boonserm P, Chatrabhuti A, Ngampitipan T and Visser M 2014 *J. Math. Phys.* **55** 112502
[54] Abedi J and Arfaei H 2014 *Class. Quantum Grav.* **31** 195005
[55] Li W, Xu L and Liu M 2009 *Class. Quantum Grav.* **26** 055008
[56] Teukolsky S A 1973 *Astrophys. J.* **185** 635
[57] Chandrasekhar S 1992 *The Mathematical Theory of Black Holes* (Oxford: Clarendon Press) p 646
Chandrasekhar S 1985 *The Mathematical Theory of Black Holes* 1st edn (Oxford: Clarendon Press) p 646
[58] Newman E and Penrose R 1962 *J. Math. Phys.* **3** 566
[59] Batic D, Nowakowski M and Morgan K 2016 *Universe* **2** 31
[60] Kanti P 2004 *Int. J. Mod. Phys.* A **19** 4899
[61] Cvetic M and Larsen F 1998 *Phys. Rev.* D **57** 6297
[62] Ben Achour J, Lamy F, Liu H and Noui K 2018 *EPL* **123** 20006
[63] Ashtekar A, Olmedo J and Singh P 2018 *Phys. Rev. Lett.* **121** 241301
[64] Ashtekar A, Olmedo J and Singh P 2018 (arXiv:1806.02406)
[65] Barrau A, Cao X, Noui K and Perez A 2015 *Phys. Rev.* D **92** 124046

3.3 Les modes quasi normaux

3.3.1 Point de vue théorique

Lorsqu'un trou noir est perturbé, et ce peu importe de quelle façon, il aura une phase de relaxation ("ringdown" en anglais) avant de se stabiliser. Lors de cette dernière étape, il va émettre des ondes gravitationnelles amorties dont les fréquences propres ω_R et leur amortissement ω_I dépendent uniquement des caractéristiques du trou noir et non du processus qui l'a perturbé. Dans cette phase, on se trouve dans le régime perturbatif. Les modes propres sont solutions des équations des perturbations avec les conditions aux bords suivantes :

— onde purement rentrante à l'horizon,

— onde purement sortante à l'infini spatial.

Les fréquences ω sont appelées modes quasi normaux (QNMs pour quasi normal modes) [4, 55, 56]. Pour les trous noirs stationnaires, la dépendance en temps est donnée par

$$e^{i\omega t} = e^{i(\omega_R + i\omega_I)t}. \tag{3.51}$$

Il existe deux types de perturbations. Pour appuyer leur différence mathématique, considérons les perturbations d'un trou noir stationnaire à symétrie sphérique. La métrique peut s'écrire sous la forme

$$ds^2 = e^{2\mu_t}dt^2 - e^{2\psi}(d\phi - q_t dt - q_r dr - q_\theta d\theta)^2 - e^{2\mu_r}dr^2 - e^{2\mu_\theta}d\theta. \tag{3.52}$$

La symétrie sphérique impose que les coefficients q_t, q_r, et q_θ soient nuls. Les perturbations telles que ces coefficients prennent une petite valeur non nulle sont appelées les modes axiaux. Ils entrainent une faible rotation du trou noir. D'autre part, lorsqu'on rajoute une petite incrémentation $\delta\mu_t$, $\delta\mu_r$, $\delta\mu_\theta$ et $\delta\psi$ aux coefficients déjà non nuls, nous décrivons les modes polaires. Ces deux types de perturbations vont se transformer différemment sous parité. Pour un moment angulaire ℓ donné, les perturbations axiales se transforment en $(-1)^{\ell+1}$, alors que les perturbations polaires se transforment en $(-1)^\ell$. La partie radiale de ces deux types d'ondes est décrite par une équation de type Schrödinger, avec des potentiels $V(r)$ différents

$$\frac{d^2Z}{dr^{*2}} + \omega^2 Z - V(r)Z = 0, \tag{3.53}$$

avec r^* la coordonnée tortoise qui tends vers $-\infty$ quand r tends vers l'horizon. Par exemple pour les trous noirs de Schwarzschild, on a

$$ds^2 = f(r)dt^2 - f(r)^{-1}dr^2 - r^2 d\Omega^2, \tag{3.54}$$

et la coordonnée tortoise est définie par $dr^* = f^{-1}dr$. Les modes axiaux sont solutions lorsqu'on a le potentiel de Regge-Wheeler

$$V_\ell^{RW}(r) = \left(1 - \frac{2M}{r}\right)\left[\frac{\ell(\ell+1)}{r^2} - \frac{6M}{r^3}\right], \tag{3.55}$$

avec $\ell \geq 2$. Les modes polaires sont solutions pour le potentiel de Zerilli

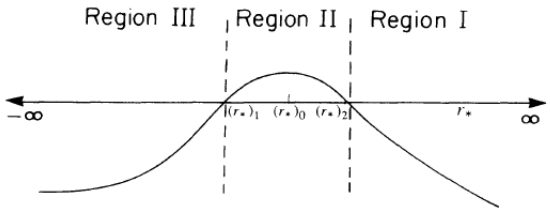

FIGURE 3.1 – Le potentiel V en fonction de la coordonnée tortoise r^* [60].

$$V_\ell^Z(r) = \frac{2}{r^3}\left(1 - \frac{2M}{r}\right) \times \frac{9M^3 + 3L^2Mr^2 + L^2(1+L)r^3 + 9M^2Lr}{(3M + Lr)^2}, \tag{3.56}$$

avec $L = \ell(\ell+1)/2 - 1$. Nous verrons, dans la section 3.3.3, qu'il existe des transformations qui relient les solutions des deux équations (Regge-Wheeler et Zerilli). Cette caractéristique est appelée isospectralité.

Pour calculer la valeur des QNMs, il est possible de déterminer leur valeur numériquement mais il est également intéressant de les calculer semi-analytiquement avec des méthodes d'approximation. Il est pertinent de calculer leur valeur avec une bonne précision car un important changement sur les paramètres du trou noir induit seulement une faible déviation dans les QNMs. Les méthodes semi-analytiques sont comparées aux calculs purement numériques afin d'établir leur précision. Il existe différentes méthodes approximatives qui permettent de calculer ces QNMs [56] avec une bonne précision. Dans les articles des sections 3.3.4 et 3.3.7, nous utilisons la méthode de WKB [57]. C'est une méthode semi-classique applicable lorsqu'on a une barrière de potentiel dont les valeurs à l'horizon et à l'infini spatial sont constantes. Elle permet d'obtenir une approximation à la solution d'une équation différentielle linéaire dont le terme de dérivée d'ordre supérieur est multiplié par un petit paramètre ϵ. L'approximation WKB pour le calcul des QNMs des trous noirs de Schwarzschild a initialement été introduit par Schutz, Will et Iyer [58, 59, 60]. Dans ces papiers, l'approximation WKB est effectuée jusqu'au 3ème ordre. Plus tard, Konoplya a prolongé l'approximation jusqu'au 6ème ordre [61].

Le terme d'ordre supérieur de l'équation (3.53) est multiplié par un paramètre de perturbation ϵ tel que

$$\epsilon^2 \frac{d^2Z}{dr^{*2}} + Q(r^*)Z = 0, \tag{3.57}$$

avec $Q(r^*) = \omega^2 - V(r^*)$. Ce "potentiel" est constant en $r^* = \pm\infty$, mais pas nécessairement le même aux deux bords. L'espace est séparé en trois régions en fonction du potentiel, comme on peut l'observer sur la Figure (3.1). Dans les régions I et III, les solutions sont approximées par une exponentielle

$$Z(r^*) \sim \exp\left(\frac{1}{\delta}\sum_{n=0}^{\infty} \delta^n S_n(r^*)\right) \quad \text{quand} \quad \delta \to 0. \tag{3.58}$$

avec δ le paramètre WKB qui indique l'ordre d'expansion. On peut alors dériver cette expression par rapport à r^* et trouver

$$Q(r^*) = \frac{\epsilon^2 S_0^{'2}}{\delta^2} + \frac{2\epsilon^2}{\delta} S_0^{'} S_1^{'} + \frac{\epsilon^2}{\delta} S_0^{''} + \epsilon^2 S_1^{''} + ... \quad \text{quand} \quad \delta \to 0. \tag{3.59}$$

Si on suppose que le terme le plus grand est

$$\frac{\epsilon^2 S_0^{'2}}{\delta^2}, \tag{3.60}$$

alors $Q(r^*) \sim \epsilon^2 S_0^{'}/\delta^2$. Donc, on a $S_0^{'} \sim \sqrt{\delta^2 Q/\epsilon^2}$ et $S_0^{''} = \delta Q/2\epsilon$. D'après l'équation (3.59), on en déduit

$$\begin{aligned} Q =& Q + 2\epsilon\sqrt{Q} S_1 + \frac{\epsilon}{2}\frac{Q'}{\sqrt{Q}} && (3.61)\\ \approx& Q \quad \text{quand} \quad \epsilon \to 0. && (3.62) \end{aligned}$$

Ainsi l'hypothèse émise (3.60) est totalement cohérente. Si, on avait supposé que le terme le plus important était

$$\frac{\epsilon^2}{\delta}(2S_0^{'} S_1^{'} + S_0^{''}), \tag{3.63}$$

alors l'équation (3.59) donnerait

$$Q = \left(\int Q(x) dx \right)^2 + \epsilon Q, \tag{3.64}$$

ce qui n'est pas cohérent lorsque $\epsilon \to 0$. Cette méthode, dite de balance dominante, nous permet de déduire le terme le plus important et en déduire $\epsilon \sim \delta$ [62]. La première équation

$$S_0^{'2} = Q(r^*) \tag{3.65}$$

amène à l'équation eikonal

$$S_0 = \pm \int \sqrt{Q(x)} dx. \tag{3.66}$$

La deuxième équation

$$2S_0^{'} S_1^{'} + S_0^{''} = 0 \tag{3.67}$$

amène à l'équation de transport

$$S_1 = -\frac{1}{4} \ln Q. \tag{3.68}$$

On peut continuer ainsi de suite pour avoir les termes S_n. Dans la région II, $Q(r^*)$ est approximé par un développement de Taylor autour du maximum du potentiel V_0. Puis, lorsque l'on fait coïncider ces solutions, on trouve, au 6ème ordre

$$\omega^2 = V_0 - i\sqrt{-2V_0''}\left(\sum_{j=2}^{6}\Lambda_j + n + \frac{1}{2}\right) \tag{3.69}$$

où les expressions Λ_j sont données dans [61]. Ainsi grâce à l'expression du potentiel et de ses dérivées au maximum de la barrière de potentiel, on a accès aux valeurs approximatives des QNMs. La valeur des QNMs dépend donc de deux nombres entiers : les harmoniques n (overtone en anglais) et du moment angulaire ℓ qui caractérise le potentiel.

3.3.2 Point de vue expérimental

Est ce que ces QNMs sont/seront détecter avec les interféromètres actuels et futurs ? La phase de relaxation est caractérisée par une sinusoïde amortie qui est une somme pondérée de tous les QNMs. Le poids, dans la reconstruction du signal, le plus important est pour le mode fondamental $n = 0$ et $\ell = 2$. La possibilité de mesurer expérimentalement les QNMs commence à peine à émerger. En effet, dans l'évènement QW150914, un ajustement de la sinuisoïde amortie a pu être effectué pour obtenir la fréquence et son temps d'amortissement pour le QNM fondamental et pour la première harmonique $n = 1$ et $\ell = 2$ [63]. L'intervalle de confiance étant de 3.5σ. Cependant la précision n'est pas assez grande pour identifier une faible déviation comparée au modèle classique. Mais le mode fondamental a déjà permis de tester certains modèles exotiques. Par exemple le modèle "gravastar" ne permet pas d'expliquer les données de l'évènement GW150914 [64]. Dans les expériences futures, telles que le Einstein Télescope, il sera possible de mesurer avec plus de précision la première harmonique $n = 1$: de quelques dizaines de pourcents la précision atteindra quelques pourcents.

3.3.3 L'isospectralité des trous noirs de Schwarzschild-de Sitter et Schwarzschild-Anti-de Sitter

Nous avons vu qu'il existait deux types de perturbations : axiales et polaires. A priori, ces pertubations ne possèdent pas le même spectre de fréquences propres. Cependant, il a été montré que les trous noirs de Schwarzschild [65], Reissner-Nordström [66] et Kerr [67] possèdent la propriété d'isospectralité. C'est-à-dire que, les modes axiaux et polaires ont le même spectre. Cependant pour d'autres modèles avec des métriques effectives, l'isospectralité n'est pas respectée. A vrai dire, cette propriété d'isospectralité a été peu investiguée et lorsqu'elle a été étudié c'était de façon numérique principalement. Les seules preuves analytiques sont celles données par Chandrasekhar citées précédemment. Ainsi, le but de cet article est d'approfondir la preuve analytique d'isospectralité pour voir si elle peut s'étendre à une catégorie plus générale de trous noirs.

Deux types de perturbations sont isospectrales, si leurs parties radiales Z_1 et Z_2 obéissent à l'équation (3.53) avec leurs potentiels respectifs V_1 et V_2 et ont pour solutions les mêmes fréquences ω. Pour que ceci ait lieu, trois conditions doivent être respectées [4]. Il faut qu'il existe deux fonctions p et q telles que :

1. $Z_1 = pZ_2 + q\dfrac{dZ_2}{dr^*}$, (3.70)
2. $V_1 = V_2 + \dfrac{2}{q}\dfrac{dp}{dr^*} + \dfrac{1}{q}\dfrac{d^2q}{dr^{*2}}$, (3.71)
3. $p^2 + \left(p\dfrac{dq}{dr^*} - \dfrac{dp}{dr^*}q\right) - q^2(V_2 - \omega^2) = C^2 = \text{cte}.$ (3.72)

On considère la métrique suivante

$$ds^2 = B(r)dt^2 - B(r)^{-1}dr^2 - r^2d\Omega^2, \tag{3.73}$$

sans préciser la forme de la fonction $B(r)$ pour le moment. On utilise le formalisme de Newman-Penrose. Étant données les symétries, le seul scalaire de Newman-Penrose (1.48) non nul est

$$\Psi_2 = \frac{-2 + 2B(r) - 2rB'(r) + r^2B''(r)}{12r^2}. \tag{3.74}$$

Les perturbations sont les quatre scalaires Ψ_0, Ψ_1, Ψ_3 et Ψ_4 (ré-échelonnés en Φ_i) et les quatre coefficients de spin κ, σ, λ et ν (ré-échelonnés en k, s, l et n). On établit les équations de Bianchi et de Ricci linéarisées qui décrivent ces perturbations

$$\mathcal{L}_2\Phi_0 - \left(\mathcal{D}_0 + \frac{3}{r}\right)\Phi_1 = 6r^3\Psi_2 k + \sqrt{2}r[R_1], \tag{3.75}$$

$$Br^2\left(\mathcal{D}_2^\dagger - \frac{3}{r}\right)\Phi_0 + \mathcal{L}_{-1}^\dagger\Phi_1 = -6r^3\Psi_2 s - 2r^2[R_2], \tag{3.76}$$

$$\left(\mathcal{D}_0 + \frac{3}{r}\right)s - \mathcal{L}_{-1}k = \frac{\Phi_0}{r}, \tag{3.77}$$

$$\left(\mathcal{D}_0 - \frac{3}{r}\right)\Phi_4 - \mathcal{L}_{-1}\Phi_3 = -6r^3\Psi_2 l + r^4[R_3], \tag{3.78}$$

$$\mathcal{L}_2^\dagger\Phi_4 + \frac{Br^2}{2}\left(\mathcal{D}_{-1}^\dagger + \frac{3}{r}\right)\Phi_3 = -6r^3\Psi_2 n + \sqrt{2}r^5[R_4], \tag{3.79}$$

$$Br^2\left(\mathcal{D}_{-1}^\dagger + \frac{3}{r}\right)l + \mathcal{L}_{-1}n = \frac{\Phi_4}{r}. \tag{3.80}$$

avec $\mathcal{D}$ et $\mathcal{L}$ des opérateurs radial et angulaire respectivement définis tels que

$$\mathcal{D}_n = \partial_r + \frac{i\omega}{B(r)} + n\left(\frac{B'(r)}{B(r)} + \frac{2}{r}\right), \tag{3.81}$$

$$\mathcal{L}_n = \partial_\theta + \frac{m}{\sin\theta} + n\cot\theta, \tag{3.82}$$

avec $\mathcal{D}_n^\dagger$ le complexe conjugué de $\mathcal{D}_n$ et $\mathcal{L}_n^\dagger(\theta) = -\mathcal{L}_n(\pi - \theta)$. Les termes $[R_i]$ sont des combinaisons du tenseur de Riemann. En appliquant $\mathcal{L}_{-1}^\dagger$ à l'équation (3.75) et $\left(\mathcal{D}_0 + \frac{3}{r}\right)$ à l'équation (3.76) on obtient

$$\begin{aligned}&\mathcal{L}_{-1}^\dagger\mathcal{L}_2\Phi_0 + \left(\mathcal{D}_0 + \frac{3}{r}\right)\left[Br^2\left(\mathcal{D}_2^\dagger - \frac{3}{r}\right)\Phi_0\right] = \\ &6r^3\Psi_2\left[\mathcal{L}_{-1}^\dagger k - \left(\mathcal{D}_0 + \frac{3}{r}\right)s\right] - 6s\partial_r(r^3\Psi_2) + \mathcal{L}_{-1}^\dagger(\sqrt{2}r[R_1]) - 2\left(\mathcal{D}_0 + \frac{3}{r}\right)(r^2[R_2]).\end{aligned} \tag{3.83}$$

Il est intéressant de remarquer que si $r^3\Psi_2$ est une constante et que $[R_1]$ et $[R_2]$ sont nuls, alors la partie gauche de l'équation (3.77) apparaît et peut être remplacée par Φ_0/r. On obtient alors une équation découplée pour Φ_0

$$\mathcal{L}_{-1}^{\dagger}\mathcal{L}_2\Phi_0 + \left(\mathcal{D}_0 + \frac{3}{r}\right)\left[Br^2\left(\mathcal{D}_2^{\dagger} - \frac{3}{r}\right)\Phi_0\right] = -6r^2\Psi_2\Phi_0. \tag{3.84}$$

De façon similaire on peut obtenir une équation découplée pour Φ_4 avec les équations (3.78), (3.79) et (3.80). Les conditions pour découpler les équations sont donc les suivantes

$$r^3\Psi_2 = \text{cte} \quad \text{et} \quad [R_1] = [R_2] = [R_3] = [R_4] = 0. \tag{3.85}$$

Ces deux conditions restreignent l'espace-temps à celui de Schwarzschild-de Sitter et Schwarzschild-Anti-de Sitter :

$$B(r) = 1 - \frac{2M}{r} - \Lambda r^2, \tag{3.86}$$

avec Λ la constante cosmologique. Mais ces conditions ne sont pas respectées pour des espace-temps plus généraux. A partir des équations découplées, il est possible de faire plusieurs transformations et changements de variables de sorte à trouver les fonctions q et p qui respectent les conditions d'isospectralité (3.70), (3.71) et (3.72) qui relient les perturbations axiales Z^- et polaires Z^+. On obtient

$$q = 2\gamma \quad \text{et} \quad p = \kappa + 2\gamma^2 f \tag{3.87}$$

avec $\mu^2 = \ell(\ell+1) - 2$, $\gamma^2 = 36M^2$, $\kappa = \mu^2(2+\mu^2)$ et $f = B/(\mu^2 r^2 + 6Mr)$.
Les potentiels s'écrivent sous la forme générales

$$V^{\pm} = \pm\gamma\frac{df}{dr^*} + \gamma^2 f^2 + \kappa f, \tag{3.88}$$

ce qui nous permet de les réécrire sous leur forme explicite

$$V^- = \left(1 + \frac{2M}{r} + \Lambda r^2\right)\left[\frac{\ell(\ell+1)}{r^2} - \frac{6M}{r^3}\right] \tag{3.89}$$

$$\tag{3.90}$$

et

$$V^+ = \frac{2}{r^3}\left(1 + \frac{2M}{r} + \Lambda r^2\right) \times \frac{9M^3 + 3L^2Mr^2 + L^2(1+L)r^3 + 9M^2r(L - \Lambda r^2)}{(Lr+3M)^2} \tag{3.91}$$

avec $2L = \mu^2$. Ce qui clôture la preuve analytique de l'isospectralité pour les trous noirs de Schwarzschild-de Sitter et Schwarzschild-Anti-de Sitter. Un des points initiaux clé à la preuve est de pouvoir découpler les équations, afin d'effectuer toutes les transformations qui suivent. Ce découplage ne peut pas être effectué dans le cas d'espace-temps plus généraux. Mais il est possible de les découpler autrement, en utilisant la jauge "fantôme" (phantom gauge). Cependant dans ce cas, nous ne pouvons pas faire certaines hypothèses qui conduisent à la preuve.

Cet article a été publié dans *General Relativity and Gravitation* [68].

General Relativity and Gravitation (2020) 52:82
https://doi.org/10.1007/s10714-020-02737-4

RESEARCH ARTICLE

Analytical proof of the isospectrality of quasinormal modes for Schwarzschild-de Sitter and Schwarzschild-Anti de Sitter spacetimes

Flora Moulin[1] · **Aurélien Barrau**[1]

Received: 2 April 2020 / Accepted: 28 August 2020

Abstract

The deep reason why the equations describing axial and polar perturbations of Schwarzschild black holes have the same spectrum is far from trivial. In this article, we revisit the original proof and try to make it clearer. Still focusing on uncharged and non-rotating black holes, we extend the results to spacetimes including a cosmological constant, which have so far mostly been investigated numerically from this perspective.

Keywords Black holes · Quasinormal modes · General relativity · Gravitational waves · Isospectrality

Contents

Aurélien Barrau
barrau@in2p3.fr

[1] Laboratoire de Physique Subatomique et de Cosmologie, CNRS/IN2P3, Université Grenoble-Alpes, 53, avenue des Martyrs, 38026 Grenoble Cedex, France

Published online: 01 September 2020

1 Introduction

The direct measurement of gravitational waves emitted by the coalescence of black holes (BHs) is now possible. Since the seminal detection by LIGO [1], several other events were recorded and a catalogue is already available [2]. The recent improvement in sensitivity has even led to a dramatic increase in the detection rate. The recorded gravitational waves carry fundamental informations about the structure of spacetime, BHs being vacuum solutions of the Einstein field equations. Three phases can be distinguished during a coalescence: the inspiral, the merger and the ringdown. The later can be partially treated perturbatively as a superposition of damped oscillations with different complex frequencies, called quasinomal modes (QNMs). An intuitive introduction can be found in [3] and a review in [4]. The ringdown does not lead to pure "normal" modes because the system looses energy through the emission of gravitational waves. The equations for the metric perturbations are somehow unusual because of their boundary conditions: the waves have to be purely outgoing at infinity and purely ingoing at the event horizon. The radial part can schematically be written as $\phi \propto e^{-i\omega t} = e^{-i(\omega_R + i\omega_I)t}$ where ω_R is proportional to the frequency and ω_I is the inverse of the decaying time scale. The process is stable when $\omega_I < 0$. Basically, QNMs are characterized by their overtone and multipole numbers: n and ℓ.

The determination of QNMs have driven a huge amount of efforts (see, *e.g.*, [5] for a historical review, [6,7] for an example of quite recent results based on a numerical approach and [8–14] for WKB treatments). This article is not about the calculation of the complex frequencies but about a remarkable—and quite strange—property. The perturbations of the metric are described by two different equations depending on their parity: whether polar or axial, they do not fulfill the same equation. They both obey a Schrödinger-like equation (Eq. 7) but with different potentials. For a spherical time-independent metric, one can write

$$\begin{aligned} ds^2 = {} & e^{2\mu_t} dt^2 - e^{2\psi}(d\phi - q_t dt - q_r dr - q_\theta d\theta)^2 \\ & - e^{2\mu_r} dr^2 - e^{2\mu_\theta} d\theta^2. \end{aligned} \tag{1}$$

For the special case such that

$$e^{2\mu_t} = e^{-2\mu_r} = B(r), \quad e^{2\mu_\theta} = r^2, \tag{2}$$

$$e^{2\psi} = r^2 sin^2(\theta) \quad \text{and} \quad q_t = q_r = q_\theta = 0, \tag{3}$$

the perturbations will be described by q_t, q_r and q_θ, being first order small quantities, and μ_t, μ_r, μ_θ, and ψ which receive small increments $\delta\mu_t$, $\delta\mu_r$, $\delta\mu_\theta$ and $\delta\psi$. The former lead to a non-static stationary distribution of mass-energy leading to a rotating BH. They are called the axial perturbations. The latter do not imply any rotation and are called the polar perturbations.

In the Schwarzschild case, the Regge-Wheeler potential (for the axial parity) is given by

$$V_\ell^{\mathrm{RW}}(r) = \left(1 - \frac{2M}{r}\right)\left[\frac{\ell(\ell+1)}{r^2} - \frac{6M}{r^3}\right], \tag{4}$$

and the Zerilli potential (for the polar parity) reads

$$V_\ell^Z(r) = \frac{2}{r^3}\left(1-\frac{2m}{r}\right)\times\frac{9M^3+3L^2Mr^2+L^2(1+L)r^3+9M^2Lr}{(3M+Lr)^2}, \tag{5}$$

with $L = \ell(\ell+1)/2-1$. The remarquable fact—known as isospectrality—is that those equations share the same spectrum of quasinormal modes. This is also true for the Reissner-Nordström and Kerr metrics. This might appear as a kind of "miracle" when using the standard tensor formalism where the axial and polar perturbations are teated independently. However, when one actually works in the Newmann–Penrose (NP) formalism [15], isospectrality comes as a quite natural feature. This property remains however true only for very specific spacetimes. It is not yet fully clear whether isospectrality is generic or happens as an incredible "stroke of luck" for classical BHs.

In [16], it was shown that isospectrality is broken down for general $f(R)$ gravity. In the case of Lovelock black holes, isospectrality is roughly recovered but not exactly [17]. It fails in Chern-Simons gravity [18]. The presence of a dilatonic field also breaks isospectrality [19,20]. Actually, a perturbative analysis shows that isospectrality seems to be quite generically lost in theories beyond GR [21]. However, it seems that Schwarzschild-(anti)-de-Sitter (S(A)dS) black holes are isospectral, although the situation is not fully clear [22–25].

In this article, we try to make clearer the quite involved historical derivation by Chandrasekhar [26] and extend it as far as it can be using the original argument. Although no spectacular new results is obtained, we elegantly end up with an analytical explanation of the isospectrality of SdS and SAdS black holes. We begin with a general metric of the form

$$ds^2 = B(r)dt^2 - B(r)^{-1}dr^2 - r^2d\Omega^2, \tag{6}$$

and explicitly show that if $B(r)$ describes a SdS or SAdS spacetime, the isospectrality property holds. This does not rigorously mean that it is a necessary condition in general but it is one if we rely on the historical strategy to approach isospectrality. The proof can be straightforwardly extended to the case of a charged BHs (the steps are the same than for going from Schwarzschild to Reissner-Nordström).

Our aim here is just to slightly generalize the original derivation and to explain in details each step of the proof. This is mainly useful for pedagogical, methodological and historical purposes. Modern and extremely efficient methods are given in [27,28]. In these references, new results are obtained on the isospectrality, traced back to the fact that the Zerilli and Regge-Wheeler equations are related by a Darboux transformation. More precisely, it is shown that although standard and binary Darboux transformations ensure isospectrality, generalized ones—associated with long-range potentials—do not solve exactly the problem. Such methods are powerful and well suited for most complex problems. They also open fascinating mathematical questions that are still unanswered. We however will not use them here and will remain close to the original derivation. The small generalization that we provide is already non-trivial.

In the first section, we review sufficient conditions for isospectrality. Then, we introduce the NP formalism which will be used to determine the radial equation. We finally proceed to the full calculation and conclude.

2 Conditions for isospectrality

To study black hole perturbations, we separate the radial and angular parts so as to obtain a wave equation for radial and time variables. This equation has a Schrödinger-like form:

$$\frac{d^2Z}{dr^{*2}} + \omega^2 Z - VZ = 0, \tag{7}$$

with r_* the tortoise coordinate defined by $dr_* = dr/B(r)$. The eigenvalue ω is the frequency of the wave satisfying the boundary conditions given in the introduction and detailed in the following sections. In full generality, if Z_2 satisfies Eq. (7) with a potential V_2, then

$$Z_1 = pZ_2 + q\frac{dZ_2}{dr^*}, \tag{8}$$

with p and q two functions, also satisfies Eq. (7) with V_1 if [26]

$$V_1 = V_2 + \frac{2}{q}\frac{dp}{dr^*} + \frac{1}{q}\frac{d^2q}{dr^{*2}}, \tag{9}$$

and

$$2p\frac{dp}{dr^*} + p\frac{d^2q}{dr^{*2}} - \frac{d^2p}{dr^{*2}}q - 2q\frac{dq}{dr^*}(V_2 - \omega^2) - q^2\frac{dV_2}{dr^*} = 0. \tag{10}$$

We don't use here an index for ω as the isopectrality precisely means that $\omega_1 = \omega_2$. Equation (10) is equivalent to

$$p^2 + \left(p\frac{dq}{dr^*} - \frac{dp}{dr^*}q\right) - q^2(V_2 - \omega^2) = C^2 = \text{cte}. \tag{11}$$

To show that Eqs. (9) and (10) imply isospectrality, we use the fact that Z_2 satisfies Eq. (7), which implies

$$\frac{d^3Z_2}{dr^{*3}} + \omega^2\frac{dZ_2}{dr^*} - \frac{dV_2}{dr^*}Z_2 - V_2\frac{dZ_2}{dr^*} = 0. \tag{12}$$

When replacing Z_1 and V_1 by their expressions given by Eqs. (8) and (9), we are led to

$$\frac{d^2Z_1}{dr^{*2}}+\omega^2 Z_1 - V_1 Z_1 = \left(\frac{d^2p}{dr^{*2}} - \frac{2p}{q}\frac{dp}{dr^*} - \frac{p}{q}\frac{d^2q}{dr^{*2}}\right)Z_2 + q\frac{dV_2}{dr^*}Z_2 + 2\frac{dq}{dr^*}\frac{d^2Z_2}{dr^{*2}}. \tag{13}$$

Using Eqs. (10) and (12), one can conclude that Z_1 satisfies Eq. (7) with V_1.

We first establish the equations governing the gravitational perturbations, we then expose the conditions required to transform it into a wave equation. Finally, we show isospectrality for SdS and SAdS spacetimes by finding the functions p and q satisfying Eqs. (9) and (11) for the potentials of axial and polar perturbations. It should be emphasized that we do not assume a S(A)dS spacetime from the beginning but, instead, are led to it by the requirement that isospectrality emerges—at least in this approach.

3 The Newman–Penrose formalism

To go ahead, the perturbations need to be analyzed in the NP formalism [15]. This is a special case of the tetrad formalism (see, *e.g.*, [29]). To guide the unfamiliar reader, we make every step leading to the result explicit in a pedagogical perspective. In this approach, one needs to set up a basis of four null vectors at each point of spacetime. This basis is made of a pair of real null vectors $\mathbf{l}$ and $\mathbf{n}$ and a pair of complex conjugate null vectors $\mathbf{m}$ and $\overline{\mathbf{m}}$:

$$\mathbf{l}.\mathbf{l} = \mathbf{n}.\mathbf{n} = \mathbf{m}.\mathbf{m} = \overline{\mathbf{m}}.\overline{\mathbf{m}} = 0. \tag{14}$$

Furthermore, these vectors satisfy the following orthogonality relations:

$$\mathbf{l}.\mathbf{m} = \mathbf{l}.\overline{\mathbf{m}} = \mathbf{n}.\mathbf{m} = \mathbf{n}.\overline{\mathbf{m}} = 0. \tag{15}$$

We also require the normalization

$$\mathbf{l}.\mathbf{n} = 1 \ \text{ and } \ \mathbf{m}.\overline{\mathbf{m}} = -1, \tag{16}$$

but this latter condition is less crucial in the NP formalism. The number of equations is conveniently reduced thanks to the use of complex numbers. Any basis with the properties given by Eqs. (14), (15) and (16) can be considered. For example, in the Schwarzschild case one usually works with the Kinnersley tetrad and sometimes the Carter one [30]. Here, we choose a Kinnersley-like tetrad:

$$l^i = \left(\frac{1}{B(r)}, 1, 0, 0\right), \tag{17}$$

$$n^i = \left(\frac{1}{2}, -\frac{B(r)}{2}, 0, 0\right), \tag{18}$$

$$m^i = \left(0, 0, \frac{1}{\sqrt{2}r}, \frac{i}{\sqrt{2}r\sin\theta}\right), \tag{19}$$

$$\overline{m}^i = \left(0, 0, \frac{1}{\sqrt{2}r}, \frac{-i}{\sqrt{2}sin\theta}\right). \tag{20}$$

In the NP formalism, the directional derivatives are usually denoted by the following symbols:

$$D = l^i\,\partial_i; \quad \Delta = n^i\,\partial_i; \quad \delta = m^i\,\partial_i; \quad \delta^* = \overline{m}^i\,\partial_i. \tag{21}$$

The equations will be written with the so-called spin coefficients [31] carrying (roughly speaking) the information on the Riemann tensor. To make things explicit, we switch, here, to the more general framework of the standard tetrad formalism. The four contravariant vectors of the basis are e^i_a, where a, b, c …are the tetrad indices, indicating the considered vector and i, j, k …are the tensor indices, indicating the considered componant (alternatively, one can also think to the lower index as an internal Lorentz one and consider the upper index as a coordinate one). The correspondance reads as $\boldsymbol{e_1} = \boldsymbol{l}$, $\boldsymbol{e_2} = \boldsymbol{n}$, $\boldsymbol{e_3} = \boldsymbol{m}$ and $\boldsymbol{e_4} = \overline{\boldsymbol{m}}$ with $\boldsymbol{e^1} = \boldsymbol{e_2}$, $\boldsymbol{e^2} = \boldsymbol{e_1}$, $\boldsymbol{e^3} = -\boldsymbol{e_4}$ and $\boldsymbol{e^4} = -\boldsymbol{e_3}$. For example, $e_{12,3}$ represents the second componant of $\mathbf{l}$, derived with respect to θ. We define the Ricci rotation coefficients (the symbol ";" referring to a covariant derivative)

$$\gamma_{cab} = e^k_c e_{ak;i} e^i_b, \tag{22}$$

or equivalently

$$e_{ak;i} = e^c_k \gamma_{cab} e^b_i. \tag{23}$$

These coefficients are antisymmetric with respect to the first pair of indices:

$$\gamma_{cab} = -\gamma_{acb}. \tag{24}$$

Let $\mathbf{X}$,$\mathbf{Y}$and $\mathbf{Z}$ be contravariant vector fields: $\mathbf{X}$,$\mathbf{Y}$, $\mathbf{Z} \in T^1_0$. The Riemann tensor field $\mathbf{R}$ is of type (1, 3):

$$\mathbf{R} : T^1_0 \times T^1_0 \times T^1_0 \to T^1_0. \tag{25}$$

It is defined as

$$\mathbf{R}(\mathbf{X}, \mathbf{Y})\mathbf{Z} = \nabla_{\mathbf{X}}\nabla_{\mathbf{Y}}\mathbf{Z} - \nabla_{\mathbf{Y}}\nabla_{\mathbf{X}}\mathbf{Z}, \tag{26}$$

with the Ricci identity

$$R^i_{jkl} Z_i = Z_{j;k;l} - Z_{j;l;k}. \tag{27}$$

This leads, for $Z = e_a$, to

$$R_{ijkl}e^i_a = e_{aj;k;l} - e_{aj;l;k}. \tag{28}$$

We project this identity on the tetrad frame and use Eqs. (22), (23) and (24). The projected Riemann tensor depends only on the rotation coefficients and their derivatives:

$$\begin{aligned} R_{abcd} &= R_{ijkl}e^i_a e^j_b e^k_c e^l_d \\ &= [e_{aj;k;l} - e_{aj;l;k}]e^j_b e^k_c e^l_d \\ &= \Big(- [\gamma_{afg}e^f_j e^g_k]_{;l} + [\gamma_{afg}e^f_j e^g_l]_{;k} \Big) e^j_b e^k_c e^l_d \\ &= -\gamma_{abc,d} + \gamma_{abd,c} + \gamma_{baf}(\gamma_c{}^f_d - \gamma_d{}^f_c) \\ &\quad + \gamma_{fac}\gamma_b{}^f_d - \gamma_{fad}\gamma_b{}^f_c. \end{aligned} \tag{29}$$

The spin coefficients of the NP formalism are also defined through the rotation coefficients:

$$\begin{aligned} \kappa = \gamma_{311}, \quad \rho = \gamma_{314}, \quad \epsilon = \frac{1}{2}(\gamma_{211} + \gamma_{341}), \\ \sigma = \gamma_{313}, \quad \mu = \gamma_{243}, \quad \gamma = \frac{1}{2}(\gamma_{212} + \gamma_{342}), \\ \lambda = \gamma_{244}, \quad \tau = \gamma_{312}, \quad \alpha = \frac{1}{2}(\gamma_{214} + \gamma_{344}), \\ \nu = \gamma_{242}, \quad \pi = \gamma_{241}, \quad \beta = \frac{1}{2}(\gamma_{213} + \gamma_{343}). \end{aligned}$$

The 36 equations (29) can be written as 18 complex equations. The 10 independent components of the Weyl tensor C_{abcd} are represented by five complex scalars:

$$\begin{aligned} \Psi_0 &= -C_{1313} = -C_{pqrs}l^p m^q l^r m^s, \\ \Psi_1 &= -C_{1213} = -C_{pqrs}l^p n^q l^r m^s, \\ \Psi_2 &= -C_{1342} = -C_{pqrs}l^p m^q \overline{m}^r n^s, \\ \Psi_3 &= -C_{1242} = -C_{pqrs}l^p n^q \overline{m}^r n^s, \\ \Psi_4 &= -C_{2424} = -C_{pqrs}n^p \overline{m}^q n^r \overline{m}^s, \end{aligned} \tag{30}$$

and the 20 linearly independent Bianchi identities can be written as eight complex and four real equations. As it will be useful later we also define the following scalars:

$$\begin{aligned} &\Phi_{00} = -\tfrac{1}{2}R_{11}; \quad \Phi_{22} = -\tfrac{1}{2}R_{22}; \quad \Phi_{02} = -\tfrac{1}{2}R_{33}; \\ &\Phi_{20} = -\tfrac{1}{2}R_{44}; \quad \Phi_{11} = -\tfrac{1}{4}(R_{12} + R_{34}); \quad \Phi_{01} = -\tfrac{1}{2}R_{13}; \\ &\Phi_{10} = -\tfrac{1}{2}R_{14}; \quad \Phi_{12} = -\tfrac{1}{2}R_{23}; \quad \Phi_{21} = -\tfrac{1}{2}R_{24}. \end{aligned} \tag{31}$$

4 Preliminaries on isospectrality

4.1 Derivation of the radial equation

We assume that the perturbations have a t and ϕ dependance given by $e^{i(\omega t+m\phi)}$ and we define the following operators (n being an integer):

$$\mathcal{D}_n = \partial_r + \frac{i\omega}{B(r)} + n\left(\frac{B'(r)}{B(r)} + \frac{2}{r}\right), \tag{32}$$

and

$$\mathcal{L}_n = \partial_\theta + \frac{m}{\sin(\theta)} + n.\cot(\theta). \tag{33}$$

The prime denotes the derivative with respect to r. Let $\mathcal{D}_n^\dagger$ be the complex conjugate of $\mathcal{D}_n$ and $\mathcal{L}_n^\dagger(\theta) = -\mathcal{L}_n(\pi-\theta)$. It is interesting to notice that

$$Br^2\mathcal{D}_{n+1} = \mathcal{D}_n Br^2. \tag{34}$$

The directional derivative given by Eq. (21) reads

$$\begin{aligned} D &= \mathcal{D}_0, \qquad \Delta = -\frac{B(r)}{2}\mathcal{D}_0^\dagger, \\ \delta &= \frac{1}{\sqrt{2}r}\mathcal{L}_0^\dagger, \qquad \delta^* = \frac{1}{\sqrt{2}r}\mathcal{L}_0. \end{aligned} \tag{35}$$

The five scalars are:

$$\Psi_2 = \frac{-2+2B(r)-2rB'(r)+r^2B''(r)}{12r^2}, \tag{36}$$

$$\Psi_0 = \Psi_1 = \Psi_3 = \Psi_4 = 0. \tag{37}$$

As Ψ_0, Ψ_1, Ψ_3 and Ψ_4 vanish but Ψ_2 doesn't, the spacetime defined by Eq. (72) is a Petrov type D spacetime. A corollary of the Goldberg-Sachs theorem [32] shows that this implies that κ, σ, λ, and ν do vanish. The explicit calculation indeed leads to:

$$\kappa = \sigma = \lambda = \nu = 0, \tag{38}$$

$$\tau = \pi = \epsilon = 0 \tag{39}$$

and

$$\begin{aligned} \rho = -\tfrac{1}{r}, \quad \mu = -\tfrac{B}{2r}, \quad \gamma = \tfrac{B'}{4}, \\ \alpha = -\beta = -\tfrac{\cot\theta}{2\sqrt{2}r}. \end{aligned} \tag{40}$$

There are 6 linearized equations, 2 from the Ricci identities (43,46) and 4 from the Bianchi identities (41,42,44, 45):

$$(\delta^* - 4\alpha)\Psi_0 - (D - 4\rho)\Psi_1 = 3\kappa\Psi_2 + [R_1], \tag{41}$$
$$(\Delta - 4\gamma + \mu)\Psi_0 - (\delta + 2\alpha)\Psi_1 = 3\sigma\Psi_2 + [R_2], \tag{42}$$
$$(D - 2\rho)\sigma - (\delta + 2\alpha)\kappa = \Psi_0, \tag{43}$$

and

$$(D - \rho)\Psi_4 - (\delta^* + 2\alpha)\Psi_3 = -3\lambda\Psi_2 + [R_3], \tag{44}$$
$$(\delta - 4\alpha)\Psi_4 - (\Delta + 2\gamma + 4\mu)\Psi_3 = -3\nu\Psi_2 + [R_4], \tag{45}$$
$$(\Delta + 2\mu + 2\gamma)\lambda - (\delta^* + 2\alpha+)\nu = -\Psi_4, \tag{46}$$

with

$$\begin{aligned}[R_1] &= -D\Phi_{01} + \delta\Phi_{00} + 2\rho\Phi_{01} + 2\sigma\Phi_{10} - 2\kappa\Phi_{11} - \kappa\Phi_{02} \\ &= \tfrac{\kappa}{4r^2}[2 - 2B(r) + r^2B''(r)] \end{aligned} \tag{47}$$
$$\begin{aligned}[R_2] &= -D\Phi_{02} + \delta\Phi_{01} + 2\alpha\Phi_{01} - 2\kappa\Phi_{12} - \lambda\Phi_{00} + 2\sigma\Phi_{11} + \rho\Phi_{02} \\ &= \tfrac{-\sigma}{4r^2}[2 - 2B(r) + r^2B''(r)] \end{aligned} \tag{48}$$
$$\begin{aligned}[R_3] &= -\Delta\Phi_{02} + \delta^*\Phi_{21} + 2\alpha\Phi_{21} + 2\nu\Phi_{10} + \sigma\Phi_{22} - 2\lambda\Phi_{11} - \mu\Phi_{20} \\ &= \tfrac{\lambda}{4r^2}[2 - 2B(r) + r^2B''(r)] \end{aligned} \tag{49}$$
$$\begin{aligned}[R_4] &= \Delta\Phi_{21} - \delta^*\Phi_{22} + 2(\mu + \gamma)\Phi_{21} - 2\nu\Phi_{11} - \nu\Phi_{20} + 2\lambda\Phi_{12} \\ &= \tfrac{\nu}{4r^2}[2 - 2B(r) + r^2B''(r)], \end{aligned} \tag{50}$$

where Ψ_0, Ψ_1, Ψ_3, Ψ_4, κ, σ, λ, and ν are the perturbations. Using Eqs. (36), (38) and (40), we obtain:

$$\frac{1}{r\sqrt{2}}\left(\mathcal{L}_0 + 2\cot\theta\right)\Psi_0 - \left(\mathcal{D}_0 + \frac{4}{r}\right)\Psi_1 = 3\kappa\Psi_2 + [R_1], \tag{51}$$
$$\begin{aligned}&-\frac{B}{2}\left(\mathcal{D}_0^\dagger + \frac{2B'}{B} + \frac{1}{r}\right)\Psi_0 - \frac{1}{r\sqrt{2}}\left(\mathcal{L}_0^\dagger - \cot\theta\right)\Psi_1 \\ &= 3\sigma\Psi_2 + [R_2], \end{aligned} \tag{52}$$
$$\left(\mathcal{D}_0 + \frac{2}{r}\right)\sigma - \frac{1}{r\sqrt{2}}\left(\mathcal{L}_0^\dagger - \cot\theta\right)\kappa = \Psi_0, \tag{53}$$
$$\left(\mathcal{D}_0 + \frac{1}{r}\right)\Psi_4 - \frac{1}{r\sqrt{2}}\left(\mathcal{L}_0 - \cot\theta\right)\Psi_3 = -3\Psi_2\lambda + [R_3], \tag{54}$$
$$\begin{aligned}&\frac{1}{r\sqrt{2}}\left(\mathcal{L}_0^\dagger + 2\cot\theta\right)\Psi_4 + \frac{B}{2}\left(\mathcal{D}_0^\dagger - \frac{B'}{B} + \frac{4}{r}\right)\Psi_3 \\ &= -3\Psi_2\nu + [R_4], \end{aligned} \tag{55}$$

$$-\frac{B}{2}\left(\mathcal{D}_0^\dagger - \frac{B'}{B} + \frac{2}{r}\right)\lambda - \frac{1}{r\sqrt{2}}\left(\mathcal{L}_0 - \cot\theta\right)\nu = \Psi_4. \tag{56}$$

We proceed to the following change of variables:

$$\Phi_0 = \Psi_0, \quad \Phi_1 = \Psi_1 r\sqrt{2}, \quad k = \frac{\kappa}{r^2\sqrt{2}}, \quad s = \frac{\sigma}{r}, \tag{57}$$

$$\Phi_4 = \Psi_4 r^4, \quad \Phi_3 = \Psi_3\frac{r^3}{\sqrt{2}}, \quad l = \frac{\lambda r}{2}, \quad n = \frac{\nu r^2}{\sqrt{2}}. \tag{58}$$

This leads to:

$$\mathcal{L}_2\Phi_0 - \left(\mathcal{D}_0 + \frac{3}{r}\right)\Phi_1 = 6r^3\Psi_2 k + \sqrt{2}r[R_1], \tag{59}$$

$$Br^2\left(\mathcal{D}_2^\dagger - \frac{3}{r}\right)\Phi_0 + \mathcal{L}_{-1}^\dagger\Phi_1 = -6r^3\Psi_2 s - 2r^2[R_2], \tag{60}$$

$$\left(\mathcal{D}_0 + \frac{3}{r}\right)s - \mathcal{L}_{-1}k = \frac{\Phi_0}{r}, \tag{61}$$

$$\left(\mathcal{D}_0 - \frac{3}{r}\right)\Phi_4 - \mathcal{L}_{-1}\Phi_3 = -6r^3\Psi_2 l + r^4[R_3], \tag{62}$$

$$\mathcal{L}_2^\dagger\Phi_4 + \frac{Br^2}{2}\left(\mathcal{D}_{-1}^\dagger + \frac{3}{r}\right)\Phi_3 = -6r^3\Psi_2 n + \sqrt{2}r^5[R_4], \tag{63}$$

$$Br^2\left(\mathcal{D}_{-1}^\dagger + \frac{3}{r}\right)l + \mathcal{L}_{-1}n = \frac{\Phi_4}{r}. \tag{64}$$

By applying $\mathcal{L}_{-1}^\dagger$ to Eq. (59) and $\left(\mathcal{D}_0 + \frac{3}{r}\right)$ to Eq. (60), we are then led to:

$$\begin{aligned}\mathcal{L}_{-1}^\dagger\mathcal{L}_2\Phi_0 + \left(\mathcal{D}_0 + \frac{3}{r}\right)\left[Br^2\left(\mathcal{D}_2^\dagger - \frac{3}{r}\right)\Phi_0\right] \\ = 6r^3\Psi_2\left[\mathcal{L}_{-1}^\dagger k - \left(\mathcal{D}_0 + \frac{3}{r}\right)s\right] - 6s\,\partial_r(r^3\Psi_2) \\ + \mathcal{L}_{-1}^\dagger(\sqrt{2}r[R_1]) - 2\left(\mathcal{D}_0 + \frac{3}{r}\right)(r^2[R_2]).\end{aligned} \tag{65}$$

It should be noticed that if $r^3\Psi_2$ is a constant and if $[R_1]$ and $[R_2]$ do vanish, then the left part of Eq. (61) does appear and can be replaced by Φ_0/r which leads to a decoupled equation for Φ_0:

$$\mathcal{L}_{-1}^\dagger\mathcal{L}_2\Phi_0 + \left(\mathcal{D}_0 + \frac{3}{r}\right)\left[Br^2\left(\mathcal{D}_2^\dagger - \frac{3}{r}\right)\Phi_0\right] = -6r^2\Psi_2\Phi_0. \tag{66}$$

In the same way, by applying $\mathcal{L}_{-1}$ to Eq. (63) and $Br^2\left(\mathcal{D}^{\dagger}_{-1}+\frac{3}{r}\right)$ to Eq. (62), we can obtain a decoupled equation for Φ_4 if, in addition, $[R_3]$ and $[R_4]$ are zero:

$$Br^2\left(\mathcal{D}^{\dagger}_{-1}+\tfrac{3}{r}\right)\left[\left(\mathcal{D}_0-\tfrac{3}{r}\right)\Phi_4\right]+\mathcal{L}_{-1}\mathcal{L}_2^{\dagger}\Phi_4=-6r^2\Psi_2\Phi_4, \tag{67}$$

where Eq. (64) has also been used. To summarize, one is led to two decoupled equations, for Φ_0 and Φ_4, if:

$$r^3\Psi_2=\text{cte} \tag{68}$$

and

$$[R_1],[R_2],[R_3],[R_4]=0. \tag{69}$$

The first condition, Eq. (68), implies that the metric must have the form

$$B(r)=1+\frac{C_1}{r}+C_2r+C_3r^2, \tag{70}$$

while the second condition, Eq. (69), implies

$$B(r)=1+\frac{D_1}{r}+D_2r^2, \tag{71}$$

with C_i and D_i some arbitrary constants. The latter condition (which contains the previous one) corresponds to Schwarzschild-de Sitter and Schwarzschild-Anti-de Sitter spacetimes:

$$B(r)=1-\frac{2M}{r}-\Lambda r^2, \tag{72}$$

with Λ the cosmological constant.

In the Reissner-Nordström case, it is possible to find new variables that mix the Φ_i functions with the spin coefficients so that a separation is possible [26]. This works because Ψ_1 does not vanish and this implies two more equations which lead to a radial equation of the form of Eq. (87) such that P and Q lead to isospectrality. As far as our argument is concerned, the extension from the Schwarzschild case to the charged case is therefore straightforward.

5 Proof of isospectrality

The Eqs. (66) and (67) read

$$\left[\mathcal{L}^{\dagger}_{-1}\mathcal{L}_2+Br^2\mathcal{D}_1\mathcal{D}_2^{\dagger}-6(\Lambda r+i\omega)r\right]\Phi_0=0, \tag{73}$$

$$\left[\mathcal{L}_{-1}\mathcal{L}_2^\dagger + Br^2\mathcal{D}_{-1}^\dagger\mathcal{D}_0 - 6(\Lambda r - i\omega)r\right]\Phi_4 = 0. \tag{74}$$

If we set

$$\Phi_0 = R_{+2}(r)S_{+2}(\theta), \quad \Phi_4 = R_{-2}(r)S_{-2}(\theta), \tag{75}$$

they are separable with a separation constant μ^2. This leads to:

$$\mathcal{L}_{-1}^\dagger\mathcal{L}_2 S_{+2} = -\mu^2 S_{+2}, \tag{76}$$

$$\left[Br^2\mathcal{D}_1\mathcal{D}_2^\dagger - 6(\Lambda r + i\omega)r\right]R_{+2} = \mu^2 R_{+2}, \tag{77}$$

$$\mathcal{L}_{-1}\mathcal{L}_2^\dagger S_{-2} = -\mu^2 S_{-2}, \tag{78}$$

$$\left[Br^2\mathcal{D}_{-1}^\dagger\mathcal{D}_0 - 6(\Lambda r + i\omega)r\right]R_{-2} = \mu^2 R_{-2}. \tag{79}$$

The separation constant is calculated with Eq. (76)—or Eq. (78)—by requiring the regularity of S_{+2} at $\theta = 0$ and $\theta = \pi$. The angular equation is the same than in the Schwarzschild case, which gives $\mu^2 = l(l+1) - 2 = 2L$.

We set

$$\mathcal{D}_0 = \frac{1}{B}\Lambda_+, \qquad \mathcal{D}_0^\dagger = \frac{1}{B}\Lambda_-. \tag{80}$$

Using the the tortoise coordinate $r*$ (with $\frac{d}{dr^*} = B\frac{d}{dr}$), we are led to

$$\Lambda_+ = \frac{d}{dr^*} + i\omega, \qquad \Lambda_- = \frac{d}{dr^*} - i\omega \quad \text{and} \quad \Lambda^2 = \Lambda_+\Lambda_-, \tag{81}$$

that is

$$\Lambda_\pm = \Lambda_\mp \pm 2i\omega. \tag{82}$$

The operator Λ^2 has no link with the cosmological constant (and cannot be confused with it as the cosmological constant never appears squared in this article). It should be pointed that the equation

$$\left[Br^2\mathcal{D}_{-1}\mathcal{D}_0^\dagger - 6(\Lambda r + i\omega)r\right]B^2r^4R_{+2} = \mu^2 B^2 r^4 R_{+2} \tag{83}$$

is the same than Eq. (77). Using the properties of Eq. (34), we obtain

$$Br^2\mathcal{D}_{-1}\mathcal{D}_0^\dagger = (Br^2)^2\mathcal{D}_0\frac{1}{Br^2}\mathcal{D}_0^\dagger = r^4 B\Lambda_+\left(\frac{1}{B^2r^2}\Lambda_-\right). \tag{84}$$

Defining Y as

$$Y = B^2 r R_{+2}, \tag{85}$$

we are led to

$$\Lambda_+\left(\frac{1}{Br^2}\Lambda_-(r^3 Y)\right) = \frac{r}{B^2}\Lambda^2 Y + \frac{d}{dr^*}\left(\frac{r}{B^2}\right)\Lambda_- Y + \frac{3}{B}\Lambda_+ Y + \frac{d}{dr^*}\left(\frac{3}{B}\right)Y. \tag{86}$$

By calculating the derivative and replacing Λ_+ by $\Lambda_- + 2i\omega$ in Eq. (86), we find that Eq. (83) is equivalent to

$$\Lambda^2 Y + P\Lambda_- Y - QY = 0, \tag{87}$$

with

$$\begin{aligned} P &= \left(\frac{4B}{r} - 2B'\right) \\ &= \frac{B^2}{r^4}\frac{d}{dr^*}\left(\frac{r^4}{B^2}\right) \\ &= \frac{d}{dr^*}\left(\log\left(\frac{r^4}{B^2}\right)\right), \end{aligned} \tag{88}$$

and

$$Q = \left(\frac{3}{r}BB' + 6B\Lambda + \mu^2\frac{B}{r^2}\right). \tag{89}$$

For the same reasons, $Y_{-2} = r^{-3}R_{-2}$, satisfies

$$\Lambda^2 Y_{-2} + P\Lambda_+ Y_{-2} - QY_{-2} = 0. \tag{90}$$

Equation (87) needs to be transformed into a wave equation in one dimension:

$$\Lambda^2 Z = VZ. \tag{91}$$

The functions Y and Z both satisfying a second order equation, we write Y as a linear combination of Z and its derivative:

$$\begin{aligned} Y &= \zeta\Lambda_+\Lambda_+ Z + W\Lambda_+ Z \\ &= \zeta VZ + (W + 2i\omega\zeta)\Lambda_+ Z, \end{aligned} \tag{92}$$

with ζ and W two functions of r^*. Applying Λ_- to Eq. (92) yields

$$\begin{aligned}\Lambda_- Y &= \left[\frac{d}{dr^*}(\zeta V) + WV\right]Z + \left[\zeta V + \frac{d}{dr^*}(W + 2i\omega\zeta)\right]\Lambda_+ Z \\ &= -\gamma\frac{B^2}{r^4}Z + R\Lambda_+ Z,\end{aligned} \tag{93}$$

with

$$R = \zeta V + \frac{d}{dr^*}(W + 2i\omega\zeta), \tag{94}$$

$$\gamma = -\frac{r^4}{B^2}\left(\frac{d}{dr^*}(\zeta V) + WV\right). \tag{95}$$

By applying again Λ_- to Eq. (93), we obtain

$$\Lambda_-\Lambda_- Y = \left[-\gamma\frac{B^2}{r^4} + \frac{dR}{dr^*}\right]\Lambda_+ Z + \left[2i\omega\gamma\frac{B^2}{r^4} - \frac{d\gamma}{dr^*}\frac{B^2}{r^4} - \gamma\frac{d}{dr*}\left(\frac{B^2}{r^4}\right) + RV\right]Z. \tag{96}$$

On the other hand, one can notice that Eq. (87) leads to:

$$\begin{aligned}\Lambda_-\Lambda_- Y = -(P + 2i\omega)\Lambda_- Y + QY &= \left[-(P + 2i\omega)R + Q(W + 2i\omega\zeta)\right]\Lambda_+ Z \\ &+ \left[(P + 2i\omega)\frac{\gamma B^2}{r^4} + Q\zeta V\right]Z.\end{aligned} \tag{97}$$

Identifying Eqs. (96) and (97), and by using the definition of P given by Eq. (88), we find:

$$\begin{aligned}&-\frac{d\gamma}{dr^*}\frac{B^2}{r^4} - \gamma\frac{d}{dr*}\left(\frac{B^2}{r^4}\right) + RV \\ &= \frac{d}{dr^*}\left(\log\left(\frac{r^4}{B^2}\right)\right)\frac{\gamma B^2}{r^4} + Q\zeta V \\ &= -\gamma\frac{d}{dr^*}\left(\frac{B^2}{r^4}\right) + Q\zeta V,\end{aligned} \tag{98}$$

which gives

$$-\frac{d\gamma}{dr^*}\frac{B^2}{r^4} = (Q\zeta - R)V, \tag{99}$$

and

$$\frac{dR}{dr^*} - \frac{B^2}{r^4}\gamma = Q(W + 2i\omega\zeta) - (P + 2i\omega)R, \tag{100}$$

$$\frac{r^4}{B^2}\frac{dR}{dr*}+\frac{r^4}{B^2}\frac{d}{dr*}\left(\log\left(\frac{r^4}{B^2}\right)\right)R=$$
$$\gamma+\frac{r^4}{B^2}Q(W+2i\omega\zeta)-2i\omega\frac{r^4}{B^2}R, \tag{101}$$
$$\frac{d}{dr*}\left(\frac{r^4}{B^2}R\right)=\gamma+\frac{r^4}{B^2}\left(Q(W+2i\omega\zeta)-2i\omega R\right). \tag{102}$$

The combination $\zeta V\times$ Eq. (102) + $R\times$ Eq. (95) - $\gamma\times$ Eq. (94) - $\frac{r^4}{B^2}(W+2i\omega\zeta)\times$ Eq. (99) leads to

$$\begin{aligned}&\zeta V\frac{d}{dr*}\left(\frac{r^4}{B^2}R\right)+\frac{r^4}{B^2}R\frac{d(\zeta V)}{dr*}\\&+\gamma\frac{d}{dr*}(W+2i\omega\zeta)+(W+2i\omega\zeta)\frac{d\gamma}{dr*}=0,\end{aligned} \tag{103}$$

that is to say

$$\frac{r^4}{B^2}R\zeta V+\gamma(W+2i\omega\zeta)=K=\text{cte}. \tag{104}$$

As we have written Y as a linear combination of Z and Λ_+Z in Eq. (92), it is possible to write Z as a linear combination of Y and Λ_+Y. Using Eqs. (92) and (93):

$$\begin{aligned}KZ&=\frac{r^4}{B^2}R\zeta VZ+\gamma(W+2i\omega\zeta)Z\\&=\frac{r^4}{B^2}RY-\frac{r^4}{B^2}(W+2i\omega\zeta)(\Lambda_-Y+\gamma\frac{B^2}{r^4}Z)\\&\quad+\gamma(W+2i\omega\zeta)Z\\&=\frac{r^4}{B^2}RY-\frac{r^4}{B^2}(W+2i\omega\zeta)\Lambda_-Y,\end{aligned} \tag{105}$$

and

$$\begin{aligned}K\Lambda_+Z&=\frac{r^4}{B^2}R\zeta V\Lambda_+Z+\gamma(W+2i\omega\zeta)\Lambda_+Z\\&=\frac{r^4}{B^2}\zeta V\Lambda_-Y+\frac{r^4}{B^2}\zeta V\gamma\frac{B^2}{r^4}Z+\gamma Y-\gamma\zeta VZ\\&=\frac{r^4}{B^2}\zeta V\Lambda_-Y+\gamma Y.\end{aligned} \tag{106}$$

By requiring $\gamma=\text{cte}$ and $\zeta=1$, Eq. (99) leads to

$$R=Q, \tag{107}$$

and from Eq. (94) one obtains

$$V = Q - \frac{dW}{dr^*}. \tag{108}$$

Equation (102) then leads to

$$\frac{d}{dr^*}\left(\frac{r^4}{B^2}R\right) = \gamma + \frac{r^4}{B^2}QW, \tag{109}$$

and Eq. (104) yields

$$\frac{r^4}{B^2}QV + \gamma W = K - 2i\omega\gamma = \kappa = \text{cte}. \tag{110}$$

Defining

$$F \equiv \frac{r^4}{B^2}Q, \tag{111}$$

Equations (109) and (110) lead to

$$W = \frac{1}{F}\left(\frac{dF}{dr^*} - \gamma\right), \tag{112}$$

and

$$FV + \gamma W = F\left(Q - \frac{dW}{dr^*}\right) + \gamma W = \kappa, \tag{113}$$

$$FQ - F\frac{d}{dr^*}\left[\frac{1}{F}\frac{dF}{dr^*} - \frac{\gamma}{F}\right] + \frac{\gamma}{F}\left(\frac{dF}{dr^*} - \gamma\right) = \kappa, \tag{114}$$

which gives

$$\frac{1}{F}\left(\frac{dF}{dr^*}\right)^2 - \frac{d^2F}{dr^{*2}} + \frac{B^2}{r^4}F^2 = \frac{\gamma^2}{F} + \kappa. \tag{115}$$

There exist constants γ and κ such that Eq. (115) is satisfied by the function (111). Depending on the square root of γ^2 chosen ($-\gamma$ or $+\gamma$), one is led to the equation for axial or polar perturbations. With

$$W^{\pm} = \frac{1}{F}\left(\frac{dF}{dr^*} \mp \gamma\right), \tag{116}$$

then

$$V^{\pm} = Q - \frac{d}{dr^*}\left(\frac{1}{F}\frac{dF}{dr} \mp \gamma\right). \tag{117}$$

Defining $f \equiv \frac{1}{F}$,

$$V^{\pm} = \pm\gamma \frac{df}{dr^*} + \gamma^2 f^2 + \kappa f, \tag{118}$$

and

$$Y = V^{\pm} Z^{\pm} + (W^{\pm} + 2i\omega)\Lambda_+ Z^{\pm}, \tag{119}$$

$$\Lambda_- Y = \mp\gamma \frac{B^2}{r^4} Z^{\pm} + Q\Lambda_+ Z^{\pm}, \tag{120}$$

$$K^{\pm} = \kappa \pm 2i\omega\gamma, \tag{121}$$

$$K^{\pm} Z^{\pm} = \frac{r^4}{B^2}[QY - (W^{\pm} + 2i\omega)\Lambda_- Y], \tag{122}$$

$$K^{\pm}\Lambda_+ Z^{\pm} = \frac{r^4}{B^2} V^{\pm}\Lambda_- Y \pm \gamma Y. \tag{123}$$

By inserting Eqs. (119) and (120) in Eq. (122), one obtains

$$\begin{aligned} K^- Z^- &= \frac{r^4}{B^2}\Bigg[Q[V^+ Z^+ + (W^+ + 2i\omega)\Lambda_+ Z^+] \\ &\quad - (W^- + 2i\omega)[-\gamma \frac{B^2}{r^4} Z^+ + Q\Lambda_+ Z^+]\Bigg] \\ &= \left[\frac{r^4}{B^2} QV^+ + \gamma(W^+ + 2i\omega) - \gamma(W^+ - W^-)\right] Z^+ \\ &\quad + F[W^+ - W^-]\Lambda_+ Z^+, \end{aligned} \tag{124}$$

which simplifies to

$$(\kappa - 2i\omega\gamma) Z^- = (\kappa + 2\gamma^2 f) Z^+ - 2\gamma \frac{dZ^+}{dr^*}. \tag{125}$$

Equivalently, one can show that

$$(\kappa + 2i\omega\gamma) Z^+ = (\kappa + 2\gamma^2 f) Z^- + 2\gamma \frac{dZ^-}{dr^*}. \tag{126}$$

By identification with the previously given condition we are led to

$$q = 2\gamma \quad \text{and} \quad p = \kappa + 2\gamma^2 f. \tag{127}$$

Conditions given by Eqs. (8), (9) and (10) are therefore respected. In [26], it is shown that if ω is a characteristic frequency and $Z^-(\omega)$ is a solution belonging to it, then the solution $Z^+(\omega)$ in accordance with the relation (126), will satisfy the

boundary conditions of the quasi normal modes:

$$Z^{\pm} \to A^{\pm}(\omega)e^{-i\omega r} \quad (r_* \to +\infty) \tag{128}$$

$$\to \quad e^{+i\omega r_*} \quad (r_* \to -\infty) \tag{129}$$

with

$$A^{+}(\omega) = A^{-}(\omega)\frac{\kappa - 2i\omega\gamma}{\kappa + 2i\omega\gamma}. \tag{130}$$

The values of κ and γ when the metric function $B(r)$ is defined by (72) now need to be determined. First, one can notice that:

$$-F\left(\frac{d^2}{dr^{*2}}\log F\right) = \frac{1}{F}\left(\frac{dF}{dr^*}\right)^2 - \frac{d^2F}{dr^{*2}}, \tag{131}$$

which implies that Eq. (115) reads as

$$-F\left[\frac{d^2}{dr^{*2}}\left(\log F\right) - \frac{B^2}{r^4}F\right] = \frac{\gamma^2}{F} + \kappa. \tag{132}$$

Moreover, F is given by

$$F = \frac{r}{B}(\mu^2 r + 6M). \tag{133}$$

This leads to

$$\frac{B}{F}\frac{dF}{dr} = \frac{\mu^2 r}{F} + \frac{1}{r} - \frac{4M}{r^2} + \Lambda r, \tag{134}$$

and

$$\begin{aligned}\frac{d}{dr}\left(\frac{B}{F}\frac{dF}{dr}\right) &= -\frac{1}{r^2} + \frac{8M}{r^3} + \Lambda + \frac{\mu^2}{F}\left(1 - \frac{r}{F}\frac{dF}{dr}\right) \\ &= -\frac{1}{r^2} + \frac{8M}{r^3} + \Lambda + \frac{\mu^2}{FBr^2}\left(2Mr - 2\Lambda r^4 - \frac{\mu^2 r^4}{F}\right),\end{aligned} \tag{135}$$

together with

$$\begin{aligned}&-FB\frac{d}{dr}\left(\frac{B}{F}\frac{dF}{dr}\right) + \frac{B^2F^2}{r^4} = \mu^4 + \mu^2 \\ &-\frac{12M^2}{r^2} + \Lambda\mu^2 r^2 + \frac{2M\mu^2}{r} + \frac{6M}{r} - 6M\Lambda r + \frac{\mu^4 r^2}{F} \\ &= \mu^4 + 2\mu^2 + \frac{36M^2}{F}.\end{aligned} \tag{136}$$

Identifying with Eq. (132), this means

$$\gamma^2 = 36M^2 \quad , \quad \kappa = \mu^2(2+\mu^2). \tag{137}$$

The functions p and q are now explicitly given thanks to Eqs. (127) and (137), which proves the isospectrality for a metric such that $B(r)$ satisfies Eq. (72).

The potentials can also be explicitly determined, from Eq. (118), for both perturbations. The axial perturbation are described by:

$$V^- = \left(1 + \frac{2M}{r} + \Lambda r^2\right)\left[\frac{l(l+1)}{r^2} - \frac{6M}{r^3}\right], \tag{138}$$

while the polar perturbations feel the potential

$$V^+ = \frac{2}{r^3}\left(1 + \frac{2M}{r} + \Lambda r^2\right) \times \frac{9M^3 + 3L^2Mr^2 + L^2(1+L)r^3 + 9M^2r(L - \Lambda r^2)}{(Lr+3M)^2}. \tag{139}$$

6 Phantom gauge

In this section, we briefly discuss the Phantom gauge. As we deal with six equations, namely Eqs. (59–64), and eight unknown variables, the solutions involve two arbitrary functions. This comes from the degrees of freedom associated with the rotation of the chosen tetrad. If first order infinitesimal rotations of the tetrad basis are performed, Ψ_0 and Ψ_4 are affected at the second order level while Ψ_1 and Ψ_3 are affected at the first order level (the interested reader can find a clear proof in [26], Chapter 17.(g) or through Eq. (7.79) in [33]). At the linear order which is considered here, Ψ_0 and Ψ_4 are therefore gauge invariant (not affected by infinitesimal rotations), contrarily to Ψ_1 and Ψ_3. We have chosen a gauge such that

$$\Psi_1 = \Psi_3 = 0. \tag{140}$$

The vanishing of Ψ_1 and Ψ_3 does not affect the behavior of Ψ_0 and Ψ_4. This gauge leads to the radial equations (66) and (67) .

Another meaningful choice could have been done: the so-called "Phantom Gauge". The previous gauge was useful to separate the equations when conditions given by Eqs. (68) and (69) were fulfilled. However, if these conditions are not respected it is still possible to obtain two decoupled equations. Thanks to the freedom associated with the rotation of the tetrad, one can impose two additional *ad hoc* constraints. By applying $Br^2\left(\mathcal{D}_2^\dagger - \frac{3}{r}\right)$ to Eq. (59) and $\mathcal{L}_2$ to Eq.(60), it is possible eliminate Φ_0.

Indeed the condition

$$-Br^2\left(\mathcal{D}_2^\dagger - \frac{3}{r}\right)\left(6r^3 k\Psi_2 + \sqrt{2}r[R_1]\right) - \mathcal{L}_2\left(6r^3 s\Psi_2 + 2r^2[R_2]\right) = 6rB'\Phi_1 \tag{141}$$

gives

$$[Br^2\mathcal{D}_2^\dagger\mathcal{D}_0 - 6i\omega r + \mathcal{L}_2\mathcal{L}_{-1}^\dagger]\Phi_1 = 0, \tag{142}$$

and therefore

$$[Br^2\mathcal{D}_2^\dagger\mathcal{D}_0 - 6i\omega r]R_1 = 0. \tag{143}$$

The same procedure can be followed for Φ_3. This gauge might have appeared to be well suited to derive isospectrality for more general metrics, that is beyond the conditions Eqs. (68) and (69) . The radial equation (143) can be written in the form of Eq. (87) with Y defined by

$$Y = rBR_1, \tag{144}$$

as well as P and Q expressed by:

$$P = \frac{d}{dr^*}\log\left(\frac{r^2}{B}\right), \tag{145}$$

and

$$Q = \frac{B}{r^2}(4rB' + r^2B'' + 2B + \mu^2). \tag{146}$$

However, in that case, it seems difficult (if not impossible) to find p and q so that Eq. (9) and Eq. (10) are fulfilled. One could follow the same procedure than previously and replace Eq. (94) and (95) with

$$R_{PG} = \zeta_{PG}V + \frac{d}{dr^*}(W + 2i\omega\zeta_{PG}), \tag{147}$$

$$\gamma_{PG} = -\frac{r^2}{B}\left(\frac{d}{dr^*}(\zeta_{PG}V) + WV\right), \tag{148}$$

where $\frac{r^2}{B}$ appears instead of $\frac{r^4}{B^2}$. Then, Eq. (104) is replaced by

$$\frac{r^2}{B}R_{PG}\zeta_{PG}V + \gamma_{PG}(W + 2i\omega\zeta_{PG}) = K_{PG} = \text{cte}. \tag{149}$$

It is however not anymore possible to require $\gamma_{PG} = \text{cte}$ and $\zeta_{PG} = 1$ as it has been previously done for γ and ζ. Indeed, if $\zeta_{PG} = 1$, then $\gamma_{PG} = \frac{B}{r^2}\gamma$ which cannot be constant. The phantom gauge does not seem to bring any new convenient way to go ahead in this approach.

7 Summary and conclusion

Let us summarize the main ingredients of the calculation. The conditions (68,69) allow to decouple equations (59–61) in the form of Eq. (87) with functions P and Q so that Eq. (104) is fulfilled. These conditions lead to the Schwarzschild-(anti-)de Sitter metric (72). This allows to write $-F\left[\frac{d^2}{dr^{*2}}\left(\log F\right) - \frac{B}{r^4}F\right]$ as $\text{cte} + \frac{\text{cte}'}{F}$, yielding explicit expressions for p and q which show the isospectrality.

In this article, we tried to go a bit deeper into the original argument from Chandrasekhar so as to make it accessible to the reader who wants to apply the method to a specific spacetime structure. We show explicitly what are the conditions to prove isospectrality in this framework. As a result, S(A)dS black holes emerge naturally as being isospectral. This also led us to obtain the exact form of the potential for the polar and axial perturbations.

Isospectrality is a beautiful property which seems to be true only for very specific geometries. As far as we know, no analytical proof of isospectrality (or of the breakdown of isospectrality) as been produced yet in full generality. This article goes slightly beyond Schwarzschild and points out the difficulties one has to face when trying to extend the proof to more general spacetimes.

References

1. Abbott, B.P., et al., (LIGO Scientific, Virgo): Observation of gravitational waves from a binary black hole merger. Phys. Rev. Lett. **116**, 061102 (2016). arxiv:1602.03837
2. Abbott, B.P., et al., (LIGO Scientific, Virgo): GWTC-1: a gravitational-wave transient catalog of compact binary mergers observed by LIGO and Virgo during the first and second observing runs (2018). arxiv:1811.12907
3. Chirenti, C.: Black hole quasinormal modes in the era of LIGO. Braz. J. Phys. **48**, 102 (2018). arXiv:1708.04476
4. Nollert, H.-P.: TOPICAL REVIEW: Quasinormal modes: the characteristic 'sound' of black holes and neutron stars. Class. Quant. Gravity **16**, R159 (1999)
5. Kokkotas, K.D., Schmidt, B.G.: Quasinormal modes of stars and black holes. Living Rev. Relativ. **2**, 2 (1999). arxiv:gr-qc/9909058
6. Berti, E., Cardoso, V., Yoshida, S.: Highly damped quasinormal modes of Kerr black holes: a complete numerical investigation. Phys. Rev. D **69**, 124018 (2004). arXiv:gr-qc/0401052
7. Dorband, E.N., Berti, E., Diener, P., Schnetter, E., Tiglio, M.: A Numerical study of the quasinormal mode excitation of Kerr black holes. Phys. Rev. D **74**, 084028 (2006). arXiv:gr-qc/0608091
8. Schutz, B.F., Will, C.M.: Black hole normal modes: a semianalytic approach. Astrophys. J. **291**, L33 (1985)
9. Iyer, S., Will, C.M.: Black hole normal modes: a WKB approach. 1. Foundations and application of a higher order WKB analysis of potential barrier scattering. Phys. Rev. D **35**, 3621 (1987)
10. Iyer, S.: Black hole normal modes: a WKB approach. 2. Schwarzschild black holes. Phys. Rev. D **35**, 3632 (1987)

11. Kokkotas, K.D., Schutz, B.F.: Black hole normal modes: a WKB approach. 3. The Reissner-Nordstrom black hole. Phys. Rev. D **37**, 3378 (1988)
12. Konoplya, R.A.: Quasinormal behavior of the d-dimensional Schwarzschild black hole and higher order WKB approach. Phys. Rev. D **68**, 024018 (2003). arXiv:gr-qc/0303052
13. Konoplya, R.A., Zhidenko, A., Zinhailo, A.F.: Higher order WKB formula for quasinormal modes and grey-body factors: recipes for quick and accurate calculations (2019). arxiv:1904.10333
14. Moulin, F., Barrau, A., Martineau, K.: An overview of quasinormal modes in modified and extended gravity. Universe **5**, 202 (2019). arXiv:1908.06311
15. Newman, E., Penrose, R.: An approach to gravitational radiation by a method of spin coefficients. J. Math. Phys. **3**, 566 (1962)
16. Bhattacharyya, S., Shankaranarayanan, S.: Quasinormal modes as a distinguisher between general relativity and f(R) gravity: charged black-holes. Eur. Phys. J. C **78**, 737 (2018). arXiv:1803.07576
17. Prasobh, C.B., Kuriakose, V.C.: Quasinormal modes of Lovelock black holes. Eur. Phys. J. C **74**, 3136 (2014)
18. Bhattacharyya, S., Shankaranarayanan, S.: Distinguishing general relativity from Chern-Simons gravity using gravitational wave polarizations (2018). arxiv:1812.00187
19. Ferrari, V., Pauri, M., Piazza, F.: Quasinormal modes of charged, dilaton black holes. Phys. Rev. D **63**, 064009 (2001). arXiv:gr-qc/0005125
20. Brito, R., Pacilio, C.: Quasinormal modes of weakly charged Einstein-Maxwell-dilaton black holes. Phys. Rev. D **98**, 104042 (2018). arXiv:1807.09081
21. Cardoso, V., Kimura, M., Maselli, A., Berti, E., Macedo, C.F.B., McManus, R.: Parametrized black hole quasinormal ringdown. I. Decoupled equations for nonrotating black holes (2019). arxiv:1901.01265
22. Cardoso, V., Konoplya, R., Lemos, J.P.S.: Quasinormal frequencies of Schwarzschild black holes in anti-de Sitter space-times: a complete study on the asymptotic behavior. Phys. Rev. D **68**, 044024 (2003). arXiv:gr-qc/0305037
23. Dias, O.J.C., Eperon, F.C., Reall, H.S., Santos, J.E.: Strong cosmic censorship in de Sitter space. Phys. Rev. D **97**, 104060 (2018a). arXiv:1801.09694
24. Dias, O.J.C., Reall, H.S., Santos, J.E.: Strong cosmic censorship: taking the rough with the smooth. JHEP **10**, 001 (2018b). arXiv:1808.02895
25. Tattersall, O.J.: Kerr-(anti-)de Sitter black holes: perturbations and quasinormal modes in the slow rotation limit. Phys. Rev. D **98**, 104013 (2018). arXiv:1808.10758
26. Chandrasekhar, S.: The Mathematical Theory of Black Holes. Clarendon, Oxford, 646 pp (1992), Clarendon, Oxford, 646 pp (1985)
27. Glampedakis, K., Johnson, A.D., Kennefick, D.: Darboux transformation in black hole perturbation theory. Phys. Rev. D **96**, 024036 (2017). arXiv:1702.06459
28. Yurov, A.V., Yurov, V.A.: A look at the generalized Darboux transformations for the quasinormal spectra in Schwarzschild black hole perturbation theory: just how general should it be? Phys. Lett. A **383**, 2571 (2019). arXiv:1809.10279
29. de Felice, F., Clarke, C.J.S.: Relativity on Curved Manifolds. Cambridge University Press, Cambridge (1992)
30. Batic, D., Nowakowski, M., Morgan, K.: The problem of embedded eigenvalues for the Dirac equation in the Schwarzschild black hole metric. Universe **2**, 31 (2016). arXiv:1701.03889
31. Newman, E.T., Penrose, R.: Spin-coefficient formalism. Scholarpedia **4**, 7445 (2009), revision #184895
32. Casals i Casanellas, M.: Electromagnetic quantum field theory on Kerr-Newman black holes. Ph.D. thesis, University Coll., Dublin, Math. Phys. (2008). arxiv:0802.1885
33. Hawking, S.W., Israel, W.: General Relativity. University Press, Cambridge. ISBN 9780521299282. http://www.cambridge.org/us/knowledge/isbn/item1131443/?site_locale=en_US (1979)

3.3.4 Les modes quasi normaux dans les différents modèles au delà de la RG

Étant donné que la fenêtre des observations expérimentales de QNMs s'ouvre, il est intéressant d'étudier comment la valeur des QNMs varie en fonction des différents modèles au delà de la RG. Plusieurs modèles possèdent une métrique de la forme

$$ds^2 = f(r)dt^2 - f(r)^{-1}dr^2 - r^2 d\Omega^2 \tag{3.92}$$

avec $f(r)$ des fonctions modifiées comparé à l'expression pour Schwarzschild. Pour ces modèles, le potentiel des perturbations axiales s'écrit :

$$V(r) = f(r)\left(\frac{\lambda + 2(f(r)-1)}{r^2} - \frac{f'(r)}{r}\right) \tag{3.93}$$

avec $\lambda = \ell(\ell+1)$. Pour d'autres modèles, toujours statiques à symétrie sphérique, la métrique est plus générale telle que

$$ds^2 = A(r)dt^2 - B(r)^{-1}dr^2 - H(r)d\Omega^2. \tag{3.94}$$

C'est le cas du modèle de trou noir en LQG considéré dans la section 3.2. Il faut alors déterminer le potentiel via les équations de perturbations. En considérant une dépendance en temps donnée par $e^{i\omega t}$ et en définissant la coordonnée tortoise telle que $dr^* = dr/\sqrt{AB}$, j'ai montré que le potentiel s'écrit

$$V(r) = \frac{1}{2H^2}\left(\frac{dH}{dr^*}\right)^2 + \frac{\mu^2 A}{H} - \frac{1}{\sqrt{H}}\frac{d^2}{dr^{*2}}\left(\sqrt{H}\right), \tag{3.95}$$

avec $\mu = (\ell-1)(\ell+2)$. Le calcul explicite se trouve dans l'article. Grâce aux expressions de potentiel nous pouvons calculer les QNMs avec la méthode WKB au 6ème ordre.

3.3.5 Les modes quasi normaux dans les différents modèles de gravité

L'étude effectuée est une étude préliminaires dans le sens où, en pratique, les trous noirs possèdent un moment cinétique. Cependant, en première approximation, nous pensons que l'ordre de grandeur des variations demeure comparable. Ainsi nous étudions des trous noirs statiques à symétries sphérique et on va pouvoir comparer les prédictions des différents modèles par rapport aux trous noirs de Schwarzschild. Dans toutes les Figures, les QNMs de Schwarzschild sont représentés par les points noirs. Nous avons investigué des modèles dont la métrique à une expression explicite afin d'utiliser l'approximation WKB au 6ème ordre. Le poids des QNMs, dans la reconstruction du signal, est d'autant plus grand lorsque n et ℓ sont petits. Le poids prépondérant est pour le mode fondamental $n = 0$ et $\ell = 2$. Nous avons calculé les QNMs pour $n = 0$ et $\ell = 2, 3, 4$.

Gravité massive

Tout d'abord nous considérons le modèle de la gravité massive. Dans cette théorie, il n'y a qu'un type de graviton et il possède une masse m. Contrairement à la gravité bimétrique où il y a un graviton massif et un sans masse. Un point intéressant de la gravité massive est que la masse du graviton va naturellement engendrer une expansion accélérée de l'univers. Une solution de trou noir s'écrit avec une métrique telle que (3.92) avec

$$f(r) = 1 - \frac{2M}{r} + \frac{\Lambda r^2}{3} + \gamma r + \epsilon, \tag{3.96}$$

avec Λ, γ et ϵ définis par

$$\begin{aligned} \Lambda &= 3m^2(1 + a + b), \\ \gamma &= -cm^2(1 + 2a + 3b), \\ \epsilon &= c^2m^2(a + 3b) \end{aligned} \tag{3.97}$$

avec a et b deux constantes, sans dimension, arbitraires et c défini positivement. On observe qu'effectivement la masse du graviton donne lieu à la constante cosmologique Λ.

Gravité scalaire-tenseur-vecteur

Dans la théorie de gravité scalaire-tenseur-vecteur (STVG pour scalar-tensor-vector gravity, appelée également MOG pour Modified Gravity), l'existence d'un champ vectoriel est postulée tandis que les constantes sont promues au rang de champs scalaires dynamiques. Loin des sources la gravitation est plus élevée qu'usuellement - ce qui permet d'expliquer les courbes de rotation des galaxies - mais à petite échelle l'effet est contrebalancé par le champ vectoriel qui produit une force répulsive [69]. La principale conséquence est que la loi d'accélération est modifiée. Ce qui est intéressant c'est que cette dernière est en concordance avec les courbes de rotation des galaxies, sans avoir à ajouter de la matière noire non baryonique. Pour des champs gravitationnels faibles, un échange de boson massif de spin 1 (dont le couplage et la masse varient en fonction de la distance) entraine un potentiel de Yukawa répulsif. Pour décrire cette théorie, l'action va être modifiée par l'ajout de termes contenant le champ vectoriel ϕ_μ. Les nouvelles équations de champ qui apparaissent possèdent une solution statique et sphérique [70] décrite par

$$f(r) = 1 - \frac{2M}{r} + \frac{\alpha(1 + \alpha)M^2}{r^2}. \tag{3.98}$$

La force de répulsion gravitationnelle se retrouve dans le terme α, la charge de cette force s'écrit

$$Q = \sqrt{\alpha G_N M} \tag{3.99}$$

avec $G = G_N(1 + \alpha)$ (ici, G_N dénote la constante de Newton). Cette solution possède deux horizons pour $\alpha < \alpha_c = 0.67$.

Gravité Hořava-Lifshitz

Étant donné que la RG n'est pas renormalisable, l'idée de la théorie de Hořava-Lifshitz [71] est de rendre la théorie renormalisable en ajoutant des termes d'ordre supérieur de courbure et de dérivées temporelles dans l'action de Einstein-Hilbert. Une conséquence est que l'invariance de Lorentz est brisée à l'échelle ultraviolette mais peut être retrouvée dans l'infrarouge. Une solution de trou noir s'écrit [72]

$$f(r) = \frac{2(r^2 - 2Mr + \beta)}{r^2 + 2\beta\sqrt{r^4 + 8\beta Mr}} \tag{3.100}$$

avec $\beta = 1/(2w)$, w étant une constante de couplage qui apparaît dans les termes d'ordre supérieur de l'action.

Correction $\hbar$

Dans [73], une métrique avec une correction quantique effective est construite. Pour modéliser cette dernière, les contraintes à respecter sont les points suivants :

— reproduire la limite Newtonienne avec une correction en $\hbar$ (notamment dans le potentiel Newtonien [74]),

— reproduire les résultats sur l'entropie des trous noirs,

— les géodésiques des particules test dans cette métrique doivent être cohérentes.

Le résultat final est décrit par la fonction

$$f(r) = 1 - \frac{2M}{r} + \frac{2M\gamma}{r^3}. \tag{3.101}$$

Des indications amènent à considérer le paramètre γ comme étant négatif. Plusieurs valeurs sont proposées dans la littérature, la dernière étant $\gamma = -41/10$. Dans l'article ci-dessous, on a choisi différentes valeurs espacées linéairement dans l'intervalle des γ proposés.

Gravitation quantique à boucles

Ici, nous considérons le métrique construite dans le cadre de la LQG, qu'on a déjà considéré dans la section 3.2. Nous rappelons que la métrique s'écrit

$$ds^2 = G(r)dt^2 - \frac{dr^2}{F(r)} - H(r)d\Omega^2, \tag{3.102}$$

$$G(r) = \frac{(r - r_+)(r - r_-)(r + r_x)^2}{r^4 + a_0} \tag{3.103}$$

$$F(r) = \frac{(r - r_+)(r - r_-)r^4}{(r + r_x)(r^4 + a_0^2)} \tag{3.104}$$

$$H(r) = r^2 + \frac{a_0^2}{r^2} \tag{3.105}$$

avec $r_+ = 2m$, $r_- = 2mP^2$, $r_x = \sqrt{r_+ r_-}$, $P = (\sqrt{1+\epsilon} - 1)/((\sqrt{1+\epsilon} + 1)$ avec $\epsilon = \gamma\delta$, $a_0 = A_{min}/8\pi$ avec A_{min} l'aire minimale du spectre de la LQG.

3.3.6 Les résultats

Dans le modèle de gravité massive (Figure 1), on observe que globalement la fréquence des QNMs augmente avec la masse du graviton. L'amortissement augmente également légèrement avec la masse, mais pas de façon significative. Nous observons également que la pente entre les harmoniques n varie quand la masse du graviton augmente. Dans le modèle scalaire-tenseur-vecteur (Figure 2), on a un comportement similaire au cas précédent. La valeurs réelle des QNMs augmente lorsque α augmente mais il n'y a aucun changement pour la valeur imaginaire. La pente entre les harmoniques reste cependant la même pour les différentes valeurs de α. Dans le modèle de Hořava-Lifshitz (Figure

3), on observe également un déplacement des QNMs vers des plus grandes valeurs réelles quand β augmente. Mais on remarque également, qu'en parallèle, la partie imaginaire va diminuer ce qui est caractéristique de cette théorie. On observe pas de changement sur la pente des harmoniques. Dans le modèle avec une correction quantique en $\hbar$ (Figure 4), on observe que contrairement aux modèles précédents, la déviation par rapport à Schwarzschild se fait vers la gauche. Étant donné que γ apporte une contribution négative à la métrique plus la valeur absolue de γ est élevée plus la partie réelle des QNMs diminuent. Ainsi, ce modèle se distingue des autres. De plus la pente des harmoniques varie. Dans le modèle des trous noirs quantiques à boucles (Figure 5), on a un léger décalage des fréquences vers la droite et la pente des harmoniques reste inchangée en fonction de δ, qui caractérise l'échelle de discrétisation.

Cet article a été publié dans *Universe* [75].

universe

MDPI

Article

An Overview of Quasinormal Modes in Modified and Extended Gravity

Flora Moulin, Aurélien Barrau * and Killian Martineau

Laboratoire de Physique Subatomique et de Cosmologie, Université Grenoble-Alpes, CNRS/IN2P3 53, avenue des Martyrs, CEDEX, 38026 Grenoble, France; floramoulin@hotmail.fr (F.M.); killian.martineau@gmail.com (K.M.)

* Correspondence: barrau@in2p3.fr

Received: 17 August 2019; Accepted: 17 September 2019; Published: 19 September 2019

Abstract: As gravitational waves are now being nearly routinely measured with interferometers, the question of using them to probe new physics becomes increasingly legitimate. In this article, we rely on a well established framework to investigate how the complex frequencies of quasinormal modes are affected by different models. The tendencies are explicitly shown for both the pulsation and the damping rate. The goal is, at this stage, purely qualitative. This opportunity is also taken to derive the Regge-Wheeler equation for general static and spherically symmetric metrics.

1. Introduction

General relativity (GR) is our best theory of spacetime. While the Lovelock theorem [1] ensures that it cannot be easily modified, there are quite a lot of attempts to relax some hypotheses and build a deeper model to describe the gravitational field. From effective quantum gravity to improved infrared properties, the motivations to go beyond GR are countless. So are the situations, both in astrophysics and cosmology, where extended gravity theories can, in principle, be tested. In practice, reaching the level of accuracy useful to probe the relevant range of parameters is obviously far from trivial. In this article we focus on a specific aspect of gravitational waves that would be emitted during the relaxation phase of a deformed black hole (BH).

We will consider quasinormal modes associated with the ringdown phase of a BH merger. The modes are not strictly normal due to energy losses of the system through gravitational waves. The boundary conditions for the equation of motion are unusual as the wave has to be purely outgoing at infinity and purely ingoing at the event horizon. The time component of the radial part reads (an introductory review can be found in [2]):

$$e^{-i\omega t} = e^{-i(\omega_R + i\omega_I)t}, \tag{1}$$

the complex pulsation ω being split into a real part ω_R, which corresponds to the frequency, and an imaginary one ω_I, which is the inverse timescale of the damping. Stability requires $\omega_I < 0$. While real-life BHs are spinning, we focus on Schwarzschild solutions in this article. The details of these predictions can not be used to directly compare with observations. We, however, expect the general tendencies and orders of magnitudes to remain correct, as they can be checked for the general relativistic case in [3].

Whether one considers "axial" or "polar" perturbations, the linearized Einstein equations lead to wave equations with different potentials. In GR, the (so-called Regge-Wheeler) potential for axial perturbations is:

$$V_\ell^{\mathrm{RG}}(r) = \left(1 - \frac{2M}{r}\right)\left[\frac{\ell(\ell+1)}{r^2} - \frac{6M}{r^3}\right], \tag{2}$$

while the (so-called Zerilli) one for polar perturbations is:

$$V_\ell^Z(r) = \frac{2}{r^3}\left(1-\frac{2M}{r}\right)\times \\ \times \quad \frac{9M^3+3a^2Mr^2+a^2(1+a)r^3+9M^2ar}{(3M+ar)^2}, \tag{3}$$

where $a=\ell(\ell+1)/2-1$. Throughout the paper we use Planck units. In the purely gravitational sector, one needs $\ell \geq 2$. Interestingly, both those equations have the very same spectrum of quasinormal modes (QNMs). This property, called isospectrality [4], is not always true in modified gravity (see [5] for an extension and a discussion of the original proof). Basically, quasinomal modes are described by their multipole number ℓ and their overtone number n. The fundamental quadrupolar mode ($n=0$ and $\ell=2$) for a Schwarzschild BH in GR is given by $M\omega \approx 0.374-0.0890i$.

There are many different ways to calculate the QNMs: Continued fractions, Frobenius series, Mashhoon's method, confluent Heun's equation, characteristic integration, shooting, Wentzel-Kramers-Brillouin (WKB) approximations, etc. In this article we focus on the last approach. For most models considered here, the QNMs have already been calculated in previous studies. However, this has most of the time been done for $s=0$ or $s=1$, not for $s=2$ as we have done it here. More importantly, it is in addition very useful to rely on the very same method to investigate all models so that the differences underlined are actually due to physical effects and not to numerical issues. Even when the same approach is considered, the way it is implemented is often different enough, between articles, so that it is hard to directly compare the results. This is why we have here tried to methodically consider several modified gravity models with a well controlled WKB approximation scheme used in the same way in all cases so as to compare the tendencies between modified gravity proposals. This is not mandatory for this qualitative step but this will become useful in future quantitative studies.

The determination of the complex frequencies of QNMs is difficult (see [6,7] for historical reviews and [8,9] for results based on numerical approaches). This work is based on the WKB approach described in [10]. Following the pioneering work in [11], the WKB method for QNMs was developed in [12–15]. This formalism leads to fairly good approximations, especially for high multipole and low overtone numbers. In the following, we restrict ourselves to $n<l$ and use the sixth order WKB method developed by Konoplya [10] (see also [16–18]). This allows one to recast the potential appearing in the effective Schrödinger equation felt by gravitational perturbations in a complex but tractable form.

The aim of this introductory paper is to investigate how several modified gravity theories impact the QNMs at the qualitative level. There are several ways to go beyond GR: Extra dimensions, weak equivalence principle violations, extra fields, diffeomorphism–invariance violations, etc. Beyond those technicalities, there are strong conceptual motivations to consider extended gravity approaches, from the building of an effective quantum gravity theory to the improvements of the renormalisation properties, through the implementation of a dynamical cosmological constant. Among many others, examples of recent relevant works on QNMs can be found in [19–22].

2. Perturbation Dynamics

The QNMs are solutions of a perturbation equation with the specific boundary conditions given in the previous section. The radial and angular parts can be separated. The radial part is governed by a Schrödinger-like equation:

$$\frac{d^2Z}{dr^{*2}}+V(r)Z=0, \tag{4}$$

where Z is the radial part of the "perturbation" variable, assumed to have a time-dependance $e^{i\omega t}$, and r^* is the tortoise coordinate. For a metric such that:

$$ds^2 = f(r)dt^2 - f(r)^{-1}dr^2 - r^2 d\theta^2 - r^2 \sin^2\theta d\phi^2, \tag{5}$$

the tortoise coordinate is defined by:

$$dr^* = \frac{1}{f(r)}dr. \tag{6}$$

It tends to $-\infty$ at the event horizon and to $+\infty$ at spatial infinity.

As explained previously, BH gravitational perturbations can be of two different types distinguished by their behavior under a parity transformation. For an angular momentum l, axial perturbations transform as $(-1)^l$ under parity, while polar perturbations transform as $(-1)^{l+1}$. This leads to the two different potentials in Equation (4). The potential for the gravitational axial perturbations reads in full generality (see [2] and references therein) for the metric given by Equation (5):

$$V(r) = f(r)\left(\frac{\lambda + 2(f(r)-1)}{r^2} - \frac{f'(r)}{r}\right). \tag{7}$$

In this work we will not consider the isospectrality-violation issues and we will focus only on such perturbations. It should anyway be kept in mind that, in principle, isospectrality might not hold.

The boundary conditions can be expressed as:

$$Z \sim e^{-i\omega r^*} \qquad r^* \to -\infty, \tag{8}$$

$$Z \sim e^{i\omega r^*} \qquad r^* \to +\infty. \tag{9}$$

We shall now derive the Regge-Wheeler equation for the more general (spherical and static) metric:

$$ds^2 = A(r)dt^2 - B(r)^{-1}dr^2 - H(r)d\theta^2 - H(r)\sin^2\theta d^2\phi. \tag{10}$$

For this metric, the tortoise coordinate is defined by:

$$\frac{d}{dr^*} = \sqrt{AB}\frac{d}{dr}. \tag{11}$$

The general form of an axisymmetric metric can be written as [4]:

$$\begin{aligned} ds^2 = \quad & e^{2\nu}(dx^0)^2 - e^{2\psi}(dx^1 - \sigma dx^0 - q_2 dx^2 - q_3 dx^3)^2 \\ & - e^{2\mu_2}(dx^2)^2 - e^{2\mu_3}(dx^3)^2, \end{aligned} \tag{12}$$

where $t = x^0$, $\phi = x^1$, $r = x^2$ and $\theta = x^3$. For the metric given by Equation (10), the correspondence is:

$$\begin{aligned} & e^{2\nu} = A(r), \quad e^{-2\mu_2} = B(r), \\ & e^{2\mu_3} = H(r), \quad e^{2\psi} = H(r)\sin^2\theta, \\ & \sigma = q_2 = q_3 = 0. \end{aligned} \tag{13}$$

A perturbation of this kind of spacetime is described by σ, q_2 and q_3, assumed to be first order quantities, and by infinitesimal increments, $\delta\nu$, $\delta\mu_2$, $\delta\mu_3$, of the other quantities. We focus here on axial perturbations. The point is to linearize the field equations about the solution given by Equation (10), considering components where σ, q_2 and q_3 are only functions of t, x^2 and x^3. The equations governing σ, q_2 and q_3 are described by the vanishing of the Ricci tensor components:

$$R_{12} = R_{13} = 0. \tag{14}$$

For Equation (12), one has [4] :

$$R_{12} = \frac{1}{2} e^{-2\psi-\nu-\mu_3} \times$$
$$[(e^{3\psi-\nu-\mu_2+\mu_3} Q_{02})_{,0} - (e^{3\psi+\nu-\mu_2-\mu_3} Q_{32})_{,3}], \tag{15}$$

with:

$$Q_{ab} = q_{a,b} - q_{b,a} \quad \text{and} \quad Q_{a0} = q_{a,0} - \sigma_{,a} \quad \text{for} \quad a, b = 2, 3. \tag{16}$$

where the comma indicates the derivative. The notation Q_{0a} is used to mean $-Q_{a0}$. The component R_{13} is also given by Equation (15) by switching indices 2 and 3.

The perturbed field equations are obtain by $\delta R_{\alpha\beta} = 0$. After replacing ν, μ_2, μ_3 and ψ by their expressions, $\delta R_{12} = 0$ leads to:

$$(H \sin^3\theta \sqrt{AB} Q_{23})_{,3} = -H^2 \sin^3\theta \sqrt{\frac{B}{A}} Q_{02,0}. \tag{17}$$

By defining:

$$Q = \sqrt{AB} H Q_{23} \sin^3\theta, \tag{18}$$

one obtains:

$$\sqrt{\frac{A}{B}} \frac{1}{H^2 \sin^3\theta} \frac{\partial Q}{\partial \theta} = Q_{20,0}. \tag{19}$$

For $\delta R_{13} = 0$, one is led to:

$$\frac{\sqrt{AB}}{H \sin^3\theta} \frac{\partial Q}{\partial r} = -Q_{30,0}. \tag{20}$$

We assume that perturbations have a time dependance given by: $e^{i\omega t}$. This implies that Equations (19) and (20) read:

$$\sqrt{\frac{A}{B}} \frac{1}{H^2 \sin^3\theta} \frac{\partial Q}{\partial \theta} = -\omega^2 q_2 - i\omega\sigma_{,2}, \tag{21}$$

$$\frac{\sqrt{AB}}{H \sin^3\theta} \frac{\partial Q}{\partial r} = \omega^2 q_3 + i\omega\sigma_{,3}. \tag{22}$$

Taking the derivative of Equation (21) with respect to θ and the derivative of Equation (22) with respect to r and combining the results leads to:

$$\sin^3\theta \frac{\partial}{\partial\theta}\left(\frac{1}{\sin^3\theta}\frac{\partial Q}{\partial\theta}\right) + \frac{H^2 B}{A}\frac{\partial}{\partial r}\left(\frac{\sqrt{AB}}{H}\frac{\partial Q}{\partial r}\right) + \sigma^2 \frac{QH}{A} = 0. \tag{23}$$

As suggested in [4], one can then separate the variables r and θ using:

$$Q(r, \theta) = R(r) C_{l+2}^{-3/2}(\theta) \tag{24}$$

with C_n^m the Gegenbauer function satisfying:

$$\left(\frac{d}{d\theta}\sin^{2m}\theta\frac{d}{d\theta} + n(n+2m)\sin^{2m}\theta\right) C_n^m(\theta) = 0. \tag{25}$$

Inserting Equation (24) into Equation (23), one is led to following radial equation:

$$H^2\frac{B}{A}\frac{\partial}{\partial r}\left(\frac{\sqrt{AB}}{H}\frac{\partial R(r)}{\partial r}\right)+\frac{H}{A}\sigma^2\mu^2R(r)=0, \tag{26}$$

where $\mu^2=(l-1)(l+2)$. Defining Z so that $R=\sqrt{H}Z$ and using the tortoise coordinate, we are led to a Schrödinger-like equation:

$$\frac{d^2Z}{dr^{*2}}+(\sigma^2-V(r))Z=0, \tag{27}$$

where the potential is:

$$V(r)=\frac{1}{2H^2}\left(\frac{dH}{dr^*}\right)^2+\frac{\mu^2A}{H}-\frac{1}{\sqrt{H}}\frac{d^2}{dr^{*2}}\left(\sqrt{H}\right). \tag{28}$$

The potential reduces to Equation (7) for $A(r)=B(r)$ and $H(r)=r^2$. This derivation is useful to calculate QNMs for general static and spherically symmetric metrics.

3. The WKB Approximation

The WKB approximation [12–14] is known for leading to good approximations (compared to numerical results) for the QNMs. The potential is written using the tortoise coordinate so as to be constant at $r^*\to 0$ (which represent the horizon of the BH) and at $r^*\to+\infty$ (which represents spatial infinity). The maximum of the potential is reached at r_0^*. Three regions can be identified: Region I from $-\infty$ to r_1, the first turning point (where the potential vanishes), region II from r_1 to r_2, the second turning point, and region III from r_2 to $+\infty$. In region II, a Taylor expansion is performed around r_0^*. In regions I and III, the solution is approximated by an exponential function:

$$Z\sim exp\left[\frac{1}{\epsilon}\sum_{n=0}^{\infty}\epsilon^nS_n(x)\right],\qquad \epsilon\to 0. \tag{29}$$

This expression can be inserted into Equation (4) so as to obtain S_j as a function of the potential and its derivative. We then impose the boundary conditions given by Equation (9) and match the solutions of regions I and III with the solution for region II at the turning points r_1 and r_2, respectively. The WKB approximation has been usefully extended from the third to the sixth order in [10].

This allows one to derive the complex frequencies as a function of the potential and its derivatives evaluated at the maximum. For the sixth order treatment, one is led to:

$$\omega^2=V_0-i\sqrt{-2V_0''}\left(\sum_{j=2}^{6}\Lambda_j+n+\frac{1}{2}\right), \tag{30}$$

where the expressions of the Λ_js can be found in [10]. In the following, we use this scheme to compare different modified gravity models and we present results only in the range of validity of the WKB approximations.

Interesting recent considerations on the convergence on the WKB series are given in [23]. Details on the expansion parameter used in this work can be found in [17]. The consistency of the WKB approximation has been checked for the presented results.

4. Modified Gravity Models and Results

Throughout this section we investigate some properties of the QNMs for several extended gravity approaches. We pretend in no way to do justice to the subtleties of those models and, when necessary, we explicitly choose specific simplified settings to make the calculations easily tractable.

As we focus on phenomenological aspects, the more interesting mode is the fundamental one: $n=0$ and $l=2$. We therefore focus on a few points around this one (keeping in mind that the accuracy

is better for higher values of l). In all the figures, the lower overtone n is the one with the smallest imaginary part.

We first consider models with a metric of the form:

$$ds^2 = f(r)dt^2 - f(r)^{-1}dr^2 - r^2 d\theta^2 - r^2 \sin^2\theta d^2\phi, \tag{31}$$

and then investigate a model with two different metric functions, using the result obtained in Equation (28).

4.1. Massive Gravity

In GR, the graviton is a massless spin-2 particle. One of the first motivations for modern massive gravity—which can be seen as a generalization of GR—was the hope to account for the accelerated expansion of the Universe by generating a kind of Yukawa-like potential for gravitation [24]. The initial linear approach to massive gravity contained a Boulware-Deser ghost, which was cured in the dRGT version [25–28]. Massive gravity also features interesting properties for holography (see, e.g., [29]).

Starting from the action:

$$S = \frac{1}{16\pi}\int \mathrm{d}^4x\sqrt{-g}\left(R + m^2\mathcal{U}(g,\phi^a)\right), \tag{32}$$

where R is the Ricci scalar and $\mathcal{U}$ is the potential for the graviton, the following black hole solution can be derived [30,31]:

$$f(r) = 1 - \frac{2M}{r} + \frac{\Lambda r^2}{3} + \gamma r + \epsilon, \tag{33}$$

where Λ, γ and ϵ are, respectively:

$$\begin{aligned} \Lambda &= 3m^2(1+a+b), \\ \gamma &= -cm^2(1+2a+3b), \\ \epsilon &= c^2m^2(a+3b), \end{aligned} \tag{34}$$

with a and b being two dimensionless constants and c being positive. It should also be pointed out that a positive value of γ might raise consistency issues [31].

The results are presented in Figure 1. The values chosen for the constants do, of course, change the amplitude of the displacement of the QNMs. The global trend, which is the point of this study, however, remains the same. Increasing the graviton mass m tends to increase the real part of QNMs, that is the frequency of the oscillations. The difference in frequency between the fundamental and the first overtone also increases with m. The effect on the imaginary part is hardly noticeable on the plot, even though a slight increase, which is actually 50% less important, in relative variation, than the shift in frequency, should be noticed. The values considered here for the mass are, of course, way out of the known bounds, but this is clearly not the point. As a specific feature, one can notice that the frequency shift due to massive corrections decreases for higher overtones. The shift patterns are mostly the same whatever the multipole number considered.

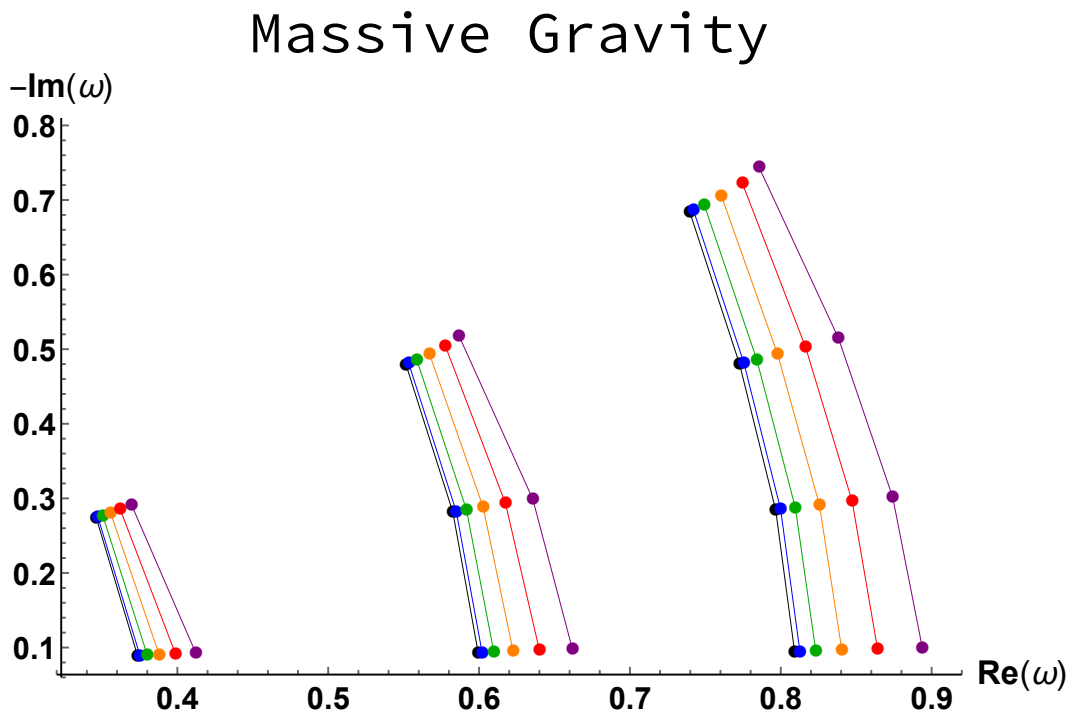

Figure 1. Quasinormal modes (QNMs) in massive gravity. The left block is for $l = 2$, the middle one corresponds to $l = 3$ and the right one is for $l = 4$. The dark points correspond to the Schwarzschild QNMs. The arbitrary constants a, b and c have been taken to one. From left to right: $m = \{15, 30, 45, 60, 75\} \times 10^{-3}$.

4.2. Modified Scalar–Tensor–Vector (STV) Gravity

The scalar–tensor–vector modified gravitational theory (MOG) allows the gravitational constant, a vector field coupling, and the vector field mass to vary with space and time [32]. The equations of motion lead to an effective modified acceleration law that can account for galaxy rotation curves and cluster observation without dark matter. While it has recently been much debated and put under pressure, the theory is still worth considering seriously. We consider the field equation for the metric tensor [33] :

$$R_{\mu\nu} = -8\pi G T_{\phi\mu\nu}, \tag{35}$$

where the gravitational coupling is $G = G_N(1+\alpha)$, with G_N being the Newton's constant. The gravitational strength of the vector field ϕ_μ (spin 1 graviton) is $Q_g = \sqrt{\alpha G_N} M$. With $B_{\mu\nu} = \partial_\mu \phi_\nu - \partial_\nu \phi_\mu$, the energy-momentum tensor for the vector field is :

$$T_{\phi\mu\nu} = -\frac{1}{4\pi}(B_\mu{}^\alpha B_{\nu\alpha} - \frac{1}{4} g_{\mu\nu} B^{\alpha\beta} B_{\alpha\beta}), \tag{36}$$

with the constant ω of [32] being set to one. Solving the vacuum field equations:

$$\nabla_\nu B^{\mu\nu} = \frac{1}{\sqrt{-g}} \partial_\nu (\sqrt{-g} B^{\mu\nu}) = 0, \tag{37}$$

and:

$$\nabla_\sigma B_{\mu\nu} + \nabla_\mu B_{\nu\sigma} + \nabla_\nu B_{\sigma\mu} = 0, \tag{38}$$

with the appropriate symmetry leads to the metric:

$$f(r) = 1 - \frac{2M}{r} + \frac{\alpha(1+\alpha)M^2}{r^2}. \tag{39}$$

We focus on the case where the field equations for $B_{\mu\nu}$ are non-linear, as the phenomenology is then richer, and we consider the relevant choice $\alpha < \alpha_c = 0.67$ where there are two horizons and appropriate potential behavior for the WKB approximation to hold. An up-to-date investigation of QNMs in MOG can be found in [34].

The results are given in Figure 2. The imaginary part of the QNMs is nearly the same whatever the value of α: The modified metric has no effect on the damping rate. However, increasing α does increase of the real part, that is the frequency. The effect is important for values near the critical value α_c. The slope of the Imaginary part versus the real one, at a given l for different values of n, is nearly independent of α. This slope is not directly observable but it shows how the structure of the QNMs changes with the overtone number. The curves remain here parallel one to the other: This means that increasing the deformation parameter does not change the frequency shift between overtones.

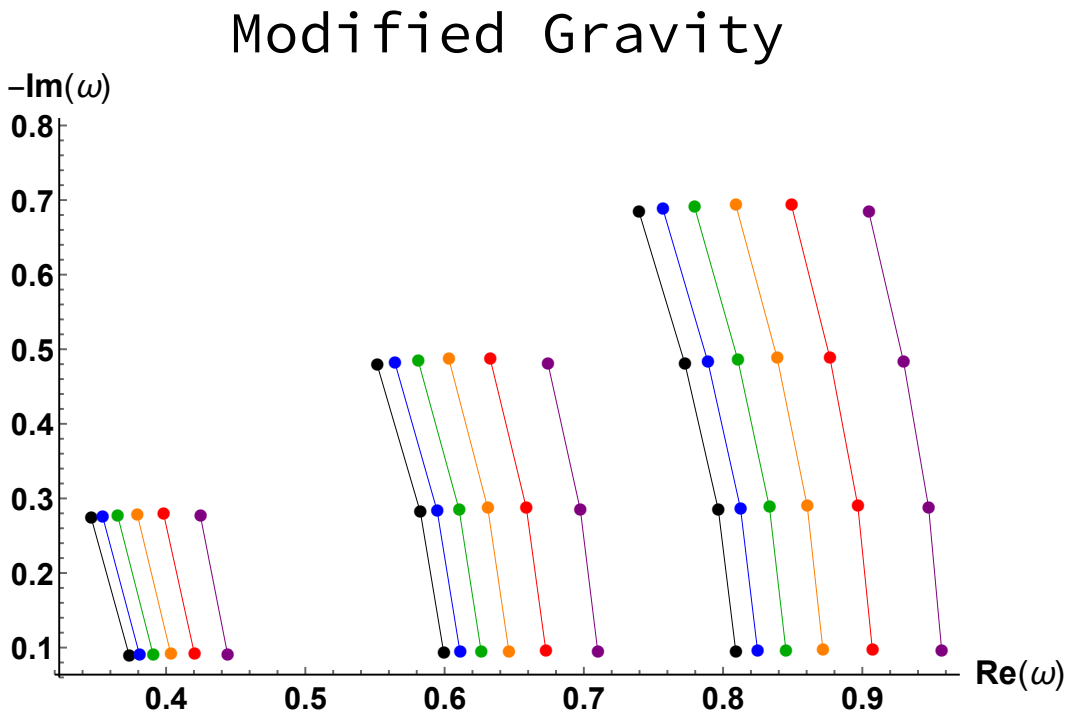

Figure 2. QNMs in modified SVT gravity. The left block is for $l = 2$, the middle one corresponds to $l = 3$ and the right one is for $l = 4$. The dark points correspond to the Schwarzschild QNMs. From left to right: $\alpha = \{1, 2, 3, 4, 5\} \times 10^{-1}$.

4.3. Hořava-Lifshitz Gravity

Hořava-Lifshitz gravity bets on the fundamental nature of the quantum theory instead of relying on GR principles. It is a renormalizable UV-complete gravitational theory which is not Lorentz invariant in 3 + 1 dimensions [35]. The relativistic time with its Lorentz invariance emerges only at large distances. Black hole solutions have been found [36–38] and QNMs were studied [39].

Using the ansatz:

$$ds^2 = -N^2(r)\,dt^2 + \frac{dr^2}{f(r)} + r^2(d\theta^2 + \sin^2\theta d\phi^2) \tag{40}$$

in the action, one is led to the Lagrangian:

$$\tilde{\mathcal{L}}_1 = \frac{\kappa^2\mu^2 N}{8(1-3\lambda)\sqrt{f}}\left(\frac{\lambda-1}{2}f'^2 - \frac{2\lambda(f-1)}{r}f' \right. \tag{41}$$

$$\left. + \frac{(2\lambda-1)(f-1)^2}{r^2} - 2w(1-f-rf')\right), \tag{42}$$

where $w = 8\mu^2(3\lambda-1)/\kappa^2$. For $\lambda = 1$, the solution is:

$$N^2 = f(r) = \frac{2(r^2-2Mr+\beta)}{r^2+2\beta+\sqrt{r^4+8\beta Mr}}, \tag{43}$$

with $\beta = 1/(2w)$, w being the deformation parameter enterring the action given in [37]. There are two horizons for $M^2 > \beta$.

The results are given in Figure 3. The frequency increases with an increase of β. Interestingly, the imaginary part of the overtones is highly sensitive to β. This remains true for higher multipoles. The relative variation of the imaginary part is nearly the same whatever the overtone number. It therefore becomes large in absolute value for high n values.

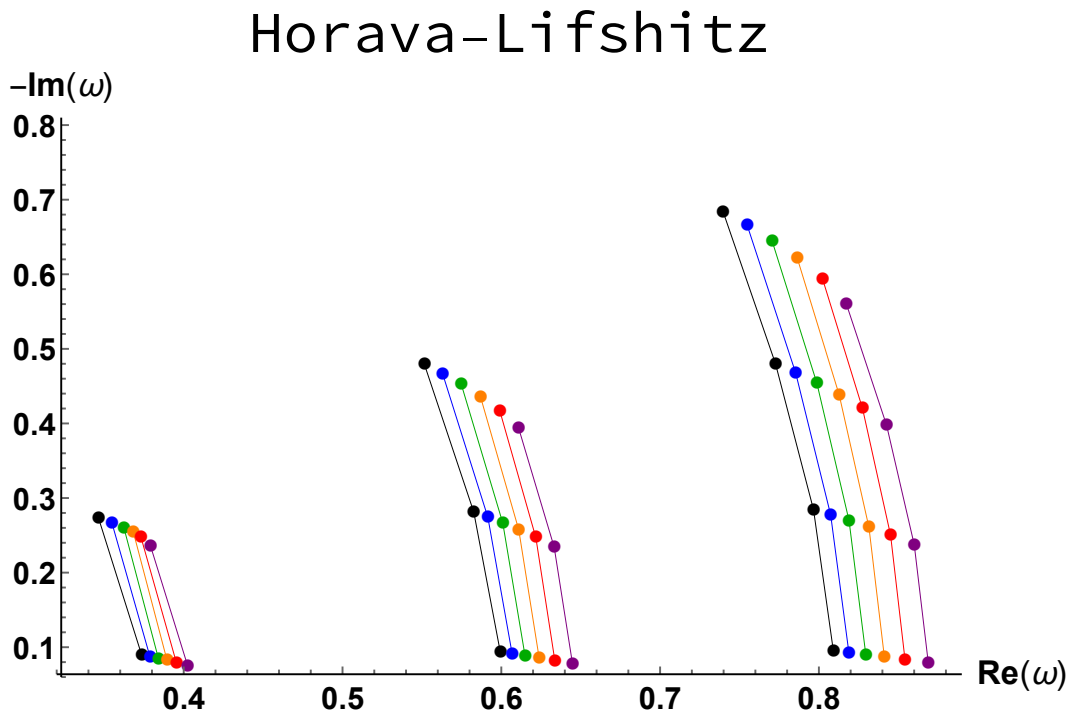

Figure 3. QNMs in Horava-Lifshits gravity. The left block is for $l = 2$, the middle one corresponds to $l = 3$ and the right one is for $l = 4$. The dark points correspond to the Schwarzschild QNMs. From left to right: $\beta = \{15, 30, 45, 60, 75\} \times 10^{-2}$.

4.4. ħ Correction

It has been known for a long time that quantum corrections to the Newtonian gravitational potential can be rigorously derived without having a full quantum theory of gravity at disposal (see, e.g., [40–44] to cite only a few works from a very long list). Recently, a quite similar approach was developed [45] requiring that the quantum mechanically corrected metric reproduces the corrected Newtonian limit, reproduces the standard result for the entropy of black holes including the known corrections and fulfills some consistency conditions regarding the geodesic motion.

The resulting metric is:

$$f(r) = 1 - \frac{2M}{r} + \gamma \frac{2M}{r^3}. \tag{44}$$

We use, as previously, natural units and the coefficients of the last term, γ, is proportional to $\hbar$ in these models. It is worth noticing that there has been a long controversy about the value and the sign of the γ factor. From the phenomenological perspective, we do not fix it to a particular value but we keep it negative, in agreement with the latest expectations.

The results are given in Figure 4. For large values of γ, the effects are noticeable on the frequency. It is remarkable that, from our analysis, the real part of the complex frequency is only decreased, which is not the case for the other models that have been considered in this study. The higher the absolute value of γ, the larger the difference of frequency between the fundamental and the overtones. This effect, however, remains quite subtle.

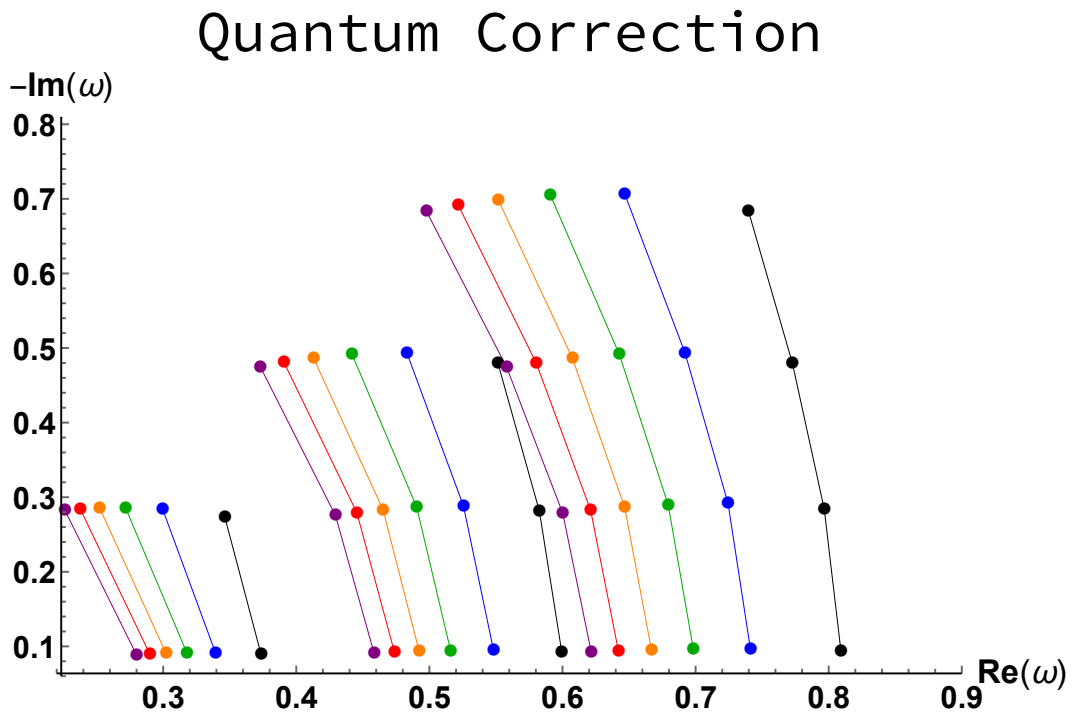

Figure 4. QNMs in quantum-corrected gravity. The left block is for $l = 2$, the middle one corresponds to $l = 3$ and the right one is for $l = 4$. The dark points correspond to the Schwarzschild QNMs. From left to right: $\gamma = \{-5, -4, -3, -2, -1\}$.

4.5. LQG Polymeric BH

Loop quantum gravity (LQG) is a non-perturbative and background-independant quantum theory of gravity [46]. In the covariant formulation, space is described by a spin network [47]. Each edge carries a "quantum of area", labelled by a half integer j, associated with a irreducible representations of $SU(2)$. Each node carries a "quantum of space" associated with an intertwiner. A key result is that the area is quantized according to:

$$A(j) = 8\pi\gamma_{BI}\sqrt{j(j+1)}, \tag{45}$$

with γ_{BI} being the Barbero-Immirzi parameter. Black holes are usually described in LQG through an isolated horizon puncturing a spin network [48] and the phenomenology is very rich, depending on the precise setting chosen [49]. We focus here on the model developed in [50], as this is the one leading to metric modifications outside the horizon, where a regular lattice with edges of lengths δ_b and δ_c is considered. Requiring the minimal area to be one derived in LQG, one is left with only one free

parameter δ. From this minisuperspace approximation, a static spherical solution can be derived and is given by:

$$
\begin{aligned}
ds^2 &= -G(r)dt^2 + \frac{dr^2}{F(r)} + H(r)d\Omega^2\,, \\
G(r) &= \frac{(r-r_+)(r-r_-)(r+r_*)^2}{r^4+a_o^2}\,, \\
F(r) &= \frac{(r-r_+)(r-r_-)r^4}{(r+r_*)^2(r^4+a_o^2)}\,, \\
H(r) &= r^2 + \frac{a_o^2}{r^2}\,,
\end{aligned}
\tag{46}
$$

where $d\Omega^2 = d\theta^2 + \sin^2\theta d\phi^2$, $r_+ = 2m$ and $r_- = 2mP^2$ are the two horizons, and $r_* = \sqrt{r_+ r_-} = 2mP$, P is the polymeric function defined by $P = (\sqrt{1+\epsilon^2}-1)/(\sqrt{1+\epsilon^2}+1)$ with $\epsilon = \gamma_{BI}\delta$, and the area parameter a_0 is given by $a_0 = A_{min}/8\pi$, A_{min} being the minimum area appearing in LQG. The parameter m in the solution is related to the ADM mass M by $M = m(1+P)^2$.

The results are given in Figure 5. The damping rate does not depend at all on the polymerization parameter. The real part of the complex frequency does, however, first decrease with δ. Noticeably, the slope is unchanged, and varying the deformation parameter just leads to a horizontal translation of the QNM frequency in the complex plane. This means that the frequency shift between the fundamental and the overtones does not depend on the amplitude of the quantum gravity corrections, as in modified gravity. Interestingly, for higher values of δ, the frequency begins to increase. This is the only model considered in this study with non-monotonic behavior. For $\delta \approx 10^{-0.7}$ the "polymerization" effect nearly exactly compensates the "area discretization" effect and one recovers the GR frequencies (and damping rates).

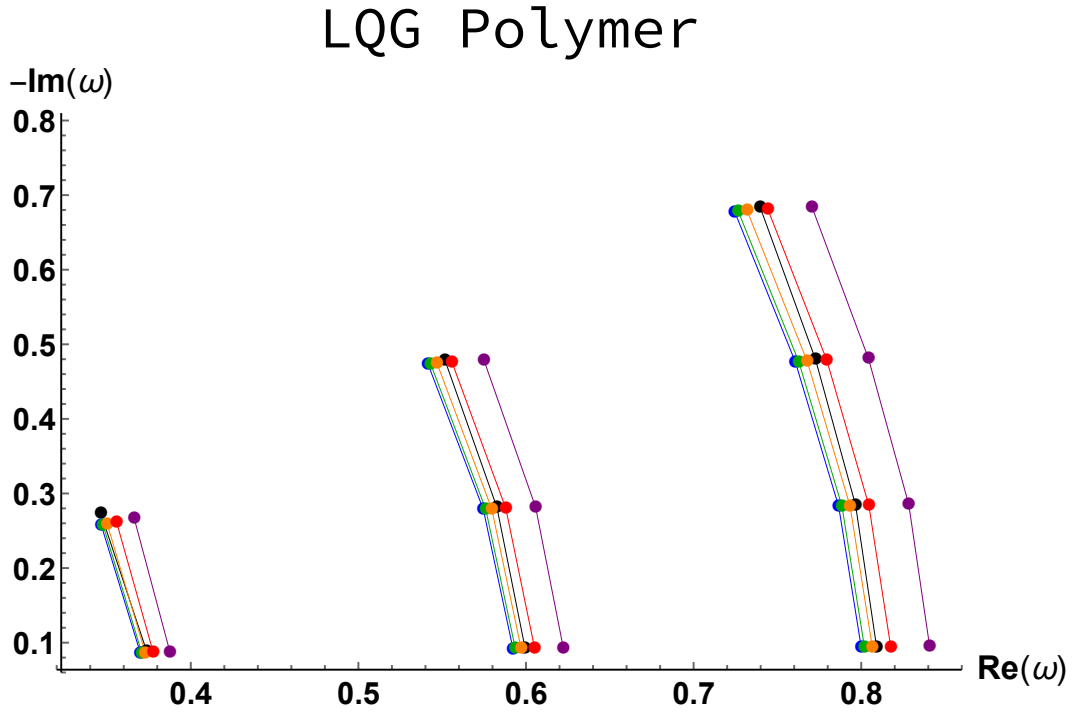

Figure 5. QNMs in loop quantum gravity (LQG) (polymer black holes (BHs)). The left block is for $l = 2$, the middle one corresponds to $l = 3$ and the right one is for $l = 4$. The dark points correspond to the Schwarzschild QNMs. The parameters are $a_0 = 1$ and from left to right: $\epsilon = 10^{-x}$ with $x \in \{-1, -0.8, -0.6, -0.4, -0.2\}$.

5. Conclusions

This study shows the evolution of the complex frequency of quasinormal modes of a Schwarzschild black hole for the fundamental and the first overtones for a few multipole numbers. We have considered massive gravity, STV gravity, Hořava-Lifshitz gravity, quantum corrected gravity and loop quantum gravity. All the results were derived using the very same WKB approximation scheme which makes a meaningful comparison possible. It will be especially useful for future quantitative studies.

Obviously, distinguishing between those models with observations is more than challenging. First, because there exist degeneracies, for given overtone and multipole numbers, between the models—when taking into account that the values of the parameters controlling the deformation are unknown. Second, because the intrinsic characteristics of the observed black holes are also unknown, which induces other degeneracies. In addition, this study should be extended to Kerr black holes, which also add some degeneracies in addition to the complexity.

Some interesting trends can, however, be underlined. For all models, the effects of modifying the gravitational theory are more important for the real part than for the imaginary part of the complex frequency of the QNMs. Stated in another way, the frequency shift is more important than the change in the damping rate. Obviously, it does not make sense to quantitatively compare the results from various models, as the deformation parameters are different. However, the "trends" are clearly specific to each studied theory and there is no need to define comparable "steps" in the deformation parameters (which do not have the same units anyway) to draw significant conclusions about the directions in which the different models considered deviate from GR. In addition, the sign of the frequency shift, and its dependance upon the overtone and multipole numbers, is characteristic of a given extension of GR. The accurate patterns are never the same, which is an excellent point for phenomenology. It can basically be concluded that a meaningful use of QNMs to efficiently investigate modified gravity requires the measurement of several relaxation modes. This is in principle possible [51], but way beyond the sensitivity of current interferometers. If features beyond GR were to be observed, the direction of the frequency shift in the complex plane would already allow the exclusion of models, as this article shows. The goal of this study was not to perform a detailed analysis of the discrimination capabilities of gravitational wave experiments, it simply aimed at exhibiting the main tendencies for currently considered extended gravity models, as an introduction to this special issue on "probing new physics with black holes".

Author Contributions: Conceptualization, F.M., A.B. and K.M.; methodology, F.M., A.B. and K.M.; software, F.M.; validation, F.M.; formal analysis, F.M., A.B. and K.M.; investigation, F.M. and A.B.; resources, F.M., A.B. and K.M.; writing–original draft preparation, F.M. and A.B.; writing–review and editing, F.M. and A.B.; supervision, A.B.; project administration, A.B.

Funding: K.M. is supported by a grant from the CFM foundation.

Conflicts of Interest: The authors declare no conflict of interest.

References

1. Lovelock, D. The Einstein tensor and its generalizations. *J. Math. Phys.* **1971**, *12*, 498–501. [CrossRef]
2. Chirenti, C. Black hole quasinormal modes in the era of LIGO. *Braz. J. Phys.* **2018**, *48*, 102–109. [CrossRef]
3. Krivan, W.; Laguna, P.; Papadopoulos, P.; Andersson, N. Dynamics of perturbations of rotating black holes. *Phys. Rev. D* **1997**, *D56*, 3395. [CrossRef]
4. Chandrasekhar, S. *The Mathematics of Black Holes*; Oxford University Press: Oxford, UK, 1985; p. 646.
5. Moulin, F.; Barrau, A. Quasinormal modes of black holes in a toy-model for cumulative quantum gravity. *Phys. Lett. B* **2019**, *795*, 346–350.
6. Kokkotas, K.D.; Schmidt, B.G. Quasi-normal modes of stars and black holes. *Living Rev. Relat.* **1999**, *2*, 2. [CrossRef]
7. Nollert, H.P. Quasinormal modes: The characteristic 'sound' of black holes and neutron stars. *Class. Quantum Gravity* **1999**, *16*, R159. [CrossRef]

8. Berti, E.; Cardoso, V.; Yoshida, S. Highly damped quasinormal modes of Kerr black holes: A complete numerical investigation. *Phys. Rev. D* **2004**, *D69*, 124018. [CrossRef]
9. Dorband, E.N.; Berti, E.; Diener, P.; Schnetter, E.; Tiglio, M. A numerical study of the quasinormal mode excitation of Kerr black holes. *Phys. Rev. D* **2006**, *D74*, 084028. [CrossRef]
10. Konoplya, R.A. Quasinormal behavior of the D-dimensional Schwarzshild black hole and higher order WKB approach. *Phys. Rev. D* **2003**, *D68*, 024018. [CrossRef]
11. Mashhoon, B. Quasinormal modes of a black hole. In Proceedings of the 3rd Marcel Grossmann Meeting on the Recent Developments of General Relativity, Shanghai, China, 30 August–2 September, 1982; pp. 599–608.
12. Schutz, B.F.; Will, C.M. Black hole normal modes: A semianalytic approach. *Astrophys. J.* **1985**, *291*, L33–L36. [CrossRef]
13. Iyer, S.; Will, C.M. Black-hole normal modes: A WKB approach. I. foundations and application of a higher-order WKB analysis of potential-barrier scattering. *Phys. Rev. D* **1987**, *D35*, 3621. [CrossRef]
14. Iyer, S. Black-hole normal modes: A WKB approach. II. Schwarzschild black holes. *Phys. Rev. D* **1987**, *D35*, 3632. [CrossRef] [PubMed]
15. Kokkotas, K.D.; Schutz, B.F. Black-hole normal modes: A WKB approach. III. The Reissner-Nordström black hole. *Phys. Rev. D* **1988**, *D37*, 3378. [CrossRef] [PubMed]
16. Konoplya, R.A. Towards constraining of the Horava–Lifshitz gravities. *Phys. Lett. B* **2009**, *B679*, 499–503. [CrossRef]
17. Konoplya, R.A.; Zhidenko, A. Quasinormal modes of black holes: From astrophysics to string theory. *Rev. Mod. Phys.* **2011**, *83*, 793. [CrossRef]
18. Konoplya, R.A.; Zhidenko, A.; Zinhailo, A.F. Higher order WKB formula for quasinormal modes and grey-body factors: Recipes for quick and accurate calculations. *Class. Quantum Gravity* **2019**, *36*, 155002. [CrossRef]
19. Blázquez-Salcedo, J.L.; Macedo, C.F.B; Cardoso, V.; Ferrari, V.; Gualtieri, L.; Khoo, F.S.; Kunz, J.; Pani, P. Perturbed black holes in Einstein-dilaton-Gauss-Bonnet gravity: Stability, ringdown, and gravitational-wave emission. *Phys. Rev. D* ***2016***, *D94*, 104024.
20. Blázquez-Salcedo, J.L.; Khoo, F.S.; Kunz, J. Quasinormal modes of Einstein-Gauss-Bonnet-dilaton black holes. *Phys. Rev. D* **2017**, *D96*, 064008 . [CrossRef]
21. Chen, C.Y.; Bouhmadi-López, M.; Chen, P. Probing Palatini-type gravity theories through gravitational wave detections via quasinormal modes. *Eur. Phys. J. C* **2019**, *C79*, 63. [CrossRef]
22. Chen, C.Y.; Chen, P. Gravitational perturbations of non-singular black holes in conformal gravity. *Phys. Rev. D* **2019**, *D99*, 104003. [CrossRef]
23. Hatsuda, Y. Quasinormal Modes of Black Holes and Borel Summation. Available online: https://arxiv.org/abs/1906.07232 (accessed on 19 September 2019).
24. D'Amico, G.; de Rham, C.; Dubovsky, S.; Gabadadze, G.; Pirtskhalava; D.; Tolley, A.J. Massive cosmologies. *Phys. Rev. D* **2011**, *D84*, 124046.
25. De Rham, C.; Gabadadze, G. Generalization of the Fierz-Pauli action. *Phys. Rev. D* **2010**, *D82*, 044020. [CrossRef]
26. De Rham, C.; Gabadadze, G.; Tolley, A.J. Resummation of massive gravity. *Phys. Rev. Lett.* **2011**, *106*, 231101. [CrossRef] [PubMed]
27. Hassan, S.F.; Rosen, R.A. On non-linear actions for massive gravity. *J. High Energy Phys.* **2011**, *7*, 9. [CrossRef]
28. De Rham, C. Massive gravity. *Living Rev. Relat.* **2014**, *17*, 7. [CrossRef] [PubMed]
29. Camara dS, U.; Constantinidis, C.P.; Sotkov, G.M. New massive gravity holography. *Int. J. Mod. Phys.* **2013**, *A28*, 1350073.
30. Ghosh, S.G.; Tannukij, L.; Wongjun, P. A class of black holes in dRGT massive gravity and their thermodynamical properties. *Eur. Phys. J.* **2016**, *C76*, 119. [CrossRef]
31. Eslam Panah, B.; Hendi, S.H.; Ong, Y.C. Black Hole Remnant in Massive Gravity. 2018. Available online: https://arxiv.org/abs/1808.07829v2 (accessed on 19 September 2019).
32. Moffat, J.W. Scalar-Tensor-Vector gravity theory. *J. Cosmol. Astropart. Phys.* **2006**, *0603*, 004. [CrossRef]
33. Moffat, J.W. Black holes in modified gravity (MOG). *Eur. Phys. J. C* **2015**, *C75*, 175. [CrossRef]
34. Manfredi, L.; Mureika, J.; Moffat, J. Quasinormal modes of modified gravity (MOG) black holes. *Phys. Lett. B* **2018**, *B779*, 492. [CrossRef]
35. Horava, P. Quantum Gravity at a Lifshitz Point. *Phys. Rev.* **2009**, *D79*, 084008.

36. Colgain, E.O.; Yavartanoo, H. Dyonic solution of Hořava-Lifshitz gravity. *J. High Energy Phys.* **2009**, *8*, 21. [CrossRef]
37. Kehagias, A.; Sfetsos, K. The black hole and FRW geometries of non-relativistic gravity. *Phys. Lett.* **2009**, *B678*, 123. [CrossRef]
38. Lu, H.; Mei, J.; Pope, C.N. New black holes in five dimensions. *Nuclear Phys.* **2009**, *B806*, 436. [CrossRef]
39. Chen, S.; Jing, J. Quasinormal modes of a black hole in the deformed Hořava-Lifshitz gravity. *Phys. Lett. B* **2009**, *B687*, 124. [CrossRef]
40. Donoghue, J.F. Leading quantum correction to the Newtonian potential. *Phys. Rev. Lett. B* **1994**, *72*, 2996. [CrossRef]
41. Donoghue, J.F. General relativity as an effective field theory: The leading quantum corrections. *Phys. Rev. D* **1994**, *D50*, 3874–3888. [CrossRef]
42. Bjerrum-Bohr, N.E.J.; Donoghue, J.F.; Holstein, B.R. Quantum corrections to the Schwarzschild and Kerr metrics. *Phys. Rev. D* **2003**, *D68*, 084005. [CrossRef]
43. Bjerrum-Bohr, N.E.J.; Donoghue, J.F.; Holstein, B.R. Quantum gravitational corrections to the nonrelativistic scattering potential of two masses. *Phys. Rev. D* **2003**, *D67*, 084033. [CrossRef]
44. Bjerrum-Bohr, N.E.J.; Donoghue, J.F.; Holstein, B.R.; Planté, L.; Vanhove, P. Bending of light in quantum gravity. *Phys. Rev. Lett.* **2015**, *114*, 061301. [CrossRef]
45. Bargueño, P.; Medina, S.B.; Nowakowski, M.; Batic, D. Quantum mechanical corrections to the Schwarzschild black hole metric. *Eur. Phys. Lett.* **2017**, *117*, 60006. [CrossRef]
46. Ashtekar, A. Introduction to loop quantum gravity. *Lect. Notes Phys.* **2013**, *863*, 31.
47. Rovelli, C. Zakopane Lectures on Loop Gravity. Available online: https://arxiv.org/abs/1102.3660 (accessed on 19 September 2019).
48. Perez, A. Black holes in loop quantum gravity. *Rept. Prog. Phys.* **2017**, *80*, 126901. [CrossRef] [PubMed]
49. Barrau, A.; Martineau, K.; Moulin, F. A status report on the phenomenology of black holes in loop quantum gravity: Evaporation, tunneling to white holes, dark matter and gravitational waves. *Universe* **2018**, *4*, 102. [CrossRef]
50. Alesci, E.; Modesto, L. Hawking radiation from loop black holes. *J. Phys. Conf. Ser.* **2012**, *360*, 012036. [CrossRef]
51. Sathyaprakash, B.; Abernathy, A.; Acernese, F.; Ajith, P.; Allen, B.; Amaro-Seoane, P.; Andersson, N.; Aoudia, S.; Arun, K.; Astone, P.; et al. Scientific objectives of Einstein telescope. *Class. Quantum Gravity* **2012**, *29*, 124013. [CrossRef]

3.3.7 Les modes quasi normaux pour un modèle jouet de trou noir avec des effets quantiques cumulatifs

Nous avons vu précédemment que des effets quantiques pouvaient exister et se cumuler en dehors de l'horizon. Dans cet article, nous étudions si ces effets quantiques pourraient être perçus dans les modes quasi-normaux. Pour celà nous investiguons un "modèle jouet" développé dans [76]. On considère un trou noir de Schwarzschild, avec des effets quantiques qui ont une empreinte sur la métrique à l'extérieur de l'horizon des événements. Le paramètre quantique qui décrit ces effets est

$$q(r) = l_{Pl}\mathcal{R}\tau = \frac{M}{r^3}\left(1 - \frac{2M}{r}\right)^{1/2} t \tag{3.106}$$

avec $\mathcal{R}$ le scalaire de Kretschmann, décrivant l'échelle de courbure, τ le temps propre et t le temps de Schwarzschild. Ce paramètre est maximal à la distance $r = 2M(1 + \frac{1}{6})$. Les effets quantiques sont représentés par une Gaussienne centrée en ce point telle que la métrique modifiée (3.92) s'écrit

$$f(r) = \left(1 - \frac{2M}{r}\right)\left(1 + Ae^{-\frac{(r-\mu)^2}{2\sigma^2}}\right)^2. \tag{3.107}$$

Cette forme particulière de métrique effective est justifiée seulement pour tenter de dépeindre les effets quantiques. Le paramètre μ décrit la distance où les effets seraient maximum. Le paramètre σ désigne l'écart-type qui caractérise l'étalement de des effets sur la métrique. Le but de cet article est de voir la tendance générale, qualitative, que les effets quantiques pourraient présenter par rapport à la théorie classique. Pour ce faire nous avons calculer les QNMs pour la métrique (3.107) avec la méthode WKB au 6ème ordre.

Dans la Figure 1, on observe la valeur des QNMs pour Schwarzschild et pour le modèle jouet considéré. La différence relative des fréquences propres entre ces deux modèles $\mathrm{Re}(\Delta\omega/\omega)$ est représentée sur la Figure 2. Elle est donnée en fonction de μ et σ. La différence est maximale lorsque la Gaussienne est centrée en $\mu = 3M$. Ceci n'est pas surprenant étant donné que cela correspond à la sphère de photon (le maximum du potentiel). Dans la Figure 3, on observe le déplacement relatif de la partie imaginaire $\mathrm{Im}(\Delta\omega/\omega)$. L'amplitude A de l'équation (3.107) représente le poids de l'effet quantique, qui sera d'autant plus grand que l'accumulation est pérenne. On a pu vérifier que le déplacement des QNMs s'effectue de façon linéaire par rapport à A. On $\mathrm{Re}(\Delta\omega/\omega) = xA$ et $\mathrm{Im}(\Delta\omega/\omega) = yA$. On observe sur les Figures 5, 6, 7 et 8 comment varient x et y en fonction de ℓ, pour différentes valeurs de μ et de σ. Sachant que la différence relative et que les coefficients de pente sont de l'ordre de 1, l'amplitude est du même ordre également. L'amplitude A peut être grossièrement apparentée au paramètre quantique q et les effets quantiques sont maximums pour

$$q_{max} = \left(\frac{3}{7}\right)\sqrt{\frac{1}{7}}\frac{t}{M^2}. \tag{3.108}$$

En fixant t à l'âge de l'univers, on remarque que les effets quantiques sont observables pour un trou noir de 10^{-8} masse solaire. Les trous noirs qu'on observe actuellement sont bien plus massifs cependant il est intéressant de noter que les effets quantiques apparaissent pour des masses bien plus élevées que celle de Planck.

Cet article a été publié dans *Physics Letters B* [77].

Physics Letters B 795 (2019) 346–350

Contents lists available at ScienceDirect

Physics Letters B

www.elsevier.com/locate/physletb

Quasinormal modes of black holes in a toy-model for cumulative quantum gravity

Aurélien Barrau *, Killian Martineau, Jeremy Martinon, Flora Moulin

Laboratoire de Physique Subatomique et de Cosmologie, Université Grenoble-Alpes, CNRS/IN2P3, 53, avenue des Martyrs, 38026 Grenoble cedex, France

ARTICLE INFO

Article history:
Received 31 May 2019
Received in revised form 13 June 2019
Accepted 15 June 2019
Available online 18 June 2019
Editor: H. Peiris

ABSTRACT

The idea that quantum gravity effects might "leak" outside the horizon of a black hole has recently been intensively considered. In this study, we calculate the quasinormal modes as a function of the location and amplitude of a generic metric perturbation distorting to the Schwarzschild spacetime. We conclude on the possible observability of quantum metric corrections by current and future gravitational wave experiments.

1. Introduction

Naively, quantum gravity is expected to show up at very small physical scales, around the Planck length (see [1] for a recent review of the phenomenology of quantum gravity). This is indeed where predictions become precise and might lead to a clear discrimination between models. In the black hole (BH) sector, it has therefore been widely believed that quantum gravity effects are confined to the vicinity of the central singularity. This is clearly the most conservative and natural hypothesis. In such a case, quantum modifications to the spacetime structure are screened by the event horizon and the external observer is not expected to notice any measurable effect, at least for macroscopic black holes. In this article, we focus on a different perspective, namely the possibility that quantum corrections to the metric "leak" outside the horizon, even for stellar or supermassive BHs. This is obviously motivated by phenomenological reasons. There are, however, quite good physical motivations to consider quantum gravity effects well beyond the vicinity of the singularity. Studying their impact, in a very simple model, on the ringdown phase of BHs is the purpose of this study.

It has recently been argued in [2] and [3] that the observation of black holes with the Event Horizon Telescope might reveal quantum gravity effects. Consistency between general relativity (GR) and quantum mechanics (QM) might require quantum effects at very large scale. Interestingly, the authors suggest that the time dependence of the shape and size of the shadow that a black hole casts on its surrounding emission might be seen around the BH at the center of the M87 galaxy (which has recently been effectively observed [4,5]). On the extreme other side, in the firewall proposal, the usual geometry might break down a Planck length away from the horizon [6,7]. Many other possibilities with strong metric modifications outside the horizon (or what replaces it) have been considered: gravastars [8], fuzzballs where string theory configurations replace the smooth manifold outside the horizon [9], or massive remnants [10]. The study of maximally entangled states of black holes has even shed a new light on the possibility of more drastic geometric effects far away from the horizon [11]. To give a final example, bouncing black holes – with quite different timescales – are also intensively considered [12,13].

In this article, we focus on a different approach which is based on heuristic considerations [14]. This is to be considered as a toy-model or a kind of "prototype" of what could be expected in optimistic quantum gravity scenarii. Our aim is to calculate the displacement of quasinormal modes and quantify the amplitude of the metric modification that would be required for an experimental detection. This might be used beyond this specific model. Focusing only on non-rotating BHs we do not search for accurate results, that would be meaningless at this stage, but just try to estimate the orders of magnitude for future studies. In the next section we briefly explain the method used to evaluate the frequency and amplitude of the ringing modes of BHs. Then, we explain the model used and explicitly show our results.

* Corresponding author.
E-mail address: barrau@in2p3.fr (A. Barrau).

https://doi.org/10.1016/j.physletb.2019.06.033

2. Quasinormal modes

Quasinormal modes (QNMs) are the decaying modes of black holes. As BHs are vacuum solutions of the Einstein field equation, QNMs can be regarded as the intrinsic vibrational and damping properties of spacetime itself. After a BH has been perturbed, three phases can be distinguished: the transient event, the quasinormal mode ringdown, and the damped tail.

The ringdown phase of a BH does not lead to precisely "normal" modes because the system looses energy through gravitational waves. The wave equation for the metric perturbation is unusual because of its boundary conditions: the wave should be purely outgoing at infinity and purely ingoing at the BH horizon. The radial part of the oscillation can be written (see [15] for an intuitive introductory review) as $\phi \propto e^{-i\omega t} = e^{-i(\omega_R + i\omega_I)t}$ where the complex pulsation ω decomposes in a real part ω_R and an imaginary part ω_I, which is the inverse timescale of the damping. The process is stable only when $\omega_I < 0$. Technically, the calculation of QNMs is quite reminiscent of the one of greybody factors (see, *e.g.*, [16] for a recent derivation with a quantum-gravity modified metric) which describes the scattering of quantum fields in a BH background.

The perturbations of the Schwarzschild metric are of two different types. One is called "axial", it gives small values to the metric coefficients that were zero, inducing a frame dragging and rotation of the black hole. The other is called "polar" and gives small increments to the already non-zero metric coefficients. They are governed by two different equations. Perturbations with the axial parity are given by the Regge-Wheeler equation with the potential

$$V_\ell^{\mathrm{RG}}(r) = \left(1 - \frac{2M}{r}\right)\left[\frac{\ell(\ell+1)}{r^2} - \frac{6M}{r^3}\right], \tag{1}$$

while perturbations with the polar parity are given by the Zerilli equation with potential

$$V_\ell^{\mathrm{Z}}(r) = \frac{2}{r^3}\left(1 - \frac{2m}{r}\right) \times \times \frac{9M^3 + 3a^2Mr^2 + a^2(1+a)r^3 + 9M^2ar}{(3M + ar)^2}, \tag{2}$$

where $a = \ell(\ell+1)/2 - 1$. For gravitational perturbations, one needs $\ell \geq 2$. Importantly, those equations have the same spectrum of quasinormal modes. This isospectrality property [17] is not always true in modified gravity (those considerations are well beyond the scope of this article and will be studied in another paper [18]). Quasinormal modes are characterized by their overtone number n and their multipole number ℓ. For example, the fundamental quadrupolar mode ($n = 0$ and $\ell = 2$) for a Schwarzschild BH is given by $M\omega \approx 0.374 - 0.0890i$.

The calculation of quasinormal modes is nearly an art in itself (see [19,20] for historical reviews and [21,22] for an example of more recent results based on numerical approaches). In this study, we use a WKB approach described in [23] for D-dimensional BHs. The WKB method for QNMs was first introduced in [24–27] and has then been widely developed. The WKB formalism is very useful to obtain good approximations without having to rely on heavy numerical techniques. The higher the multipole number and the lower the overtone, the better the accuracy. We restrict ourselves to $n < l$ as the approximations otherwise break down. Details on the validity of the WKB approximation can be found in [24] but, in any case, it requires the multipole number to be smaller than (or equal to, if the accuracy requirement is relaxed) the overtone number, otherwise the basic condition $|k'| \ll k^2$ (where k^2 is the potential of the considered effective Schrödinger equation) does not hold.

In order to have a good numerical accuracy, we have used the 6th order WKB method developed by Konoplya. It is presented in details in [23] (see also [28]). This allows one to recast the potential appearing in the effective Schrödinger equation ($\frac{d^2\Psi}{dx^2} = k(x)\Psi(x)$) felt by gravitational perturbations in the form

$$\frac{ik_0}{\sqrt{2k_0''}} - \Lambda_2 - \Lambda_3 - \Lambda_4 - \Lambda_5 - \Lambda_6 = n + \frac{1}{2}, \tag{3}$$

where the terms Λ_i are complicated – but known – expressions given in [23] whereas k_0 stands for the maximum of the potential and the derivative is to be understood with respect to the tortoise coordinate r_* (defined by $dr_* = dr/f$ where f is the metric function).

3. The model and its consequences

We now focus on the toy model developed in [14]. The idea is very simple. The curvature scale is of the order of $l_R \sim \mathcal{R}^{-1/2}$, where the Kretschmann scalar is $\mathcal{R}^2 := R_{\mu\nu\rho\lambda}R^{\mu\nu\rho\lambda}$. If one estimates the intensity of quantum gravitational effects through the ratio of Planck length over the curvature scale, the result is vanishingly small for stellar or supermassive BHs. This vision however disregards possible cumulative effects (also considered in [29–32]). Dimensional arguments lead to the conclusion that the "quantumness" of spacetime, integrated over a proper time τ, might be given by $q = l_P\ \mathcal{R}\ \tau$. As the proper time is related to the Schwarzschild time by

$$\tau = \sqrt{1 - \frac{2M}{r}}\, t, \tag{4}$$

one is led to

$$q(r) = \frac{M}{r^3}\left(1 - \frac{2M}{r}\right)^{\frac{1}{2}} t. \tag{5}$$

Throughout all this study, we use Planck units. The maximum of this function is reached for $r = 2M\left(1 + \frac{1}{6}\right)$ and this is therefore where quantum gravity effects could be expected to be intense.

The arguments previously given are obviously purely heuristic and should be considered as a rough indication of what might happen when time-integrated quantum corrections are optimistically considered. To remain quite generic, we parametrize a possible metric modification outside the horizon by a simple Gaussian function:

$$ds^2 = -f(r)dt^2 + f^{-1}(r)dr^2 - r^2d\Omega^2, \tag{6}$$

with

$$f(r) = \left(1 - \frac{2M}{r}\right)\left(1 + Ae^{-\frac{(r-\mu)^2}{2\sigma^2}}\right)^2. \tag{7}$$

This Gaussian truncation of the Schwarzschild metric is *not* justified by any serious theoretical arguments. It should be seen as an effective metric encoding possible cumulative quantum effects outside the horizon. In addition it has the advantage not to shift the event horizon position. By varying the parameters A, μ, σ, one can explore different shapes and positions for the "quantum bump". In the following, we shall quantify the displacement of the real and imaginary parts of the QNMs as a function of the parameters (μ and σ are expressed in units of M).

The complex frequencies are displayed in Fig. 1. The black dots correspond to the general relativistic case whereas the blue ones,

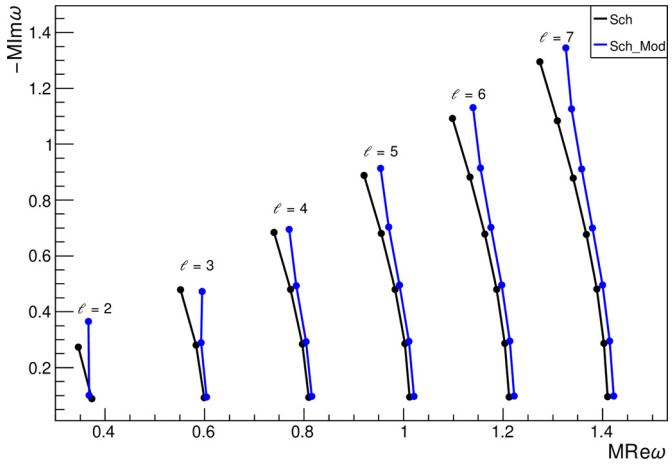

Fig. 1. Quasinormal mode complex frequencies for different multipolar orders (from $\ell = 2$ to $\ell = 7$ from the left to the right) and for different overtone numbers n (increasing from the lower points to the upper points). The black dots on the left correspond to the usual Schwarzschild case and the blue dots on the right correspond to the modified metric with $\mu/M = 2.3$ and $\sigma/M = 1.5$.

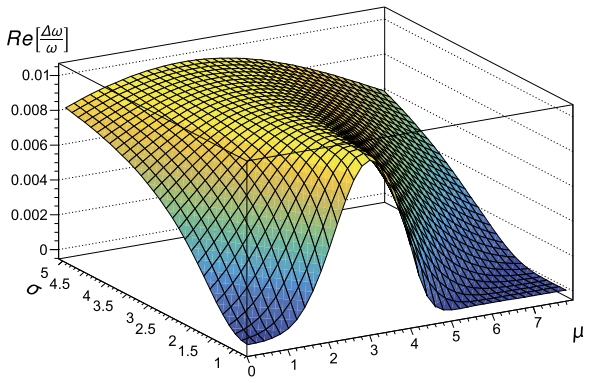

Fig. 2. Relative displacement of the real part of the quasinormal mode ($\ell = 8, n = 0$) as a function of μ and σ for $A = 0.01$.

on the right, correspond to the considered modified case with $\mu = (7/6)R_S$, $A = 0.01$, and $\sigma/M = 1.5$.

In Fig. 2, the relative displacement of the real part of the quasinormal mode ($\ell = 8, n = 0$) is displayed as a function of μ and σ for $A = 0.01$. The trend does not radically depend on the specific mode chosen. We have therefore plotted here a quite high multipolar number as the WKB approximation is more reliable in this case. Interestingly – but not that surprisingly – it appears that the maximum displacement is obtained for $\mu \approx 3M$. In the limit of very large l, the value tends exactly to $3M$, which corresponds to the photon sphere and to the maximum of the potential. We have also considered in this figure a case where the maximum of the quantum correction is inside the horizon. Then, only the "tail" of the Gaussian does affect the external spacetime. Even if the effect is smaller, it is still clearly non-vanishing. Interestingly the 2-dimensional surface is actually an ensemble of Gaussian functions whose width on the μ axis happens to be (non trivially) equal to the considered value of σ.

In Fig. 3, the relative displacement of the imaginary part of the quasinormal mode ($\ell = 8, n = 0$) is displayed as a function of μ and σ for $A = 0.01$. For quite low values of σ, the displacement can be either positive or negative for different values of μ. This means that depending on its position the "metric bump" can either increase on decrease the damping of gravitational waves.

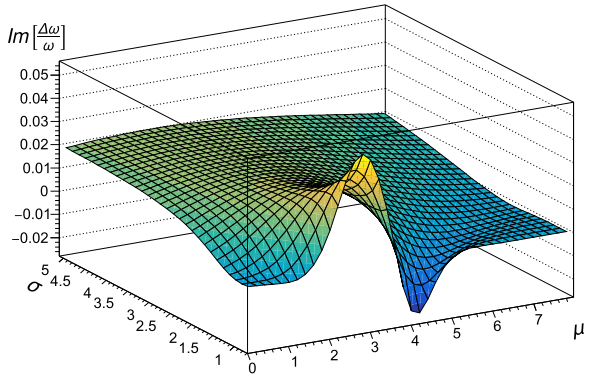

Fig. 3. Relative displacement of the imaginary part of the quasinormal mode ($\ell = 8, n = 0$) as a function of μ and σ for $A = 0.01$.

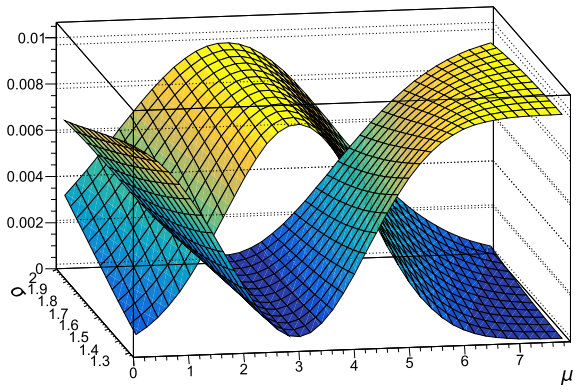

Fig. 4. Relative displacement of the real part of the quasinormal mode ($\ell = 8, n = 0$) as a function of μ and σ for $A = 0.01$ (upper curve at $\mu = 3$) and $A = -0.01$.

Finally, Fig. 4 shows the influence of the sign of the parameter A. The displacement is basically symmetrical.

For most of the considered parameter space, the displacement of the real part – that is of the frequency – is of the same order than the one of the imaginary part – that is of the damping time. The easiest effect to measure is probably a frequency shift which happens to be always positive. Quite obviously, when the metric perturbation is very wide, its precise position looses any notable influence.

4. Observability

Although gravitational waves have been "detected" decades ago thanks to the Hulse-Taylor binary pulsar, the recent LIGO-Virgo detections (see [33] for the seminal paper and [34] for a first catalogue) have completely changed the game. Real astrophysical objects have spin and a modified Kerr solution should be considered, which is far beyond this prospective study. However, the global trends are expected to be the same and the orders of magnitude of the effects should be correct. Surprisingly, the very first event measured, GW150914, has already led to a detection of the fundamental quasinormal mode. It is not obvious to determine precisely the accuracy at which the characteristics of the QNMs are constrained by the current measurements. A relative accuracy of 50% is a conservative estimate. In the future, the Einstein Telescope (ET) should lead to a one order of magnitude better precision [35].

The most important parameter for this study is obviously the constant A which determines the amplitude of the correction. We have checked that the displacement of the QNMs complex fre-

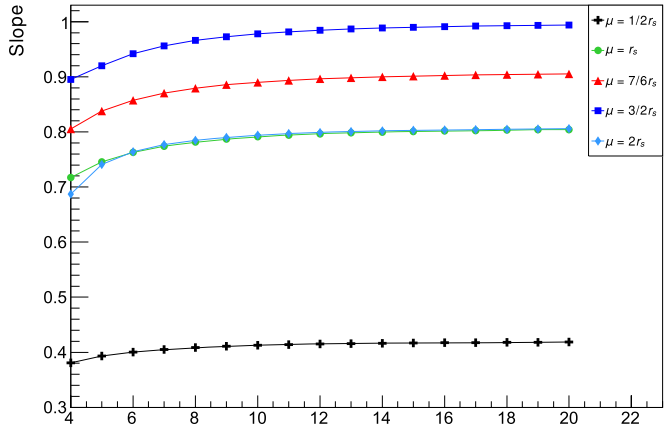

Fig. 5. Slope x of the real part of the quasinormal modes ($n = 0$) relative frequency evolution as a function of A for $\sigma/M = 1.5$. The different curves correspond to different values of μ.

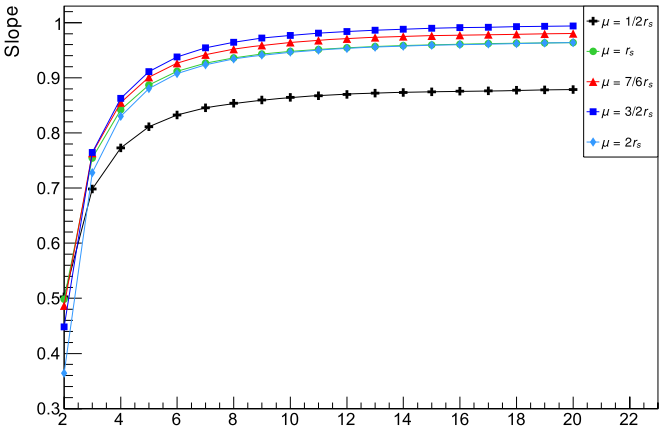

Fig. 7. Slope x of the real part of the quasinormal modes ($n = 0$) relative frequency evolution as a function of A for $\sigma/M = 4$. The different curves correspond to different values of μ.

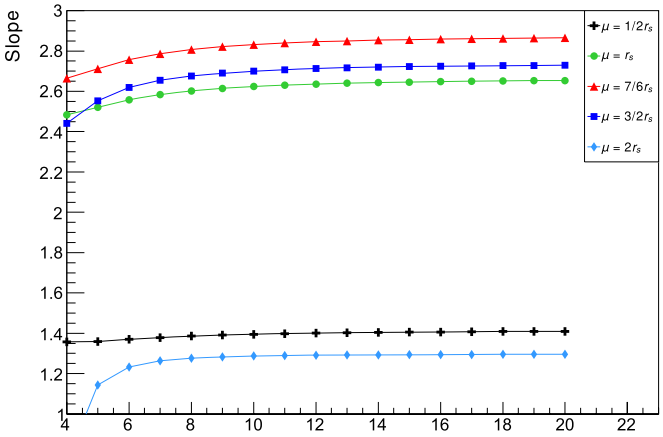

Fig. 6. Slope y of the imaginary part of the quasinormal modes ($n = 0$) relative frequency evolution as a function of A for $\sigma/M = 1.5$. The different curves correspond to different values of μ.

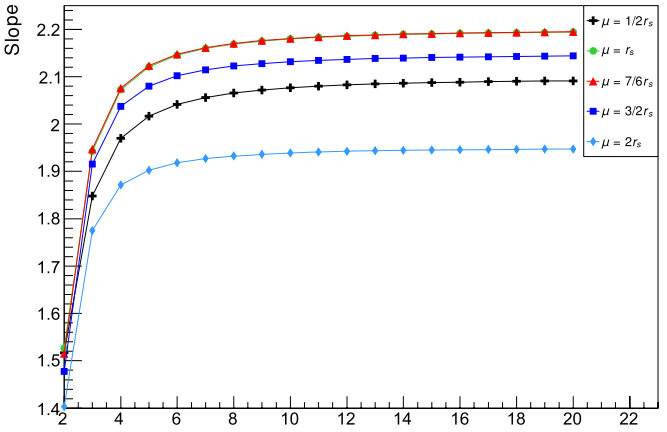

Fig. 8. Slope y of the imaginary part of the quasinormal modes ($n = 0$) relative frequency evolution as a function of A for $\sigma/M = 4$. The different curves correspond to different values of μ.

quency is linear as a function of A over the interesting range. In Fig. 5, we plot the slope of the real part of the QNM displacement versus A (*i.e.* the x parameter of $Re(\Delta\omega/\omega) = xA$) as a function of ℓ, for $\sigma/M = 1.5$. The different curves correspond to different values of the position μ of the quantum bump. In Fig. 6, the very same thing is represented for the imaginary part of the QNM (*i.e.* the y parameter of $Im(\Delta\omega/\omega) = yA$). In Fig. 7 and Fig. 8, the value $\sigma/M = 4$ is instead chosen. It should be pointed out that in some cases the lowest values of ℓ are not displayed as the WKB approximation breaks down and calculations could therefore be dubious.

Let us now get an order of magnitude of how those estimates relate to the toy model previously considered. As the x and y slopes are of order one, and as the relative displacement that could be measured is also of order one, this means that the A parameter has to be of order unity so that the kind of quantum gravity effects studied here could be measured. If A is assumed to be roughly comparable to the "quantumness" q introduced in the second section, one is led to the conclusion that q should be of order one. It is easy to check that

$$q_{max} = \left(\frac{3}{7}\right)^3 \sqrt{\frac{1}{7}}\frac{t}{M^2}. \tag{8}$$

If one sets t to be the age of the Universe, the mass value required so that the quantum gravity effects can be observed is of the order of 10^{-8} (or less) solar mass, that is roughly the mass of the Moon. Although far smaller than the mass of stellar black holes, this value is not ridiculously small and way higher than the Planck mass. An important property of the QNMs lies in the fact that the relevant value is the one of $M\omega$: it is the product of the mass by the frequency that has a given (complex) value. The characteristics of the QNMs of a lighter BH are exactly the same than those of a heavier one, they are simply shifted to higher frequencies by the mass ratio. Some quantum corrections might explicitly break this scaling law. This is the case of the Hayward metric considered below.

It should first be pointed out that the work presented here aims at being quite generic and is not directly linked with the proposal [14]. The plots previously shown can be used to get an estimate of the QNMs displacement for any model with a roughly gaussian modification to the metric. In addition, and very speculatively, it could be argued that the maximum possible time to be used to evaluate the mass (the higher the time, the higher the mass) is not necessarily bounded by the age of the Universe: in quantum gravity a "bounce" is possible [36] and black holes could survive during this bounce [37]. In principle it is therefore conceivable that a time much larger than the inverse Hubble parameter could used [38,39], leading to measurable quantum gravity effects in QNMs at much higher masses

5. The Hayward metric

Recently, an effective metric for Planck stars [13] has been proposed in [40]. The idea is to cure two usual inconsistencies of most metrics: the absence of a correct treatment of the time dilatation between the center and infinity and the failure to reproduce 1-loop quantum corrections (as calculated *e.g.* in [41]). As a step in this direction, the authors make use of the Hayward metric (revived in a quantum gravity context [42]):

$$F(r) = 1 - \frac{2m(r)}{r}\,. \tag{9}$$

Several proposals were made for the function $m(r)$. We consider here the original version [43] where

$$m(r) = \frac{M r^3}{r^3 + 2ML^2}, \tag{10}$$

where L has the dimensions of a length. We consider only the case where $L < \frac{4}{3\sqrt{3}}M$, otherwise there is no horizon. We have investigated the displacement of QNMs as a function of L – which intuitively quantifies the scale of "quantumness" – for a given mass. As expected, the minimal required value of L, for a given relative QNM move, is proportional to M. If we require $(\frac{\Delta\omega}{\omega})$ to be of the order of a few percent (that is in the ET sensitivity range), the minimum value of L is of the order of 0.7 mass units. More specifically $(\frac{\Delta\omega}{\omega}) \sim 5\%$ is achieved for $L/M \sim 0.72$. For a macroscopic BH, this is much larger than the Planck length and this means that in such approaches the quantum modifications would need to be extending substantially beyond the usually assumed length scale.

6. Conclusion and prospects

We have shown that if quantum gravity effects leak outside the horizon of a Schwarzschild black hole, the quasinormal modes can – as expected – be substantially modified. Using a gaussian truncation of the metric structure, we have studied the influence of all the parameters describing the perturbations. In particular, we have quantified the amplitude of the quantum bump required for observation. Using a toy-model, we have translated the derived values into an upper limit on the mass leading to observable effects.

In the future, this approach should be refined by considering a rotating black hole. It would also be important to estimate de possible degeneracies: could the change in frequency and damping rate mimic a usual BH of different mass and spin?

Finally, it would be welcome to consider more realistic metrics based on heuristic quantum gravity arguments, in particular based either on loop quantum gravity black holes (see [44] for a review) of on string black holes (see [9] for interesting new ideas).

Acknowledgements

K.M is supported by a grant from the CFM foundation. The authors thank deeply R.A. Konoplya who provided us with his code.

References

[1] A. Barrau, C. R. Phys. 18 (2017) 189, arXiv:1705.01597.
[2] S.B. Giddings, D. Psaltis, Phys. Rev. D 97 (2018) 084035, arXiv:1606.07814.
[3] S.B. Giddings, arXiv:1904.05287, 2019.
[4] K. Akiyama, et al., Event Horizon Telescope, Astrophys. J. 875 (2019) L1.
[5] K. Akiyama, et al., Event Horizon Telescope, Astrophys. J. 875 (2019) L6.
[6] A. Almheiri, D. Marolf, J. Polchinski, J. Sully, J. High Energy Phys. 02 (2013) 062, arXiv:1207.3123.
[7] A. Almheiri, D. Marolf, J. Polchinski, D. Stanford, J. Sully, J. High Energy Phys. 09 (2013) 018, arXiv:1304.6483.
[8] P.O. Mazur, E. Mottola, Proc. Natl. Acad. Sci. USA 101 (2004) 9545, arXiv:gr-qc/0407075.
[9] S.D. Mathur, arXiv:0810.4525, 2008.
[10] S.B. Giddings, Phys. Rev. D 46 (1992) 1347, arXiv:hep-th/9203059.
[11] J. Maldacena, L. Susskind, Fortschr. Phys. 61 (2013) 781, arXiv:1306.0533.
[12] C. Barceló, R. Carballo-Rubio, L.J. Garay, J. High Energy Phys. 05 (2017) 054, arXiv:1701.09156.
[13] H.M. Haggard, C. Rovelli, Phys. Rev. D 92 (2015) 104020, arXiv:1407.0989.
[14] H.M. Haggard, C. Rovelli, Int. J. Mod. Phys. D 25 (2016) 1644021, arXiv:1607.00364.
[15] C. Chirenti, Braz. J. Phys. 48 (2018) 102, arXiv:1708.04476.
[16] F. Moulin, K. Martineau, J. Grain, A. Barrau, arXiv:1808.00207, 2018.
[17] S. Chandrasekhar, Clarendon, Oxford, UK, 1992, p. 646, Clarendon, Oxford, UK, 1985, p. 646.
[18] Flora Moulin, Aurélien Barrau, Isospectrality of quasinormal modes for black holes beyond Schwarzschild, arXiv:1906.05633 [gr-qc], 2019.
[19] K.D. Kokkotas, B.G. Schmidt, Living Rev. Relativ. 2 (1999) 2, arXiv:gr-qc/9909058.
[20] H.-P. Nollert, Class. Quantum Gravity 16 (1999) R159.
[21] E. Berti, V. Cardoso, S. Yoshida, Phys. Rev. D 69 (2004) 124018, arXiv:gr-qc/0401052.
[22] E.N. Dorband, E. Berti, P. Diener, E. Schnetter, M. Tiglio, Phys. Rev. D 74 (2006) 084028, arXiv:gr-qc/0608091.
[23] R.A. Konoplya, Phys. Rev. D 68 (2003) 024018, arXiv:gr-qc/0303052.
[24] B.F. Schutz, C.M. Will, Astrophys. J. 291 (1985) L33.
[25] S. Iyer, C.M. Will, Phys. Rev. D 35 (1987) 3621.
[26] S. Iyer, Phys. Rev. D 35 (1987) 3632.
[27] K.D. Kokkotas, B.F. Schutz, Phys. Rev. D 37 (1988) 3378.
[28] R.A. Konoplya, A. Zhidenko, A.F. Zinhailo, arXiv:1904.10333, 2019.
[29] C. Rovelli, F. Vidotto, Int. J. Mod. Phys. D 23 (2014) 1442026, arXiv:1401.6562.
[30] A. Barrau, C. Rovelli, Phys. Lett. B 739 (2014) 405, arXiv:1404.5821.
[31] A. Barrau, C. Rovelli, F. Vidotto, Phys. Rev. D 90 (2014) 127503, arXiv:1409.4031.
[32] A. Barrau, F. Moulin, K. Martineau, Phys. Rev. D 97 (2018) 066019, arXiv:1801.03841.
[33] B.P. Abbott, et al., LIGO Scientific, Virgo, Phys. Rev. Lett. 116 (2016) 061102, arXiv:1602.03837.
[34] B.P. Abbott, et al., LIGO Scientific, Virgo, arXiv:1811.12907, 2018.
[35] B. Sathyaprakash, et al., Class. Quantum Gravity 29 (2012) 124013, Erratum: Class. Quantum Gravity 30 (2013) 079501, arXiv:1206.0331.
[36] A. Ashtekar, P. Singh, Class. Quantum Gravity 28 (2011) 213001, arXiv:1108.0893.
[37] T. Clifton, B. Carr, A. Coley, Class. Quantum Gravity 34 (2017) 135005, arXiv:1701.05750.
[38] B. Carr, T. Clifton, A. Coley, arXiv:1704.02919, 2017.
[39] A. Barrau, K. Martineau, F. Moulin, Phys. Rev. D 96 (2017) 123520, arXiv:1711.05301.
[40] T. De Lorenzo, C. Pacilio, C. Rovelli, S. Speziale, Gen. Relativ. Gravit. 47 (2015) 41, arXiv:1412.6015.
[41] N.E.J. Bjerrum-Bohr, J.F. Donoghue, B.R. Holstein, Phys. Rev. D 67 (2003) 084033, Erratum: Phys. Rev. D 71 (2005) 069903, arXiv:hep-th/0211072.
[42] V.P. Frolov, J. High Energy Phys. 05 (2014) 049, arXiv:1402.5446.
[43] S.A. Hayward, Phys. Rev. Lett. 96 (2006) 031103, arXiv:gr-qc/0506126.
[44] A. Barrau, K. Martineau, F. Moulin, Universe 4 (2018) 102, arXiv:1808.08857.

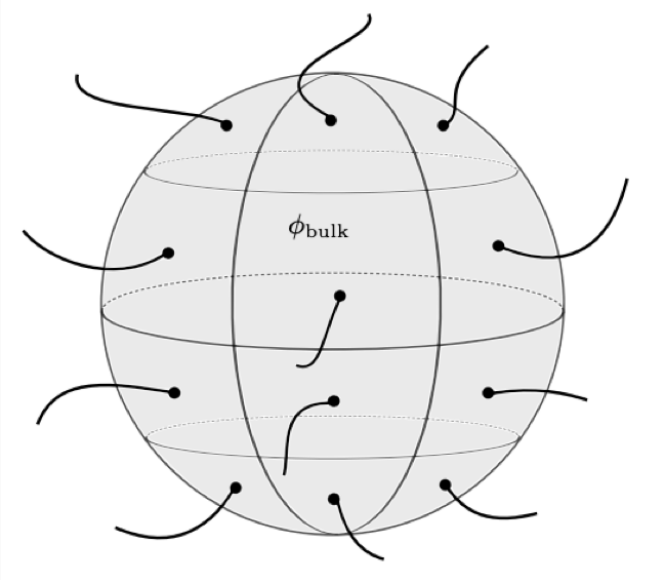

FIGURE 3.2 – La surface d'un trou noir en LQG, caractérisée par l'ensemble des aires qui intersectionnent les liens du réseau de spin à l'horizon du trou noir [78].

3.4 Revue sur les différents aspects des trous noirs en LQG

Dans cette revue, on présente plusieurs caractéristiques associés à la LQG sur la phénoménologie des trous noirs. Certains aspects ont déjà été abordés dans les articles précédents : la phénoménologie des trous noirs en rebond (section 3.1) et la section efficace des trous noirs quantiques à boucles (section 3.2). Le reste ne concerne pas mes travaux directement ainsi je ne vais pas m'étendre sur cette revue. Cependant, je vais tout de même présenter un aspect important.

En LQG, nous avons vu qu'un des résultats majeurs était la quantification de l'aire (1.154). On peut alors définir l'aire d'un trou noir en LQG comme la somme des aires associées aux liens (du réseau de spin) qui intersectent la sphère d'horizon du trou noir (voir Figure 3.2). On a

$$A_j = 8\pi\gamma \sum_{n=1}^{N} \sqrt{j_n(j_n+1)}, \tag{3.109}$$

avec N le nombre de liens qui intersectent la surface. Ainsi l'évaporation d'un trou noir en LQG ne s'effectue pas de façon continue mais par transition d'aires discrètes (parmi les aires autorisées du spectre (1.154)).
Cette structure discrète va se retrouver dans le rayonnement de Hawking. Pour étudier ce phénomène, une simulation Monte Carlo a été effectuée

— une particule aléatoire est choisie selon son poids en dégrées de liberté dans le modèle standard ,

— la probabilité de passer d'une aire A à une autre est décrite par

$$P(A \to A - \delta A) = \Gamma e^{-\delta S}, \tag{3.110}$$

avec Γ qui dépend de la particule et S l'entropie.

— l'énergie de la particule émise donnée par la perte de masse du trou noir : $E = dM$.

Sur la Figure 1 de l'article, on présente le nombre de trous noirs qui devraient être observés afin de distinguer le modèle classique du modèle LQG à partir du spectre de photon émis en fonction de l'erreur relative sur la reconstruction en énergie. La théorie classique décrit la relation entre A et S via l'équation de Hawking-Bekenstein

$$S = \frac{A}{4}. \tag{3.111}$$

En LQG, le paramètre de Barbero-Immirzi γ est un paramètre a priori libre de la théorie. En prenant en compte la dégénérescence de la matière, ce paramètre modifie la relation aire/entropie

$$S = \frac{A}{4} + \sqrt{\frac{\pi A}{6\gamma}} + o(\sqrt{A}). \tag{3.112}$$

Sur la Figure 3, on observe comment le spectre intégré dépend de γ. Le fond du spectre correspond à la partie continue du modèle classique mais à cela s'ajoute pics qui caractérisent la discrétisation du modèle.

La gravité quantique n'est pas élaborée totalement, il existe d'ailleurs plusieurs modèles. Du point de vue expérimental, il semble presque impossible de pouvoir sonder directement des effets de gravité quantique. Mais on observe que grâce aux trous noirs (et également la cosmologie), de tels effets pourraient être observables. Du point vue théorique, la LQG connait encore des difficultés. Néanmoins, à partir de la théorie mère il est déjà possible de décrire des modèles simplifiés auxquels on peut associer de la phénoménologie. Et il apparaît que ces prédictions sont différentes de celle décrites par la RG. Ainsi, la phénoménologie des trous noirs fait de la LQG, non plus un simple modèle mathématiques, mais la fait rentrer dans le domaine de la science grâce à ses prédictions a priori observables.

Cet article a été publié dans *Universe* [79].

universe

MDPI

Article

A Status Report on the Phenomenology of Black Holes in Loop Quantum Gravity: Evaporation, Tunneling to White Holes, Dark Matter and Gravitational Waves

Aurélien Barrau *, Killian Martineau and Flora Moulin

Laboratoire de Physique Subatomique et de Cosmologie, Université Grenoble-Alpes, CNRS-IN2P3 53, Avenue des Martyrs, 38026 Grenoble Cedex, France; martineau@lpsc.in2p3.fr (K.M.); moulin@lpsc.in2p3.fr (F.M.)

* Correspondence: barrau@in2p3.fr

Received: 28 August 2018; Accepted: 21 September 2018; Published: 2 October 2018

Abstract: The understanding of black holes in loop quantum gravity is becoming increasingly accurate. This review focuses on the possible experimental or observational consequences of the underlying spinfoam structure of space-time. It addresses both the aspects associated with the Hawking evaporation and the ones due to the possible existence of a bounce. Finally, consequences for dark matter and gravitational waves are considered.

Keywords: loop quantum gravity; loop quantum cosmology; black holes

1. Introduction

The Planck length is 10^{15}-times smaller than scales probed at colliders. Linking quantum gravity with observations is therefore extremely hard (see, e.g., [1] for a recent review and [2–4] for complementary viewpoints). Most works devoted to the connection of quantum gravity with experiments are focused on cosmology or astroparticle physics. In the cosmological sector, the main goal consists of calculating scalar and tensor power spectra (see, e.g., [5,6]), together with the background dynamics (see, e.g., [7,8]). In the astroparticle physics sector, the main idea is to investigate the possible consequences of the granular structure of space (see, e.g., [9] for a recent investigation).

Although black holes (BH) have been intensively studied in quantum gravity, those investigations were mostly disconnected from observations and focused on consistency issues. Recovering, at the leading order, the Bekenstein–Hawking entropy is, for example, obviously a major requirement for all tentative theories (see, e.g., [10] and the references therein). Curing the central singularity—understood as a classical pathology—is another one (see, e.g., [11,12]). Solving the information paradox (see, e.g., [13] and the references therein) would also be highly desirable (this is clearly connected to the previous issues).

In this article, we focus on black holes as possible probes for loop quantum gravity (LQG). We begin by a very short summary of the basics of black hole physics in this framework. We then switch to consequences for the Hawking evaporation, considering different possible perspectives. The quite recent (within the LQG setting) hypothesis of black holes bouncing into white holes is presented with the possible associated signals. Finally, we critically review the possible links with dark matter and conclude with the prospect for gravitational waves.

2. Basics of Black Holes in Loop Quantum Gravity

The study of black holes is an incredibly fruitful field of theoretical physics. Black holes are simple objects. They are pure geometry. There is no equation of state needed: they are just vacuum solutions

to the Einstein equations. This is their first fundamental characteristic. The second specificity of black holes lies in the fact that they are (classically) scale invariant [14]. They can, in principle, exist at any mass.

As far as quantum gravity is concerned, the major breakthrough came from black hole thermodynamics. Because of the no-hair theorem, in Einstein gravity, the most general stationary black hole geometry is described by the Kerr–Newman (KN) solution with mass M, electric charge q and angular momentum j as the only parameters. One can define three length scales characterizing the BH [14]: $m \equiv GMc^{-2}$, $Q \equiv \sqrt{G}qc^{-2}$ and $a \equiv jM^{-1}c^{-1}$. There exists a BH solution only when $Q^2 + a^2 \leq m^2$. One can show, from the area expression, that:

$$d(Mc^2) = \Theta dA + \Phi dQ + \Omega dj \tag{1}$$

with

$$\Theta \equiv c^4(2GA)^{-1}(r_g - m), \tag{2}$$
$$\Phi \equiv q\, r_g(r_g^2 + a^2)^{-1}, \tag{3}$$
$$\Omega \equiv j\, m^{-1}(r_g^2 + a^2)^{-1}, \tag{4}$$

$r_g = 2m$ being the gravitational radius. The parameters Θ, Φ and Ω can be understood as the surface gravity, the electrostatic potential and the angular momentum.

As Mc^2 is the energy, this equation looks like the first law of thermodynamics $TdS = dE - \Phi dQ - \Omega dj$. This led to the introduction of a temperature:

$$T_H = (2c\hbar/A)\sqrt{M^2 - Q^2 - a^2}, \tag{5}$$

and entropy:

$$S_{BH} = A/4{\ell_P}^2, \tag{6}$$

yielding the evaporation process [15]. The second BH law expresses the fact that the sum of the BH entropy together with the entropy outside the BH cannot decrease (from now on, unless otherwise stated, we use Planck units).

The description of BHs in LQG heavily relies on the concept of isolated horizons (IH) [16–20]. This is an intrinsically quasilocal notion, which has the advantage of not requiring the knowledge of whole spacetime to determine whether horizons are present, as is the case with event horizons. The most important characteristics of isolated horizons are [10]: their quasilocality, the availability of a Hamiltonian description for the sector of GR containing the IH, the possibility of finding physical versions of the laws of BH thermodynamics and the existence of local definitions of the energy and angular momentum.

This article focuses on the consequences and not on the theoretical definition of an LQG BH, but recent pedagogical reviews on BH in LQG can be found, e.g., [21–27].

Very schematically, the isolated horizon plays the role of a boundary for the underlying manifold before quantization. Given the area A of a Schwarzschild BH horizon, the geometry states of the BH horizon arise from a punctured sphere. Each puncture carries quantum numbers (see, e.g., [28–31] for details): two labels (j, m), where j is a spin half-integer carrying information about the area and m is the corresponding projection carrying information about the curvature. They fulfill the condition:

$$A - \Delta \leq 8\pi\gamma \sum_p \sqrt{j_p(j_p + 1)} \leq A + \Delta, \tag{7}$$

where γ is the Barbero–Immirzi parameter entering the definition of LQG (see, e.g., [32]), Δ is the "smearing" area parameter (or coarse-graining scale) used to recover the classical description and p refers to different punctures. In addition, one requires:

$$\sum_p m_p = 0, \tag{8}$$

which means that the horizon has a spherical topology. Many aspects of the BH entropy were studied in this framework, and we shall mention some of them in the following.

3. Modified Hawking Spectrum

One cannot directly measure the entropy of a BH. Therefore, even if some quantum gravity approaches do predict some corrections with respect to the Bekenstein–Hawking law, this can hardly be considered as a smoking gun for observational aspects of quantum geometry. On the other hand, one might observe the evaporation of a black hole. This would require light black holes (the temperature of a solar-mass BH is far below the one of the cosmological microwave background) whose existence is far from obvious. At this stage, the Hawking evaporation of BHs therefore remains purely theoretical (although there are some hints that this could have been observed in analog systems [33]). However, it is in principle observable and might constitute a path toward experimental quantum gravity.

There exist quite a few attempts to deal with evaporating black holes in effective approaches to quantum gravity. Among such attempts, one can mention results derived from the generalized uncertainty principle, which aims at generalizing the Heisenberg uncertainty relation by introducing gravity effects. In this framework, one case shows that there exist a maximum and a minimum temperature for BHs [34–36]. Some models also lead to a vanishing temperature close to the end of the evaporation (see, e.g., [36,37]). The path considered in the following is different and tries to use the exact area spectrum form the full theory. There are no bounds on the temperature (beyond trivial ones), but the energy spectrum of emitted particles can become discrete and keep the footprints of the underlying quantum gravity theory.

3.1. Global Perspective

The first obvious idea to investigate LQG footprints is to consider the deep Planckian regime of an evaporating BH by taking into account the discrete structure of the area operator eigenvalues in LQG. An edge with spin representation j of SU(2) carries an area of eigenvalue:

$$A_j = 8\pi\gamma\sqrt{j(j+1)}, \tag{9}$$

where j is, again, a half-integer. A BH surface punctured by N edges therefore exhibits, as explained previously, a spectrum given by:

$$A_j = 8\pi\gamma \sum_{n=1}^{N} \sqrt{j_n(j_n+1)}, \tag{10}$$

where the sum is carried out over all intersections of the edges with the isolated horizon. As the area spectrum in discrete, BHs can only make discontinuous jumps, and the evaporation spectrum will inevitably be modified.

In [38], a Monte Carlo simulation was carried out to investigate to what extent the associated line structure can be discriminated from the usual continuous (envelope of the) spectrum. The algorithm was based on an improved version of the method given in [39], enhanced by an efficient numeration scheme based on a breadth-first search. The probability for the transition from a BH state to another is expressed as the exponential of the entropy difference, weighted by the greybody factor. As the optical limit was not satisfactory to derive accurate results, the full greybody factor obtained by solving the wave equation in the (classical) Schwarzschild background was used. The simulation was started at 200 A_{Pl}, where A_{Pl} is the Planck area.

At each step n of the simulation, starting from a BH mass M_n, a new mass M_{n+1} is randomly determined within the available spectrum, according to the probability law previously given. A particle

type is then randomly selected from the standard model, according to the weighted number of internal degrees of freedom (and among those with a mass smaller than ΔM). The available energy $M_n - M_{n+1}$ is assigned to this particle, and the process is repeated. The analysis presented in the following was carried out considering only the emitted photons, that is approximately 1.5% of the emitted quanta. This choice is motivated by the fact that they keep their initial energy (quarks and gluons lead to jets), and they are easy to detect (neutrinos are not), stable (muons or tau leptons do decay) and unaffected by magnetic fields (electrons are).

The simulation was repeated many times to account for different possible realizations of the process. As expected, the time-integrated spectrum exhibits lines that are not present in the standard Hawking spectrum. The time integrated differential Hawking spectrum scales as E^{-3}, where E is the energy of the emitted photons. In this case, it becomes a truncated power-law as the available energy is limited. To test to what extent the LQG spectrum can be distinguished from a standard Hawking spectrum, a Kolmogorov–Smirnov (K-S) test was implemented. The K-S statistics measures the distance between the cumulative distribution functions of the considered distributions and can be used for a systematic study of discrimination capabilities.

Figure 1 shows the number of evaporating BHs, seen in their final stages, that would be required to discriminate at a given confidence level between the Hawking spectrum and the LQG spectrum, depending on the experimental uncertainty of the measure of the energy of the detected photons. This latter parameter is mandatory. If the resolution were infinite, a single photon could nearly allow one to discriminate, but this is obviously never the case. The results are theoretically appealing, but experimentally challenging.

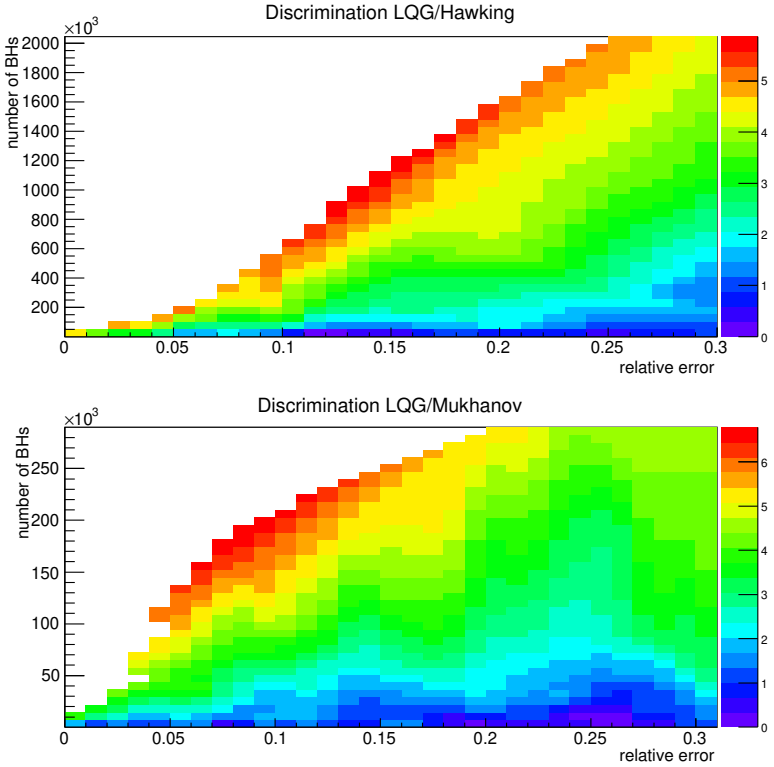

Figure 1. Number of BHs that would have to be observed as a function of the relative error on the energy measurement for different confidence levels (the color scale corresponds to the number of standard deviations). Upper plot: discrimination between loop quantum gravity (LQG) and the Hawking spectrum. Lower plot: discrimination between LQG and the Mukhanov–Bekenstein hypothesis [40]. From [38].

Another interesting feature is the following. The end of the evaporation in the LQG framework consists of the emission of a few particles, whose energies are given by the mass difference between BH states. In the usual Hawking view, the situation is very different. The evaporation is expected to stop somehow slowly (when compared to the previous stages). Because the energy available inevitably becomes, at some point, smaller that it should be (in the sense that M becomes smaller that the associated temperature $1/(8\pi M)$), the process slows down and the energy of the emitted particles decreases. In [38], it was shown that this might be used as another discrimination tool between models.

It could also be that a periodicity with broader peaks does appear in the emitted spectrum, due to the "large scale" structure of the area spectrum. This has been discussed in [39]. In that case, the Hawking/LQG spectra could also be discriminated for higher mass black holes [38]. This possibility is however extremely unlikely, and we will not discuss it further, as a damping in the pseudo-periodicity is expected to take place [41–43].

This analysis was pushed further in [44], where recent results are accounted for. The fundamental excitations are now better understood as living on the horizon and as being elements of the Hilbert space of a SU(2) Chern–Simons theory [45,46]. The quantization of such a Chern–Simons theory with a compact gauge group is well defined, and the kinematical characteristics of a quantum black hole become quite clear [47–49]. The role of the Barbero–Immirzi parameter γ was studied in detail, and recovering the Bekenstein–Hawking entropy has been considered as a way to fix its value. It is however the coupling constant with a topological term in the action of gravity, with no consequence on the classical equations of motion. The strong dependence of the entropy calculation on γ therefore remains controversial. Much progress has been recently made [50–54]. The canonical ensemble formulation of the entropy making use of a quasi-local description shed a new light on the subject. The semi-classical thermodynamical properties can actually be recovered for any value of γ if one assumes a non-trivial chemical potential conjugate to the number of horizon punctures. A possible fundamental explanation to the exponential degeneracy would be to consider the area degeneracy as an analytic function of γ and to make an analytical continuation from real γ to complex γ. This suggests that the quantum gravitational theory, defined in terms of self-dual variables, could account for the holographic degeneracy of the area spectrum of the BH horizon.

Two models of black holes were studied by a full MC simulation in [44]. The first is based on the naive microcanonical view. It takes into account only the quantum geometry excitations, leading to [55]:

$$S = \frac{\gamma_0}{\gamma}\frac{A}{4} + o(log(A)), \tag{11}$$

where γ_0 is of order one. Then, holographic black holes, where one uses the matter degeneracy suggested by quantum field theory with a cut-off at the vicinity of the horizon (that is, an exponential growth of vacuum entanglement in terms of the BH area), were considered. The entropy becomes:

$$S = \frac{A}{4} + \sqrt{\frac{\pi A}{6\gamma}} + o(\sqrt{A}). \tag{12}$$

The simulation has been performed with 10^7 evaporating black holes. Figure 2 shows the results for different values of the Barbero–Immirzi parameter γ. This γ dependence interestingly shows up even though the leading order term of the black hole entropy, which mainly governs the transitions during the evaporation process, does not depend on γ. This phenomenon is fully quantum gravitational in nature and is both due to the fact that γ enters in the discretization of the area spectrum and shows up in the sub-leading corrections to the entropy. The effects of a detector finite energy resolution are shown in Figure 3.

This shows that the Hawking spectrum of a LQG BH has two distinct parts: a nearly continuous background corresponding to the semi-classical stages of the evaporation and a series of discrete peaks associated with the deep quantum structure. Interestingly, γ has an effect on both parts and becomes

somehow measurable. In all cases, there are significant differences with the usual Hawking picture in the last stages.

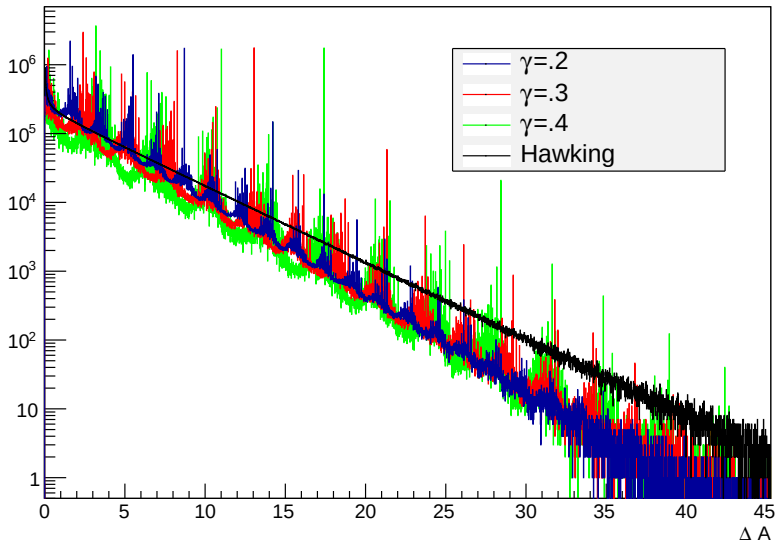

Figure 2. Spectrum of a holographic black hole for different values of γ as a function of ΔA. From [44].

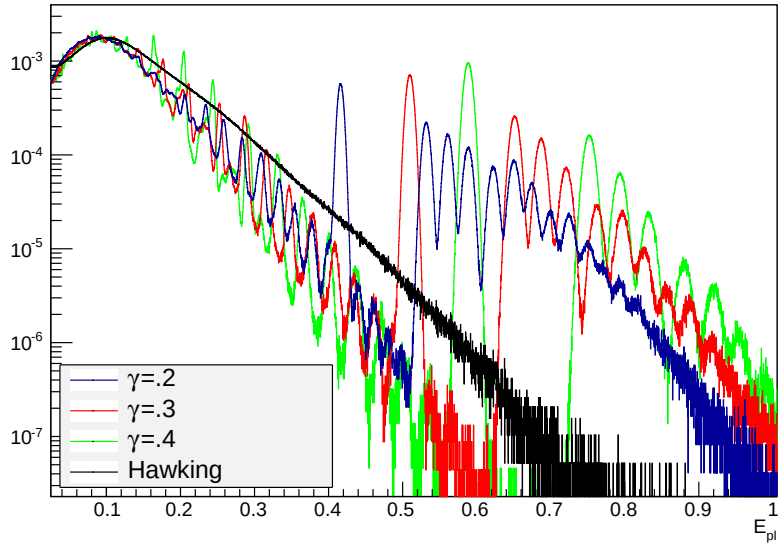

Figure 3. γ dependence of the integrated spectrum, as function of the energy of the emitted particle, in the holographic model, with a detector energy resolution of 5%. From [44].

3.2. Greybody Factors

When dealing with evaporating black holes, a key element is the greybody factor; closely related to the absorption cross-section. The Hawking effect is approximated by a blackbody spectrum at temperature $T_H = 1/(8\pi M)$ with M the mass of the BH. However, the emitted particles have to cross a (gravitational and centrifugal) potential barrier before escaping to infinity. This induces a slight modification of the spectrum, captured by the cross-section σ. The spectrum reads as:

$$\frac{dN}{dt} = \frac{1}{e^{\frac{\omega}{T_H}} \pm 1} \sigma(M, s, \omega) \frac{d^3k}{(2\pi)^3}, \tag{13}$$

with s the particle spin, ω its energy and k its momentum. The cross-section is, in general, given by:

$$\sigma(\omega)_s = \sum_{l=0}^{\infty} \frac{(2j+1)\pi}{\omega^2} |A_{l,s}|^2, \tag{14}$$

where $A_{l,s}$ is the transmission coefficient of the mode with angular momentum l and $j = l + s$ is the total angular momentum. It has been shown, in many different frameworks, to encode much information on the chosen gravitational theory or on the underlying background spacetime. In the framework of LQG, those cross=sections have been studied only in [56].

The emphasis was put on BHs as described in [57,58], where, instead of all a priori possible closed graphs, a regular lattice with edges of lengths δ_b and δ_c was chosen. The resulting dynamical solution inside the horizon is analytically continued to the region outside the horizon. Requiring that the minimum area is the one found in the LQG area operator spectrum, the model is reduced to one free parameter δ, the so-called dimensionless polymeric parameter. The effective LQG-corrected Schwarzschild metric is then given by:

$$\begin{aligned} ds^2 &= -G(r)dt^2 + \frac{dr^2}{F(r)} + H(r)d\Omega^2 \,, \\ G(r) &= \frac{(r-r_+)(r-r_-)(r+r_*)^2}{r^4+a_o^2} \,, \\ F(r) &= \frac{(r-r_+)(r-r_-)r^4}{(r+r_*)^2(r^4+a_o^2)} \,, \\ H(r) &= r^2 + \frac{a_o^2}{r^2} \,, \end{aligned} \tag{15}$$

where $d\Omega^2 = d\theta^2 + \sin^2\theta d\phi^2$, $r_+ = 2m$ and $r_- = 2mP^2$ are the two horizons and $r_* = \sqrt{r_+ r_-} = 2mP$, P being the polymeric function defined by $P = (\sqrt{1+\epsilon^2} - 1)/(\sqrt{1+\epsilon^2} + 1)$, with $\epsilon = \gamma\delta$, and the area parameter a_o is given by $a_0 = A_{min}/8\pi$. The parameter m in the solution is related to the ADM mass M by $M = m(1+P)^2$.

The case of massless scalar fields is quite easy to deal with. Since the BH is static and spherical, the field can be written as $\Phi(r,\theta,\phi,t) = R(r)S(\theta)e^{i(\omega t + m\phi)}$ and the generalized Klein–Gordon equation is:

$$\frac{1}{\sqrt{-g}}\partial_\mu(g^{\mu\nu}\sqrt{-g}\partial_\nu\Phi) = 0, \tag{16}$$

Leading the metric given in Equation (15) to the radial equation:

$$\frac{\sqrt{GF}}{H}\frac{\partial}{\partial r}\left(H\sqrt{GF}\frac{\partial R(r)}{\partial r}\right) + \left(\omega^2 - \frac{G}{H}l(l+1)\right)R(r) = 0. \tag{17}$$

Using the tortoise coordinate $dr^{*2} \equiv \frac{dr^2}{GF}$, one can impose the appropriate boundary conditions, fit the asymptotic solutions and sum over the different values of l to get the final cross-section, which is given in Figure 4.

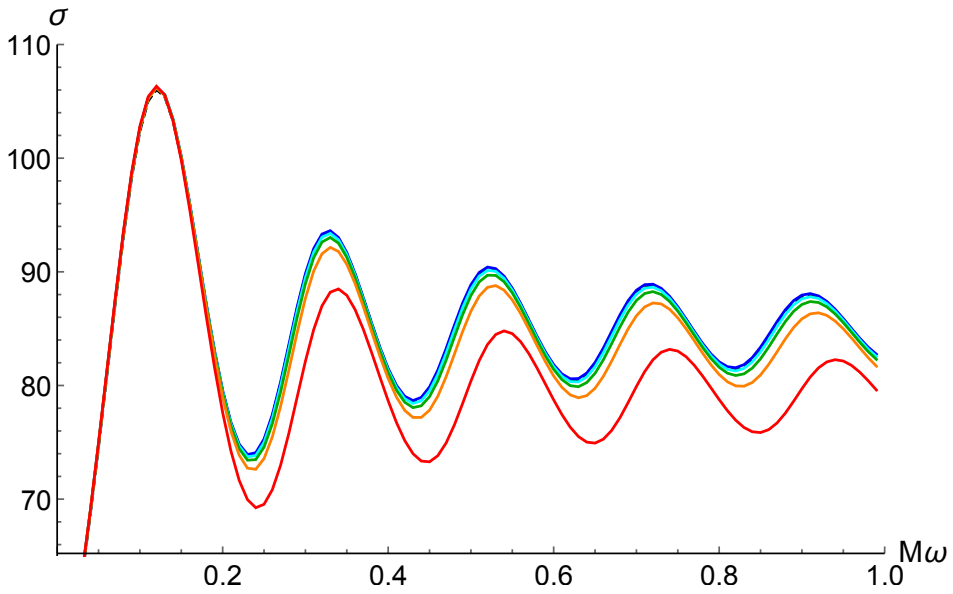

Figure 4. Emission cross-section for a scalar field with energy ω for a loop BH of mass M for different values of ϵ. From bottom to top: $\epsilon = 10^{\{-0.3,-0.6,-0.8,-1,-3\}}$. The blue line, corresponding to $\epsilon = 10^{-3}$, is superposed with the cross-section for a Schwarzschild BH. From [56].

The cross-section decreases when ϵ increases. One can also notice a shift of the pseudo-periodic oscillations toward a lower frequency (in $M\omega$). When $\epsilon < 10^{-0.8}$, it is hard to distinguish between the solutions. From the phenomenological viewpoint, it seems that taking into account the quantum corrections does not substantially influence the cross-section of a scalar field for reasonable values of ϵ (that is $\epsilon \ll 1$). The main trend is however clear, and if the actual value of ϵ happened to be unexpectedly high, it could be probed by a reduced cross-section.

The case of fermions is more complicated, and a specific derivation of the Dirac equation in the Newman–Penrose formalism had to be developed in [56].

The Dirac equation in the Newman–Penrose formalism reads:

$$(D+\epsilon-\rho)P^0+(\delta^*+\pi-\alpha)P^1 = i\mu_*\overline{Q}^{1'}, \tag{18}$$

$$(\Delta+\mu-\gamma)P^1+(\delta+\beta-\tau)P^0 = -i\mu_*\overline{Q}^{0'}, \tag{19}$$

$$(D+\epsilon^*-\rho^*)\overline{Q}^{0'}+(\delta+\pi^*-\alpha^*)\overline{Q}^{1'} = -i\mu_*P^1, \tag{20}$$

$$(\Delta+\mu^*-\gamma^*)\overline{Q}^{1'}+(\delta^*+\beta^*-\tau^*)\overline{Q}^{0'} = i\mu_*P^0, \tag{21}$$

Using the tetrad given in [56] and the following ansatz:

$$P^0 = \frac{e^{i(\omega t+m'\phi)}}{\sqrt{H(r)}(G(r)F(r))^{\frac{1}{8}}}R_+(r)S_+(\theta), \tag{22}$$

$$P^1 = \frac{e^{i(\omega t+m'\phi)}}{\sqrt{H(r)}(G(r)F(r))^{\frac{1}{8}}}R_-(r)S_-(\theta), \tag{23}$$

$$\overline{Q}^{0'} = -\frac{e^{i(\omega t+m'\phi)}}{\sqrt{H(r)}(G(r)F(r))^{\frac{1}{8}}}R_+(r)S_-(\theta), \tag{24}$$

$$\overline{Q}^{1'} = \frac{e^{i(\omega t+m'\phi)}}{\sqrt{H(r)}(G(r)F(r))^{\frac{1}{8}}}R_-(r)S_+(\theta), \tag{25}$$

which makes the system separable. Basically, one is led to the following equation for the R_+ component of the Dirac spinor (the equation for R_- is the conjugate):

$$\sqrt{HF}\mathcal{D}\left(\frac{\sqrt{HF}\mathcal{D}^\dagger}{\lambda - im_e\sqrt{H}}R_+\right) - (\lambda + im_e\sqrt{H})R_+ = 0, \tag{26}$$

with $\mathcal{D}$ a radial operator:

$$\mathcal{D} = \partial_r + \left(\frac{G'}{8G} - \frac{F'}{8F}\right) + \frac{iw}{\sqrt{GF}}. \tag{27}$$

The separation constant λ is obtained by solving the angular equation, leading to $\lambda^2 = (l+1)^2$ for fermions. Results are given in Figure 5. Once again, the general trend is a decrease of the cross-section when the "quantumness" increases. In addition, it was shown that the existence of a non-vanishing a_0 is the reason for the slight increase of the cross-section on the first peak. The polymerization parameter and the minimal area do have different consequences.

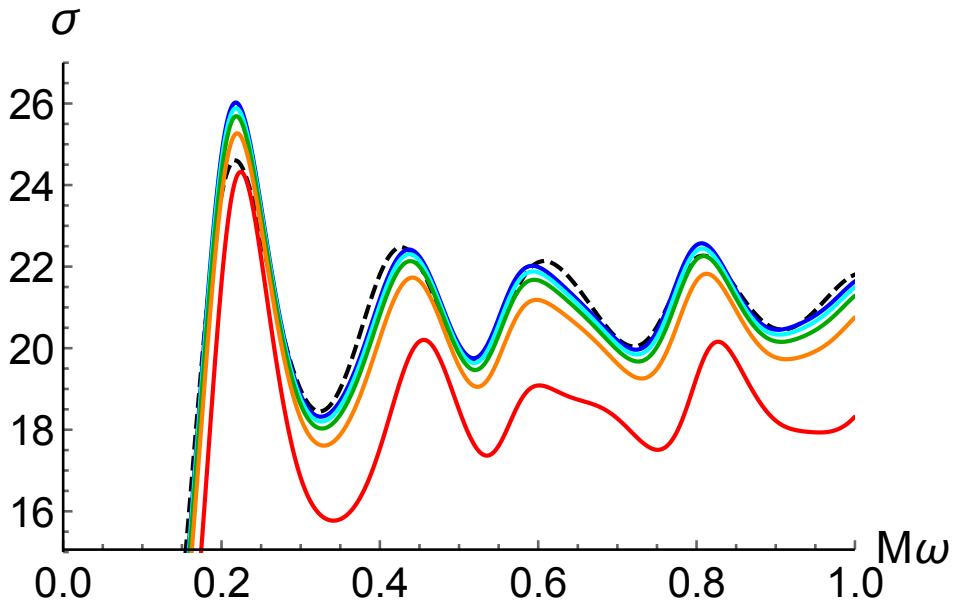

Figure 5. Emission cross-section for a fermionic field, with energy ω, for a loop BH of mass M. From bottom to top: $\epsilon = 10^{\{-0.3,-0.6,-0.8,-1,-3\}}$. The dashed dark curve corresponds to the Schwarzschild cross-section. From [56].

The considered polymerized model [57] is just a first attempt and by no means a final statement on the quantum corrected geometry around an LQG BH. The same work on greybody factors should be carried out for models like [59–61], to cite only a few. This however shows that some non-trivial features can be expected.

3.3. Local Perspective

The previous view is based on the idea that the Hawking evaporation should be considered as a global phenomenon. The BH emits a particle and undergoes a transition from one area eigenstate to another one. When the BH is large, the density of states grows exponentially and reads (we make the Newton constant dependance explicit here) as $\rho(M) \sim \exp(\mathrm{M}\sqrt{4\text{ß}\mathrm{G}/3})$, which means that the spectral lines are virtually dense in frequency for high enough masses. No quantum gravity effects are therefore expected well above the Planck mass.

This view is however not that straightforward. When the BH undergoes a transition from the mass M_1 to the mass M_2, which is extremely close to M_1 if the black hole is massive, the quantum state after the jump is—in the global perspective—completely different from the initial one. The final state corresponds to values of the spins (labeling the $SU(2)$representations of the edges puncturing the horizon or colors of the graph) that are generically deeply different from the ones of the initial state. Assuming that the quasidense distribution of states is correct requires a full reassigning of the quantum numbers for every single transition, which is in tension with a quantum gravitational origin of the evaporation process. As we will explain later, if, instead, one assumes that the evaporation is due to a change of state of an "elementary area cell", there is no reason for all of the other surfaces paving the horizon to change simultaneously their quantum state (as argued, e.g., in [62]). This even raises a causality issue: how can a "far away" elementary cell know how it should change to adjust to the others?

Another view, to account for this issue, was however suggested in [63] (somehow in the line of [64]), assuming that each particle emitted is basically due to the relaxation of the BH following a change of state of a single elementary cell. This was called a local quantum gravity dynamics. This does not assume that local processes magically know the global BH quantities like temperature, entropy and mass: after the quantum jump, without any a priori knowledge of the picture, the BH relaxes through a semiclassical process consistent with the energy available. This naturally leads to a spectrum whose properties fit the Hawking description.

This hypothesis leads to phenomenological results comparable to those of [40], but with a clear foundation in the LQG framework. The key point is that the same change of area dA ($\sim A_{Pl}$) implies a relative peak separation in the spectrum dE/T, which is independent of the BH mass. Quantum gravity effects can therefore be expected to be measured for masses arbitrarily far above the Planck mass. This deeply contrasts with what was believed to be expected in initial LQG studies. The density of reachable states is no longer quasidense.

The eigenvalues of the area operator given by Equation (44) are not equally spaced: only in the large-j limit does a regular line spectrum arise. It is shown in [63] that this interesting feature could allow one to distinguish between different LQG models of black holes (in particular those in the line of [28] favoring low spin values and the holographic ones [51] where higher spins could dominate).

If one calls $nA_0/2$ the area variation associated with one quantum jump, n being an integer and A_0 the basic area $\sim A_{Pl}$, the relative variation of energy of the emitted particles between emissions is $\Delta E/E \approx nA_0/(2A)$. The change in energy is therefore negligible, and the line structure should be observable if it exists: the BH mass evolution during its evaporation does not erase this feature.

The criterion for the detection of a signal coming from an evaporating primordial black hole (PBH) [65] consists of asking for a mean time Δt between two measured photons smaller than a given reference time interval Δt_0. This allows one to estimate a maximum distance for detection of:

$$R_{max} \approx \sqrt{\frac{S\Delta t_0}{M}}. \tag{28}$$

The realistic case however corresponds to the signal emitted by a distribution of PBHs with different masses. Does the global line structure remain? It was shown that if the temperature of the universe does not change by more that 5–10% during the formation of the considered PBHs, the line structure holds.

Another issue had to be considered seriously: when the temperature of the BH is higher than the quantum chromodynamics (QCD) confinement scale, the evaporating BH also emits partons that

will fragment into hadrons. Some of those will then decay into gamma-rays, denoted as "secondary". The secondary instantaneous spectrum reads as:

$$\begin{aligned} \frac{d^2N_\gamma}{dEdt} &= \sum_j \int_{Q=E}^{\infty} \alpha_j \Gamma_j(Q,T) \left(e^{\frac{Q}{T}} - (-1)^{2s_j}\right)^{-1} \\ &\times \frac{dg_{j\gamma}(Q,E)}{dE} dQ, \end{aligned} \tag{29}$$

where $j = 1, ...6$ is the flavor, $s_j = 1/2 \ \forall j$, $dg(Q,E)/dE$ is the normalized differential fragmentation function (determined using the "Lund Monte Carlo" PYTHIAcode [66]), Q being the quark energy, T the temperature of the black holes, α the number of degrees of freedom, Γ the cross-section and E the photon energy. The time-integrated spectrum is then given by:

$$\frac{dN_\gamma}{dE} = \int_{M_i}^{M_f} \frac{d^2N_\gamma}{dEdt} \frac{dt}{dM} dM. \tag{30}$$

Those secondary photons will obviously not exhibit the line structure of quantum gravitational origin. The numerical simulation performed in [63] however shows that, quite surprisingly, those electromagnetic quanta are not numerous enough to wash out the primary signal and its line structure, which could indeed still be measured. The amplitude of the secondary component is indeed comparable to the amplitude of the primary one.

If this local view for the evaporation of black holes is correct, this means that this should lead to a line structure in the spectrum, even arbitrarily far away from the Planck mass.

4. Bouncing Black Holes

4.1. The Model

Recently, the possibility that black holes could actually be bouncing objects has been revived. In its current "LQG-compatible" version, the model was first introduced in [67], and its consequences were studied in [68]. It was then refined in [69,70]. Basically, the idea is that what happens to the Universe in LQC, that is a bounce, should also happen to black holes. As the contracting Friedmann solution is connected to the expanding one by a quantum tunneling, the classical black hole solution is expected to be glued to the white hole one by quantum gravitational effects. This is in line with other works based on different assumptions, e.g., [71,72]. The process takes a time proportional to M^2, whereas the Hawking process requires a time of order M^3. Black holes would therefore bounce before they evaporate, and the Hawking radiation would be seen as a kind of a dissipative correction.

The important result of [69] is that a metric exists for a bouncing black-to-white hole. It is a solution to the Einstein equations outside a finite region and beyond a finite time duration. This means that it is possible to have a bounce from a black hole into a white hole without any spacetime modification at a large radius. The quantum region extends slightly outside the Schwarzschild radius and can have a short duration. The associated Penrose diagram is shown in Figure 6.

Because of the gravitational redshift, the bounce is seen as nearly "frozen" by a distant observer, but it is extremely fast for a clock co-mobile with the collapsing null shell. In this sense, a BH is a star that is collapsing and bouncing, seen at very slow motion from the exterior.

The key-point is to assume that classicality might not be determined by, e.g., the Kretschmann invariant ($\mathcal{R}^2 = R^{abcd}R_{abcd}$), but by:

$$q = l_P^{2-b} \, \mathcal{R} \, \tau^b, \tag{31}$$

with b of order unity and τ the (asymptotic) proper time. In this expression, units have been reinserted for clarity. This opens the door to a possible cumulative effect like in the decay of an unstable nucleus.

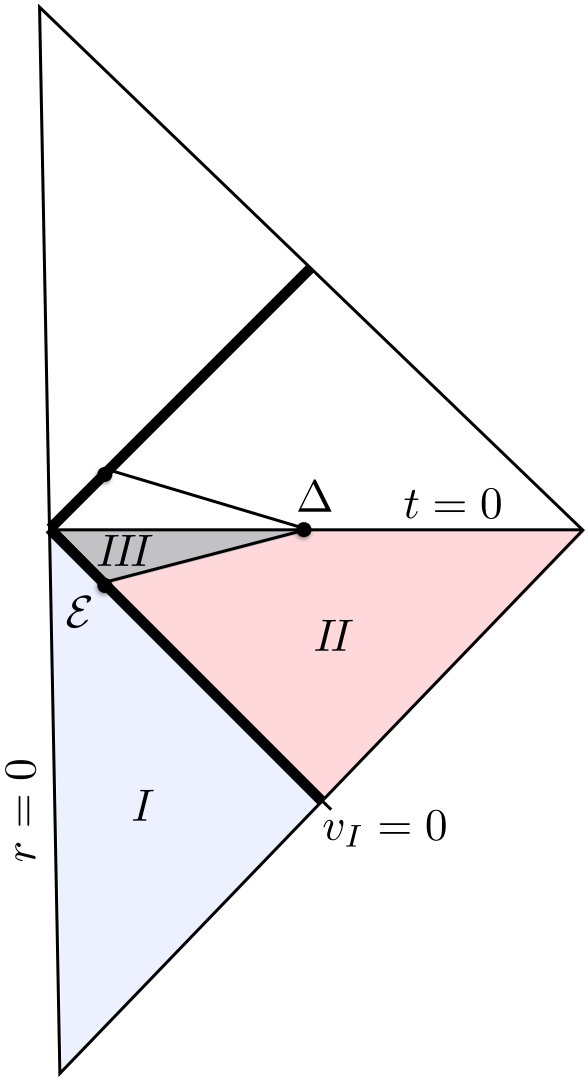

Figure 6. Causal diagram for a bouncing black hole, from [69]. (I) is flat; (II) is Schwarzschild; and (III) is the "quantum gravity" region.

The metric is entirely determined by two functions of u and v,

$$ds^2 = -F(u,v)dudv + r^2(u,v)(d\theta^2 + \sin^2\theta d\phi^2), \tag{32}$$

whose explicit expression has been calculated in [69]. Interestingly, this also means that strong quantum gravity effects may appear outside the event horizon (which becomes, in this context, a trapping horizon) at $R = (7/6)R_S$ [73]. As far as this study is concerned, the key-point is that the bouncing time is given by $\tau = 4kM^2$ (although this expression is hard to recover from the full theory [74]). The k parameter has a lower bound ($k > 0.05$) and will be varied in the next sections.

4.2. Individual Events and Fast Radio Bursts

The question of the detectability of those bouncing black holes naturally arises. At this stage, a detailed model for the emission from the white hole is missing. Two hypothesis can however reasonably by made.

The first one is simply based on dimensional analysis. The hole size is the only scale of the problem. It is therefore expected that the wavelength of the emitted radiation is of the order of the

bouncing BH diameter. This makes clear sense, and this is in agreement with what happens, e.g., during the Hawking evaporation. The associated signal is called the low-energy component.

The second hypothesis relies on the symmetry of the process (this might not be completely true [75], but this does not change the argument). What goes out of the white hole is what went in the black hole. In this model, the bouncing star is formed by a collapsing null shell. The energy of the emitted radiation should therefore be the same as the one of the incoming photons. If we consider PBHs formed in the early universe by the collapse of over-densities, the correspondence between the mass and the time is known. Time is also in one-to-one correspondence with the temperature of the Universe. Therefore, for a given BH mass, one can calculate the energy of the emitted radiation, called the high-energy component.

The idea of explaining fast radio bursts (FRBs) by bouncing black holes was suggested in [76]. Basically, FRBs are intense radio signals with a very brief duration. Events were, among others, observed at the Parkes radio telescope [77–79] and by the Arecibo Observatory [80]. Could they be explained by (the low-energy component of) bouncing black holes?

As mentioned before, the bouncing time can be estimated to be of the order of:

$$\tau = 4k\, M^2. \tag{33}$$

For the phenomenology of FRBs, one sets the parameter to its lowest possible value: $k = 0.05$. PBHs with an initial mass around:

$$M_{t_H} = \sqrt{\frac{t_H}{4k}} \sim 10^{26}\ \mathrm{g}, \tag{34}$$

where t_H is the Hubble time, would therefore be expected to explode today. One can notice that, naturally, this mass is much higher than $M_\star \sim 10^{15}$ g, corresponding to black holes that would require a Hubble time to evaporate by the Hawking process. In the case of the low energy channel of bouncing BH, the emitted radiation wavelength should be of the order of 200 microns, three orders of magnitude below the measured 20 cm of FRBs.

This apparent discrepancy has been addressed and solved in [81]. The key idea lies in the fact that if the black-to-white hole transition is to be understood as a tunneling process, the lifetime of a BH should be considered as a random variable. The probability for a black hole not to have bounced after a time t is given by:

$$P(t) = \frac{1}{\tau} e^{-\frac{t}{\tau}}. \tag{35}$$

Let us model the shape of the signal emitted by a single black hole by a simple Gaussian function of width σ_E. The full signal due to a local distribution of bouncing black holes is given by:

$$\frac{dN_\gamma}{dE} = \int_{M_{Pl}}^{\infty} A e^{-\frac{(E-E_0)^2}{2\sigma_E^2}} \cdot \frac{dN}{dM}(M) \cdot \frac{1}{4kM^2} e^{-\frac{t_H}{4kM^2}}. \tag{36}$$

The key-point is that the mean energy of the detected signal is not necessarily the naively expected one, that is may not be $E \sim 1/(4M_{t_H})$ where M_{t_H} is such that $t_H = 4kM_{t_H}^2$ (this corresponds to BHs having a characteristic lifetime of the order of the age of the Universe, leading to the emitted wavelength three orders of magnitude too small to account for FRBs). If the mass spectrum of PBHS is however peaked around a mass M_0,

$$\frac{dN}{dM} \propto e^{-\frac{(M-M_0)^2}{2\sigma_M^2}}, \tag{37}$$

which can be different than M_{t_H}, the mean emitted energy will be around $1/(4M_0)$, which can differ from $1/(4M_{t_H})$. This happens because of the distributional nature of the bouncing time.

In Figure 7, the emitted photon flux is shown for different values of the mean mass M_0 of the mass spectrum: M_{t_H}, $10M_{t_H}$, $100M_{t_H}$ and $1000M_{t_H}$. This shows that the energy of the radiation does depend on this value, even if the parameters of the model are otherwise fixed. Since a given mean lifetime $\tau = 4$ kM^2 does not imply a fixed expected energy, the three orders of magnitudes needed to match the measured energy of FRBs can be accounted for with a mass $M_0 = 1000M_{t_H}$, which corresponds to the left curve in Figure 7.

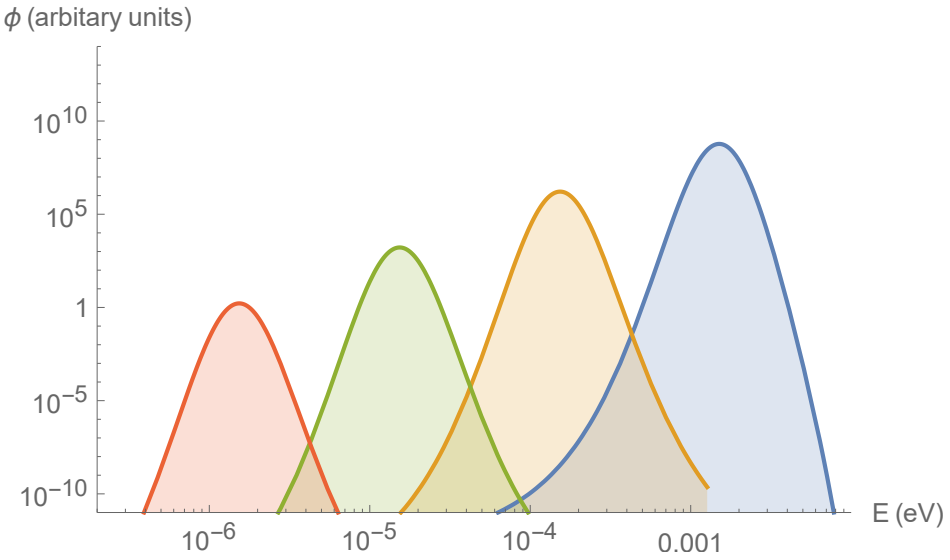

Figure 7. Electromagnetic flux emitted by bouncing BHs for a mean mass M_0 of (from right to left) M_{t_H}, $10M_{t_H}$, $100M_{t_H}$ and $1000M_{t_H}$, normalized such that the total mass going into primordial black holes (PBHs) is the same. From [81].

This explanation for FRBs is unquestionably exotic when compared to more conventional astrophysical interpretations (especially when considering that one "repeater" has been observed; it could however well be that there are different populations of FRBs). What makes the scenario however meaningful is that it is testable, due to a specific redshift dependance. When observing a galaxy at redshift z, the measured energy of the signal emitted by any astrophysical object (including decaying dark matter) will be $E/(1+z)$ for a rest-frame energy E. This is not the case for bouncing black holes: BHs that have bounced far away and are observed today had a shorter bouncing time and consequently a smaller mass. The energy of the emitted radiation is therefore higher, and this compensates for the redshift effect. The observed wavelength of the signal from an object at redshift z can be written as:

$$\lambda_{obs}^{BH} \sim \frac{2Gm}{c^2}(1+z) \times \sqrt{\frac{H_0^{-1}}{6\,k\Omega_\Lambda^{1/2}} \sinh^{-1}\left[\left(\frac{\Omega_\Lambda}{\Omega_M}\right)^{1/2}(z+1)^{-3/2}\right]}, \tag{38}$$

where we have reinserted the physical constants; H_0, Ω_Λ and Ω_M being respectively the Hubble rate, the cosmological constant and the matter density. This is to be contrasted with what happens for standard sources whose measured wavelength is related to the observed wavelength by:

$$\lambda_{obs}^{other} = (1+z)\lambda_{emitted}^{other}, \tag{39}$$

as shown in Figure 8.

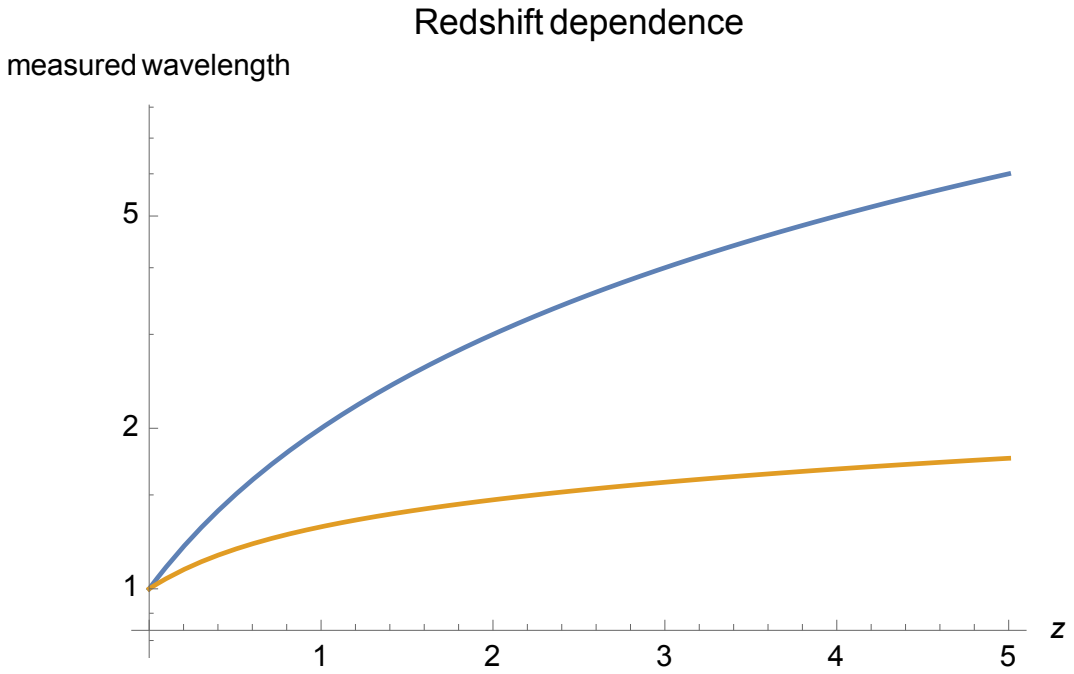

Figure 8. Measured wavelength, normalized to the rest-frame one, as a function of the redshift. The upper curve is for a conventional astrophysical signal, and the lower one is for bouncing black holes. Reproduced from [82], with the permission of AIP Publishing.

Importantly, is was also shown in [81] that even if the mass spectrum is wide, it could still be possible to explain FRBs. It could be that most bouncing BHs lead to a signal of a wavelength of 0.02 cm and that only the tail (whose existence is due to the probabilistic nature of the lifetime) of the distribution is actually detected by radio-telescopes. If the real emission peak is in the infrared band—which should naturally occur if the mass spectrum is, itself, not peaked—it could very well be that it is just unobserved today. Observatories in the infrared have time constants that are too high to allow for the measurement of fast transient phenomena, and no large survey is being carried out. In this case, a prediction of the model is that one should expect a higher flux as the energy increases.

Finally, it is worth considering the high-energy emission. The bouncing BHs then act as "redshift freezing machines" for collapsing fields, which are emitted back at the energy they had when being absorbed. However, in the meantime, the age of the surrounding Universe has grown tremendously. In simple models, PBHs form with a mass of the order of the Hubble mass at the formation time. For BH masses as considered here (around 10^{26} g), this corresponds to a temperature of the Universe around the TeV. New very high energy telescopes, like the Cherenkov Telescope Array (CTA), could detect bursts is this energy range, as suggested by this model.

The redshift dependance for this component is qualitatively the same as for the low-energy one, but for different reasons. For a BH exploding at redshift z and cosmic time t, the energy is determined by the temperature of the Universe when the formation took place. It is proportional to the inverse square root of the time, which is in turn proportional to the horizon mass, that is to the BH mass. Therefore, the emitted wavelength is proportional to the square root of the mass of the BH. This leads to an observed wavelength:

$$\lambda_{obs} \propto (1+z)\left(\sinh^{-1}\left[\left(\frac{\Omega_\Lambda}{\Omega_M}\right)^{\frac{1}{2}}(z+1)^{-\frac{3}{2}}\right]\right)^{\frac{1}{4}}. \quad (40)$$

As previously stated, this is a flatter dependance than for astrophysical effects.

It is meaningful to evaluate the maximal distance at which one could observe a bouncing black hole. This question was addressed in [83], allowing the k parameter, which determines the bouncing time, to vary. The minimum value of k is such that the quantum effects have enough time to make the bounce happen, and the maximum is such that the bouncing time remains smaller than the Hawking time. The study was carried out taking into account the size of the detector (and its detection efficiency), the absorption during the propagation over cosmological distances and the number of measured photons required for the detection to be statistically significant. As k increases, the global trend is a decrease of the maximum distance at which the bouncing BH can be observed. This comes both from the fact that BHs are lighter for higher values of k (for a given bouncing time) and from the fact that they emit higher energy (and therefore fewer) particles. However, quite subtle effects also appear. For example, the distance can slightly decrease above the threshold of emission of a new stable particle (leaving less energy available for the considered photons), whereas it can increase when new particles decaying into gamma-rays are produced. For k varying between 0.05 and 10^{22}, the maximum detectable distance varies from the Hubble scale to 10^{19} m for the low-energy component, as shown in Figure 9, and from 10^{24}–10^{16} m for the high energy component.

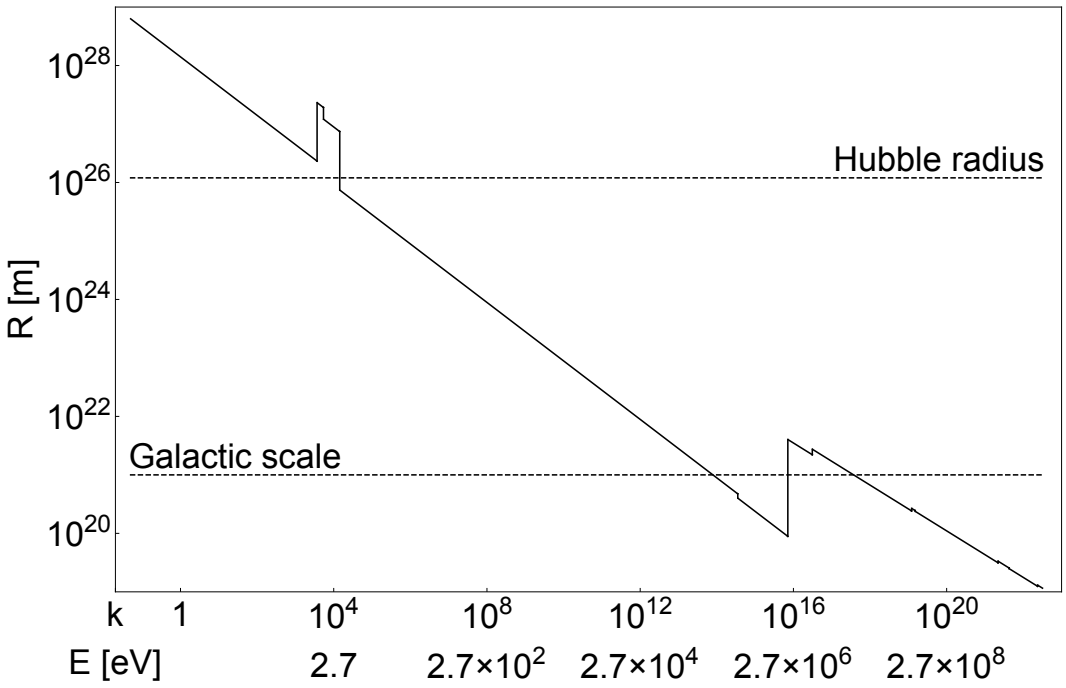

Figure 9. Maximum distance at which a single bouncing BH can be observed through its low-energy component, as a function of the k parameter, from [83] (Copyright IOP Publishing. Reproduced with permission. All rights reserved.).

4.3. Background

It is also important to consider a possible background emission. In this case, one does not look for a single event, but from the diffuse emission due to a distribution of BHs. The number of photons detected per time unit, surface unit and energy unit is given by:

$$\frac{dN_{mes}}{dEdtdS} = \int \Phi_{ind}((1+z)E, R) \cdot n(R) \cdot A(E) \cdot f(E, R) dR, \tag{41}$$

where $\Phi_{ind}(E, R)$ is the flux emitted by a single BH at distance R and at energy E, $n(R)$ is the number of BHs bouncing at distance R per unit time and volume, $A(E)$ is the acceptance of the detector convoluted with its efficiency and $f(E, R)$ is the absorption. The $n(R)$ term does depend on the shape of the initial mass spectrum of PBHs, which is unknown. It has however been checked that varying this shape has no significant impact on the results.

The study was carried out for both the low-energy and the high-energy components. In this latter case, it is important to take into account the hadronization of emitted quarks that will produce hadrons potentially decaying into gamma-rays. This was modeled using the PYTHIA Monte Carlo program [66]. Quite surprisingly, the result is that, due to a kind of redshift-compensation effect, the integrated signal is very similar to the single event one. It basically appears as a distorted Gaussian function [83].

This also raised the question about whether it could be possible to explain the gamma-ray excess coming from the galactic center, as observed by the Fermi satellite. This has been reported in [84–86] and even observed at higher galactic latitudes [86,87]. Once again, many astrophysical interpretations have been suggested. Millisecond pulsars are probably the most convincing hypothesis (see, e.g., [88]); it is however not yet fully satisfactory [87], and their is room for new physics. Interestingly, it was demonstrated in [82] that bouncing BHs can indeed explain the Fermi excess if the k parameter is chosen at its higher possible value. It is worth noticing that the values required to explain either the FRBs or the GeV gamma-ray excess are not "random", but either the smallest or the highest possible ones.

In [82], the secondary spectrum, mostly due to the decay of neutral pions, was shown to be well approximated by:

$$f(E, \epsilon) = \frac{a\epsilon^b}{\pi\gamma} \left[\frac{\gamma^2}{(\epsilon - \epsilon_0)^2 + \gamma^2} \right] e^{-\left(\frac{4\epsilon}{E}\right)^3}, \tag{42}$$

E being the quark energy, ϵ the photon energy, $a = 50.7$, $b = 0.847$, $\gamma = 0.0876$ and $\epsilon_0 = 0.0418$ (the energies being in GeV), whereas the direct emission due to the low-energy component (the high-energy component cannot be smaller than a TeV and is not relevant for this study) is given by:

$$g(E, \epsilon) = Ae^{-\frac{(\epsilon - E)^2}{2\sigma^2}} + 3N\sqrt{2\pi}A\sigma f(E, \epsilon), \tag{43}$$

where N is the number of flavors of quarks with $m < E$.

The best fit is shown in Figure 10. The fact that the bouncing BH signal can account for the data is in itself non-trivial. It is, for example, absolutely impossible to reproduce the measurements with evaporating BHs. In addition, the most important result here lies in the amplitude of the little bump on the left of the plot. It is associated with the secondary emission (that is the one coming from the hadronization and subsequent decay of emitted partons). As the number of emitted quarks and gluons is much higher than the number of directly emitted photons (responsible for the main bump), it could have been (wrongly) expected that this indirect emission conflicts with the background displayed as the horizontal green dashed line on the plot. Due to the subtle energy distribution in the jets, this is not the case, and at this stage, the explanation by bouncing BHs does work satisfactorily.

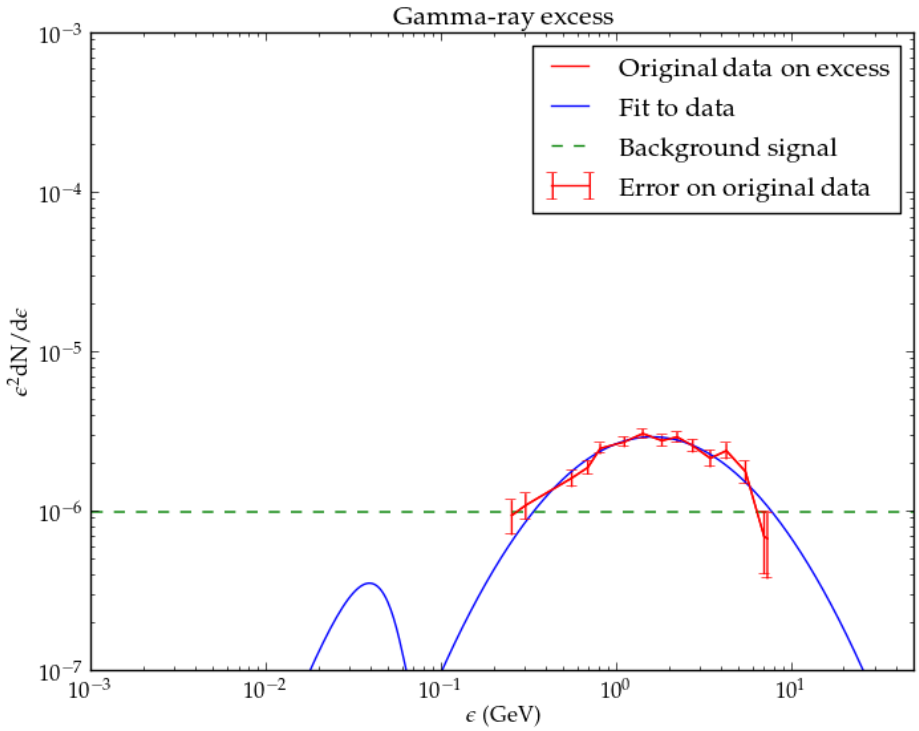

Figure 10. Fit to the Fermi excess with bouncing black holes. Reprinted from [82].

5. Dark Matter

The idea that if bouncing BHs are a substantial part of dark matter (DM), this might have an effect on galaxy clustering was introduced in [89]. Several possible constraints were considered.

Only recently, however, was a new scenario for the evolution of black holes proposed [90], with possible important consequences for DM, but in a different way than what was suggested in [91,92]. In this model, a black hole first evaporates, according to the usual Hawking process. The whole process preserves unitarity. When it becomes Planckian, the tunneling probability to turn into a white hole, estimated to be of the order of:

$$P \sim e^{-\frac{M^2}{M_p^2}}, \tag{44}$$

becomes large. Old black holes have a large interior volume [93]: even if the Schwarzschild radius is fixed, the "physical" volume available inside does increase with time. This remains true for the formed white hole, although its mass is small (the volume is of the order of M_i^4 where M_i is the initial mass). The white hole lifetime is also of the order of M_i^4. This scenario meets the conditions required to solve the information paradox.

It can be seen as a "less radical" proposal than the one presented in the previous sections. There is still a black-to-white hole transition, in agreement with the arguments given before, but instead of the very small bouncing time M_i^2, it takes the time suggested by the usual instanton solution. This is probably a more conservative and natural scenario.

In addition, following [91], it was suggested that dark matter could be formed by such white hole relics [94]. In [95], the central argument is pushed forward. For those objects to be still present in the contemporary Universe, one needs their lifetime to be larger than the Hubble time t_H, that is:

$$M_i^4 > t_H. \tag{45}$$

On the other hand, for those relics to be formed by evaporated black holes, one needs:

$$M_i^3 < t_H, \tag{46}$$

where M_i^3 is the Hawking evaporation time. This leads to:

$$10^{10}\ \mathrm{g} < M_i < 10^{15}\ \mathrm{g}. \tag{47}$$

It is argued in [95] that this corresponds to typical Hubble masses at reheating, making the scenario convincing.

It should be emphasized that quite a few models leading to stable relics at the end of the Hawking evaporation process have been proposed so far, relying on many different assumptions (see [37,96–108] to mention only a few historical references among many others). In those models, the relics are completely stable. This makes the situation easier: the only constraint is then that initial primordial black holes did evaporate within the Hubble time, but there is no lower bound on M_i. From this point of view, the new model [95] is more challenging than the usual pictures, which does not make it wrong.

The key-point is of course to find a way to produce enough primordial black holes so that the white hole relics account for dark matter, without relying on too exotic physics, as this is one of the motivations for this new scenario. As the CMB-measured amplitude and slope of the primordial power spectrum would lead to a vanishingly small number of primordial black holes, an extra input is obviously needed. A possibility would be to follow [109] and use Starobinsky's broken scale invariance spectrum [110]. The main idea is that power is increased at small scales through a step in the power spectrum.

Let us call $M_{H,e}$ the Hubble mass at the end of inflation, p^2 the ratio of the power on large scales with respect to that on small scales, δ_{min} the minimum density contrast required to form a black hole, M_{WH} the mass of the white hole, $\Omega^2_{WH,0}$ the abundance of white holes today, LW the Lambert-W function and σ_H the mass variance. One can then show that:

$$p \approx \frac{\sigma_H^{CMB}}{\delta_{min}} \sqrt{LW\left\{\frac{8.0\times10^{-6}}{2\pi\Omega^2_{WH,0}}\left[\frac{M_{WH}}{M_p}\right]^2\left[\frac{10^{15}\ \mathrm{g}}{M_{H,e}}\right]^3\right\}}. \tag{48}$$

Requiring $\Omega_{WH,0} \approx 0.3$, $\delta_{min} \approx 0.7$ and $M_{WH} \approx M_p$ allows one to perform an explicit evaluation of p, and this fixes the parameters of the scenario assuming that the reheating temperature is high enough.

However, a major problem remains to be solved. If the white hole relics are to be made by primordial black holes with initial masses between 10^{10} g and 10^{15} g, one must consider the severe constraints associated with nucleosynthesis. The D/H, Li^6/Li^7 and He^3/D ratios must not be distorted by the evaporation of black holes (assumed to be the "seeds" of the white hole relics) beyond observed values [65]. This forbids the easy formation of enough relics, unless a way to evade those constraints is found. This is the major challenge for future studies (which is fortunately easier to deal with when extended mass functions are taken into account [111]).

Another possibility was imagined in [112]. Here, the objects are assumed to be formed before the bounce in a cosmological model where the Big Bang singularity is replaced by a tunneling between the classically contracting and the classically expanding Friedmann solutions, as suggested by loop quantum cosmology [113]. This is in principle consistent, and other theories of quantum gravity might lead to this new paradigm. This evades the previously mentioned problem. However, in a different setting, the possibility was already considered in [114–116].

Very interestingly, the proposal is also related to the idea that the entropy and arrow of time could be perspectival [117]. This approach sheds new light on the old paradox of the apparently low entropy of the initial state of the Universe: the Universe is not anymore homogeneous at the bounce, and our observed entropy is determined by the fact that we cannot access the huge volume inside the abundant white hole remnants. It might seem puzzling that the authors explain the "un-naturally" low entropy

of the Universe by arguing that the probability for us to be where we are (outside of a relic) is only one part in 10^{120}. It is however meaningful in the sense that a special position is much more anthropically "acceptable" than a special state.

More importantly, it seems hard for the dark matter remnants to be already present at the bounce time. The current density of the universe is $\rho_0 \sim 10^{-30}$ g cm^{-3}. If we assume the usual cosmological evolution, we had at least 60 e-folds of inflation followed by approximately 60 e-folds of radiation, matter and cosmological constant-dominated expansion. This means that the scale factor has increased by at least a factor 10^{52} since the bounce. The density of remnants should then be at least $10^{156} \times 10^{-30} = 10^{126}$ g.cm^{-3} at the bounce, that is $10^{33}\rho_{Pl}$. Leaving apart the fact that this value is probably unphysical (the bounce would have happened before when thinking in the positive time direction), this is anyway incompatible with Planck mass and Planck size remnants (which cannot lead to a density higher than the Planck density without merging).

This could be evaded by assuming that no inflation took place, but this would require a quite exotic cosmological evolution. A nice feature of bouncing models is precisely to be compatible with inflation [7,8,118–120]. However, a possible way out could be to focus on a matter bounce (as white hole remnants would probably behave as pressure-less matter from the viewpoint of cosmological evolution) [121]. This requires a much lower-than-Planckian density at the bounce time.

The new scenario put forward in [90] constitutes an exciting new paradigm in black hole physics. It would be very nice to link it with the dark matter mystery, but quite a great deal remains to be understood.

6. Gravitational Waves

Gravitational waves from merging black holes are now observed for real by interferometers [122–126]. This opens a new era with important interesting constraints on black hole physics and modified gravity.

6.1. Spin in Gravitational Wave Observations

For a rotating black hole, the Bekenstein–Hawking entropy is given by:

$$S(M, j) = 2\pi M^2(1 + \sqrt{1 - j^2}), \tag{49}$$

where $j = J/M^2$ is the dimensionless spin parameter. It follows from Equation (49) that, at fixed mass M, BHs with larger spin have a smaller entropy. If one assumes that PBHs were indeed formed in the early Universe, following a microcanonical ensemble statistics, and if we make a statistical interpretation of the BH entropy in terms of microstates, the previous statement indicates that there are fewer microstates with large spin than with small spin. In this context, the existence of a population of black holes with nearly vanishing spins is naturally predicted [127]. This is to be contrasted with astrophysical black holes, formed by the collapse of rotating stars, which are expected to be generically rotating quite fast.

If gravitational wave interferometers were to observe a specific distribution of events with very small spins, this would both be evidence for the primordial origin of the considered BHs (at microcanonical equilibrium) and for the physical relevance of the Hawking–Bekenstein entropy formula.

To go in this direction, one would need to consider the entropic factor $e^{S(m,j)}$ as the weighting of a spin distribution of PBHs determined by the physical process responsible for their creation. This distribution is however not known at this time (which means in no way that it can be approximated by a flat distribution).

6.2. Quasinormal Modes

In the current LIGO/Virgo era, it would be highly desirable to make clear predictions about gravitational waves in LQG. The possibility of detecting gravitational waves emitted by BHs before the bounce was mentioned in [128]. This could be extremely promising for opening a new window on the pre-bounce Universe thanks to the non-trivial behavior of the luminosity distance in the contracting

phase, leading to a natural amplification of the signal (if the Universe is, e.g., matter dominated). This, however, does not address the question of the specific modification to the gravitational wave shape induced by LQG corrections.

The best way to face this difficult question is probably to focus first on quasinormal modes (QNMs). They correspond to the ringdown phase between the transient and the exponential or power law tail in a BH merging. The radial part of the perturbed metric is described by:

$$\Psi = Ae^{-i\omega t} = Ae^{-i(\omega_R + i\omega_I)t}, \tag{50}$$

where ω_R characterizes the oscillations and ω_I the characteristic damping timescale τ:

$$\tau = \frac{1}{\omega_I}.$$

Very importantly, the frequencies of the QNMs form a countable set of discrete frequencies [129]. There are actually two types of perturbations (axial and polar) in the linearized Einstein field equations described by the Regge–Wheeler and Zerilli equations. In GR, those equations are isospectral, but it is not clear whether this fundamental property still holds in LQG.

The Regge–Wheeler equation is very close to the one used to calculate greybody factors (although the question is different: the problem of QNM is to study the relaxation of the BH itself, not the way it scatters a quantum field). It reads for a Schwarzschild BH:

$$V_\ell^{\text{axial}}(r) = \left(1 - \frac{2M}{r}\right)\left[\frac{\ell(\ell+1)}{r^2} - \frac{6M}{r^3}\right], \tag{51}$$

for a mode of angular momentum ℓ. The know-how recently gained on greybody factors could therefore be usefully recycled for this purpose. It should however be clear that the technique is different (one does not search for the solution of an equation for all frequencies, but for the values of the frequencies allowing for a solution with different boundary conditions) and that only models leading to substantial metric modification around the horizon might lead to observational effects. This is one of the most promising ways to relate LQG corrections to BHs with observations.

7. Conclusions

The description of black holes in loop quantum gravity has much improved in the last years. A globally consistent picture is now emerging. In this article, we have reviewed its possible experimental consequences.

The main results are the following:

- First, the Hawking evaporation spectrum should be modified in its last stages. We have shown that it could not only allow for the observation of a clear signature of LQG effects, but also, in principle, to the discrimination between different LQG models. In particular, holographic models lead to specific features. The value of the Barbero–Immirzi parameter could even by measured.
- Second, attempts to calculate the greybody factors were presented. They should keep a subtle footprint of the polymerization of space and of the existence of a non-vanishing minimum area gap.
- Third, it was emphasized that a local quantum gravity perspective would lead to an observable modification to the Hawking spectrum (line structure), even arbitrarily far away from the Planck mass. This prediction is not washed out by the secondary emission from the BH.
- Fourth, a model with BHs bouncing into white holes with a characteristic time proportional to M^2 was presented and shown to have astrophysical consequences. It can be fine-tuned to explain ether fast radio bursts or the Fermi gamma-ray excess, depending on the values of the parameters. The possible associated background was also studied. A specific redshift dependence allows one to discriminate the model from other possible explanations.

- Fifth, the possibility of having a large amount of dark matter in the form of white holes appearing after quantum gravitational tunneling is presented together with possible weaknesses and future improvements of the model.
- Sixth, observable effects on gravitational wave detections associated with the BHs' spin distribution expected are presented.
- Seventh, promising prospects for quasinormal modes are outlined.

It could be that black holes will play a major role in making quantum gravity become an experimental science.

Author Contributions: Conceptualization, A.B. and K.M.; Methodology, A.B., K.M. and F.M.; Software, K.M. and F.M.; Validation, A.B., K.M. and F.M.; Formal Analysis, A.B., K.M. and F.M.; Investigation, A.B., K.M. and F.M.; Writing—Original Draft Preparation, A.B. and K.M.; Writing—Review & Editing, A.B. and K.M.; Visualization, A.B. and K.M.; Supervision, A.B..; Project Administration, A.B.

Funding: This research was funded by CFM foundation.

Conflicts of Interest: The authors declare no conflict of interest.

References

1. Barrau, A. Testing different approaches to quantum gravity with cosmology: An overview. *C. R. Phys.* **2017**, *18*, 189–199. [CrossRef]
2. Hossenfelder, S.; Smolin, L. Phenomenological Quantum Gravity. *Phys. Can.* **2010**, *66*, 99–102.
3. Liberati, S.; Maccione, L. Quantum Gravity phenomenology: Achievements and challenges. *J. Phys. Conf. Ser.* **2011**, *314*, 012007. [CrossRef]
4. Amelino-Camelia, G. Quantum Spacetime Phenomenology. *Living Rev. Rel.* **2013**, *16*, 5. [CrossRef] [PubMed]
5. Barrau, A.; Bojowald, M.; Calcagni, G.; Grain, J.; Kagan, M. Anomaly-free cosmological perturbations in effective canonical quantum gravity. *J. Cosmol. Astropart. Phys.* **2015**, *2015*, 051. [CrossRef]
6. Agullo, I.; Ashtekar, A.; Nelson, W. A Quantum Gravity Extension of the Inflationary Scenario. *Phys. Rev. Lett.* **2012**, *109*, 251301. [CrossRef] [PubMed]
7. Martineau, K.; Barrau, A.; Schander, S. Detailed investigation of the duration of inflation in loop quantum cosmology for a Bianchi-I universe with different inflaton potentials and initial conditions. *Phys. Rev. D* **2017**, *95*, 083507. [CrossRef]
8. Ashtekar, A. Sloan, D. Probability of Inflation in Loop Quantum Cosmology. *Gen. Relat. Grav.* **2011**, *43*, 3619. [CrossRef]
9. Vasileiou, V.; Granot, J.; Piran, T.; Amelino-Camelia, G. A Planck-scale limit on spacetime fuzziness and stochastic Lorentz invariance violation. *Nat. Phys.* **2015**, *11*, 344–346. [CrossRef]
10. Barbero, G.J.F.; Perez, A. Quantum Geometry and Black Holes. *arXiv* **2015**, arXiv:1501.02963.
11. Ashtekar, A.; Bojowald, M. Quantum geometry and the Schwarzschild singularity. *Class. Quant. Grav.* **2006**, *23*, 391–411. [CrossRef]
12. Bojowald, M. Nonsingular Black Holes and Degrees of Freedom in Quantum Gravity. *Phys. Rev. Lett.* **2005**, *95*, 061301. [CrossRef] [PubMed]
13. Mathur, S.D. The information paradox: A pedagogical introduction. *Class. Quant. Grav.* **2009**, *26*, 224001. [CrossRef]
14. Bekenstein, J.D. Black holes and information theory. *Contemp. Phys.* **2003**, *45*, 31–43. [CrossRef]
15. Hawking, S.W. Particle Creation by Black Holes. *Commun. Math. Phys.* **1975**, *43*, 199–220. [CrossRef]
16. Ashtekar, A.; Beetle, C.; Fairhurst, S. Isolated Horizons: A Generalization of Black Hole Mechanics. *Class. Quant. Grav.* **1999**, *16*, L1–L7. [CrossRef]
17. Ashtekar, A.; Beetle, C.; Fairhurst, S. Mechanics of Isolated Horizons. *Class. Quant. Grav.* **2000**, *17*, 253–298. [CrossRef]
18. Ashtekar, A.; Beetle, C.; Dreyer, O.; Fairhurst, S.; Krishnan, B.; Lewandowski, J.; Wisniewski, J. Generic Isolated Horizons and their Applications. *Phys. Rev. Lett.* **2000**, *85*, 3564–3567. [CrossRef] [PubMed]
19. Lewandowski, J. Space-Times Admitting Isolated Horizons. *Class. Quant. Grav.* **2000**, *17*, L53–L59. [CrossRef]
20. Lewandowski, J.; Pawlowski, T. Geometric Characterizations of the Kerr Isolated Horizon. *Int. J. Mod. Phys. D* **2002**, *11*, 739-746. [CrossRef]

21. Perez, A. Black Holes in Loop Quantum Gravity. *Rep. Prog. Phys.* **2017**, *80*, 126901. [CrossRef] [PubMed]
22. Olmedo, J. Brief review on black hole loop quantization. *Universe* **2016**, *2*, 12. [CrossRef]
23. Gambini, R.; Pullin, J. An introduction to spherically symmetric loop quantum gravity black holes. In Proceedings of the Cosmology and gravitation in the Southern Cone (CosmoSur II), Valparaiso, Chile, May 27-31, 2013.
24. Gambini, R.; Olmedo, J.; Pullin, J. Quantum black holes in Loop Quantum Gravity. *Class. Quant. Grav.* **2014**, *31*, 095009. [CrossRef]
25. Roken, C. On the Nature of Black Holes in Loop Quantum Gravity. *Class. Quant. Grav.* **2013**, *30*, 015005. [CrossRef]
26. Agullo, I.; Fernando Barbero, G.J.; Borja, E.F.; Diaz-Polo, J.; Villasenor, E.J.S. Black hole entropy in loop quantum gravity. *J. Phys. Conf. Ser.* **2012**, *360*, 012035. [CrossRef]
27. Diaz-Polo, J.; Pranzetti, D. Isolated Horizons and Black Hole Entropy in Loop Quantum Gravity. *Symmetry Integrability Geom. Methods Appl.* **2012**, *8*, 48–58. [CrossRef]
28. Ashtekar, A.; Baez, J.; Corichi, A.; Krasnov, K. Quantum Geometry and Black Hole Entropy. *Phys. Rev. Lett.* **1998**, *80*, 904–907. [CrossRef]
29. Ashtekar, A.; Baez, J.C.; Krasnov, K. Quantum Geometry of Isolated Horizons and Black Hole Entropy. *Adv. Theor. Math. Phys.* **2000**, *4*, 1–94. [CrossRef]
30. Corichi, A.; Diaz-Polo, J.; Fernandez-Borja, E. Black hole entropy quantization. *Phys. Rev. Lett.* **2007**, *98*, 181301. [CrossRef] [PubMed]
31. Corichi, A.; Diaz-Polo, J.; Fernandez-Borja, E. Quantum geometry and microscopic black hole entropy. *Class. Quant. Grav.* **2007**, *24*, 243–251. [CrossRef]
32. Rovelli, C.; Vidotto, F. *Covariant Loop Quantum Gravity*; Cambridge Monographs on Mathematical Physics; Cambridge University Press: Cambridge, UK, 2014; ISBN 1107069629, 9781107069626, 9781316147290.
33. Steinhauer, J. Observation of quantum Hawking radiation and its entanglement in an analogue black hole. *Nat. Phys.* **2016**, *12*, 959. [CrossRef]
34. Nowakowski, M.; Arraut, I. The Minimum and Maximum Temperature of Black Body Radiation. *Mod. Phys. Lett. A* **2009**, *24*, 2133. [CrossRef]
35. Arraut, I.; Batic, D.; Nowakowski, M. Comparing two approaches to Hawking radiation of Schwarzschild-de Sitter black holes. *Class. Quant. Grav.* **2009**, *26*, 125006. [CrossRef]
36. Nowakowski, M.; Arraut, I. Living with Λ. *Braz. J. Phys.* **2008**, *38*, 425–430. [CrossRef]
37. Alexeyev, S.; Barrau, A.; Boudoul, G.; Khovanskaya, O.; Sazhin, M. Black-hole relics in string gravity: Last stages of Hawking evaporation. *Class. Quant. Grav.* **2002**, *19*, 4431–4444. [CrossRef]
38. Barrau, A.; Cailleteau, T.; Cao, X.; Diaz-Polo, J.; Grain, J. Probing Loop Quantum Gravity with Evaporating Black Holes. *Phys. Rev. Lett.* **2011**, *107*, 251301. [CrossRef] [PubMed]
39. Agullo, I.; Fernando Barbero, J.; Borja, E.F.; Diaz-Polo, J.; Villasenor, E.J.S. Detailed black hole state counting in loop quantum gravity. *Phys. Rev. D* **2010**, *82*, 084029. [CrossRef]
40. Bekenstein, J.D.; Mukhanov, V.F. Spectroscopy of the quantum black hole. *Phys. Lett. B* **1995**, *360*, 7–12. [CrossRef]
41. Barbero, G.J.F.; Villasenor, E.J.S. On the computation of black hole entropy in loop quantum gravity. *Class. Quant. Grav.* **2009**, *26*, 035017.
42. Fernando Barbero, G.J.; Villasenor, E.J.S. Statistical description of the black hole degeneracy spectrum. *Phys. Rev. D* **2011**, *83*, 104013. [CrossRef]
43. Cao, X.; Barrau, A. The entropy of large black holes in loop quantum gravity: A combinatorics/analysis approach. *arXiv* **2011**, arXiv:1111.1975.
44. Barrau, A.; Cao, X.; Noui, K.; Perez, A. Black hole spectroscopy from Loop Quantum Gravity models. *Phys. Rev. D* **2015**, *92*, 124046. [CrossRef]
45. Engle, J.; Noui, K.; Perez, A.; Pranzetti, D. Black hole entropy from an SU(2)-invariant formulation of Type I isolated horizons. *Phys. Rev. D* **2010**, *82*, 044050. [CrossRef]
46. Engle, J.; Noui, K.; Perez, A.; Pranzetti, D. The SU(2) Black Hole entropy revisited. *J. High Energy Phys.* **2011**, *2011*, 016. [CrossRef]
47. Buffenoir, E.; Noui, K.; Roche, P. Hamiltonian Quantization of Chern-Simons theory with SL(2,C) Group. *Class. Quant. Grav.* **2002**, *19*, 4953. [CrossRef]

48. Noui, K. Three Dimensional Loop Quantum Gravity: Particles and the Quantum Double. *J. Math. Phys.* **2006**, *47*, 102501. [CrossRef]
49. Noui, K. Three dimensional Loop Quantum Gravity: Towards a self-gravitating Quantum Field Theory. *Class. Quant. Grav.* **2007**, *24*, 329–360. [CrossRef]
50. Ghosh, A.; Perez, A. Black hole entropy and isolated horizons thermodynamics. *Phys. Rev. Lett.* **2011**, *107*, 241301. [CrossRef] [PubMed]
51. Ghosh, A.; Noui, K.; Perez, A. Statistics, holography, and black hole entropy in loop quantum gravity. *Phys. Rev. D* **2014**, *89*, 084069,
52. Solodukhin, S.N. Entanglement entropy of black holes. *Living Rev. Rel.* **2011**, *14*, 8. [CrossRef] [PubMed]
53. Geiller, M.; Noui, K. Near-Horizon Radiation and Self-Dual Loop Quantum Gravity. *EPL (Europhys. Lett.)* **2014**, *105*, 60001. [CrossRef]
54. Ben Achour, J.; Mouchet, A.; Noui, K. Analytic Continuation of Black Hole Entropy in Loop Quantum Gravity. *J. High Energy Phys.* **2015**, *2015*, 145.
55. Agullo, I.; Fernando Barbero, G.J.; Borja, Diaz-Polo, E.F.; Villasenor, J. Combinatorics of the SU(2) black hole entropy in loop quantum gravity. *Phys. Rev. D* **2009**, *80*, 084006. [CrossRef]
56. Moulin, F.; Martineau,K.; Grain, J.; Barrau, A. Quantum fields in the background spacetime of a loop quantum gravity black hole. *arXiv* **2018**, arXiv:1808.00207.
57. Alesci, E.; Modesto, L. Particle Creation by Loop Black Holes. *Gen. Relat. Grav.* **2014**, *46*, 1656. [CrossRef]
58. Modesto, L. Space-Time Structure of Loop Quantum Black Hole. *Int. J. Theor. Phys.* **2010**, *49*, 1649. [CrossRef]
59. Ben Achour, J.; Lamy, F.; Liu, H.; Noui, K. Polymer Schwarzschild black hole: An effective metric. *EPL (Europhys. Lett.)* **2018**, *123*, 20006. [CrossRef]
60. Ashtekar, A.; Olmedo, J.; Singh, P. Quantum Transfiguration of Kruskal Black Holes. *arXiv* **2018**, arXiv:1806.00648.
61. Ashtekar, A.; Olmedo, J.; Singh, P. Quantum Extension of the Kruskal Space-time. *arXiv* **2018**, arXiv:1806.02406.
62. Makela, J. Partition Function of the Schwarzschild Black Hole. *Entropy* **2011**, *13*, 1324–1354. [CrossRef]
63. Barrau, A. Evaporation Spectrum of Black Holes from a Local Quantum Gravity Perspective. *Phys. Rev. Lett.* **2016**, *117*, 271301. [CrossRef] [PubMed]
64. Yoon, Y. Quantum corrections to the Hawking radiation spectrum. *J. Korean Phys. Soc.* **2016**, *68*, 730. [CrossRef]
65. Carr, B.J.; Kohri, K.; Sendouda, Y.; Yokoyama, J. New cosmological constraints on primordial black holes. *Phys. Rev. D* **2010**, *81*, 104019. [CrossRef]
66. Sjöstrand, T. ; Ask, S.; Christiansen, J.R.; Corke, R.; Desai, N.; Ilten, P.; Mrenna, S.; Prestel, S.; Rasmussen, C.O.; Skands, P.Z. An Introduction to PYTHIA 8.2. *Comput. Phys. Commun.* **2015**, *191*, 159–177. [CrossRef]
67. Rovelli, C.; Vidotto, F. Planck stars. *Int. J. Mod. Phys. D* **2014**, *23*, 1442026. [CrossRef]
68. Barrau, A.; Rovelli, C. Planck star phenomenology. *Phys. Lett. B* **2014**, *739*, 405–409. [CrossRef]
69. Haggard, H.M.; Rovelli, C. Black hole fireworks: quantum-gravity effects outside the horizon spark black to white hole tunneling. *Phys. Rev. D* **2015**, *92*, 104020. [CrossRef]
70. Haggard, H.M.; Rovelli, C. Black to white hole tunneling: An exact classical solution. *Int. J. Mod. Phys. A* **2015**, *30*, 1545015. [CrossRef]
71. Giddings, S.B. Black Holes and Massive Remnants. *Phys. Rev. D* **1992**, *46*, 1347–1352. [CrossRef]
72. Hajicek, P.; Kiefer, C. Singularity avoidance by collapsing shells in quantum gravity. *Int. J. Mod. Phys. D* **2001**, *10*, 775–780. [CrossRef]
73. Haggard, H.M.; Rovelli, C. Quantum Gravity Effects around Sagittarius A*. *Int. J. Mod. Phys. D* **2016**, *25*, 1644021. [CrossRef]
74. Christodoulou, M.; Rovelli, C.; Speziale, S.; Vilensky, I. Realistic Observable in Background-Free Quantum Gravity: The Planck-Star Tunnelling-Time. *Phys. Rev. D* **2016**, *94*, 084035. [CrossRef]
75. De Lorenzo, T.; Perez, A. Improved Black Hole Fireworks: Asymmetric Black-Hole-to-White-Hole Tunneling Scenario. *Phys. Rev. D* **2016**, *93*, 124018. [CrossRef]
76. Barrau, A.; Rovelli, C.; Vidotto, F. Fast Radio Bursts and White Hole Signals. *Phys. Rev. D* **2014**, *90*, 127503. [CrossRef]
77. Lorimer, D.R.; Bailes, M.; McLaughlin, M.A.; Narkevic, D.J.; Crawford, F. A bright millisecond radio burst of extragalactic origin. *Science* **2007**, *318*, 777–780. [CrossRef] [PubMed]
78. Keane, E.F.; Stappers, B.W.; Kramer, M.; Lyne, A.G. On the origin of a highly-dispersed coherent radio burst. *Mon. Not. R. Astron. Soc.* **2012**, *425*, L71–L75. [CrossRef]

79. Thornton, D.; Stappers, B.; Bailes, M.; Barsdell, B.R.; Bates, S.D.; Bhat, N.D.R.; Burgay, M.; Burke-Spolaor, S.; Champion, D.J.; Coster, P.; et al. A Population of Fast Radio Bursts at Cosmological Distances. *Science* **2013**, *341*, 53–56. [CrossRef] [PubMed]
80. Spitler, L.G.; Cordes, J.M.; Hessels, J.W.T.; Lorimer, D.R.; McLaughlin, M.A.; Chatterjee, S.; Crawford, F.; Deneva, J.S.; Kaspi, V.M.; Wharton, R.S.; et al. Fast Radio Burst Discovered in the Arecibo Pulsar ALFA Survey. *Astrophys. J.* **2014**, *790*, 101. [CrossRef]
81. Barrau, A.; Moulin, F.; Martineau, K. Fast radio bursts and the stochastic lifetime of black holes in quantum gravity. *Phys. Rev. D* **2018**, *97*, 066019. [CrossRef]
82. Barrau, A.; Bolliet, B.; Schutten, M.; Vidotto, F. Bouncing black holes in quantum gravity and the Fermi gamma-ray excess. *Phys. Lett. B* **2017**, *772*, 58. [CrossRef]
83. Barrau, A.; Bolliet, B.; Vidotto, F.; Weimer, C. Phenomenology of bouncing black holes in quantum gravity: A closer look. *J. Cosmol. Astropart. Phys.* **2016**, *1602*, 022. [CrossRef]
84. Hooper, D.; Goodenough, L. Dark Matter Annihilation in The Galactic Center As Seen by the Fermi Gamma Ray Space Telescope. *Phys. Lett. B* **2011**, *697*, 412–428. [CrossRef]
85. Abazajian, K.N.; Kaplinghat, M. Detection of a Gamma-Ray Source in the Galactic Center Consistent with Extended Emission from Dark Matter Annihilation and Concentrated Astrophysical Emission. *Phys. Rev. D* **2012**, *86*, 083511. [CrossRef]
86. Gordon, C.; Macias, O. Dark Matter and Pulsar Model Constraints from Galactic Center Fermi-LAT Gamma Ray Observations. *Phys. Rev. D* **2013**, *88*, 083521. [CrossRef]
87. Daylan, T.; Finkbeiner, D.P.; Hooper, D.; Linden, T.; Portillo, S.K.N.; Rodd, N.L.; Slatyer, T.R. The Characterization of the Gamma-Ray Signal from the Central Milky Way: A Compelling Case for Annihilating Dark Matter. *Phys. Dark Univ.* **2016**, *12*, 1. [CrossRef]
88. Bartels, R.; Krishnamurthy, S.; Weniger, C. Strong Support for the Millisecond Pulsar Origin of the Galactic Center GeV Excess. *Phys. Rev. Lett.* **2016**, *116*, 051102. [CrossRef] [PubMed]
89. Raccanelli, A.; Vidotto, F.; Verde, L. Effects of primordial black holes quantum gravity decay on galaxy clustering. *J. Cosmol. Astropart. Phys.* **2018**, *2018*, 003. [CrossRef]
90. Bianchi, E.; Christodoulou, M.; D'Ambrosio, F.; Rovelli, C.; Haggard, H.M. White Holes as Remnants: A Surprising Scenario for the End of a Black Hole. *arXiv* **2018**, arXiv:1802.04264.
91. MacGibbon, J.H. Can Planck-mass relics of evaporating black holes close the Universe? *Nature* **1987**, *329*, 308–309. [CrossRef]
92. Adler, R.J.; Chen, P.; Santiago, D.I. The Generalized Uncertainty Principle and Black Hole Remnants. *Gen. Relat. Grav.* **2001**, *33*, 2101–2108. [CrossRef]
93. Christodoulou, M.; Rovelli, C. How big is a black hole? *Phys. Rev. D* **2015**, *91*, 064046. [CrossRef]
94. Vidotto, F.; Rovelli, C. White-hole dark matter and the origin of past low-entropy. *arXiv* **2018**, arXiv:1804.04147.
95. Rovelli, C.; Vidotto, F. Small black/white hole stability and dark matter. *arXiv* **2018**, arXiv:1805.03872.
96. Barrow, J.D.; Copeland, E.J.; Liddle, A.R. The cosmology of black hole relics. *Phys. Rev.* **1992**, *D46*, 645. [CrossRef]
97. Zeldovich, Y.B.; Novikov, I.D. *Relativistic Astrophysics*; University of Chicago Press: Chicago, IL, USA, 1983; ISBN 9780226979571.
98. Aharonov, Y.; Casher, A.; Nussinov, S. The unitarity puzzle and Planck mass stable particles. *Phys. Lett. B* **1987**, *191*, 51–55. [CrossRef]
99. Banks, T.; Dabholkar, A.; Douglas, M.R.; O'Loughlin, M. Are horned particles the end point of Hawking evaporation? *Phys. Rev. D* **1992**, *45*, 3607. [CrossRef]
100. Banks, T.; O'Loughlin, M.; Strominger, A. Black hole remnants and the information puzzle. *Phys. Rev. D* **1993**, *47*, 4476–4482. [CrossRef]
101. Bowick, M.J.; Giddings, S.B.; Harvey, J.A.; Horowitz, G.T.; Strominger, A. Axionic Black Holes and an Aharonov-Bohm Effect for Strings. *Phys. Rev. Lett.* **1988**, *61*, 2823. [CrossRef] [PubMed]
102. Coleman, S.R.; Preskill, J.; Wilczek, F. Growing hair on black holes. *Phys. Rev. Lett.* **1991**, *67*, 1975. [CrossRef] [PubMed]
103. Lee, K.-M.; Nair, V.P.; Weinberg, E.J. A Classical Instability of Reissner-Nordstrom Solutions and the Fate of Magnetically Charged Black Holes. *Phys. Rev. Lett.* **1992**, *68*, 1100–1103. [CrossRef] [PubMed]
104. Gibbons, G.W.; Maeda, K.I. Black holes and membranes in higher-dimensional theories with dilaton fields. *Nucl. Phys. B* **1988**, *298*, 741–775. [CrossRef]

105. Torii, T.; Maeda, K.I. Black holes with non-Abelian hair and their thermodynamical properties. *Phys. Rev. D* **1993**, *48*, 1643. [CrossRef]
106. Callan, C.G., Jr.; Myers, R.C.; Perry, M.J. Black holes in string theory. *Nucl. Phys. B* **1989**, *311*, 673–698. [CrossRef]
107. Myers, R.C.; Simon, J.Z. Black-hole thermodynamics in Lovelock gravity. *Phys. Rev. D* **1988**, *38*, 2434–2444. [CrossRef]
108. Whitt, B. Spherically symmetric solutions of general second-order gravity. *Phys. Rev. D* **1988**, *38*, 3000. [CrossRef]
109. Barrau, A.; Blais, D.; Boudoul, G.; Polarski, D. Peculiar Relics from Primordial Black Holes in the Inflationary Paradigm. *Ann. Phys.* **2004**, *13*, 115. [CrossRef]
110. Starobinsky, A.A. Spectrum of adiabatic perturbations in the universe when there are singularities in the inflation potential. *JETP Lett.* **1992**, *55*, 489–494.
111. Carr, B.; Raidal, M.; Tenkanen, T.; Vaskonen, V.; Veermäe, H. Primordial black hole constraints for extended mass functions. *Phys. Rev. D* **2017**, *96*, 023514. [CrossRef]
112. Rovelli, C.; Vidotto, F. Pre-big-bang black-hole remnants and the past low entropy. *arXiv* **2018**, arXiv:1805.03224.
113. Ashtekar, A.; Singh, P. Loop Quantum Cosmology: A Status Report. *Class. Quant. Grav.* **2011**, *28*, 213001. [CrossRef]
114. Carr, B.J.; Coley, A.A. Persistence of black holes through a cosmological bounce. *Int. J. Mod. Phys. D* **2011**, *20*, 2733. [CrossRef]
115. Clifton, T.; Carr, B.; Coley, A. Persistent Black Holes in Bouncing Cosmologies. *Class. Quant. Grav.* **2017**, *34*, 135005. [CrossRef]
116. Carr, B.; Clifton, T.; Coley, A. Black holes as echoes of previous cosmic cycles. *arXiv* **2017**, arXiv:1704.02919.
117. Rovelli, C. Is Time's Arrow Perspectival? *arXiv* **2015**, arXiv:1704.02919.
118. Linsefors, L.; Barrau, A. Duration of inflation and conditions at the bounce as a prediction of effective isotropic loop quantum cosmolog. *Phys. Rev. D* **2013**, *87*, 123509. [CrossRef]
119. Linsefors, L.; Barrau, A. Exhaustive investigation of the duration of inflation in effective anisotropic loop quantum cosmology. *Class. Quant. Grav.* **2015**, *32*, 035010. [CrossRef]
120. Bolliet, B.; Barrau, A.; Martineau, K.; Moulin, F. Some Clarifications on the Duration of Inflation in Loop Quantum Cosmology. *Class. Quant. Grav.* **2017**, *34*, 145003. [CrossRef]
121. Wilson-Ewing, E. The Matter Bounce Scenario in Loop Quantum Cosmology. *J. Cosmol. Astropart. Phys.* **2013**, *2013*, 026. [CrossRef]
122. Abbott, B.P.; Jawahar, S.; Lockerbie, N.A.; Tokmakov, K.V. [LIGO Scientific Collaboration and Virgo Collaboration]. Observation of Gravitational Waves from a Binary Black Hole Merger. *Phys. Rev. Lett.* **2016**, *116*, 061102. [CrossRef] [PubMed]
123. Abbott, B.P.; Jawahar, S.; Lockerbie, N.A.; Tokmakov, K.V. [LIGO Scientific Collaboration and Virgo Collaboration]. GW151226: Observation of Gravitational Waves from a 22-Solar-Mass Binary Black Hole Coalescence. *Phys. Rev. Lett.* **2016**, *116*, 241103. [CrossRef] [PubMed]
124. Abbott, B.P.; Jawahar, S.; Lockerbie, N.A.; Tokmakov, K.V. [LIGO Scientific Collaboration and Virgo Collaboration]. GW170104: Observation of a 50-Solar-Mass Binary Black Hole Coalescence at Redshift 0.2. *Phys. Rev. Lett.* **2017**, *118*, 221101. [CrossRef] [PubMed]
125. Abbott, B.P.; Jawahar, S.; Lockerbie, N.A.; Tokmakov, K.V. [LIGO Scientific Collaboration and Virgo Collaboration]. GW170608: Observation of a 19-solar-mass Binary Black Hole Coalescence. *Astrophys. J.* **2017**, *851*, L35. [CrossRef]
126. Abbott, B.P.; Jawahar, S.; Lockerbie, N.A.; Tokmakov, K.V. [LIGO Scientific Collaboration and Virgo Collaboration]. GW170814: A Three-Detector Observation of Gravitational Waves from a Binary Black Hole Coalescence. *Phys. Rev. Lett.* **2017**, *119*, 141101. [CrossRef] [PubMed]
127. Bianchi, E.; Gupta, A.; Haggard, H.; Sathyaprakash, B. Unpublished work in progress. 2018.
128. Barrau, A.; Martineau, K.; Moulin, F. Seeing through the cosmological bounce: Footprints of the contracting phase and luminosity distance in bouncing models. *Phys. Rev. D* **2017**, *96*, 123520. [CrossRef]
129. Chirenti, C. Black hole quasinormal modes in the era of LIGO. *Braz. J. Phys.* **2018**, *48*, 102. [CrossRef]

3.5 La matière noire faite de reliques de trous noirs microscopique

Les évidences de l'existence de la matière noire sont nombreuses [80]. Cette matière noire est contrainte d'être électriquement neutre et non-baryonique. Mais de quoi est elle constituée ? Quelle est son origine ? Ces questions restent ouvertes mais de nombreux candidats et modèles sont étudiés.

Dans cet article, on s'intéresse au scénario où la matière noire serait constituée de reliques de Planck. Dans l'univers primordiale, si deux particules trans-Planckiennes entrent en collision et que le paramètre d'impact est plus petit que le rayon de Schwarzschild, alors ce processus inélastique mène à la formation de trou noir. La production de trou noir est décrite par la section efficace suivante

$$\sigma(s) = F(s)\pi R_S^2 \tag{3.113}$$

avec $\sqrt{s}$ l'énergie du centre de masse, R_s le rayon de Schwarzschild et $F(s)$ de l'ordre de 1. La gravité quantique doit être prise en compte pour une description plus rigoureuse mais les caractéristiques principales sont indépendantes du modèle. Ici, nous ne considérons pas la production de trous noirs microscopiques lié à l'existence de dimensions supplémentaires ou d'une énergie de Planck basse. La fin du processus d'évaporation ne peut pas être traitée de façon semi-classique. Dans les théories au delà de la RG, beaucoup d'entre elles argumentent qu'un trou noir ne s'évapore pas totalement mais, au contraire, existe sous la forme d'une relique de Planck stable (ou à long temps de vie) [81]. Dans ce cas, il serait possible de résoudre le paradoxe de l'information.

Soient des trous noirs primordiaux (PBHs) formés par des particules trans-Planckiennes pendant la période de réchauffement. Les reliques qui en découlent sont constituées de matière non-relativiste et leur densité se comporte comme a^{-3}. La densité du fond, constitué de rayonnement, se dilue plus rapidement en a^{-4}. Ainsi on peut avoir

$$\Omega_{rel} = \frac{\rho_{rel}}{\rho_{cr}} \approx 1, \tag{3.114}$$

avec ρ_{rel} la densité des reliques et ρ_{cr} la densité critique cosmologique définie telle que $\rho_{cr} = 3H^2/\kappa$ (elle représente la densité pour définir un univers plat, elle est différente de la densité ρ_c définie en LQC). L'amplification relative de la densité des reliques par rapport au fond de rayonnement est donné par

$$T_{RH}/T_{eq} \approx 3 \times 10^{27} T_{RH} \tag{3.115}$$

avec T_{RH} la température de réchauffement et T_{eq} la température au temps de l'équilibre. Le nombre de particules avec une énergie au delà de la température moyenne décroit de façon exponentielle. Ainsi pour que, dans la queue de distribution, il y ait suffisamment de trous noirs formés pour rendre compte de la matière noire, il faut que l'énergie de l'inflation soit plus élevée que celle usuellement considérée. C'est l'unique hypothèse exotique de l'article ci-joint. En effet, l'échelle d'énergie de l'inflation est contrainte expérimentalement par le ratio scalaire-tenseur mais

— si on considère une inflation à champs multiples on peut avoir un ratio faible et une échelle d'énergie élevée,

— si la gravité n'est pas quantifiée, alors il n'y a pas de mode même à une énergie d'inflation haute.

Soit E_t l'énergie des particules pour former un trou noir, on a une distribution de Maxwell-Boltzmann pour décrire le nombre de particules d'énergie supérieure à E_t

$$n_{part} \approx T_{RH} e^{\frac{-E_t}{T_{RH}}}. \tag{3.116}$$

Pour une section efficace de collision σ_{BH}, indépendante de l'énergie en première approximation, la densité relative au temps d'équilibre est donnée par

$$\Omega_{rel}^{eq} = \frac{30\sigma_{BH} m_{rel}}{1.66\pi^2 g_*^{3/2}} \cdot \frac{e^{-\frac{2E_t}{T_{RH}}}}{T_{eq} T_{RH}^3}, \tag{3.117}$$

avec m_{rel} la masse des reliques et g_* le nombre total des degrés de liberté sans masse (pour décrire les radiations) [82]. La densité relative de reliques en fonction de la température de réchauffement est tracée sur la Figure 1, avec un zoom sur la Figure 2. Ainsi on observe qu'avec une température de réchauffement de l'ordre de 10^{-2} en unités de Planck, on obtient une fraction de reliques proche de 1, ce qui permettrai d'avoir assez de reliques pour rendre compte de la quantité de matière noire.

Il serait possible de détecter de telles reliques si deux d'entre elles coalescent. Le taux de coalescence actuel, à $t = t_0$, est donné par

$$n_{merg} = \frac{3H_0^2}{8\pi G} \frac{\Omega_{rel}}{m_{rel}} \frac{dP}{dt}, \tag{3.118}$$

avec H_0 le paramètre de Hubble actuel et P la probabilité de coalescence. Ce taux est de l'ordre de $10^{-45}\mathrm{m}^{-3}\mathrm{s}^{-1}$. Avec un instrument tel que Euso-like et en utilisant les planètes géantes en tant que détecteurs cosmiques on pourraient atteindre 12 évènements par an ce qui est très faible mais tout de même dans la fenêtre de ce qui est expérimentable.

Cet article a été publié dans *Physical Review D* [83].

Dark matter as Planck relics without too exotic hypotheses

Aurélien Barrau, Killian Martineau, Flora Moulin, and Jean-Frédéric Ngono
Laboratoire de Physique Subatomique et de Cosmologie, Université Grenoble-Alpes, CNRS/IN2P3 53, avenue des Martyrs, 38026 Grenoble cedex, France

(Received 23 August 2019; published 3 December 2019)

The idea that dark matter could be made of stable relics of microscopic black holes is not new. In this article, we revisit this hypothesis, focusing on the creation of black holes by the scattering of trans-Planckian particles in the early Universe. The only new physics required in this approach is an unusually high-energy scale for inflation. We show that dark matter emerges naturally and we study the question of fine-tuning. We finally give some lines of thoughts for a possible detection.

DOI: 10.1103/PhysRevD.100.123505

I. INTRODUCTION

Dark matter is a very old problem. On the experimental side, it is being actively searched for, by direct detection (see, e.g., [1–3] for reviews), by indirect detection (see, e.g., [4–6] for reviews), and by accelerator production (see, e.g., [7,8] for reviews). Many "little anomalies" are known, from the Fermi excess of GeV gamma rays [9] to the PAMELA and AMS-02 overabundance of positrons [10–12]. All of them can however be quite simply accounted for by conventional astrophysical processes and at this stage no clear signal for nonbaryonic dark matter has been unambiguously recorded.

On the theoretical side, many hypotheses are being considered. They are actually too numerous to be exhaustively mentioned here (see, e.g., [13] for an introductory review). From supersymmetry [14] to axions [15], most of them imply some amount of "new physics." Recent developments even include an impressive list of highly speculative hypotheses.

Obviously, estimating the "exoticity" of a model is quite subjective. In this brief article, we revisit the idea of dark matter made of Planck relics and we argue that this scenario might be much less exotic than most models. The only nonstandard hypothesis is a higher than usual reheating temperature.

II. TRANS-PLANCKIAN SCATTERING

Most studies considering primordial black holes (PBHs) are relying on production mechanisms that involve the collapse of overdense regions (see, e.g., [16] for an early detailed calculation, [17,18] for studies of phase transitions, and [19,20] for reviews). Those scenarios are however very unlikely as the density contrast required to form a PBH is close to 1, whereas the primordial power spectrum measured in the cosmological microwave background (CMB) has a much lower normalization. This bound could have been circumvented by a blue power spectrum as the scales involved in the formation of PBHs are much smaller than those probed by the CMB. The actual spectrum, however, happens to be red ($n_s \approx 0.965$) [21], making the production of primordial black holes by "historical" mechanisms very difficult. Other scenarios like the collapse of cosmic strings were also considered [22] but they are also disfavored—if not ruled out—by recent measurements. Interesting new ideas are, however, now being considered [23,24].

Nevertheless, there exists a very different way to produce small black holes, namely, through the scattering of trans-Planckian particles. As initially argued in [25], when the impact parameter is smaller than the Schwarzschild radius (associated with the considered center-of-mass energy of a particle collision), the cross section for the scattering of trans-Planckian particles is dominated by an inelastic process leading to the formation of a single black hole. The key point is that the main features of high-energy scattering above the Planck energy can be studied from semiclassical considerations in general relativity and are therefore reliable.

Basically, at impact parameters greater than the Schwarzschild radius, elastic and inelastic processes (gravitational radiation, bremsstrahlung for charged particles, etc.) are described by solving the classical equations of the low-energy theory with initial conditions described by a pair of shock waves with appropriate quantum numbers. At smaller impact parameters, scattering is dominated by the resonant (in a sense different from the classical Breit-Wigner one) production of a black hole with mass equal to

the center-of-mass energy. The elastic cross section is suppressed by a Boltzmann factor and the incoming particles never get close enough together to perform a hard QCD scattering. In this limit the eikonal approximation for the initial state becomes valid and is described by a metric containing a pair of Aichelburg-Sexl shock waves with the associated impact parameter.

In [26], the study was refined and it was also concluded that the cross section for black hole production should be of the order of $\sigma(s) = F(s)\pi R_S^2(s)$ with $F(s)$ being factor of order 1, $\sqrt{s}$ the center-of-mass energy, and R_S the Schwarzschild radius. The details obviously depend on the considered quantum gravity theory but the main features are basically model independent.

Those ideas were applied to the possible production and observation of microscopic black holes at colliders (see, e.g., [26–29] for early works) in theories with a low Planck scale—typically in the TeV range (usually associated with the existence of large extra dimensions [30] or with many new particle species [31]). A nice review including astrophysical effects, like those mentioned in [32], can be found in [33]. In this article, we do not rely on the existence of extra dimensions and we do not assume a low Planck scale.

III. STABLE RELICS

The Hawking temperature $T_H = 1/(8\pi M)$ [34] is vanishingly small for astrophysical black holes but becomes significant for very small black holes. The mass loss rate during the evaporation is proportional to M^{-2} and the process is therefore highly explosive. In itself, the evaporation mechanism is well understood from many different perspectives and is very consensual (see, e.g., [35] for a simple introduction). Although it has not been observationally confirmed, there are indications that it might have been revealed in analog systems [36].

The status of the end point of the evaporation process is less clear. Obviously, the semiclassical treatment breaks down in the last stages and the divergence of the temperature together with the appearance of a naked singularity is nonphysical. Many different arguments have been pushed forward in favor of the existence of stable Planck relics at the end of the evaporation process (see [37–50] to mention only a few historical references, among many others). There are excellent arguments from quantum gravity, string gravity, or modified gravity theories in favor or remnants. Those are however obviously based on new physics. One of the best arguments for Planck relics using only known physics was given by Giddings in [51]. Locality, causality, and energy conservation considered within the information paradox framework (see, e.g., the first sections of [52] for a precise description) do suggest that the time scale for the final decay of BHs is larger than the age of the Universe.

Although no clear consensus exists on the status of BHs at the end of the evaporation process, it is fair to suggest that the existence of relics is somehow simpler from the viewpoint of usual physics. A recent review on the pros and cons of stable remnants can be found in [53]. It is concluded that if relics contain a large interior geometry—which is supported by [54,55]—, they help solve the information loss paradox and the firewall controversy.

IV. REHEATING SCALE

The idea that dark matter could be made of Planck relics was first suggested in [56]. This seminal work was, however, focused on PBHs formed by the collapse of overdense regions (or similar mechanisms), which is now believed to be extremely unlikely as previously pointed out. We focus here on the possibility that PBHs are formed by the collision of trans-Planckian particles in the early Universe. This has already been considered in [57] and in [58,59] (see also references therein) for the case with extra dimensions.

In this work, we do not assume a lower than usual Planck scale due to extra dimensions. We quite simply consider the standard cosmological scenario in a $(3+1)$-dimensional spacetime and just take into account the "tail" of trans-Planckian particles at the reheating time. The key point lies in the fact that the potentially produced relics behave nonrelativistically and are therefore much less diluted (their energy density scales as a^{-3}) than the surrounding radiation (whose energy density scales as a^{-4}). Hence, it is possible to reach a density of relics (normalized to the critical density) close to 1, $\Omega_{\rm rel} \equiv \rho_{\rm rel}/\rho_{\rm cr} \approx 1$, with only a tiny fraction of relics at the formation time. The relative "amplification" of the relics density compared to the radiation density between the reheating and the equilibrium times is given by $T_{\rm RH}/T_{\rm eq} \approx 3 \times 10^{27} T_{\rm RH}$ when $T_{\rm RH}$ is given in Planck units. To fix ideas, for a reheating temperature at the grand unified theory (GUT) scale, a relics fraction of only 10^{-24} at the formation time would be enough to nearly close the Universe at the equilibrium time.

For a thermal distribution of particles at temperature T, the number of particles above $E_{\rm th} > T$ is exponentially suppressed. This is why, even with the amplification factor given above, the scenario presented here requires a reheating temperature not much below the Planck scale. This constitutes, in our view, the only "nonstandard" input of this model. The Planck experiment final results lead to an upper limit on the tensor-to-scalar ratio of primordial perturbations $r < 0.1$ [60], which is even tightened to $r < 0.064$ by combining the data with the BICEP2/Keck Array BK14 measurements. This is usually interpreted as an upper limit on the energy scale of inflation around the GUT scale (the higher the energy scale, the larger the normalization of tensor modes), which is too low for the process considered here. There are, however, at least two ways to circumvent this bound (we assume for simplicity a sudden reheating).

The first one consists in noticing that the upper limit on the energy scale of inflation holds firmly only for

rudimentary models. In k inflation [61], the relation basically becomes $r = -8C_S n_t$ (instead of $r = -8n_t$), where n_t is the tensor index and $C_S < 1$ is the speed of sound for perturbations. This relaxes the bound. In two-field inflation [62], the upper limit is also relaxed to $r = -8n_t \sin^2(\theta)$, where θ accounts for the possible evolution of adiabatic scalar modes on super-Hubble scales. In multifield inflation the relation between r and n_T even becomes an inequality.

A second and probably more provocative argument would be the following. Whereas temperature anisotropies originate from usual quantum physics, namely, from the quantum fluctuations of the inflaton field, the tensor perturbations leading to B modes in the CMB should come from the quantum fluctuations of the polarization modes of the graviton. In a sense (and although some counterexamples have been constructed but for artificial models), B modes would be a signature of perturbative quantum gravity (dimensional arguments are given in [63]). Quantum gravity is a fascinating area of research but it has still no connection with experiments and assuming gravity not to be quantized is also legitimate, especially when considering how difficult and paradoxical the quantization of the gravitational field is [64]. It is therefore meaningful to consider the possibility that *no* B mode is produced, even with a very high-energy scale for inflation, just because gravity might not be quantum in nature (this would also raise many consistency questions but is obviously worth being considered, as advocated in [65,66]). In such a case, the usual upper bound could also be ignored.

Obviously, the normalization of the scalar spectrum would also be in tension with such a high scale (violating the slow-roll conditions in the most simple cases). We do *not* mean that a higher than usual energy scale for inflation is unavoidable or even favored. We simply state that this is not ruled out by the tensor-to-scalar ratio and might be, in our opinion, less "exotic" than most assumptions required for usual DM candidates.

V. DARK MATTER ABUNDANCE

The threshold energy E_t to produce a BH in a head on collision of particles is expected to be of the order of the Planck energy but, depending on the details of the considered model, might be slightly different and we keep it as a free parameter. To estimate the number density of particles above E_t, one simply needs to integrate the thermal distribution, which leads to

$$n_{\rm part} \approx T_{\rm RH} e^{-E_t/T_{\rm RH}},$$

where we use Planck units (as everywhere in this work except otherwise specified). Obviously, if the reheating temperature is too small when compared to the threshold energy of BH production, the number of PBHs will be exponentially suppressed and the process will be inefficient. The cross section, in principle, depends on the energy of the collision but, as a fist step, can be assumed to be a constant $\sigma_{\rm BH}$ above the threshold. The collision rate is therefore given by $\Gamma = n_{\rm part}\sigma_{\rm BH} v \approx n_{\rm part}\sigma_{\rm BH}$. The energy density of radiation is

$$\rho_R = \frac{\pi^2}{30} g_* T_{\rm RH}^4,$$

with g_* being the total number of effectively massless degrees of freedom, that is, species with masses $m_i \ll T_{\rm RH}$. The Hubble parameter is

$$H = 1.66 g_*^{1/2} T_{\rm RH}^2.$$

If relics are assumed to have a mass $m_{\rm rel}$ (necessarily lower than $E_{\rm th}$), the energy density of relics is given by

$$\rho_{\rm rel} \approx \frac{n_{\rm part} m_{\rm rel} \Gamma}{H} \approx \frac{e^{-\frac{2E_t}{T_{\rm RH}}} \sigma_{\rm BH} m_{\rm rel}}{1.66 g_*^{1/2}}.$$

The relative density of relics at the formation time is

$$\Omega_{\rm rel}^f = \frac{30\sigma_{\rm BH} m_{\rm rel}}{1.66\pi^2 g_*^{3/2}} \cdot \frac{e^{-\frac{2E_t}{T_{\rm RH}}}}{T_{\rm RH}^4},$$

leading, in agreement with [59], to a relative density at the equilibrium time of

$$\Omega_{\rm rel}^{\rm eq} = \frac{30\sigma_{\rm BH} m_{\rm rel}}{1.66\pi^2 g_*^{3/2}} \cdot \frac{e^{-\frac{2E_t}{T_{\rm RH}}}}{T_{\rm eq} T_{\rm RH}^3}.$$

Let us first assume that the cross section is of order 1 in Planck units ($\sigma \sim A_{\rm Pl}$) above the threshold and that the mass of the relics is also of order 1 in Planck units ($m_{\rm rel} \sim m_{\rm Pl}$). In Fig 1, the relative abundance of relics at the equilibrium time is plotted at the function of the reheating temperature. Figure 2 is a zoom on the relevant region. For a reheating temperature slightly above 10^{-2},

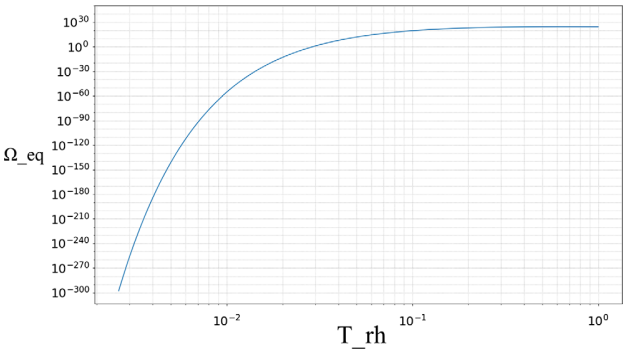

FIG. 1. Fraction of relics at the equilibrium time as a function of the reheating temperature (in Planck units).

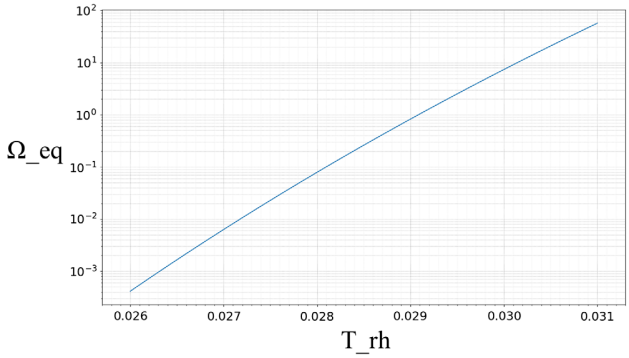

FIG. 2. Zoom on the fraction of relics at the equilibrium time as a function of the reheating temperature (in Planck units), around the relevant zone.

one is led to a density of relics that can account for dark matter.

Although the influence is negligible, from now on we use the cross section $\sigma(s) = F(s)\pi R_S^2(s)$, where $R_S = 2s$. We set $F = 1$ above the threshold, but with the dependency being linear it is easy to extrapolate to any reasonable value. In Fig. 3, we show the influence of the threshold energy. The influence of the threshold energy is—as expected—very large. Interestingly, if nonperturbative effects were to lower the threshold by 1 order of magnitude with respect to the expected value, a reheating temperature around the GUT scale would be enough to produce the required density of remnants.

It is worth noticing that in the case with extra dimensions [59], the "allowed" parameter space is defined by ensuring that the Hubble rate during inflation H_i, together with the maximal temperature are smaller than the D-dimensional Planck scale. Meanwhile H_i must remain much larger than the nucleosynthesis temperature. The formed relics account for dark matter basically between a Hubble rate of 10^{-16} (in usual four-dimensional Planck units) for a D-dimensional Planck scale of 10^{-7} to a Hubble rate of 10^{-3} for a D-dimensional Planck scale equal to $M_{\rm Pl}$.

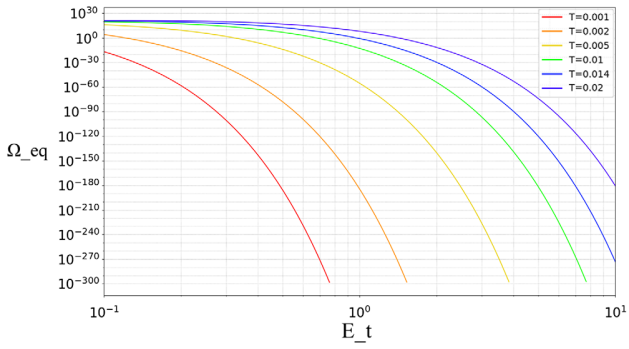

FIG. 3. Fraction of relics at the equilibrium time as a function of the energy threshold for different reheating temperatures (in Planck units), from 10^{-3} to 2×10^2 from bottom to top.

VI. THE FINE-TUNING ISSUE

The model presented here seems to require a high level of fine-tuning. In particular, as the dependency upon the reheating temperature is exponential, varying slightly its value leads to a large variation in the density of relics. One can easily check that

$$\frac{dT_{\rm RH}}{T_{\rm RH}} = \frac{d\Omega_{\rm eq}^{\rm rel}}{\Omega_{\rm eq}^{\rm rel}}\left(\frac{2E_T}{T_{\rm RH}} + 3\right)^{-1} \approx \frac{T_{\rm RH}}{2E_T}\frac{d\Omega_{\rm eq}^{\rm rel}}{\Omega_{\rm eq}^{\rm rel}} \sim 10^{-4},$$

to remain in agreement with data. Unquestionably, the model requires a very high level of fine-tuning.

The question of fine-tuning is, however, tricky. It is only well defined relatively to an *a priori* specific state. In the cosmological framework, the value $\Omega = 1$ is clearly such a special case. As is well known, inflation fixes a vanishing (or nearly so) curvature. Basically, as $(\Omega^{-1} - 1) = -\frac{3k}{8\pi\rho a^2}$ with ρ remaining constant and the scale factor increasing by at least 60 e-folds, Ω is fixed (close) to 1 at the end of inflation. There is obviously nothing magical here as Ω involves a normalization to the critical density that, itself, depends on the Hubble parameter. Should the content of the Universe be different, we would still have $\Omega = 1$, with a different expansion rate. This means that changing the parameters of this model would, in fact, not drive the Universe out of the specific situation $\Omega = 1$. In this sense it does *not* require fine-tuning.

One might argue that if the reheating temperature were different, other parameters of the Universe—e.g., the (unnormalized) matter density, the equilibrium time, etc.—would be different. This is correct. But, in our opinion, this is not a fine-tuning issue. This is just the obvious statement that things could have been different and that changing parameters do, of course, change the final state. This is not problematic as long as the "lost" state was not a very peculiar one.

To summarize, the parameters of the model need to be fine-tuned so that the relic density closes the Universe at the equilibrium time—which is a contingent fact—but not to ensure $\Omega = 1$, which is indeed the *a priori* specific feature.

VII. DETECTABILITY

Testing this model is challenging. A Planck relic has the weight of a grain of dust and no other interaction than gravity to reveal itself to the outer world. Even though the Planck mass is very small from the gravitational viewpoint, it is very large from the particle physics viewpoint. The number density of relics is therefore extremely small, even if they are to account for all the dark matter. A density of 10^{-18} relics par cubic meter—that is, one relic per volume of a million times the one of planet Earth—is enough to close the Universe. Detection seems hopeless. The cross section (or greybody factor) hopefully does *not* tend to 0 for the absorption of fermions in the low-energy limit [67]. However, even avoiding this catastrophic suppression

(which does exist for higher spins), the area involved is of the order of the Planck one, 10^{-66} cm^2, which indeed makes direct detection impossible in practice.

We consider here another possibility associated with the coalescences of relics that have occurred during the history of the Universe. Contrarily to what is sometimes done for PBHs we shall not focus on the emission of gravitational waves whose amplitude would be negligible and frequency way too high for any detector. However, something else is also expected to happen in this model. When two remnants merge, a higher-mass black hole is formed and evaporates until it reaches again $m_{\rm rel} \sim m_{\rm Pl}$ assumed to be the minimal one. This should happen preferably via the emission of one (or a few) quantum close to the Planck energy. Each merging should therefore emit about a Planck-energy particle, which is, in principle, detectable. This sketch should of course be refined but the hypothesis is realistic enough to investigate whether this path is potentially fruitful.

We estimate the merging rate following [68], which builds on [69]. It is not hard to show that the probability of coalescence in the time interval $(t, t+dt)$ is given by

$$dP = \frac{3}{58}\left[-\left(\frac{t}{T}\right)^{3/8} + \left(\frac{t}{T}\right)^{3/37}\right]\frac{dt}{t},$$

where $T \equiv \bar{x}^4 \frac{3}{170}(Gm_{\rm rel})^{-3}$,

$$\bar{x} = \left(\frac{M_{\rm rel}}{\rho_{\rm rel}(z_{\rm eq})}\right)^{1/3} = \frac{1}{(1+z_{\rm eq})}\left(\frac{8\pi G}{3H_0^2}\frac{m_{\rm rel}}{\Omega_{\rm rel}}\right)^{1/3}$$

being the mean separation of relics at the equilibrium time. In those formulas, we have reinserted the constants to make the use easier. The event rate is then given by

$$n_{\rm merg} = \frac{3H_0^2}{8\pi G}\frac{\Omega_{\rm rel}}{m_{\rm rel}}\left.\frac{dP}{dt}\right|_{t_0}.$$

This is of the order of 10^{-45} m^{-3} s^{-1}. It is then straightforward to estimate the measured flux on a detector of surface S_d and solid angle acceptance $\Omega_{\rm acc}$, integrated up to a distance $R_{\rm max}$,

$$\Phi_{\rm mes} = \int_0^{R_{\rm max}} n_{\rm merg} S_d \frac{\Omega_{\rm acc}}{4\pi} dR.$$

Although it is well known that TeV photons are absorbed by interactions with the infrared background and PeV photons by interactions with the CMB photons, there is no strong absorption to be expected for Planck-energy photons. The wavelength of the background photons that would lead to a center-of-mass energy close to the electron mass is way larger than any expected background. The $R_{\rm max}$ value can therefore be assumed to be much larger than for usual high-energy cosmic-ray estimations. For detectors like Auger [70], the expected flux is too small for a detection. For Euso-like instruments [71]—looking at the atmosphere from the space station—we are led to an order of magnitude not far from a fraction of an event per year. For speculative ideas about using giant planets as cosmic-ray detectors [72], we reach a dozen events per year. This is obviously a hard task but, interestingly, the model is clearly not unfalsifiable.

Furthermore, the idea that the Hawking radiation due to the formed black holes before they become stable relics might play a role in baryogenesis was considered in [73]. The possibility that they might have an effect on the primordial nucleosynthesis should also be considered. In the case considered in this article—with a true Planck scale at the four-dimensional value—, the relics are so heavy and heir number density so small that it is easy to check that the associated signal would be entirely negligible.

VIII. CONCLUSION

The idea that dark matter could be made of Planck relics is not new. Nor is the possibility that black holes could be formed by the scattering of trans-Planckian particles in the early Universe. In this article we have gathered all the ingredients and argued that the resulting model is not (that) exotic. Unquestionably, the very high reheating temperature required raises questions. We have however explained that the upper bounds usually considered can be circumvented. Still, building a consistent cosmological model with such a high scale for inflation is not trivial and should be considered as a challenge.

There is no obvious solution to the dark matter problem, which is one of the oldest enigmas of contemporary cosmology. The scenario suggested here is based on a minimum amount of new physics, if not only on known physics. It requires a quite unusual cosmological behavior but no new particle physics input is needed. From this point of view, it might be worth being considered seriously.

Several developments would be worth being considered.

(i) The possibility that nonthermal processes do happen during the reheating, eventually enhancing the high-energy tail of the distribution, should be studied with care.
(ii) The model presented in this article should be investigated in the context of noninflationary bouncing cosmologies, expected to be more favorable to this scenario.
(iii) The experimental possibilities that were outlined should be made more precise thanks to Monte Carlo simulations.
(iv) in addition to the possible detection of extremely high-energy gamma rays, it might be interesting to consider a possible low-energy (in the 100 MeV range) signal due to the disintegration of neutral pions produced by the hadronization of quarks or gluons emitted by the merging of relics.

ACKNOWLEDGMENTS

K. M is supported by a grant from the CFM foundation.

[1] B. Censier, EAS Publ. Ser. **53**, 59 (2012).
[2] J. Gascon, EPJ Web Conf. **95**, 02004 (2015).
[3] F. Mayet *et al.*, Phys. Rep. **627**, 1 (2016).
[4] M. Cirelli, Pramana **79**, 1021 (2012).
[5] J. Conrad, in *Interplay between Particle and Astroparticle Physics (IPA2014) London, United Kingdom* (2014), arXiv:1411.1925.
[6] J. M. Gaskins, Contemp. Phys. **57**, 496 (2016).
[7] F. Kahlhoefer, Int. J. Mod. Phys. A **32**, 1730006 (2017).
[8] M. Felcini, in *53rd Rencontres de Moriond on Cosmology La Thuile, Italy* (ARIFS, 2018).
[9] M. Ackermann *et al.* (Fermi-LAT Collaboration), Astrophys. J. **840**, 43 (2017).
[10] O. Adriani *et al.* (PAMELA Collaboration), Nature (London) **458**, 607 (2009).
[11] L. Accardo *et al.* (AMS Collaboration), Phys. Rev. Lett. **113**, 121101 (2014).
[12] M. Aguilar *et al.* (AMS Collaboration), Phys. Rev. Lett. **113**, 121102 (2014).
[13] M. Bauer and T. Plehn, arXiv:1705.01987.
[14] E. A. Bagnaschi *et al.*, Eur. Phys. J. C **75**, 500 (2015).
[15] V. B. Klaer and G. D. Moore, J. Cosmol. Astropart. Phys. 11 (2017) 049.
[16] B. J. Carr, Astrophys. J. **201**, 1 (1975).
[17] D. B. Cline, Nucl. Phys. **A610**, 500C (1996).
[18] K. Jedamzik and J. C. Niemeyer, Phys. Rev. D **59**, 124014 (1999).
[19] B. J. Carr, K. Kohri, Y. Sendouda, and J. Yokoyama, Phys. Rev. D **81**, 104019 (2010).
[20] A. M. Green, Fundam. Theor. Phys. **178**, 129 (2015).
[21] N. Aghanim *et al.* (Planck Collaboration), arXiv:1807.06209.
[22] S. W. Hawking, Phys. Lett. B **231**, 237 (1989).
[23] J. Garca-Bellido, B. Carr, and S. Clesse, arXiv:1904.11482.
[24] B. Carr, S. Clesse, and J. Garca-Bellido, arXiv:1904.02129.
[25] T. Banks and W. Fischler, arXiv:hep-th/9906038.
[26] S. B. Giddings and S. D. Thomas, Phys. Rev. D **65**, 056010 (2002).
[27] S. Dimopoulos and G. L. Landsberg, Phys. Rev. Lett. **87**, 161602 (2001).
[28] A. Barrau, J. Grain, and S. O. Alexeyev, Phys. Lett. B **584**, 114 (2004).
[29] B. C. Paul and D. Paul, Phys. Rev. D **74**, 084015 (2006).
[30] N. Arkani-Hamed, S. Dimopoulos, and G. R. Dvali, Phys. Lett. B **429**, 263 (1998).
[31] G. Dvali, Fortschr. Phys. **58**, 528 (2010).
[32] A. Barrau, C. Feron, and J. Grain, Astrophys. J. **630**, 1015 (2005).
[33] P. Kanti, Int. J. Mod. Phys. A **19**, 4899 (2004).
[34] S. W. Hawking, Commun. Math. Phys. **43**, 199 (1975).
[35] P.-H. Lambert, Proc. Sci., Modave2013 (**2013**) 001 [arXiv:1310.8312].
[36] J. Steinhauer, Nat. Phys. **12**, 959 (2016).
[37] J. D. Barrow, E. J. Copeland, and A. R. Liddle, Phys. Rev. D **46**, 645 (1992).
[38] Y. B. Zeldovich and I. D. Novikov, *Relativistic Astrophysics* (University of Chicago Press, Chicago, 1983).
[39] Y. Aharonov, A. Casher, and S. Nussinov, Phys. Lett. B **191**, 51 (1987).
[40] T. Banks, A. Dabholkar, M. R. Douglas, and M. O'Loughlin, Phys. Rev. D **45**, 3607 (1992).
[41] T. Banks, M. O'Loughlin, and A. Strominger, Phys. Rev. D **47**, 4476 (1993).
[42] M. J. Bowick, S. B. Giddings, J. A. Harvey, G. T. Horowitz, and A. Strominger, Phys. Rev. Lett. **61**, 2823 (1988).
[43] S. R. Coleman, J. Preskill, and F. Wilczek, Phys. Rev. Lett. **67**, 1975 (1991).
[44] K.-M. Lee, V. P. Nair, and E. J. Weinberg, Phys. Rev. Lett. **68**, 1100 (1992).
[45] G. W. Gibbons and K.-i. Maeda, Nucl. Phys. **B298**, 741 (1988).
[46] T. Torii and K.-i. Maeda, Phys. Rev. D **48**, 1643 (1993).
[47] C. G. Callan, Jr., R. C. Myers, and M. J. Perry, Nucl. Phys. **B311**, 673 (1989).
[48] R. C. Myers and J. Z. Simon, Phys. Rev. D **38**, 2434 (1988).
[49] B. Whitt, Phys. Rev. D **38**, 3000 (1988).
[50] S. Alexeyev, A. Barrau, G. Boudoul, O. Khovanskaya, and M. Sazhin, Classical Quantum Gravity **19**, 4431 (2002).
[51] S. B. Giddings, Phys. Rev. D **46**, 1347 (1992).
[52] S. D. Mathur, Pramana **79**, 1059 (2012).
[53] P. Chen, Y. C. Ong, and D.-h. Yeom, Phys. Rep. **603**, 1 (2015).
[54] M. Christodoulou and C. Rovelli, Phys. Rev. D **91**, 064046 (2015).
[55] M. Christodoulou and T. De Lorenzo, Phys. Rev. D **94**, 104002 (2016).
[56] J. H. MacGibbon, Nature (London) **329**, 308 (1987).
[57] A. Saini and D. Stojkovic, J. Cosmol. Astropart. Phys. 05 (2018) 071.
[58] J. A. Conley and T. Wizansky, Phys. Rev. D **75**, 044006 (2007).
[59] T. Nakama and J. Yokoyama, Phys. Rev. D **99**, 061303 (2019).
[60] O. E. Núñez, J. Socorro, and R. Hernández-Jiménez, Astrophys. Space Sci. **364**, 69 (2019).
[61] C. Armendariz-Picon, T. Damour, and V. F. Mukhanov, Phys. Lett. B **458**, 209 (1999).
[62] D. Wands, Lect. Notes Phys. **738**, 275 (2008).
[63] L. M. Krauss and F. Wilczek, Int. J. Mod. Phys. D **23**, 1441001 (2014).
[64] D. Oriti, *Approaches to Quantum Gravity: Toward a New Understanding of Space, Time and Matter* (Cambridge University Press, Cambridge, England, 2009).
[65] T. Jacobson, Phys. Rev. Lett. **75**, 1260 (1995).
[66] C. Eling, R. Guedens, and T. Jacobson, Phys. Rev. Lett. **96**, 121301 (2006).
[67] J. H. MacGibbon and B. R. Webber, Phys. Rev. D **41**, 3052 (1990).
[68] M. Sasaki, T. Suyama, T. Tanaka, and S. Yokoyama, Phys. Rev. Lett. **117**, 061101 (2016); **121**, 059901(E) (2018).
[69] T. Nakamura, M. Sasaki, T. Tanaka, and K. S. Thorne, Astrophys. J. **487**, L139 (1997).
[70] C. Covault *et al.* (Telescope Array Collaboration), EPJ Web Conf. **210**, 05004 (2019).
[71] N. Inoue, K. Miyazawa, and Y. Kawasaki (JEM-EUSO Collaboration), Nucl. Phys. B, Proc. Suppl. **196**, 135 (2009).
[72] P. B. Rimmer, C. R. Stark, and C. Helling, Astrophys. J. **787**, L25 (2014).
[73] S. Alexander and P. Meszaros, arXiv:hep-th/0703070.

CHAPITRE 4

Le formalisme polaire

Sommaire

4.1 La forme polaire

Avec l'étude des spineurs en espace courbe dans la section (3.2), on a pu voir que seulement une séparation de variables très précise (3.44,3.45,3.46,3.47) permettait de découpler les équations. Les spineurs sont des objets très sensibles à la structure de l'espace-temps, il est donc intéressant de les étudier pour mieux appréhender leur interaction avec ce dernier. Un spineur est un objet à quatre composantes complexes

$$\psi = \begin{pmatrix} \psi_1 \\ \psi_2 \\ \psi_3 \\ \psi_4 \end{pmatrix} \tag{4.1}$$

qui lors d'une transformation de Lorentz se transforme selon

$$\psi' = \Lambda_{\frac{1}{2}} \psi, \tag{4.2}$$

avec $\Lambda_{\frac{1}{2}}$ définie par (1.53). Un spineur obéit à l'équation de Dirac

$$i\gamma^\mu \nabla_\mu \psi + i\omega F_{\mu\nu}\sigma^{\mu\nu}\psi - m\psi = 0. \tag{4.3}$$

avec $F_{\mu\nu}$ le potentiel d'un champ externe, où on a utilisé la notation de [84]. Dans ce cadre, $F_{\mu\nu}$ ne représente par le tenseur électromagnétique, sa forme pour l'oscillateur harmonique sera explicitée dans la section (4.3.2). L'équation (4.3) est invariante sous transformation de Lorentz. Il existe 16 générateurs des matrices 4×4

$$\mathbb{I},\ \gamma^a,\ \sigma^{ab},\ \gamma^5 \text{ et } \gamma^a\gamma^5. \tag{4.4}$$

avec $\sigma^{ab} = \frac{1}{4}[\gamma^a, \gamma^b]$. Avec le spineur ψ et son adjoint $\overline{\psi} = \psi^\dagger\gamma_0$, on définit les quantités suivantes

$$\Phi = \overline{\psi}\psi, \tag{4.5}$$
$$\Theta = i\overline{\psi}\gamma^5\psi, \tag{4.6}$$
$$U^a = \overline{\psi}\gamma^a\psi, \tag{4.7}$$
$$S^a = \overline{\psi}\gamma^a\gamma^5\psi, \tag{4.8}$$
$$M^{ab} = 2i\overline{\psi}\sigma^{ab}\psi,. \tag{4.9}$$

Ce sont tous des tenseurs réels. Les spineurs de Majorana et de Weyl sont décrits par $\Phi = \Theta = 0$ et les spineurs de Dirac par $\Phi \neq 0$ ou $\Theta \neq 0$. Nous considérons, ici, le cas des spineurs de Dirac. On a respectivement un scalaire, un pseudo-scalaire, le vecteur de la densité de vitesse, le vecteur axial de la densité de spin et un tenseur antisymétrique de rang 2. Les identités de Fierz donnent

$$U_aU^a = -S_aS^a = \Theta^2 + \Phi^2, \tag{4.10}$$
$$U_aS^a = 0. \tag{4.11}$$

Ainsi nous avons

$$U_aU^a > 0 \quad \text{et} \quad S_aS^a < 0. \tag{4.12}$$

Nous précisons qu'on travaille avec la convention $+,-,-,-$. Donc U^a est de type temps et nous pouvons toujours trouver un référentiel tel que sa partie spatiale soit nulle. De même S^a est de type espace. Ainsi il existe trois boosts tels que $U^1 = U^2 = U^3 = 0$ et $S^0 = 0$. De plus, il existe deux rotations telles que $S^1 = S^2 = 0$ et enfin, nous pouvons effectuer une rotation autour de l'axe 3 pour supprimer la phase. Après avoir utilisé les six libertés des transformations de Lorentz, le spineur s'écrit

$$\psi = \phi\begin{pmatrix} e^{i\frac{\beta}{2}} \\ 0 \\ e^{-i\frac{\beta}{2}} \\ 0 \end{pmatrix} \tag{4.13}$$

en représentation chirale. Il reste deux dégrées de libertés qui sont scalaires, on ne peut donc pas les éliminer. Le paramètre ϕ, le module, décrit l'amplitude du spineur et le paramètre β, l'angle d'Yvon-Takabayashi, décrit une phase entre la partie gauche et droite du spineur. Lorsqu'on utilise l'hypothèse de l'onde plane en TQC cela revient à supposer que l'amplitude ϕ est constante et l'angle β est nul. Les quantités (4.5)-(4.9) s'écrivent

$$\Phi = 2\phi^2 \cos\beta, \tag{4.14}$$
$$\Theta = 2\phi^2 \sin\beta, \tag{4.15}$$
$$U^a = 2\phi^2 u^a, \tag{4.16}$$
$$S^a = 2\phi^2 s^a, \tag{4.17}$$
$$M^{ab} = 2\phi^2(\cos\beta u_j s_k \varepsilon^{jkab} + \sin\beta u^{[a} s^{b]}). \tag{4.18}$$

Les identités de Fierz s'écrivent alors

$$u_a u^a = -s_a s^a = 1, \tag{4.19}$$
$$u_a s^a = 0. \tag{4.20}$$

Théorème : Il existe toujours une matrice de Lorentz $\Lambda_{\frac{1}{2}} = e^{\frac{1}{2}\theta_{ab}\sigma^{ab}}$ telle qu'un spineur puisse s'écrire sous la forme polaire

$$\psi = \Lambda_{\frac{1}{2}} \phi e^{-\frac{i\beta\gamma^5}{2}} \begin{pmatrix} 1 \\ 0 \\ 1 \\ 0 \end{pmatrix} = \Lambda_{\frac{1}{2}} \psi_{pol}, \tag{4.21}$$

avec ψ_{pol} le spineur dans le référentiel tel qu'on a utilisé les trois boosts pour avoir $U^1 = U^2 = U^3 = 0$ et $S^0 = 0$, deux rotations telles que $S^1 = S^2 = 0$ et une troisième rotation pour enlever la phase. Étant donné que les équations sont covariantes, on peut toujours se placer dans le référentiel où le spineur s'écrit sous sa forme polaire (4.21) pour faire les calculs.

4.2 Les équations polaires

La dérivée covariante en représentation spinorielle s'écrit

$$\nabla_\mu \psi = \partial_\mu \psi + \Omega_\mu \psi = \partial_\mu \psi + \frac{1}{2}\Omega_{ij\mu}\sigma^{ij}\psi + iqA_\mu \psi, \tag{4.22}$$

avec Ω_μ la connexion de spin déjà définie par l'équation (1.55). Ici, nous avons également pris en compte l'électromagnétisme avec q la charge et A_μ le potentiel vecteur. La transformation de Lorentz en représentation spinorielle $\Lambda_{\frac{1}{2}}$ peut être définie telle que

$$\Lambda_{\frac{1}{2}} \partial_\mu \Lambda_{\frac{1}{2}}^{-1} = i\partial_\mu \lambda \mathbb{I} + \frac{1}{2}\partial_\mu \theta_{ab}\sigma^{ab}. \tag{4.23}$$

En utilisant la dérivée covariante (4.22) sur la forme polaire du spineur (4.21), nous avons

$$\nabla_\mu \psi = (\nabla_\mu \ln\phi \mathbb{I} - \tfrac{i}{2}\nabla_\mu \beta\gamma^5 - iP_\mu \mathbb{I} - \tfrac{1}{2}R_{ij\mu}\sigma^{ij})\psi, \tag{4.24}$$

avec

$$P_\mu = \partial_\mu \lambda - qA_\mu, \tag{4.25}$$
$$R_{ij\mu} = \partial_\mu \theta_{ij} - \Omega_{ij\mu}, \tag{4.26}$$

l'impulsion et la connexion tensorielle respectivement. A partir de (4.24), on peut montrer que

$$\nabla_\mu u_a = R_{ia\mu} u^i, \tag{4.27}$$
$$\nabla_\mu s_a = R_{ia\mu} s^i. \tag{4.28}$$

On peut voir qu'avec ce formalisme l'interaction électromagnétique et l'interaction gravitationnelle sont traitées de façon similaire. Mais le point le plus intéressant concerne l'objet $R_{ij\mu}$. En effet, il est composé de $\partial_\mu \theta_{ij}$ et $\Omega_{ij\mu}$ qui individuellement ne sont pas des tenseurs. Par contre $R_{ij\mu}$ est un tenseur. La connexion $\Omega_{ij\mu}$ contient l'information sur la force inertielle et sur la gravité. L'objet $\partial_\mu \theta_{ij}$ contient l'information sur le repère. De sorte, que même en l'absence de gravité, l'objet $R_{ij\mu}$ contient de l'information sur la force inertielle mais c'est un tenseur. C'est pour cela qu'on dit que c'est une force inertielle covariante et que $R_{ij\mu}$ est appelé la connexion tensorielle [85]. C'est l'analogue gravitationnel de ce qu'est le moment P_μ pour l'électromagnétisme. Le tenseur $R_{ij\mu}$ est antisymétrique par permutation des deux premiers indices. Dans le cadre de la TQC, avec l'hypothèse d'onde plane, on a $R_{ij\mu} = 0$, ϕ = constante et $\beta = 0$, ainsi on a également $\nabla_\mu \ln \phi = 0$ et $\nabla_\mu \beta = 0$. Alors que dans le cadre du formalisme polaire, on ne fait pas de telles hypothèses et le calcul montre que dans certains cas ϕ et β ne sont effectivement pas constants. C'est ce que nous verrons dans l'article suivant.

On insère l'expression (4.24) dans l'équation de Dirac (4.3). Puis, on applique la décomposition de Gordon, c'est-à-dire on multiplie le coté gauche par $\overline{\psi}\mathbb{I}$, $\overline{\psi}\gamma^a$, $\overline{\psi}\sigma^{ab}$, $\overline{\psi}\gamma^5$ et $\overline{\psi}\gamma^a\gamma^5$. Ceci donne 16 équations complexes. La partie imaginaire des quatre équations multipliées par $\overline{\psi}\gamma^a$ est

$$\nabla_\alpha \phi - 2(\overline{\psi}\sigma_{\mu\alpha}\nabla^\mu \psi - \nabla^\mu \overline{\psi}\sigma_{\mu\alpha}\psi) = 0. \tag{4.29}$$

La partie réelle des quatre équations multipliées par $\overline{\psi}\gamma^a\gamma^5$ est

$$\nabla_\alpha \Theta - 2i(\overline{\psi}\sigma_{\mu\alpha}\gamma^5\nabla^\mu \psi - \nabla^\mu \overline{\psi}\sigma_{\mu\alpha}\gamma^5\psi) + 2mS_\alpha = 0. \tag{4.30}$$

Ces huit équations permettent de trouver les 32 équations de la décomposition de Gordon et sont donc strictement équivalentes à l'équation de Dirac. On peut alors écrire les équations (4.29) et (4.30) sous la forme polaire. Ensuite on diagonalise en prenant les deux combinaisons linéaires suivantes : $\cos\beta \times (4.29) + \sin\beta \times (4.30)$ et $\sin\beta \times (4.29) - \cos\beta \times (4.30)$. Ceci donne les deux équations covariantes suivantes

$$-2\omega F_{\mu\nu}u^\nu \sin\beta - \omega\varepsilon_{\mu\rho\eta\sigma}F^{\rho\eta}u^\sigma \cos\beta + \frac{1}{2}\varepsilon_{\mu\alpha\nu\iota}R^{\alpha\nu\iota} - 2P^\iota u_{[\iota}s_{\mu]} + \nabla_\mu\beta + 2s_\mu m\cos\beta = 0 \tag{4.31}$$
$$2\omega F_{\mu\nu}u^\nu \cos\beta - \omega\varepsilon_{\mu\rho\eta\sigma}F^{\rho\eta}u^\sigma \sin\beta + R_{\mu a}{}^a - 2P^\rho u^\nu s^\alpha \varepsilon_{\mu\rho\nu\alpha} + 2s_\mu m\sin\beta + \nabla_\mu \ln\phi^2 = 0 \tag{4.32}$$

Les huit équations (4.31) et (4.32) sont totalement équivalentes aux huit équations (4.3) [86]. Ceci nous permet donc d'avoir les équations de Dirac sous une nouvelle forme qui révèle les dégrées de liberté

physiques du spineur : ϕ et β. Du point de vue de l'interprétation, on observe que sans les termes de potentiel $F_{\mu\nu}$, l'angle β apparaît dans le terme de masse. En effet, comme nous l'avions vu dans le Langragien (1.101), l'interaction entre la partie droite et gauche du spineur n'apparaît que dans le cas d'un spineur massif.

L'interprétation du terme $R_{ij\mu}$ n'est pas encore entièrement comprise. Dans les articles [87, 88], on observe qu'une solution exacte de l'équation de Dirac a les termes R_{rtt}, $R_{\varphi rt}$, $R_{\theta tt}$ et $R_{\varphi\theta t}$ qui dépendent du paramètre ϵ. Ce dernier est une énergie négative qui décrit une force attractive sur le spineur même dans le cas d'un système sans source. L'interprétation donnée est donc la présence d'une force attractive qui tend à localiser la particule. En fait, en TQC on sait que l'hypothèse d'onde plane est une très bonne approximation mais on sait également que dans la réalité les particules sont localisées dans une région. Ainsi on voit que les termes $R_{\mu\nu\sigma}$ permettent d'expliquer cette localisation. D'autres termes du tenseur $R_{ij\mu}$ vont être interprétés dans la section suivante 4.3 pour décrire l'effet Aharonov-Bohm gravitationnel.

Dans les articles suivants, on utilise une notation légèrement différente. La matrice γ^5 est notamment dénotée par le symbole $\boldsymbol{\pi}$ et la transformation de Lorentz $\Lambda_{\frac{1}{2}}$ est dénoté par $\boldsymbol{S}$. Les vecteurs sont indiqués avec une flèche et le gras est utilisé pour les matrices. Dans la présentation des articles je garderais néanmoins la même notation que précédemment, ainsi le gras désigne les vecteurs spatiaux.

4.3 Vers un effet Aharonov-Bohm gravitationel

Dans cet article, on montre que même en absence de gravité, c'est-à-dire avec un tenseur de Riemann nul $R^i{}_{j\mu\nu} = 0$, certains termes de la connexion tensorielle sont non nuls et cela donne lieu à un effet Aharonov-Bohm gravitationnel. Nous étudions le cas d'un potentiel d'hydrogène et d'oscillateur harmonique. Nous écrivons en parallèle le cas électromagnétique pour mettre en avant l'analogie. Le tenseur électromagnétique $F_{\mu\nu}$ en fonction de potentiel vecteur A_μ s'écrit

$$F_{\mu\nu} = \partial_\mu A_\nu - \partial_\nu A_\mu. \tag{4.33}$$

Il est également possible d'écrire le tenseur de Riemann $R^i{}_{j\mu\nu}$ en fonction de la connexion spinorielle $\Omega^i{}_{j\nu}$

$$R^i_{j\mu\nu} = \partial_\mu \Omega^i{}_{j\nu} - \partial_\nu \Omega^i{}_{j\mu} + \Omega^i{}_{k\mu}\Omega^k{}_{j\nu} - \Omega^i{}_{k\nu}\Omega^k{}_{j\mu}. \tag{4.34}$$

A partir des relations (4.33) et (4.34), on peut en déduire

$$qF_{\mu\nu} = -(\nabla_\mu P_\nu - \nabla_\nu P_\mu). \tag{4.35}$$

$$R^i_{j\mu\nu} = -(\nabla_\mu R^i{}_{j\nu} - \nabla_\nu R^i{}_{j\mu} + R^i{}_{k\mu}R^k{}_{j\nu} - R^i{}_{k\nu}R^k{}_{j\mu}). \tag{4.36}$$

Nous allons étudier deux types de potentiels : l'atome d'hydrogène [86] et l'oscillateur harmonique.

4.3.1 L'atome d'hydrogène

Le potentiel de Coulomb est décrit par

$$qA_t = -\frac{\alpha}{r}, \tag{4.37}$$

avec $\alpha = q^2$ la constante de structure fine. L'équation de Dirac (4.3) s'écrit

$$(E+\tfrac{\alpha}{r})\begin{pmatrix} \mathbb{I} & 0 \\ 0 & -\mathbb{I} \end{pmatrix}\psi + \tfrac{i}{r}\begin{pmatrix} 0 & \boldsymbol{\sigma}\cdot\boldsymbol{r} \\ -\boldsymbol{\sigma}\cdot\boldsymbol{r} & 0 \end{pmatrix}\partial_r\psi - \tfrac{i}{r^2}\begin{pmatrix} 0 & (\boldsymbol{\sigma}\cdot\boldsymbol{r})\,(\boldsymbol{\sigma}\cdot\boldsymbol{L}) \\ -(\boldsymbol{\sigma}\cdot\boldsymbol{r})\,(\boldsymbol{\sigma}\cdot\boldsymbol{L}) & 0 \end{pmatrix}\psi - m\psi = 0$$

On se place dans le référentiel où le spineur est sous forme polaire et les deux dégrées de liberté sont calculés

$$\beta = -\arctan\left(\frac{\alpha}{\Gamma}\cos\theta\right), \tag{4.38}$$

$$\phi = r^{\Gamma-1}e^{-\alpha m r}/\sqrt{\Delta} \tag{4.39}$$

avec $\Gamma = \sqrt{1-\alpha^2}$ et $\Delta(\theta) = 1/\sqrt{1-\alpha^2|\sin\theta|^2}$. On observe, comme précédemment mentionné, que l'amplitude ϕ et l'angle β ne sont pas constants. L'angle β n'a pas de dépendance radiale, ce qui est cohérent avec le fait que pour un potentiel d'hydrogène l'amplitude on peut effectuer une séparation des variables r et θ. L'impulsion est donnée par

$$P_t = E + \alpha/r, \tag{4.40}$$

$$P_\varphi = -1/2, \tag{4.41}$$

et on observe que bien qu'il n'y ait pas de courbure, certains termes $R_{\mu\nu\sigma}$ sont non nuls

$$R_{t\varphi\theta} = -\alpha r \sin\theta\cos\theta|\Delta|^2, \tag{4.42}$$

$$R_{r\theta\theta} = -r(1-\Gamma|\Delta|^2), \tag{4.43}$$

$$R_{r\varphi\varphi} = -r|\sin\theta|^2, \tag{4.44}$$

$$R_{\theta\varphi\varphi} = -r^2\sin\theta\cos\theta. \tag{4.45}$$

On peut également calculer d'autres scalaires notamment la trace du tenseur énergie-impulsion définie telle que $T = \mathcal{L} + m\Psi\overline{\Psi}$, avec $\mathcal{L}$ le Langrangien. On obtient

$$T = 2\phi^2\Delta E. \tag{4.46}$$

Le comportement de T à petit et grand r est similaire, ce qui ne sera pas le cas pour l'oscillateur harmonique. Le calcul d'autres scalaires montre qu'ils ont tous le même comportement radial.

4.3.2 L'oscillateur harmonique

Dans le cas de l'oscillateur harmonique, le potentiel est donné par [84]

$$F_{\mu\nu} = v_\mu x_\nu - v_\nu x_\mu, \tag{4.47}$$

avec v_μ un vecteur de type temps et x_μ le vecteur position. Avec $v_\mu = (1,0,0,0)$, l'équation de Dirac s'écrit

$$E\begin{pmatrix} \mathbb{I} & 0 \\ 0 & -\mathbb{I} \end{pmatrix}\psi + \frac{i}{r}\begin{pmatrix} 0 & \boldsymbol{\sigma}\cdot\boldsymbol{r} \\ -\boldsymbol{\sigma}\cdot\boldsymbol{r} & 0 \end{pmatrix}\partial_r\psi$$
$$-\frac{i}{r^2}\begin{pmatrix} 0 & (\boldsymbol{\sigma}\cdot\boldsymbol{r})\,(\boldsymbol{\sigma}\cdot\boldsymbol{L}) \\ -(\boldsymbol{\sigma}\cdot\boldsymbol{r})\,(\boldsymbol{\sigma}\cdot\boldsymbol{L}) & 0 \end{pmatrix}\psi - i\omega\begin{pmatrix} 0 & \boldsymbol{\sigma}\cdot\boldsymbol{r} \\ \boldsymbol{\sigma}\cdot\boldsymbol{r} & 0 \end{pmatrix}\psi - m\psi = 0. \tag{4.48}$$

Comme précédemment, nous nous plaçons dans le référentiel où le spineur est dans sa forme polaire et nous calculons les scalaires

$$\beta = \arctan\left(\frac{2ar\cos\theta}{r^2 - a^2}\right), \tag{4.49}$$
$$\phi = Ke^{-\frac{1}{2}\omega r^2}\sqrt{A/2}, \tag{4.50}$$

avec K une constante, $a = (E-m)/2\omega$ et A une fonction telle que $A(r,\theta) = \sqrt{r^4 + a^4 + 2r^2a^2\cos(2\theta)}$. On a la limite $r = a$ où la densité scalaire Φ, défini par l'équation (4.14), change de signe. Pour l'impulsion et la connexion tensorielle on obtient

$$P_t = E, \tag{4.51}$$
$$P_\varphi = -1/2, \tag{4.52}$$

$$R_{t\varphi\theta} = -2ar^2\sin\theta\cos\theta(r^2+a^2)A^{-2}, \tag{4.53}$$
$$R_{r\theta\theta} = -2r^3[r^2 + a^2\cos(2\theta)]A^{-2}, \tag{4.54}$$
$$R_{t\varphi r} = 2ar|\sin\theta|^2(r^2-a^2)A^{-2}, \tag{4.55}$$
$$R_{r\theta r} = -2a^2r^2\sin(2\theta)A^{-2}, \tag{4.56}$$
$$R_{r\varphi\varphi} = -r|\sin\theta|^2, \tag{4.57}$$
$$R_{\theta\varphi\varphi} = -r^2\sin\theta\cos\theta. \tag{4.58}$$

La trace du tenseur énergie-impulsion s'écrit

$$T = 2\phi^2A^{-1}(r^2E - a^2m), \tag{4.59}$$

on observe que le signe de ce scalaire change à $r = a\sqrt{m/E}$. Pour des petits r on a $T \approx -2\phi^2m$ alors que pour des grands r, on a $T \approx 2\phi^2E$. La limite non relativiste, telle $\psi_P \to 0$, est décrite, dans le formalisme polaire, par $\beta \to 0$. On en déduit $a = 3/2m$, ce qui entraîne qu'on a la limite non relativiste lorsque la masse est grande. On peut séparer l'espace en trois régions, on a une première sphère $a\sqrt{m/E}$, puis une région entre cette sphère et la sphère a et enfin la région extérieure. Dans la limite non relativiste, les sphères $r = a$ où Φ change de signe et $r = a\sqrt{m/E}$ où T change de signe coïncident. Il existe une sphère de rayon $a\sqrt{m/E}$ à l'intérieur de laquelle les effets relativistes ne peuvent pas être supprimés. Dans cette sphère les effets de la dynamique interne sont dominants. Ils sont d'autant plus important lorsque $\beta = \pi$, c'est à dire lorsque la partie gauche et droite sont en opposition de phase.

4.3.3 L'effet Aharanov-Bohm

Dans les deux études précédentes, on a pu voir que certaines composantes des tenseurs P_μ et $R_{\mu\nu\sigma}$ sont non nulles même en l'absence de courbure. Du point de vue de l'électromagnétisme, pour P_μ, ce phénomène est déjà connu comme étant l'effet Aharonov-Bohm. D'un point vue gravitationnel cet effet a déjà été étudié [89, 90]. Ici, on propose de l'étudier avec le tenseur $R_{\mu\nu\sigma}$ avec lequel on peut faire un parallèle franc avec le cas électromagnétique.

Lorsque le spineur se trouve dans sa forme polaire, on observe que les équations (4.27, 4.28) se réduisent à

$$\nabla_\mu s_i = R_{3i\mu}, \tag{4.60}$$
$$\nabla_\mu u_i = R_{0i\mu}. \tag{4.61}$$

Ainsi la dynamique de la vitesse u_a et du spin s_a dépend uniquement des composantes de $R_{ij\mu}$ avec $i = 0, 3$. Étant donné que ce dernier est antisymétrique par permutation des deux premiers indices, les termes $R_{12\mu}$ n'apparaissent jamais dans les équations de la dynamique de la vitesse et du spin, comme c'est le cas pour P_μ en électromagnétisme. En intégrant (4.25) on a une phase $\Delta\lambda$. L'intégrale sur une boucle fermée donne

$$\oint_\gamma (P_\mu + qA_\mu)dx^\mu = \oint_\gamma \partial_\mu \lambda dx^\mu = 2\pi n, \tag{4.62}$$

avec n un nombre entier. De façon analogue l'intégrale de (4.26) pour $\Delta\theta_{12}$ donne

$$\oint_\gamma (R_{12\mu} + \Omega_{12\mu})dx^\mu = \oint_\gamma \partial_\mu \theta_{12} dx^\mu = -4\pi n. \tag{4.63}$$

Dans le cas où l'impulsion et la connexion tensorielle sont nulles, avec $\gamma = \partial S$, le théorème de Stoke donne

$$q \oint_{\partial S} \boldsymbol{A}\cdot d\boldsymbol{x} = q \iint_S \mathrm{rot}\boldsymbol{A}\cdot d\Lambda_{\frac{1}{2}} = 2\pi n, \tag{4.64}$$
$$\oint_{\partial S} \boldsymbol{\Omega}_{12}\cdot d\boldsymbol{x} = \iint_S \mathrm{rot}\boldsymbol{\Omega}_{12}\cdot d\Lambda_{\frac{1}{2}} = -4\pi n. \tag{4.65}$$

Ainsi les équations (4.64) et (4.65) décrivent respectivement l'effet Aharonov-Bohm électromagnétique et gravitationnel. Même en l'absence de source, le potentiel gravitationnel peut donner lieu à un déphase du champ. On peut alors écrire

$$\psi = e^{-i\lambda} e^{-\frac{1}{2}\theta_{12}\sigma^{12}} \psi_{pol}, \tag{4.66}$$

avec ψ_{pol} le spineur sous forme polaire (4.21). On a une phase abélienne λ et une phase non abélienne θ_{12} qui peuvent être présentes même sans champ électromagnétique et gravitationnel.

Cet article a été publié dans *European Physical Journal C* [91].

Eur. Phys. J. C (2019) 79:875
https://doi.org/10.1140/epjc/s10052-019-7380-5

THE EUROPEAN PHYSICAL JOURNAL C

Regular Article - Theoretical Physics

Non-trivial effects of sourceless forces for spinors: toward an Aharonov–Bohm gravitational effect?

Luca Fabbri[1,a], **Flora Moulin**[2], **Aurélien Barrau**[2]

[1] DIME Sezione di Metodi e Modelli Matematici, Università degli studi di Genova, via all'Opera Pia 15, 16145 Genova, Italy
[2] Laboratoire de Physique Subatomique et de Cosmologie, Université Grenoble-Alpes CNRS/IN2P3, 53 avenue des Martyrs, 38026 Grenoble cedex, France

Received: 27 August 2019 / Accepted: 3 October 2019 / Published online: 24 October 2019

Abstract Spinor fields are written in polar form so as to compute their tensorial connection, an object that contains the same information of the connection but which is also proven to be a real tensor. From this, one can still compute the Riemann curvature, encoding the information about gravity. But even in absence of gravity, when the Riemann curvature vanishes, it may still be possible that the tensorial connection remains different from zero, and thih can have effects on matter. This is shown with examples in the two known integrable cases: the hydrogen atom and the harmonic oscillator. The fact that a spinor can feel effects due to sourceless actions is already known in electrodynamics as the Aharonov–Bohm phenomenon. A parallel between the electrodynamics case and the situation encountered here will be drawn. Some ideas about relativistic effects and their role for general treatments of quantum field theories are also underlined.

1 Introduction

Quantum field theory (QFT) is one of the most impressive successes of contemporary science. From the standard model of particle physics to condensed matter theory, this framework works remarkably well and delivers high-precision predictions. The mathematical foundations of QFT however remain quite confusing. Some of the best known problems are the following (see [1]): all calculations are performed by expanding fields in plane waves, which are not square integrable (and do not really exist as physical objects); in this expansion the coefficients are interpreted as creation and annihilation operators, lacking a precise definition [2]; and the calculations rely on the so-called interaction picture, which is in tension with the concept of a Lorentz-covariant field theory [3]. For all those reasons, it is clearly meaningful to consider a more general framework than ordinary QFT. This is the setting used in this work. As QFT works extremely well in all know situations, possible new results will obviously arise only in subtle cases.

As it is well known, Dirac spinor fields can be classified using the so-called Lounesto classification according to two classes: singular spinor fields are those subject to the conditions $i\overline{\psi}\boldsymbol{\pi}\psi=0$ and $\overline{\psi}\psi=0$ while regular spinor fields are all those for which the two above conditions do not identically hold [4–10]. For the regular spinor fields, it is possible to perform what is known as the polar decomposition of the Dirac spinor field [11]: this is the way in which it can be written in the Madelung form, that is with all the complex quantities expressed as a real module times a unitary complex exponential (21) while respecting the transformation properties of a 1/2-spin spinor field. In this form, the 8 real components of spinors are re-arranged so as to show the physical information: of these 8 components in fact, 3 are shown to be the spatial directions of the velocity, 3 are the spatial directions of the spin, 1 is the usual expression of the module, and a last 1 is a phase shift between left-handed and right-handed chiral parts of the spinor. This exhibits a possible an intern dynamics, not taken into account in QFT. New effects can be associated with this phase.

Details about the spinor field equations in this form can be found in [12]. By implementing the Madelung form, so as to write every spinorial component as a module times a unitary exponential, and using the Gordon decompositions, so as to respect covariance, it is possible to convert the Dirac spinor field equation into a pair of coupled and non-linear vector field equations which are equivalent to the Dirac one.

These field equations determine the dynamics and the structure of the degrees of freedom of the spinor field in terms of two quantities collectively called the tensorial connection. They are built in terms of the connection but are also proven to be real tensors [13]. In [14], we eventually proved

[a] e-mail: fabbri@dime.unige.it

that with the tensorial connection it is possible to calculate the Riemann tensor, which represents the space-time curvature thus deciphering the information about the gravitational field.

In absence of gravitation the space-time curvature vanishes, and the Riemann tensor becomes zero identically. In this case, just as the connection, the tensorial connection may still be different from zero, but just like any tensor, if the tensorial connection happens to be non-zero then it will remain such in any system of reference: if this were to happen, we would be in presence of an object which, on the one hand, would represent a potential having a non-trivial structure, while on the other hand, it would have a vanishing strength.

This circumstance is the sourceless case, that is when the gravitational impact of the considered matter is identically zero (the Riemann tensor vanishes, so the Ricci tensor vanishes, which means that the energy density is not large enough to source gravity). Nevertheless, an influence on matter can still arise if the tensorial connection is not identically equal to zero.

As far-fetched as this situation may look, we will show that it is indeed what might happen in two notable examples, given by the two integrable cases known: the hydrogen atom and the harmonic oscillator.

These two examples, both from some remarkable physical potentials, and both exact solutions, should convince the skeptical reader of the fact that the structure of the wave function of a relativistic quantum matter distribution is in fact due to the non-vanishing tensorial connection even when it has no space-time curvature.

One should also keep in mind that a similar situation is already known. In the same way in which a relativistic quantum matter distribution can be affected by a non-vanishing connection, even when it has no space-time curvature, it can also be affected by some non-zero potential even when it has no gauge curvature. This is the Aharonov–Bohm effect, which happens when wave functions display a phase-shift due to potentials even in regions where they give rise to no electrodynamic forces. Thus, in a way, we may say that what we are going to present consists in exhibiting the effects on matter of a gravitational Aharonov–Bohm effect.

This effect for gravity seems to be richer than for electrodynamics as in this case the full wave function, and not only its phase, can be modified. A comparative analysis of the two Aharonov–Bohm effects will be given.

As a bonus, we will show how it could be possible to obtain, in analogy to the Born rule for the discretization of electrodynamic degrees of freedom, a kind of Born rule for the discretization of gravitational degrees of freedom.

Some comments regarding the non-relativistic limit will eventually be sketched in one final section.

2 Polar spinors

2.1 Kinematic quantities

We will consider the Clifford matrices $\boldsymbol{\gamma}^a$ from which $\left[\boldsymbol{\gamma}_a, \boldsymbol{\gamma}_b\right] = 4\boldsymbol{\sigma}_{ab}$ and $2i\boldsymbol{\sigma}_{ab} = \varepsilon_{abcd}\boldsymbol{\pi}\boldsymbol{\sigma}^{cd}$ defining the $\boldsymbol{\sigma}_{ab}$ and $\boldsymbol{\pi}$ matrices (this latter is what is usually called $\boldsymbol{\gamma}^5$ or $\boldsymbol{\gamma}_5$ with a sign ambiguity that has to be fixed by convention).

As known, Clifford matrices account for a total of 16 linearly independent generaotrs for the space of 4×4 complex matrices, given by

$$\mathbb{I},\ \ \boldsymbol{\gamma}^a,\ \ \boldsymbol{\sigma}^{ab},\ \ \boldsymbol{\pi},\ \ \boldsymbol{\gamma}^a\boldsymbol{\pi} \tag{1}$$

and it is possible to prove that they verify

$$\boldsymbol{\gamma}_i\boldsymbol{\gamma}_j\boldsymbol{\gamma}_k = \boldsymbol{\gamma}_i\eta_{jk} - \boldsymbol{\gamma}_j\eta_{ik} + \boldsymbol{\gamma}_k\eta_{ij} + i\varepsilon_{ijkq}\boldsymbol{\pi}\boldsymbol{\gamma}^q \tag{2}$$

which is a spinorial matrix identity (notice that this identity shows the pseudo-scalar character of the $\boldsymbol{\pi}$ matrix).

Given the spinor field ψ, its complex conjugate spinor field $\overline{\psi}$ is defined in such a way that bi-linear quantities

$$\Sigma^{ab} = 2\overline{\psi}\boldsymbol{\sigma}^{ab}\boldsymbol{\pi}\psi \tag{3}$$
$$M^{ab} = 2i\overline{\psi}\boldsymbol{\sigma}^{ab}\psi \tag{4}$$

with

$$S^a = \overline{\psi}\boldsymbol{\gamma}^a\boldsymbol{\pi}\psi \tag{5}$$
$$U^a = \overline{\psi}\boldsymbol{\gamma}^a\psi \tag{6}$$

as well as

$$\Theta = i\overline{\psi}\boldsymbol{\pi}\psi \tag{7}$$
$$\Phi = \overline{\psi}\psi \tag{8}$$

are all real tensors, and it is possible to prove that they verify

$$\Sigma^{ab} = -\frac{1}{2}\varepsilon^{abij}M_{ij} \tag{9}$$
$$M^{ab} = \frac{1}{2}\varepsilon^{abij}\Sigma_{ij} \tag{10}$$

together with

$$M_{ab}\Phi - \Sigma_{ab}\Theta = U^j S^k \varepsilon_{jkab} \tag{11}$$
$$M_{ab}\Theta + \Sigma_{ab}\Phi = U_{[a}S_{b]} \tag{12}$$

alongside to

$$M_{ik}U^i = \Theta S_k \tag{13}$$
$$\Sigma_{ik}U^i = \Phi S_k \tag{14}$$
$$M_{ik}S^i = \Theta U_k \tag{15}$$
$$\Sigma_{ik}S^i = \Phi U_k \tag{16}$$

and also

$$\frac{1}{2}M_{ab}M^{ab} = -\frac{1}{2}\Sigma_{ab}\Sigma^{ab} = \Phi^2 - \Theta^2 \tag{17}$$

$$\frac{1}{2}M_{ab}\Sigma^{ab} = -2\Theta\Phi \tag{18}$$

and

$$U_a U^a = -S_a S^a = \Theta^2 + \Phi^2 \tag{19}$$

$$U_a S^a = 0 \tag{20}$$

called Fierz re-arrangement identities.

These identities are important because in the general case of regular spinors, for which $i\overline{\psi}\boldsymbol{\pi}\psi \neq 0$ or $\overline{\psi}\psi \neq 0$, we can use (19) to see that the U^a vector is time-like. Three boosts can therefore be used to remove its spatial components and two rotations can be used to rotate S^a along the third axis, while the third one eliminates the general phase. When these operations are performed, the most general spinor field compatible with those restrictions is

$$\psi = \phi e^{-\frac{i}{2}\beta\boldsymbol{\pi}}\boldsymbol{S}\begin{pmatrix}1\\0\\1\\0\end{pmatrix} \tag{21}$$

in chiral representation. The matrix $\boldsymbol{S}$ is a generic complex Lorentz transformation, β called Yvon-Takabayashi angle and represents the phase shift between right-handed and left-handed chiral parts of the spinor while ϕ is the module. The full spinor field is then said to be in *polar form* [11]. In this polar form, the two antisymmetric tensors reduce to

$$\Sigma^{ab} = 2\phi^2(\cos\beta u^{[a}s^{b]} - \sin\beta u_j s_k \varepsilon^{jkab}) \tag{22}$$

$$M^{ab} = 2\phi^2(\cos\beta u_j s_k \varepsilon^{jkab} + \sin\beta u^{[a}s^{b]}) \tag{23}$$

with the two vectors

$$S^a = 2\phi^2 s^a \tag{24}$$

$$U^a = 2\phi^2 u^a \tag{25}$$

and the two scalars

$$\Theta = 2\phi^2 \sin\beta \tag{26}$$

$$\Phi = 2\phi^2 \cos\beta \tag{27}$$

in terms of the Yvon-Takabayashi angle and module.

All Fierz identities trivialize except for

$$u_a u^a = -s_a s^a = 1 \tag{28}$$

$$u_a s^a = 0 \tag{29}$$

which show that the velocity and the spin are constrained, so that in general they amout to three components each. The most general spinor therefore possesses four components, or eight real components, given by the three real components of the velocity and the three real components of the spin, which can always be boosted or rotated away, plus the Yvon-Takabayashi angle and module, whose scalar character makes them impossible to be removed with a choice of frame. The latter are therefore the only two real degrees of freedom of the spinor field.

From the metric, we define the symmetric connection as usual with $\Lambda^{\sigma}_{\alpha\nu}$ from which, with the tetrads, we define the spin connection $\Omega^a_{b\pi} = \xi^{\nu}_b \xi^a_{\sigma}(\Lambda^{\sigma}_{\nu\pi} - \xi^{\sigma}_i \partial_{\pi}\xi^i_{\nu})$. With the gauge potential, we then define the spinor connection

$$\boldsymbol{\Omega}_{\mu} = \frac{1}{2}\Omega^{ab}_{\mu}\boldsymbol{\sigma}_{ab} + iqA_{\mu}\mathbb{I} \tag{30}$$

needed to define

$$\boldsymbol{\nabla}_{\mu}\psi = \partial_{\mu}\psi + \boldsymbol{\Omega}_{\mu}\phi \tag{31}$$

which is the spinorial covariant derivative.

Writing spinor fields in polar form does not only allow us to distill the spinor components into the real degrees of freedom, but it also provides the definition of the $\boldsymbol{S}$ matrix, which verifies

$$\boldsymbol{S}\partial_{\mu}\boldsymbol{S}^{-1} = i\partial_{\mu}\lambda\mathbb{I} + \frac{1}{2}\partial_{\mu}\theta_{ij}\boldsymbol{\sigma}^{ij} \tag{32}$$

where λ is a generic complex phase and $\theta_{ij} = -\theta_{ji}$ are the six parameters of the Lorentz group. It is then possible to define

$$\partial_{\mu}\theta_{ij} - \Omega_{ij\mu} \equiv R_{ij\mu} \tag{33}$$

$$\partial_{\mu}\lambda - qA_{\mu} \equiv P_{\mu} \tag{34}$$

which can be proven to be real tensors. The spin connection $\Omega_{ij\mu}$ carries information about gravity and coordinate systems while the derivative $\partial_{\mu}\theta_{ij}$ carries information about the coordinate system, and therefore $R_{ij\mu}$ carries information about gravity and coordinate systems. However, while independently non-tensorial quantities, their combination makes the non-tensorial spurious terms cancel, and the result is that $R_{ij\mu}$ is a real tensor. This is the reason why it is called *tensorial connection*. Similarly, qA_{μ} contains information about electrodynamics and gauge phases while $\partial_{\mu}\lambda$ about gauge phases. While independently they are not gauge invariant, their combination P_{μ} is a real gauge-invariant vector. This is why it is called *gauge-invariant vector momentum*. Due to their analogy, we will collectively call them tensorial connections, for simplicity [13]. One can show that

$$\boldsymbol{\nabla}_{\mu}\psi = \left(\nabla_{\mu}\ln\phi\mathbb{I} - \frac{i}{2}\nabla_{\mu}\beta\boldsymbol{\pi} - iP_{\mu}\mathbb{I} - \frac{1}{2}R_{ij\mu}\boldsymbol{\sigma}^{ij}\right)\psi \tag{35}$$

from which

$$\nabla_\mu s_i = R_{ji\mu} s^j \tag{36}$$
$$\nabla_\mu u_i = R_{ji\mu} u^j \tag{37}$$

which are valid as general geometric identities.

2.2 Dynamical equations

The commutator of spinorial covariant derivatives can be used to define

$$R^i{}_{j\mu\nu} = \partial_\mu \Omega^i{}_{j\nu} - \partial_\nu \Omega^i{}_{j\mu} + \Omega^i{}_{k\mu}\Omega^k{}_{j\nu} - \Omega^i{}_{k\nu}\Omega^k{}_{j\mu} \tag{38}$$
$$F_{\mu\nu} = \partial_\mu A_\nu - \partial_\nu A_\mu \tag{39}$$

which are the space-time and gauge curvatures.

It is straightforward to prove that

$$R^i{}_{j\mu\nu} = -(\nabla_\mu R^i{}_{j\nu} - \nabla_\nu R^i{}_{j\mu} + R^i{}_{k\mu} R^k{}_{j\nu} - R^i{}_{k\nu} R^k{}_{j\mu}) \tag{40}$$
$$q F_{\mu\nu} = -(\nabla_\mu P_\nu - \nabla_\nu P_\mu) \tag{41}$$

showing that the Riemann tensor can be written in terms of the tensorial connection while the Maxwell tensor can be written in terms of the gauge-invariant vector momentum. The tensorial connection and the gauge-invariant vector momentum are therefore the potentials of the gravitational and electrodynamic fields [14]. However, in absence of gravity or electrodynamics, when the curvatures vanish identically, differently from the connection and the gauge potential, which can always be vanished with a choice of frame or gauge, there is no way to vanish the tensorial connection and the gauge-invariant vector momentum, if they do not vanish identically already.

For the matter field, the dynamics is defined in terms of the Dirac spinor field equation

$$i\boldsymbol{\gamma}^\mu \nabla_\mu \psi + i\omega F_{\mu\nu} \boldsymbol{\sigma}^{\mu\nu} \psi - m\psi = 0 \tag{42}$$

in which the ω term is an additional potential describing the coupling of the dipole moment of the spinor to an external field, which will be used to represent the potential of the harmonic oscillator later in this work.

It is now possible to substitute (35) into (42) to write the Dirac spinor field equation in polar form. We then proceed to the Gordon decomposition by multiplying on the left with $\overline{\psi}$, $\overline{\psi}\boldsymbol{\gamma}^a$, $\overline{\psi}\boldsymbol{\sigma}^{ab}$, $\overline{\psi}\boldsymbol{\pi}$ and $\overline{\psi}\boldsymbol{\gamma}^a\boldsymbol{\pi}$ so to get 16 scalar equations, and then we split into real and imaginary parts getting 32 real scalar equations. Of these 32 real equations, we must expect that 8 taken together will be equivalent to the 8 real components of the Dirac equation (42). These 8 equations are those obtained by selecting the imaginary part of the contraction with $\boldsymbol{\gamma}^a$ and the real part of the contraction with with $\boldsymbol{\gamma}^a\boldsymbol{\pi}$: multiplying the first by $\cos\beta$ and the second by $\sin\beta$ and adding them and multiplying the first by $\sin\beta$ and the second by $\cos\beta$ and substracting them produces the diagonalization that leads to

$$\begin{aligned} &-2\omega F_{\mu\nu} u^\nu \sin\beta - \omega \varepsilon_{\mu\rho\eta\sigma} F^{\rho\eta} u^\sigma \cos\beta \\ &+\frac{1}{2}\varepsilon_{\mu\alpha\nu\iota} R^{\alpha\nu\iota} - 2P^\iota u_{[\iota} s_{\mu]} \\ &+\nabla_\mu \beta + 2 s_\mu m \cos\beta = 0 \end{aligned} \tag{43}$$

$$\begin{aligned} &2\omega F_{\mu\nu} u^\nu \cos\beta - \omega \varepsilon_{\mu\rho\eta\sigma} F^{\rho\eta} u^\sigma \sin\beta \\ &+R^a_{\mu a} - 2P^\rho u^\nu s^\alpha \varepsilon_{\mu\rho\nu\alpha} \\ &+2 s_\mu m \sin\beta + \nabla_\mu \ln\phi^2 = 0 \end{aligned} \tag{44}$$

which can be proven, in return, to derive the polar form of the Dirac spinor field equation. This proves the equivalence between (44, 45) and (42) itself. So the four spinorial field equations, which are eight real field equations, can be converted into one vector field equation and one axial-vector field equation, specifying the first-order derivatives of the module and of the Yvon-Takabayashi angle, determining the dynamics of the real degrees of freedom [12].

3 Application to two systems

The theory developed so far is general, but applications can also be studied so as to better understand what are the properties of the tensorial connections: our goal is to see what happens in the sourceless case, that is in situations where the energy density is not large enough to be a source of gravitation. We can assume that there is no gravity, a flat space-time, and an indentically vanishing Riemann tensor (40). The tensorial connection can however still be different from zero. In this case we would have some non-trivial potential with no strength.

To prove that such a non-vanishing tensorial connection can have an effect on a relativistic quantum matter distribution, we consider explicit examples. To make our examples stronger, we will choose exact solutions of integrable potentials: one is given by the Coulomb potential, leading to the description of the hydrogen atom; and the other is given by the elastic potential, leading to the description of the harmonic oscillator.

Both cases are interesting because they account for all integrable potentials known in physics. In the following we start by reviewing the case of the hydrogen atom as it was treated in [14]. Then we consider the harmonic oscillator in three-dimensional case as presented in [15].

The harmonic oscillator has not yet been studied in the polar form, and thus we will present it with more details.

3.1 Non-trivial integrable cases

3.1.1 The hydrogen atom model

The case of the hydrogen atom is very widely known and can be found in common textbooks.

The interaction is given in terms of the Coulomb potential, that is the temporal component of the gauge potential vector

$$qA_t = -\alpha/r \tag{45}$$

where $\alpha = q^2$ is the fine-structure constant given in units in which it is the square of the electric charge.

Looking for solutions in stationary form $i\partial_t\psi = E\psi$ and with the choice of spherical coordinates

$$\vec{r} = \begin{pmatrix} r\sin\theta\cos\varphi \\ r\sin\theta\sin\varphi \\ r\cos\theta \end{pmatrix} \tag{46}$$

the Dirac spinor equations are written according to

$$(E+\frac{\alpha}{r})\begin{pmatrix}\mathbb{I} & 0\\ 0 & -\mathbb{I}\end{pmatrix}\psi + \frac{i}{r}\begin{pmatrix}0 & \vec{\boldsymbol{\sigma}}\cdot\vec{r}\\ -\vec{\boldsymbol{\sigma}}\cdot\vec{r} & 0\end{pmatrix}\partial_r\psi - \\ -\frac{i}{r^2}\begin{pmatrix}0 & \vec{\boldsymbol{\sigma}}\cdot\vec{r}\,\vec{\boldsymbol{\sigma}}\cdot\vec{L}\\ -\vec{\boldsymbol{\sigma}}\cdot\vec{r}\,\vec{\boldsymbol{\sigma}}\cdot\vec{L} & 0\end{pmatrix}\psi - m\psi = 0 \tag{47}$$

where

$$\vec{L}F = \begin{pmatrix} i\sin\varphi\partial_\theta F + i\cot\theta\cos\varphi\partial_\varphi F \\ -i\cos\varphi\partial_\theta F + i\cot\theta\sin\varphi\partial_\varphi F \\ -i\partial_\varphi F \end{pmatrix} \tag{48}$$

for any function F, given in terms of the elevation and azimuthal angles. This form is well suited to study all cases where a separation of variables is possible.

We will focus on the ground-state, the $1S$ orbital.

In this case, defining the constant $\Gamma = \sqrt{1-\alpha^2}$ as well as the function $\Delta(\theta) = 1/\sqrt{1-\alpha^2|\sin\theta|^2}$ of the elevation angle alone, it is possible to see that the energy is given by $E = m\Gamma$ and the spinor

$$\psi = \tfrac{1}{\sqrt{1+\Gamma}} r^{\Gamma-1} e^{-\alpha m r} e^{-iEt}\begin{pmatrix} 1+\Gamma \\ 0 \\ i\alpha\cos\theta \\ i\alpha\sin\theta e^{i\varphi}\end{pmatrix} \tag{49}$$

is an exact solution of (47) with (48). To see this, one can insert (49) into and (48) and (47) and check directly.

This is the standard treatment, but equations (47, 48) are just the Dirac spinor equations (42) for $\omega = 0$ written in spherical coordinates

$$g_{tt} = 1 \tag{50}$$
$$g_{rr} = -1 \tag{51}$$
$$g_{\theta\theta} = -r^2 \tag{52}$$
$$g_{\varphi\varphi} = -r^2|\sin\theta|^2 \tag{53}$$

with connection

$$\Lambda^\theta_{\theta r} = \frac{1}{r} \tag{54}$$
$$\Lambda^r_{\theta\theta} = -r \tag{55}$$
$$\Lambda^\varphi_{\varphi r} = \frac{1}{r} \tag{56}$$
$$\Lambda^r_{\varphi\varphi} = -r|\sin\theta|^2 \tag{57}$$
$$\Lambda^\varphi_{\varphi\theta} = \cot\theta \tag{58}$$
$$\Lambda^\theta_{\varphi\varphi} = -\cot\theta|\sin\theta|^2 \tag{59}$$

in the case in which the tetrad vectors are chosen to be

$$e^0_t = 1 \tag{60}$$
$$e^1_r = \sin\theta\cos\varphi \quad e^2_r = \sin\theta\sin\varphi \quad e^3_r = \cos\theta \tag{61}$$
$$e^1_\theta = r\cos\theta\cos\varphi \quad e^2_\theta = r\cos\theta\sin\varphi \quad e^3_\theta = -r\sin\theta \tag{62}$$
$$e^1_\varphi = -r\sin\theta\sin\varphi \quad e^2_\varphi = r\sin\theta\cos\varphi \tag{63}$$

and

$$e^t_0 = 1 \tag{64}$$
$$e^r_1 = \sin\theta\cos\varphi \quad e^r_2 = \sin\theta\sin\varphi \quad e^r_3 = \cos\theta \tag{65}$$
$$e^\theta_1 = \frac{1}{r}\cos\theta\cos\varphi \quad e^\theta_2 = \frac{1}{r}\cos\theta\sin\varphi \quad e^\theta_3 = -\frac{1}{r}\sin\theta \tag{66}$$
$$e^\varphi_1 = -\frac{1}{r\sin\theta}\sin\varphi \quad e^\varphi_2 = \frac{1}{r\sin\theta}\cos\varphi \tag{67}$$

as the choice for which the spin connection vanishes.

Nevertheless, another specific choice is possible. It consists in taking the tetrad vectors as

$$e^0_t = \Delta \quad e^2_t = -\alpha\sin\theta\Delta \tag{68}$$
$$e^1_r = \Gamma\sin\theta\Delta \quad e^3_r = \cos\theta\Delta \tag{69}$$
$$e^1_\theta = r\cos\theta\Delta \quad e^3_\theta = -\Gamma r\sin\theta\Delta \tag{70}$$
$$e^0_\varphi = -\alpha r|\sin\theta|^2\Delta \quad e^2_\varphi = r\sin\theta\Delta \tag{71}$$

and

$$e^t_0 = \Delta \quad e^t_2 = \alpha\sin\theta\Delta \tag{72}$$
$$e^r_1 = \Gamma\sin\theta\Delta \quad e^r_3 = \cos\theta\Delta \tag{73}$$
$$e^\theta_1 = \frac{1}{r}\cos\theta\Delta \quad e^\theta_3 = -\frac{\Gamma}{r}\sin\theta\Delta \tag{74}$$
$$e^\varphi_0 = \frac{\alpha}{r}\Delta \quad e^\varphi_2 = \frac{1}{r\sin\theta}\Delta \tag{75}$$

which means that we are in the system of reference where the spinor field is in polar form.

We have then that

$$\beta = -\arctan\left(\frac{\alpha}{\Gamma}\cos\theta\right) \tag{76}$$

and

$$\phi = r^{\Gamma-1}e^{-\alpha m r}/\sqrt{\Delta} \tag{77}$$

for the Yvon-Takabayashi angle and module.

Then we can compute

$$R_{t\varphi\theta} = -\alpha r\sin\theta\cos\theta|\Delta|^2 \tag{78}$$
$$R_{r\theta\theta} = -r(1-\Gamma|\Delta|^2) \tag{79}$$

$$R_{r\varphi\varphi} = -r|\sin\theta|^2 \tag{80}$$
$$R_{\theta\varphi\varphi} = -r^2 \sin\theta\cos\theta \tag{81}$$

and

$$P_t = E + \alpha/r \tag{82}$$
$$P_\varphi = -1/2 \tag{83}$$

as it is well known for the momentum.

One can check that the pair of equations (44, 45) is satisfied, as expected since (42) is equivalent to (44, 45).

For more details on the hydrogen atom we refer to [14].

3.1.2 The harmonic oscillator model

The case of the harmonic oscillator is also well known although its relativistic treatment is not so thoroughly investigated. In the following we will refer to [15].

The interactions are given in terms of a coupling between the dipole moment of the spinor and an external field, like the one given in (42):

$$F_{\mu\nu} = v_\mu x_\nu - v_\nu x_\mu \tag{84}$$

with v_μ a time-like vector and x_μ the position vector. In the case we intend to study, the time-like vector will be chosen in the configuration in which only its temporal component remains and is normalized to unity.

We still look for solutions in the stationary form and in spherical coordinates, where (42) is given by

$$\begin{aligned} &E\begin{pmatrix}\mathbb{I} & 0\\ 0 & -\mathbb{I}\end{pmatrix}\psi + \frac{i}{r}\begin{pmatrix}0 & \vec{\boldsymbol{\sigma}}\cdot\vec{r}\\ -\vec{\boldsymbol{\sigma}}\cdot\vec{r} & 0\end{pmatrix}\partial_r\psi \\ &-\frac{i}{r^2}\begin{pmatrix}0 & \vec{\boldsymbol{\sigma}}\cdot\vec{r}\;\vec{\boldsymbol{\sigma}}\cdot\vec{L}\\ -\vec{\boldsymbol{\sigma}}\cdot\vec{r}\;\vec{\boldsymbol{\sigma}}\cdot\vec{L} & 0\end{pmatrix}\psi \\ &-i\omega\begin{pmatrix}0 & \vec{\boldsymbol{\sigma}}\cdot\vec{r}\\ \vec{\boldsymbol{\sigma}}\cdot\vec{r} & 0\end{pmatrix}\psi - m\psi = 0 \end{aligned} \tag{85}$$

and as it is easy to see, this form is well suited for a separation of variables. However, we shall not implement this separation because it is known that this property does not hold for the harmonic oscillator, in the general case, when no non-relativistic limit is taken.

As before, we focus only on the ground-state.

Defining the constant $a = (E-m)/2\omega$ together with the function $A(r,\theta) = \sqrt{r^4+a^4+2r^2a^2\cos(2\theta)}$ of the radial coordinate and elevation angle, one can see that the energy is given by $E^2 = m^2 + 6\omega$ with the spinor given by

$$\psi = Ke^{-\frac{1}{2}\omega r^2}e^{-iEt}\begin{pmatrix} r\cos\theta \\ r\sin\theta e^{i\varphi} \\ -ia \\ 0\end{pmatrix} \tag{86}$$

as an exact solution of (85) for any constant K.

Equations (85) are the Dirac spinor equations (42) with no electric charge and written in spherical coordinates in the case in which the tetrad vectors are chosen as before.

And as before, another possibility is to Lorentz transform everything so to get the polar form. To this purpose, one first needs to implement a rotation along the third axis so as to perform a shift of $\varphi/2$ giving

$$\psi = Ke^{-\frac{1}{2}\omega r^2}e^{-i\left(Et-\frac{\varphi}{2}\right)}\begin{pmatrix} r\cos\theta \\ r\sin\theta \\ -ia \\ 0\end{pmatrix} \tag{87}$$

in standard representation. With this solution we can calculate all bi-linear spinor quantities

$$\Theta = K^2e^{-\omega r^2}(r^2 - a^2) \tag{88}$$
$$\Phi = K^2e^{-\omega r^2}(2ar\cos\theta) \tag{89}$$
$$U^0 = K^2e^{-\omega r^2}(r^2 - a^2) \tag{90}$$
$$U^2 = K^2e^{-\omega r^2}(2ar\sin\theta) \tag{91}$$
$$S^1 = K^2e^{-\omega r^2}(2r^2\sin(2\theta)) \tag{92}$$
$$S^3 = K^2e^{-\omega r^2}(r^2\cos(2\theta) + a^2) \tag{93}$$

and with $U^1 = U^3 = S^0 = S^2 = 0$ identically. In order to force $U^2 = S^1 = 0$ too, the only transformations of interest remain the boost along the second axis and the rotation around the second axis, given by

$$\boldsymbol{B}_2 = \begin{pmatrix}\cosh\xi & 0 & \sinh\xi & 0\\ 0 & 1 & 0 & 0\\ \sinh\xi & 0 & \cosh\xi & 0\\ 0 & 0 & 0 & 1\end{pmatrix} \tag{94}$$

and

$$\boldsymbol{R}_2 = \begin{pmatrix}1 & 0 & 0 & 0\\ 0 & \cos\chi & 0 & \sin\chi\\ 0 & 0 & 1 & 0\\ 0 & -\sin\chi & 0 & \cos\chi\end{pmatrix} \tag{95}$$

in terms of the rapidity

$$\tanh\xi = \left(\frac{-2ar\sin\theta}{r^2+a^2}\right) \tag{96}$$

and the angle

$$\tan\chi = \left(\frac{-r^2\sin(2\theta)}{r^2\cos(2\theta)+a^2}\right) \tag{97}$$

precisely because these are the rapidity and angle in terms of which $\boldsymbol{B}_2$ and $\boldsymbol{R}_2$ vanish U^2 and S^1 identically, respectively.

This would mean that we have boosted into the rest frame and rotated the spin along the third axis, and therefore that we have written the spinor in polar form, which reads

$$\psi = \phi e^{-\frac{i}{2}\beta\boldsymbol{\pi}} \boldsymbol{S} \begin{pmatrix} \sqrt{2} \\ 0 \\ 0 \\ 0 \end{pmatrix} \tag{98}$$

in standard representation. Here $\boldsymbol{S} = \boldsymbol{B}_2^{-1}\boldsymbol{R}_2^{-1}\boldsymbol{R}_3^{-1}$ with

$$\beta = \arctan\left(\frac{2ar\cos\theta}{r^2 - a^2}\right) \tag{99}$$

and

$$\phi = Ke^{-\frac{1}{2}\omega r^2}\sqrt{A/2} \tag{100}$$

for the Yvon-Takabayashi angle and module.

The same rapidity and angle, but for the real representation of Lorentz transformations, would boost and rotate tetrads so as to write them according to

$$e_t^0 = (r^2+a^2)A^{-1} \quad e_t^2 = -2ar\sin\theta A^{-1} \tag{101}$$
$$e_r^1 = -\sin\theta(r^2-a^2)A^{-1} \quad e_r^3 = \cos\theta(r^2+a^2)A^{-1} \tag{102}$$
$$e_\theta^1 = r\cos\theta(r^2+a^2)A^{-1} \quad e_\theta^3 = r\sin\theta(r^2-a^2)A^{-1} \tag{103}$$
$$e_\varphi^0 = -2ar^2|\sin\theta|^2A^{-1} \quad e_\varphi^2 = r\sin\theta(r^2+a^2)A^{-1} \tag{104}$$

and

$$e_0^t = (r^2+a^2)A^{-1} \quad e_2^t = 2ar\sin\theta A^{-1} \tag{105}$$
$$e_1^r = -\sin\theta(r^2-a^2)A^{-1} \quad e_3^r = \cos\theta(r^2+a^2)A^{-1} \tag{106}$$
$$e_1^\theta = \frac{1}{r}\cos\theta(r^2+a^2)A^{-1} \quad e_3^\theta = \frac{1}{r}\sin\theta(r^2-a^2)A^{-1} \tag{107}$$
$$e_0^\varphi = 2aA^{-1} \quad e_2^\varphi = \frac{1}{r\sin\theta}(r^2+a^2)A^{-1} \tag{108}$$

and in terms of which it is now possible to calculate $R_{ij\mu}$ with (33) getting

$$R_{t\varphi\theta} = -2ar^2\sin\theta\cos\theta(r^2+a^2)A^{-2} \tag{109}$$
$$R_{r\theta\theta} = -2r^3[r^2+a^2\cos(2\theta)]A^{-2} \tag{110}$$
$$R_{t\varphi r} = 2ar|\sin\theta|^2(r^2-a^2)A^{-2} \tag{111}$$
$$R_{r\theta r} = -2a^2r^2\sin(2\theta)A^{-2} \tag{112}$$
$$R_{r\varphi\varphi} = -r|\sin\theta|^2 \tag{113}$$
$$R_{\theta\varphi\varphi} = -r^2\sin\theta\cos\theta \tag{114}$$

while we also have

$$P_t = E \tag{115}$$
$$P_\varphi = -1/2 \tag{116}$$

as it is again well known for the momentum.

One can see that the pair of equations (44, 45) is satisfied, as expected since (42) is equivalent to (44, 45).

With the case of the harmonic oscillator completed it is now possible to compare the two physical examples.

3.2 The comparison in parallel

3.2.1 Bi-linear invariant quantities

In order to make the comparison meaningful, it is easier to consider quantities that are free of any superfluous information. For this reason, we focus on scalars, since they are the only quantities that can be invariant while still being non-trivial. To make the comparison easy to read, in the following, we express the considered quantities for the hydrogen atom first and for the harmonic oscillator just below.

To begin, the Yvon-Takabayashi angles are

$$\beta = \arctan\left(-\frac{\alpha}{\Gamma}\cos\theta\right) \tag{117}$$
$$\beta = \arctan\left(\frac{2ar\cos\theta}{r^2-a^2}\right) \tag{118}$$

and the modules are

$$\phi = r^{\Gamma-1}e^{-\alpha mr}/\sqrt{\Delta} \tag{119}$$
$$\phi = Ke^{-\frac{1}{2}\omega r^2}\sqrt{A/2} \tag{120}$$

where some information already becomes visible: for instance, the Yvon-Takabayashi angle must be an odd function of $\cos\theta$ because of its pseudo-scalar character, and we see no radial dependence in the Yvon-Takabayashi angle in concomitance with the separability of variables of the module in the case of the hydrogen atom, while no such feature exists for the harmonic oscillator.

This is obvious from the fact that whenever the separability of variables is demanded, the module must be a product of the form $\phi = R(r)Y(\theta)$ while at the same time the Yvon-Takabayashi angle must be a sum of the form $\beta = S(r)+Z(\theta)$ since it is the argument of an exponential function. Because under parity the Yvon-Takabayashi angle flips its sign, we then must have $S = 0$ necessarily.

It should however be noticed that when the separation of variable does not hold, as for the harmonic oscillator, the radial dependence can carry surprises: for instance, it is easy to see that at $r = a$ the Yvon-Takabayashi angle is equal to $\pm\pi/2$. This defines the boundary between the regions where $\cos\beta$ is positive and regions where it is negative. Because of this, the sphere of radius a is the limit through which the scalar density Φ changes sign.

The five scalars coming from the squares of the tensorial connections are given by

$$R_{ac}{}^{c}R^{ai}{}_{i} = -\frac{1}{r^2}\left[(2-\Gamma\Delta^2)^2+|\cot\theta|^2\right] \tag{121}$$
$$R_{ac}{}^{c}R^{ai}{}_{i} = 4(a^2-2r^2)A^{-2} - \left|\frac{1}{r\sin\theta}\right|^2 \tag{122}$$
$$\frac{1}{4}R_{ijk}R^{abc}\varepsilon^{pijk}\varepsilon_{pabc} = -\frac{1}{r^2}\alpha^2|\cos\theta|^2\Delta^4 \tag{123}$$

$$\frac{1}{4}R_{ijk}R^{abc}\varepsilon^{pijk}\varepsilon_{pabc} = -4a^2A^{-2} \tag{124}$$

$$\frac{1}{2}R_{ijk}R^{ijk} = \frac{1}{r^2}\left[\alpha^2|\cos\theta|^2\Delta^4 - (1-\Gamma\Delta^2)^2 - \frac{1}{|\sin\theta|^2}\right] \tag{125}$$

$$\frac{1}{2}R_{ijk}R^{ijk} = 4(a^2-r^2)A^{-2} - \left|\frac{1}{r\sin\theta}\right|^2 \tag{126}$$

$$\frac{1}{2}R_{pq}{}^{q}R_{ijk}\varepsilon^{pijk} = \frac{1}{r^2}\alpha\cos\theta\Delta^2(2-\Gamma\Delta^2) \tag{127}$$

$$\frac{1}{2}R_{pq}{}^{q}R_{ijk}\varepsilon^{pijk} = 8ar\cos\theta A^{-2} \tag{128}$$

$$\frac{1}{4}R_{ijc}R_{pq}{}^{c}\varepsilon^{ijpq} = \frac{2}{r^2}\alpha\cos\theta\Delta^2(1-\Gamma\Delta^2) \tag{129}$$

$$\frac{1}{4}R_{ijc}R_{pq}{}^{c}\varepsilon^{ijpq} = 8ar\cos\theta A^{-2} \tag{130}$$

and something interesting is also emerging here: while in the large-r regime, in both cases, all scalars tend to zero, in the small-r region, for the hydrogen atom all scalars behave as $1/r^2$ whereas for the harmonic oscillator only $R^c_{ac}R^{ai}_i$ and $R_{ijk}R^{ijk}$ behave as $1/r^2$. As it is expected, both pseudo-scalars tend to zero with a linear behaviour in the radial coordinate but $R_{ijk}R^{abc}\varepsilon^{pijk}\varepsilon_{pabc} \approx -16/a^2$ and the fact that some scalar tends to a non-vanishing constant looks a very astonishing circumstance.

This is a consequence of the fact that for the hydrogen atom all scalars must have the same radial behavior to ensure dimensional consistency while for the harmonic oscillator the constant a has the dimension of a length and can therefore be substituted to the radial coordinate in some expressions. Nevertheless, for cases in which there is a natural constant with the dimension of a length, we do not think that it is possible to guess the actual radial behavior. There is in fact no a priori difference between the three scalars and still one of them has a radial behavior that is very different from the one of the others.

3.2.2 Energy density tensor components

Albeit scalars are the invariants of the theory, it might also be instructive to see what happens for a non-scalar quantity. Even if we are considering situations where the energy is not large enough to be a relevant source for the gravitational field, it can still be different from zero and as such, it may contain some interesting information.

The energy density tensor which is the source term of the Einstein field equations is given, in polar form, according to

$$T_{qa} = 2\phi^2\left(s_q\nabla_a\beta/2 + u_qP_a + \frac{1}{4}\varepsilon_{kijq}s^kR^{ij}{}_a\right) \tag{131}$$

and it results in

$$T_{tt} = 2\phi^2\Delta(E+\alpha/r) \tag{132}$$

$$T_{tt} = 2\phi^2A^{-1}(r^2+a^2)E \tag{133}$$

$$T_{t\varphi} = -\phi^2\Delta(1-\Gamma)|\sin\theta|^2 \tag{134}$$

$$T_{t\varphi} = -2\phi^2A^{-1}r^2|\sin\theta|^2 \tag{135}$$

$$T_{rr} = 0 \tag{136}$$

$$T_{rr} = 2\phi^2A^{-1}a \tag{137}$$

$$T_{\theta\theta} = \phi^2\Delta\alpha r \tag{138}$$

$$T_{\theta\theta} = 2\phi^2A^{-1}ar^2 \tag{139}$$

$$T_{\varphi t} = -2\phi^2\Delta\alpha r|\sin\theta|^2(E+\alpha/r) \tag{140}$$

$$T_{\varphi t} = -4\phi^2A^{-1}ar^2|\sin\theta|^2E \tag{141}$$

$$T_{\varphi\varphi} = \phi^2\Delta\alpha r|\sin\theta|^2 \tag{142}$$

$$T_{\varphi\varphi} = 2\phi^2A^{-1}ar^2|\sin\theta|^2 \tag{143}$$

in which an obvious lack of symmetry can be noticed in the fact that in the case of the hydrogen atom there is no radial–radial component is once again a consequence of the separability of variables.

It is possible to compute the traces, which give

$$T = 2\phi^2\Delta E \tag{144}$$

$$T = 2\phi^2A^{-1}(r^2E - a^2m) \tag{145}$$

and exhibit an interesting property: while for the hydrogen atom the large-r and small-r behaviors are the same, for the harmonic oscillator the large-r behavior is $T = 2\phi^2E$ but the small-r behavior becomes $T = -2\phi^2m$ flipping the sign of the scalar trace of the energy density.

So the sphere of radius $a\sqrt{m/E}$ defines the limit through which the scalar trace of the energy density T changes from positive values to negative values. Because the trace is such that $T = \mathscr{L} + m\overline{\psi}\psi$ with $\mathscr{L}$ the Langragian functional, we may think at the energy trace as what encodes information about the total energy.

4 The tensorial connections

In the first section we have seen that R_{ijk} and P_a have the character of connections while being true tensors: R_{ijk} is the tensorial connection in a strict sense since it is directly related to the Lorentz transformation while P_a is called the gauge-invariant vector momentum to highlight its relation to the gauge transformations. Although the concept of a tensorial connection seems a contradiction, because connections can be vanished with a choice of frame whereas tensors cannot, this should not appear as something drastically new: the orbital angular momentum can be vanished when calculated in specific points but the spin cannot. The tensorial connection and the spin share this property of being truly covariant.

However, tensorial connections still behave as connections in their lacking of couplings to sources. In fact, the components of R_{ijk} and P_a might well be different from zero

but their curvatures are vanishing if, respectively, no gravity or no electrodynamic phenomenon is present.

Situations where some physical effects can be ascribed to potentials that are present (as non-zero connections) despite having no strength (since they have zero curvature) is something that may be strange for R_{ijk} but for P_a is that we already know as Aharonov–Bohm effect.

For P_a the technicalities can be worked out by taking expression (34) and integrating it as

$$\int_\gamma (P_\mu + q A_\mu) dx^\mu = \int_\gamma \partial_\mu \lambda dx^\mu = \int_\gamma d\lambda = \Delta\lambda \tag{146}$$

along the trajectory γ, and where the last term is just the difference of phase between the starting and the ending points. Similarly, from (33) we get

$$\int_\gamma (R_{ij\mu} + \Omega_{ij\mu}) dx^\mu = \int_\gamma \partial_\mu \theta_{ij} dx^\mu = \int_\gamma d\theta_{ij} = \Delta\theta_{ij} \tag{147}$$

in total analogy with the case above. Recall that Lorentz indices designate quantities that are tensor under a (local) Lorentz transformation but scalar under coordinate transformations. The integral is therefore well-defined.

When the spinor is in polar form, (36, 37) reduce to

$$\nabla_\mu s_i = R_{3i\mu} \tag{148}$$

$$\nabla_\mu u_i = R_{0i\mu} \tag{149}$$

showing that the dynamics of the velocity vector or of the spin axial-vector is determined only by those components of $R_{ij\mu}$ for which the first index is equal to either zero or three. The antisymmetry in the first two indices implies that any of the first two indices has to be either zero or three, so that $R_{12\mu}$ never appears. This makes this component somehow analogous to the momentum since P_μ never appears in the dynamics of the velocity vector and of the spin axial-vector in the first place.

This is in line with the fact that for a spinor that is an eigenstate of the spin, that is for rotations around the third axis, as the one in the polar form, rotations around the third axis have the same effect than gauge shifts: in fact, a suitable rotation around the third axis generates a component of $R_{12\mu}$ which is related by $R_{12\mu} \equiv -2P_\mu$ to the momentum generated by an equivalent gauge shift.

If the trajectory is a close circuit, $\Delta\theta$ is just a whole turn times an integer

$$\oint_\gamma (P_\mu + q A_\mu) dx^\mu = 2\pi n \tag{150}$$

and analogously for $\Delta\theta_{12}$ we have

$$\oint_\gamma (R_{12\mu} + \Omega_{12\mu}) dx^\mu = -4\pi n \tag{151}$$

where n is usually called winding number.

4.1 Discretizing the connection

If we consider the free cases, requiring the electromagnetic field to vanish means that

$$\oint_\gamma P_\mu dx^\mu = 2\pi n \tag{152}$$

while requiring the gravitational field to vanish means that it is always possible to find a frame where

$$\oint_\gamma R_{12\mu} dx^\mu = -4\pi n \tag{153}$$

as it is clear because of the formal analogy. Whereas the former is clearly the Born rule for discretizing momenta in closed orbits, the latter should be regarded as the Born rule for discretizing some components of the connection in closed orbits. Such an occurrence brings about an important point in the discussion around the quantization of gravitational degrees of freedom, because the tensorial connection is precisely where the geometrical information is encoded. The process of discretization is entirely independent on the structure of the tensorial connection.

Much in the same way in which tensorial connections can be discrete in the free case, the same might happen even if gravity were present. In this case the quantization would happen on the gravitational degrees of freedom. We do not claim that this approach solves the long standing problem of quantum gravity. It might however give some hints about the fundamentally quantum nature of some geometrical degrees of freedom.

4.2 Aharonov–Bohm Effects

If the gauge-invariant vector momentum and the tensorial connection happen to vanish, and we choose a close circuit to be the boundary of a given surface $\gamma = \partial S$, then

$$q \oint_{\partial S} \vec{A} \cdot d\vec{x} = 2\pi n \tag{154}$$

and analogously

$$\oint_{\partial S} \vec{\Omega}_{12} \cdot d\vec{x} = -4\pi n \tag{155}$$

in which we accounted for the spatial parts only. Using the Stokes theorem we obtain

$$q \iint_S \mathrm{rot}\vec{A} \cdot d\vec{S} = 2\pi n \tag{156}$$

and analogously

$$\iint_S \mathrm{rot}\vec{\Omega}_{12} \cdot d\vec{S} = -4\pi n \tag{157}$$

where we now have fluxes on the left-hand side. While the former is recognized to be the condition giving rise to the Aharonov–Bohm effect, the latter should be interpreted as the condition giving rise to the gravitational analogous of the Aharonov–Bohm effect. This would not only entail the quantization of the electromagnetic as well as of the gravitational fluxes, as discussed above. But it also means that there can be a phase-shift in the wave function of the matter field due to the electromagnetic as well as to the gravitational potentials even in regions with neither electromagnetic nor gravitational forces.

In fact, writing (21) in the form

$$\psi = \boldsymbol{S}\psi_{\text{pol}} \tag{158}$$

where ψ_{pol} is the spinor in full polar form, we have that

$$\boldsymbol{S} = e^{-i\lambda} e^{-\frac{1}{2}\theta_{ij}\boldsymbol{\sigma}^{ij}} \tag{159}$$

in terms of one phase-shift of abelian type in λ and another of non-abelian type in θ_{12} which, according to the above (156, 157), can be present even in regions where no electrodynamic or gravity are present. However, electrodynamics or gravity must be present in nearby regions so to let the fluxes be non-zero at least somewhere.

The analogy of the two types of Aharonov–Bohm effect, electrodynamic and gravitational, can be appreciated in its full extent in the fact that in (159) both abelian gauge phase and third-axis rotation angle have identical impact on the structure of the spinor field matter distribution.

Nevertheless, it is important to stress that the usual electrodynamic Aharonov–Bohm effect parallels only one of the six vector potentials describing the gravitational Aharonov–Bohm effect, and therefore the latter is inevitably richer in potential physical applications.

5 Special approximations

As concluding remarks, we would like to investigate what happens in the case of specific limits. A first approximation is the one for which the two coupling constants are small: in such a case, the above solution for the hydrogen atom automatically reduces to the non-relativistic solution for the considered system. Instead, the solution for the harmonic oscillator has $a \approx \frac{3}{2m}$ which reduces to the non-relativistic solution only in the case of large masses. In fact, even if the mass is large, it would still be possible to consider radial distances small enough, and the non-relativistic approximation still fails.

In fact, quite generally, for the harmonic oscillator we can always find regions where relativistic effects cannot be suppressed. To see this, just consider the scalar quantity $\cos\beta$ and the energy trace T. The first changes sign on the sphere of radius a and the second changes sign on the sphere of radius $a\sqrt{m/E}$ with $a > a\sqrt{m/E}$ since ω is positive. For small values of ω, we can expand the energy and write it according to

$$T \approx 2\phi^2 \left(m\cos\beta + \frac{3\omega r^2}{Am} \right) \tag{160}$$

which isolates the kinetic energy $m\cos\beta$ from the potential energy $3\omega r^2 A^{-1}/m$. The kinetic energy becomes negative across the sphere of radius $a\sqrt{m/E}$ and it becomes negative and large enough so to overcome the positive potential and make the total energy negative as well across the sphere of radius $a > a\sqrt{m/E}$. Apart from this shift due to the potential, the reason for which both the energy and the modulus become negative is the same, that is the fact that $\cos\beta$ becomes negative. As $\cos\beta \to -1$ then $\beta \to \pi$ which means that left-handed and right-handed chiral parts are in maximal phase opposition with respect to one another. The deep interpretation of such unusual new effects is still to be understood but, at the heuristic levels, calculation of observables are in principle possible.

Because the Yvon-Takabayashi angle is what describes the differences between the two chiral parts even in the rest frame, it can be interpreted as what describes the internal dynamics of spinor fields. Thus, close to the center of the matter distribution, where β tends to its maximal value, there appears a region where the internal dynamics is dominant. This is the region where relativistic effects can never be suppressed, as we argued above.

Such an internal dynamics is confined within a sphere whose radius can be evaluated, for small values of ω, to be approximately one fourth of the Compton wavelength.

From the viewpoint of ordinary QFT, this is a strange occurrence as the scalar density Φ is always assumed to be strictly positive in QFT. This implies that the harmonic oscillator has solutions which, as fields, cannot be quantized, or at least not with usual methods.

We will not deal, however, with second quantization.

6 Conclusion

In this work, we have shown that when the spinor fields are written in polar form, it becomes possible to define a pair of objects that contain the very same information of the space-time connection and the gauge potential but which are covariant under Lorentz and phase transformations: they are called tensorial connection and the gauge-invariant vector momentum. We have discussed that they are generally non-zero even when they have neither space-time curvature nor gauge curvature: this means that they can have effects even when sourceless. Although this may look surprising, we have shown that it consistently happens in specific cases, such as the Coulomb and elastic potentials. A final compari-

son between the hydrogen atom and the harmonic oscillator was also performed, in particular for the scalars and for the energy density tensor.

The fact that there could be non-trivial effects even when considering sourceless actions is not new, since a phase shift can occur in what is known as the Aharonov–Bohm effect. We have shown that such a phenomenon occurs not only for the gauge-invariant vector momentum but also for the tensorial connection. To highlight this, we have built a parallel between the two cases. We have also underlined that as the Aharonov–Bohm effect can entail information about the quantization of electromagnetic fluxes, the gravitational version of the Aharonov–Bohm effect may encode information about the quantization of at least some of gravitational fluxes.

We have concluded with comments on non-relativistic limits, and in particular we have underlined the fact that for the harmonic oscillator it is not possible to get non-relativistic approximations in regions that are too close to the center of the matter distribution because these are the regions where the internal dynamics is dominant.

The fact that for the harmonic oscillator, both the energy and the modulus may become negative seems to lead to some conceptual problems in the perspective of QFT, since several results of QFT are based on assumptions that we show not to be fulfilled in general. For example, some hypotheses of spin-statistic theorems, like the positivity of energy and norms, should be questioned when harmonic oscillations are taken into account. Nevertheless, while critical in QFT, these features of the harmonic oscillator are a consequence of exact solutions in presence of elastic potentials within the Dirac equation, and so there does not seem to be much room for improvement.

The only possibility could be that the problems come from the elastic potential, but the elastic potential is just a dipole coupling to an external tensor field, like the one that occurs in presence of radiative processes.

We leave such considerations, and possible experimental signatures, for a future work.

Data Availability Statement This manuscript has associated data in a data repository. [Authors' comment: This manuscript has associated data as arXiv:1909.01733.]

Funded by SCOAP[3].

References

1. L. Fabbri, Geometry, zitterbewegung, quantization. Int. J. Geom. Methods Mod. Phys. **16**, 1950146 (2019)
2. R.F. Streater, A.S. Wightman, *PCT, Spin and Statistics, and All That* (Princeton University, Princeton, 2014)
3. R. Haag, On quantum field theories. Mat. Fys. Med. **29**, 12 (1995)
4. P. Lounesto, *Clifford Algebras and Spinors* (Cambridge University Press, Cambridge, 2001)
5. R.T. Cavalcanti, Classification of singular spinor fields and other mass dimension one fermions. Int. J. Mod. Phys. D **23**, 1444002 (2014)
6. J.M. Hoff da Silva, R.T. Cavalcanti, Revealing how different spinors can be: the Lounesto spinor classification. Mod. Phys. Lett. A **32**, 1730032 (2017)
7. J.M. da Hoff Silva, R. da Rocha, Unfolding physics from the algebraic classification of spinor fields. Phys. Lett. B **718**, 1519 (2013)
8. R. Rocha, J.M. Hoff da Silva, ELKO, flagpole and flag-dipole spinor fields, and the instanton Hopf fibration. Adv. Appl. Clifford Algebras **20**, 847 (2010)
9. C.H. Coronado Villalobos, J.M. da Hoff Silva, R. da Rocha, Questing mass dimension 1 spinor fields. Eur. Phys. J. C **75**, 266 (2015)
10. R. Abłamowicz, I. Gonçalves, R. da Rocha, Bilinear covariants and spinor fields duality in quantum clifford algebras. J. Math. Phys. **55**, 103501 (2014)
11. L. Fabbri, A generally-relativistic gauge classification of the Dirac fields. Int. J. Geom. Methods Mod. Phys. **13**, 1650078 (2016)
12. L. Fabbri, Torsion gravity for Dirac fields. Int. J. Geom. Methods Mod. Phys. **14**, 1750037 (2017)
13. L. Fabbri, General dynamics of spinors. Adv. Appl. Clifford Algebras **27**, 2901 (2017)
14. L. Fabbri, Covariant inertial forces for spinors. Eur. J. Phys. C **78**, 783 (2018)
15. M. Moshinsky, Y.F. Smirnov, *The Harmonic Oscillator in Modern Physics* (Harwood Academic Publishers, Amsterdam, 1996)

4.4 La section efficace Compton dans le formalisme polaire

Ici le quadri-vecteur vitesse est dénoté par g^a au lieu de u^a étant donné que usuellement la lettre u est utilisée pour indiquer un spineur en TQC.

Dans cet article, nous étudions la section efficace associée à la diffusion de spineurs dans le cadre du formalisme polaire et on observe les différences avec les résultats de la TQC. Nous rappelons que, sans potentiel externe, l'équation de Dirac s'écrit

$$i\gamma^\mu \nabla_\mu \psi - m\psi = 0, \tag{4.67}$$

avec la dérivée covariante telle que

$$\nabla_\mu \psi = (\nabla_\mu \ln\phi \mathbb{I} - \frac{i}{2}\nabla_\mu \beta\gamma^5 - iP_\mu \mathbb{I} - \frac{1}{2}R_{ij\mu}\sigma^{ij})\psi = 0. \tag{4.68}$$

On retrouve la TQC pour ϕ = constante, $\beta = 0$ et $R_{ij\mu} = 0$. On a vu que l'équation de Dirac est équivalente aux deux équations du formalisme polaire (4.31, 4.32). Sans le terme de potentiel $F_{\mu\nu}$, ces équations se réduisent à

$$B_\mu - 2P^\iota g_{[\iota} s_{\mu]} + \nabla_\mu \beta + 2s_\mu m\cos\beta = 0, \tag{4.69}$$
$$R_\mu - 2P^\rho g^\nu s^\alpha \varepsilon_{\mu\rho\nu\alpha} + 2s_\mu m\sin\beta + \nabla_\mu \ln\phi^2 = 0, \tag{4.70}$$

avec $B_\mu = \frac{1}{2}\varepsilon_{\mu\alpha\nu\iota}R^{\alpha\nu\iota}$ et $R_\mu = R_{\mu a}{}^a$. Avec les équations (4.69, 4.70), on peut écrire l'impulsion

$$P^\mu = m\cos\beta g^\mu - y_k s^{[k} g^{\mu]} - x_k s_j g_i \varepsilon^{kji\mu}, \tag{4.71}$$

avec $x_k = \frac{1}{2}(\nabla_k \ln\phi^2 + R_k)$ et $y_k = \frac{1}{2}(\nabla_k\beta + B_k)$. En TQC, ces deux derniers sont supposés nuls. Ici, ce n'est plus le cas et l'impulsion n'est plus proportionnelle à la vitesse, mais dépend également du spin s^a. On observe encore une fois que l'angle β apparaît dans le terme de masse, ainsi l'interaction des parties gauche et droite change de façon effective la masse du spineur. Dans le cadre de la TQC, on a

$$P^\mu = mg^\mu, \tag{4.72}$$

ces quatre conditions impliquent que l'équation de Dirac (4.69, 4.70) (soit huit équations) avec ϕ = constante et $\beta = 0$ est vérifiée. Si l'équation (4.72) était valide, il serait toujours possible d'effectuer un boost dans le référentiel où la limite non-relativiste serait retrouvée, ce qui n'est pas le cas. En effet, cette limite n'est pas retrouvée car même dans le référentiel au repos il existe une dynamique interne due au spin s^a et à l'angle β.

Ici, on souhaite prendre en compte x_k et y_k dans l'amplitude de diffusion. L'équation de Dirac s'écrit donc

$$(F_k\gamma^k + y_k\gamma^k\gamma^5 - m)\psi = 0, \tag{4.73}$$

avec $F_k = P_k + ix_k$. Ainsi le propagateur G va être modifié et être solution de l'équation

$$(F_k\gamma^k + y_k\gamma^k\gamma^5 - m)G = \mathbb{I}. \tag{4.74}$$

On trouve que le propagateur s'écrit

$$G = (|F^2 + y^2 + m^2|^2 - |2F\cdot y|^2 - 4F^2m^2)^{-1} \times [F_k\gamma^k - y_k\gamma^k\gamma^5 - m] \times [(F^2 + y^2 + m^2)\mathbb{I} + 2F\cdot y\gamma^5 + 2mF_a\gamma^a].$$

On retrouve effectivement le propagateur de la TQC pour $x_k = y_k = 0$.

On veut calculer l'amplitude de transition pour l'effet Compton. Les particules initiales sont un photon d'impulsion k et un électron dans un potentiel d'hydrogène d'impulsion p. A l'état final on a un photon d'impulsion k' et un électron d'impulsion p'. L'amplitude pour le canal s est donnée par

$$\tfrac{1}{4}\sum_{\text{spin}}|\mathcal{M}^s|^2 = \tfrac{e^4}{4}\text{Tr}\Big[S(p')\gamma^\nu G(q)\gamma^\mu S(p)\gamma_\mu\overline{G(q)}\gamma_\nu\Big], \tag{4.75}$$

avec $q = p + k$ et $S(p)$ la somme sur les spins. Dans le formalisme polaire, on a

$$S(p) = \sum_{spins}\psi\overline{\psi} = \phi^2(g_a\gamma^a + e^{-i\beta\gamma^5}). \tag{4.76}$$

En considérant seulement les corrections au premier ordre, on a

$$S(p) = \phi^2\Big(\not{g} + \mathbb{I} - i\beta\gamma^5\Big), \tag{4.77}$$

$$S(p') = \phi'^2\Big(\not{g}' + \mathbb{I} - i\beta'\gamma^5\Big) = m\not{g}' + m\mathbb{I}, \tag{4.78}$$

car l'électron final est libre donc on a $\beta' = 0$ et $\phi'^2 = m$. Au contraire, l'électron initial orbite autour du proton, et l'angle d'Yvon-Takabayashi est donné par

$$\beta = -\arctan\Big(\frac{\alpha}{\Gamma}\cos\theta\Big), \tag{4.79}$$

avec α la constante structure fine et $\Gamma = \sqrt{1-\alpha^2}$. L'amplitude s'écrit

$$\phi = \sqrt{m}r^{\Gamma-1}e^{-\alpha mr}/\sqrt{\Delta}, \tag{4.80}$$

avec $\Delta(\theta) = (1-|\alpha\sin\theta|^2)^{-\frac{1}{2}}$. Étant donné la performance des résultats de la TQC, on peut en déduire que les valeurs de x_k et y_k sont petites. On effectue une approximation au premier ordre pour le propagateur et on obtient

$$G(q) \approx (q^2 - m^2 + 4iq\cdot x)^{-1} \times \Big[W\mathbb{I} + X_a\gamma^a + Y_a\gamma^a\gamma^5 + Z_{ab}\sigma^{ab}\gamma^5\Big],$$

avec

$$W = m + \frac{2im(x\cdot q)}{q^2 - m^2}, \tag{4.81}$$

$$X_a = q_a + ix_a + \frac{2i(x\cdot q)}{q^2 - m^2}q_a, \tag{4.82}$$

$$Y_a = \frac{1}{q^2 - m^2}[-(q^2 + m^2)y_a + 2(y\cdot q)q_a], \tag{4.83}$$

$$Z_{ab} = \frac{4m}{q^2 - m^2}y_aq_b. \tag{4.84}$$

En TQC, il n'y a pas de terme imaginaire au dénominateur et on le rajoute à la main pour utiliser le Lemme de Jordan. Or on remarque ici que le terme $4iq \cdot x$ apparaît naturellement. En utilisant l'équation (4.71), on calcule l'impulsion de l'électron initial

$$\begin{pmatrix} p^0 \\ p^1 \\ p^2 \\ p^3 \end{pmatrix} = \begin{pmatrix} m + \frac{\alpha}{r} \\ -\sin\varphi/(2r\sin\theta) \\ \cos\ \varphi/(2r\sin\theta) \\ 0 \end{pmatrix}. \tag{4.85}$$

Sa vitesse g^a est donnée par

$$\begin{pmatrix} g^0 \\ g^1 \\ g^2 \\ g^3 \end{pmatrix} = \begin{pmatrix} 1 \\ -\alpha\sin\theta\sin\varphi \\ \alpha\sin\theta\cos\varphi \\ 0 \end{pmatrix}. \tag{4.86}$$

La section efficace différentielle est donnée par

$$\frac{d\sigma}{d\cos\theta'} = \frac{1}{2\omega}\frac{1}{2(m+\alpha/r)} \mid M(\{k,p\} \to \{k',p'\}) \mid^2 \times \frac{1}{4\pi}\frac{\omega'^2}{2m\alpha/r - 1/(2r\sin\theta)^2 + 2\omega(m+\alpha/r)}, \tag{4.87}$$

le terme $\mid M(\{k,p\} \to \{k',p'\}) \mid$ dans le cadre du formalisme polaire se différencie du terme de TQC car on ne peut plus remplacer p par mg, ainsi les produits scalaires vont avoir des valeurs différentes. Dans la limite $r \to \infty$, on en déduit la section efficace différentielle

$$\begin{aligned} \frac{d\sigma}{dY} = \frac{\pi\alpha^2}{m\omega(m+\omega-Y\omega)^3}\Big[& m^2(1+Y^2)\omega - m(Y-1)(1+Y^2)\omega^2 + (Y-1)^2\omega^3 \\ & + \sqrt{1-Y^2}\alpha\sin\theta\sin\varphi \times \Big(m^3 + m^2(3-2Y)\omega + m(Y-1)^2\omega^2\Big)\Big]. \end{aligned} \tag{4.88}$$

avec $Y \equiv \cos\theta'$, θ' étant l'angle de diffusion du photon final défini sur la Figure 1 de l'article. Ainsi, avec le formalisme polaire on peut calculer la section efficace lorsque l'électron initial n'est pas libre, mais se trouve dans un potentiel d'hydrogène. Dans ce cas, il y a une dynamique interne entre les parties droite et gauche de l'électron qui se traduit par un angle β non nul et une brisure de la symétrie sphérique. On retrouve, en effet, les résultats de la TQC lorsque α tend vers zero. La section efficace (4.88) dépend des angles θ et φ étant donné la brisure de symétrie. Cependant, en pratique, nous effectuons une étude statistique et la section efficace (4.88) doit être moyennée sur θ et φ. Il en résulte que statiquement il n'existe pas de correction en α et on retrouve la section efficace calculée en TQC.

Dans cet article nous avons utilisé le formalisme polaire pour décrire la diffusion de spineurs. Dans ce cadre l'expression générale du propagateur a été calculée. La partie imaginaire du dénominateur usuellement ajoutée pour effectuer le calcul des pôles apparaît ici naturellement. De plus, avec ce formalisme, il est possible de décrire la diffusion pour des champs en interaction ce qui n'est pas le cas en TQC. Il en résulte que la probabilité d'interaction pour un événement va être modifiée par cette interaction. Cependant, d'un point de vue statistique, les résultats de la TQC sont retrouvés.

Cet article a été soumis à *Physics Letters B*.

Cross section for Bhabha and Compton scattering beyond quantum field theory

Flora Moulin[1], Luca Fabbri[2], Aurélien Barrau[1]
[1] *Laboratoire de Physique Subatomique et de Cosmologie, Université Grenoble-Alpes CNRS/IN2P3, 53 avenue des Martyrs, 38026 Grenoble cedex, FRANCE*
[2] *DIME Sezione di Metodi e Modelli Matematici, Università degli studi di Genova, via all'Opera Pia 15, 16145 Genova, ITALY*
(Dated: March 2, 2020)

We consider the theory of spinor fields written in the polar formalism. The components are given as a module times a complex unitary phase respecting full Lorentz covariance. In this formalism, spinors can be treated in their most general mathematical form, without the need to restrict them to the case of plane waves. As a consequence, calculations of scattering amplitudes can be performed by employing new fermion propagators and spin-sum relationships. In this article, we perform such calculations for two processes: the electron-positron and Compton scatterings. We show how the results differ from the ones calculated by using only plane waves, as usually done in quantum field theory.

I. INTRODUCTION

Quantum field theory (QFT) is a magnificent theory in its predictive power. It has successfully passed all experimental tests put forward up to now. Its core consists in taking plane-wave solutions to the fundamental equations, promoting fields to be operators and expanding scattering amplitudes in terms of radiative corrections (or loop diagrams).

In this framework, predictions for the anomaly of the magnetic moment of leptons and for the hyper-fine splitting of hydrogen-like atoms have been confirmed to an astonishing precision. The philosophy that lies at the foundations of QFT is that, in the perturbative expansion, all propagators are given for the free fields, the full information about the interactions being encoded through quantization protocols within the vertices. Giving propagators in terms of free fields is the reason why plane-wave solutions can be used, and having all the information contained in the vertices is the reason why radiative corrections account for the full interaction. Naively, one may consider the process as a Taylor expansion of the entire interaction.

Nevertheless, the mathematical structure still needs a proper definition. Inconsistencies range from the fact that equal-time commutation relationships may lack a precise sense [1] to the fact that the interaction picture used for the perturbative expansion may not, and in fact in some cases does not, exist [2]. Even worse may be the fact that all calculations are done in terms of plane-wave solutions, which are not square-integrable so that, strictly speaking, are not physically acceptable.

In this respect, one may wonder if, to describe a given interaction, it could be possible to get rid of the perturbative series of vertex corrections, since they are not necessarily well-defined on free propagators, and find a way to describe the interaction as a whole.

This means that one would have, first, to find the most general expression of interacting propagators and, then, should recover the results of QFT in some limit.

In this study, we present the most general expression of the interacting propagator for fermion fields. Then, we use it to calculate some processes typically calculated in QFT: the Bhabha (electron-positron) scattering and the Compton scattering in the specific case where the electron is in a hydrogen-like potential. Finally, we make some comments on the comparison between what we obtain and QFT in its standard form.

In order to get the general propagator for spinors, we need to make a considerable use of the so called polar form, the form in which spinor fields can be written in such a way that each of their components is a module times a complex unitary phase.

Generally speaking, this process spoils manifest covariance. However, recent developments made it possible to use an explicitly covariant approach. We thus take advantage of this formalism, and the ensuing polar form, for the calculation of the general spinor propagator together with the scattering amplitude.

II. GENERAL SPINOR THEORY

To treat spinors, we begin by introducing the Clifford matrices $\boldsymbol{\gamma}^{\mu}$ satisfying the Clifford algebra

$$\{\boldsymbol{\gamma}^{a},\boldsymbol{\gamma}^{b}\}=2\eta^{ab}\mathbb{I}, \tag{1}$$

in terms of which

$$\boldsymbol{\sigma}^{ab}=\tfrac{1}{4}\left[\boldsymbol{\gamma}^{a},\boldsymbol{\gamma}^{b}\right] \tag{2}$$

are the generators of the complex Lorentz group,

$$\boldsymbol{S}\left[\Lambda\right]=e^{\frac{1}{2}\theta_{ab}\boldsymbol{\sigma}^{ab}}, \tag{3}$$

where $\theta_{ab}=-\theta_{ba}$ are the parameters of the real Lorentz transformation Λ mentioned above. The relation

$$\boldsymbol{\gamma}_{i}\boldsymbol{\gamma}_{j}\boldsymbol{\gamma}_{k}=\boldsymbol{\gamma}_{i}\eta_{jk}-\boldsymbol{\gamma}_{j}\eta_{ik}+\boldsymbol{\gamma}_{k}\eta_{ij}+i\varepsilon_{ijkq}\boldsymbol{\pi}\boldsymbol{\gamma}^{q} \tag{4}$$

implicitly defines the odd-parity $\boldsymbol{\pi}$ matrix (which is usually referred to as $\boldsymbol{\gamma}_5$ but since, in the 4-dimensional space-time, this index has no meaning we prefer to use a notation with no index at all).

A spinor field ψ is defined as a vector field in the space of spin, or complex Lorentz transformations. It is a "column" of 4 complex scalars satisfying

$$\psi \to \boldsymbol{S}\psi \tag{5}$$

as a general transformation law. Its adjoint $\overline{\psi} = \psi^\dagger \boldsymbol{\gamma}_0$ is defined in this way because then the spinorial bi-linear quantities

$$2i\overline{\psi}\boldsymbol{\sigma}^{ab}\psi = M^{ab}, \tag{6}$$
$$\overline{\psi}\boldsymbol{\gamma}^a\boldsymbol{\pi}\psi = S^a, \tag{7}$$
$$\overline{\psi}\boldsymbol{\gamma}^a\psi = G^a, \tag{8}$$
$$i\overline{\psi}\boldsymbol{\pi}\psi = \Theta, \tag{9}$$
$$\overline{\psi}\psi = \Phi, \tag{10}$$

are all real tensorial quantities.

The dynamical character is determined by the Dirac spinor field equation

$$i\boldsymbol{\gamma}^\mu \boldsymbol{\nabla}_\mu \psi - m\psi = 0, \tag{11}$$

where m is the mass of the field. This field equation could be complemented by additional interaction terms, but for our purpose we will need nothing more.

Using the bi-linear quantities, one may perform a classification of spinor fields. For instance, if Θ and Φ do not both vanish identically, the spinors are called regular and they are essentially the Dirac spinors. If they both vanish identically, then they are called singular, or flag-dipole, and split in further sub-classes. If, in addition, M^{ab} vanishes, then they are the so-called "dipole". In this class, one finds Weyl spinors. If S^a vanishes, then they are the "flagpole". In this class one finds Majorana spinors. Consequently, it is not generally possible to dismiss singular spinors as a whole. In this article, our interest will however be focused on regular spinors. For those spinors, it was shown in [3] that it is always possible to write them as

$$\psi = \phi e^{-\frac{i}{2}\beta\boldsymbol{\pi}}\boldsymbol{S}\begin{pmatrix}1\\0\\1\\0\end{pmatrix} \tag{12}$$

in the chiral representation, where ϕ is called the module, β is the Yvon-Takabayashi angle, and $\boldsymbol{S}$ is a generic spin transformation. For regular spinors, one has

$$M_{ab} = (\Phi^2+\Theta^2)^{-1}(G^j S^k \varepsilon_{jkab}\Phi + G_{[a}S_{b]}\Theta), \tag{13}$$

showing that only the vector and axial-vector with scalar and pseudo-scalar are independent. The spin transformation $\boldsymbol{S}$ is the one that takes the most general spinor in the frame in which its velocity vector G^a loses its spatial part and where the spin axial-vector S^a is aligned along the third axis. We can normalize these vectors as

$$S^a = 2\phi^2 s^a, \tag{14}$$
$$G^a = 2\phi^2 g^a, \tag{15}$$

where

$$\Theta = 2\phi^2 \sin\beta, \tag{16}$$
$$\Phi = 2\phi^2 \cos\beta, \tag{17}$$

and show that the two scalar fields ϕ and β are the only true real degrees of freedom of the spinor. The spinorial field consists in 8 real components, and the above form makes their meaning clear: the scalar ϕ is what in non-relativistic quantum mechanics gives the amplitude of probability while β describes the dynamics between right-handed and left-handed chiral projections. As such, the latter disappears in the non-relativistic limit. The 3 components of the velocity and spin are described as rapidities and angles in terms of the parameters of the $\boldsymbol{S}$ transformation and thus can always be transferred to the underlying space-time structure, as we will see.

Among other useful relationships, one should mention

$$\psi\overline{\psi} \equiv \tfrac{1}{2}\phi^2[(g_a\mathbb{I}+s_a\boldsymbol{\pi})\boldsymbol{\gamma}^a + e^{-i\beta\boldsymbol{\pi}}(\mathbb{I}-2g_a s_b\boldsymbol{\sigma}^{ab}\boldsymbol{\pi})], \tag{18}$$

which is valid in the most general case, and in terms of which it is possible to see that the spin-sum relationships are given by

$$\textstyle\sum_{\text{spin}} \psi\overline{\psi} \equiv \phi^2(g_a\boldsymbol{\gamma}^a + e^{-i\beta\boldsymbol{\pi}}), \tag{19}$$

where the sum is performed on all spin states [4].

By considering the polar form (12) and since in general

$$\boldsymbol{S}\partial_\mu\boldsymbol{S}^{-1} = i\partial_\mu\theta\mathbb{I} + \tfrac{1}{2}\partial_\mu\theta_{ij}\boldsymbol{\sigma}^{ij}, \tag{20}$$

where θ is a generic complex phase and $\theta_{ij} = -\theta_{ji}$ are the six parameters of the Lorentz group, we can define

$$\partial_\mu\theta_{ij} - \Omega_{ij\mu} \equiv R_{ij\mu}, \tag{21}$$
$$\partial_\mu\theta - qA_\mu \equiv P_\mu, \tag{22}$$

with the gauge potential qA_μ and the spin connection $\Omega_{ij\mu}$. Because equations (21,22) contain the same information than the gauge potential and the spin connection but are proven to be real tensors, they are called the gauge-invariant vector momentum and the tensorial connection. Writing the spinor field in polar form thus consists in re-arranging the components so as to isolate the real degrees of freedom from the components that can be transferred through the frame into the underlying space-time structure where they combine with the gauge potential and the connection leading to (22,21). Using those variables, the spin covariant derivative is given by

$$\boldsymbol{\nabla}_\mu\psi = (\nabla_\mu \ln\phi\mathbb{I} - \tfrac{i}{2}\nabla_\mu\beta\boldsymbol{\pi} - iP_\mu\mathbb{I} - \tfrac{1}{2}R_{ij\mu}\boldsymbol{\sigma}^{ij})\psi \tag{23}$$

in the most general case. We therefore have

$$\nabla_\mu s_i = R_{ji\mu} s^j, \tag{24}$$
$$\nabla_\mu g_i = R_{ji\mu} g^j, \tag{25}$$

as general identities on the velocity and spin. The Dirac spinor field equations are equivalently written according to

$$B_\mu - 2P^\iota g_{[\iota} s_{\mu]} + \nabla_\mu \beta + 2 s_\mu m \cos\beta = 0, \tag{26}$$
$$R_\mu - 2P^\rho g^\nu s^\alpha \varepsilon_{\mu\rho\nu\alpha} + 2 s_\mu m \sin\beta + \nabla_\mu \ln\phi^2 = 0, \tag{27}$$

where we have called $\frac{1}{2}\varepsilon_{\mu\alpha\nu\iota} R^{\alpha\nu\iota} = B_\mu$ and $R_{\mu a}{}^a = R_\mu$ for simplicity. The Dirac spinorial field equations are 8 real equations that, in polar form, are converted into 2 vector equations that specify all the space-time derivatives of the two real degrees of freedom. The angle β is the phase-shift between the chiral parts and, as such, it encodes the information about the mass term, as it has been discussed in [5].

One can also to prove that

$$R^i{}_{j\mu\nu} = -(\nabla_\mu R^i{}_{j\nu} - \nabla_\nu R^i{}_{j\mu} + R^i{}_{k\mu} R^k{}_{j\nu} - R^i{}_{k\nu} R^k{}_{j\mu}) \tag{28}$$
$$qF_{\mu\nu} = -(\nabla_\mu P_\nu - \nabla_\nu P_\mu), \tag{29}$$

leading to the Maxwell strength and Riemann curvature of the underlying gauge and space-time structures. A gauge-covariant type of electrodynamic information is therefore encoded in (22) while (21) encodes a covariant type of gravitational and inertial acceleration. From (28,29), one can see that the physical information is still the one that enters the strength and curvature, so that the non-zero solutions of equations

$$\nabla_\mu R^i{}_{j\nu} - \nabla_\nu R^i{}_{j\mu} + R^i{}_{k\mu} R^k{}_{j\nu} - R^i{}_{k\nu} R^k{}_{j\mu} = 0, \tag{30}$$
$$\nabla_\mu P_\nu - \nabla_\nu P_\mu = 0, \tag{31}$$

describe a covariant type of gauge potential and inertial acceleration that are not related to sources [6].

For electrodynamics such a strenghtless gauge potential is known to be related to the Aharonov-Bohm effect. A similar phenomenon is expected in the gravitational sector for the curvatureless covariant inertial acceleration [7].

Finally, one notices that by combining the Dirac equations in polar form (26,27) it is possible to establish a link between P_a and R_{ijk} as

$$P^\mu = m\cos\beta g^\mu - y_k s^{[k} g^{\mu]} - x_k s_j g_i \varepsilon^{kji\mu}, \tag{32}$$

having set $x_k = \frac{1}{2}(\nabla_k \ln\phi^2 + R_k)$ and $y_k = \frac{1}{2}(\nabla_k \beta + B_k)$ for the sake of simplifying the form of the expression. It should be noticed that these two terms are proportional to an interaction between the velocity and the spin. In fact, the angle β intervenes to change the length of the momentum while x_k and y_k intervene in concomitance with the spin to change the direction of the momentum [8].

In view of the QFT treatment, it is also important to establish the most complete form of the propagator for the spinor field. For this purpose, we write the Dirac spinor field equation in polar form (23) as

$$(F_k \boldsymbol{\gamma}^k + y_k \boldsymbol{\gamma}^k \boldsymbol{\pi} - m)\psi = 0, \tag{33}$$

where $F_k = P_k + i x_k$ in terms of the momentum. The propagator is hence the solution of the equation

$$(F_k \boldsymbol{\gamma}^k + y_k \boldsymbol{\gamma}^k \boldsymbol{\pi} - m) G = \mathbb{I}, \tag{34}$$

and is found to be given by

$$\begin{aligned} G = (|F^2 + y^2 + m^2|^2 - |2F\cdot y|^2 - 4F^2 m^2)^{-1} \\ \times [F_k \boldsymbol{\gamma}^k - y_k \boldsymbol{\gamma}^k \boldsymbol{\pi} - m] \\ \times [(F^2 + y^2 + m^2)\mathbb{I} + 2F\cdot y \boldsymbol{\pi} + 2mF_a \boldsymbol{\gamma}^a], \end{aligned} \tag{35}$$

as proven by a direct substitution.

We will have the opportunity to use this expression in the next sections when dealing with scattering processes. It is however also necessary to see how QFT happens to be recovered from this more general approach.

III. REDUCTION TO QFT

As mentioned in the introduction, the computations are carried out in QFT by considering plane-wave solutions of the fundamental equations. The implementation of this requirement is performed by using

$$i\boldsymbol{\nabla}_\mu \psi = P_\mu \psi, \tag{36}$$

which has to be compared with the general form (23). It is easy to see that

$$(\nabla_\mu \ln\phi \mathbb{I} - \tfrac{i}{2}\nabla_\mu \beta \boldsymbol{\pi} - \tfrac{1}{2} R_{ij\mu} \boldsymbol{\sigma}^{ij})\psi = 0, \tag{37}$$

which has to be true for any spinor field. Then, because $\boldsymbol{\sigma}^{ij}$, $\mathbb{I}$ and $\boldsymbol{\pi}$ are linearly independent we must have $R_{ij\mu} = 0$ with ϕ and β constant. Since a constant pseudo-scalar has to vanish we get that QFT essentially requires ϕ to be constant with β and $R_{ij\mu}$ equal to zero.

For the spin-sum relationships, and with the commonly used normalization $\phi^2 = m$, one would be led to

$$\textstyle\sum_{\text{spin}} \psi\overline{\psi} \equiv (P_a \boldsymbol{\gamma}^a + m\mathbb{I}), \tag{38}$$

in which we have used the fact that according to (32) we do have in this case

$$P^\mu = m g^\mu, \tag{39}$$

as widely used in QFT calculations. It should be however noticed that (39) cannot account for the full dynamical behavior of the Dirac spinor because its validity implies

the one of the Dirac spinor field equations. However a set of four conditions can not imply the validity of a system of eight equations in general. In this case, the lost information is the one involving the internal dynamics. In fact, if it were possible that $P^\mu = mg^\mu$ then any boost in the rest frame, which is always possible for a massive particle, would also mean a boost into the frame in which the non-relativistic limit is recovered exactly. As a consequence, for a massive particle, it would always be possible to have a non-relativistic description, which is not true. Thus, the proportionality between the velocity and the momentum cannot hold in general. In general, boosting to rest frame does not mean boosting to the frame in which the non-relativistic approximation is accurate because even in their rest frame particles still have an internal dynamics. It is solely when the internal dynamics is lost, by requiring the spin to vanich, that (32) can be approximated by (39), as we would have in QFT.

To conclude this section, we must show that the propagator found above indeed reduces to the propagator of QFT. The conditions for the restriction to QFT are, as we said, $R_{ij\mu} = 0$ with $\beta = 0$ and ϕ constant, which means $x_a = y_a = 0$. As, then, $F_k = P_k$ identically, the propagator reduces to

$$\begin{aligned} G &= (|P^2 + m^2|^2 - 4P^2m^2)^{-1} \\ &\times [P_k\boldsymbol{\gamma}^k - m][(P^2 + m^2)\mathbb{I} + 2mP_a\boldsymbol{\gamma}^a] \\ &\equiv (P^2 - m^2)^{-1}[P_k\boldsymbol{\gamma}^k + m\mathbb{I}], \end{aligned} \tag{40}$$

which is in fact the propagator of QFT exactly.

The conditions $R_{ij\mu} = 0$, $\beta = 0$ and $\nabla_\nu\phi = 0$ are therefore those implementing the reduction to QFT from the most general case, whether it is in terms of the covariant derivative of the spinor, the spin-sum relationships or the propagator.

The vanishing of the Yvon-Takabayashi angle and of the tensorial connection might appear as a reasonable assumption. Its validity however leads to a number of disturbing consequences. One is that under those hypotheses, the Dirac-Maxwell system of field equations has no solution [9].

That tensorial connection and Yvon-Takabayashi angle are quite generally different from zero is clear from the fact that they are non-zero in some remarkable situations such as those given by the integrable potentials associated with the hydrogen atom and the harmonic oscillator [7].

IV. SCATTERING PROCESSES

We now proceed to calculate the transition amplitude for the Bhabha and Compton scatterings.

A. Bhabha scattering

To begin with, we consider an electron-positron scattering, which is simpler since, in this case, the propagator is a photon and no correction is taken.

For this process, we focus on the two main usual Feynman diagrams. The matrix element is the sum

$$i\mathcal{M}_{fi} = i\mathcal{M}^s_{fi} + i\mathcal{M}^t_{fi}, \tag{41}$$

where s and t refer to the photon channels. We will compute the two channels separately, although calculations are analogous. The momenta of the particles are given by (32).

The calculation of the amplitude leads to

$$\begin{aligned} \mathcal{M}^s_{fi} &= \left[\overline{u(q_1)}(ie\gamma^\nu)v(q_2)\right]\left[\frac{\eta_{\mu\nu}}{s}\right]\left[\overline{v(p_2)}(ie\gamma^\mu)u(p_1)\right] \\ &= -\frac{e^2}{s}\overline{u(q_1)}\gamma_\mu v(q_2)\overline{v(p_2)}\gamma^\mu u(p_1), \end{aligned} \tag{42}$$

and to

$$\overline{\mathcal{M}^s_{fi}} = -\tfrac{e^2}{s}\overline{u(p_1)}\gamma^\nu v(p_2)\overline{v(q_2)}\gamma_\nu u(q_1), \tag{43}$$

as it is well known in QFT.

However, differently from what is done in standard QFT, we consider a more general spin-sum: for the particle u we have

$$\begin{aligned} &\textstyle\sum_{\text{spin}} u\overline{u} = \phi^2(g_a\boldsymbol{\gamma}^a + e^{-i\beta\boldsymbol{\pi}}) \\ &\approx \phi^2[\not{g} + \mathbb{I}(1-\beta^2/2) - i\beta\boldsymbol{\pi}], \end{aligned} \tag{44}$$

while for the antiparticle v with $v = \boldsymbol{\pi}u$ we have

$$\begin{aligned} &\textstyle\sum_{\text{spin}} v\overline{v} = \phi^2(g_a\boldsymbol{\gamma}^a - e^{-i\beta\boldsymbol{\pi}}) \\ &\approx \phi^2[\not{g} - \mathbb{I}(1-\beta^2/2) + i\beta\boldsymbol{\pi}], \end{aligned} \tag{45}$$

up to second order in β, which is the level of approximation we consider here.

From these spin-sums, we get the transition amplitudes

$$\begin{aligned} &\tfrac{1}{4}\textstyle\sum_{\text{spin}} |\mathcal{M}^s|^2 = \frac{e^4\phi^8}{s^2} \\ &\times \text{Tr}\Big[[\not{h}_1 + \mathbb{I}(1-\beta^2/2) - i\beta\boldsymbol{\pi}]\gamma_\mu \\ &\quad [\not{h}_2 - \mathbb{I}(1-\beta^2/2) + i\beta\boldsymbol{\pi}]\gamma_\nu\Big] \\ &\times \text{Tr}\Big[[\not{g}_2 - \mathbb{I}(1-\beta^2/2) + i\beta\boldsymbol{\pi}]\gamma^\mu \\ &\quad [\not{g}_1 + \mathbb{I}(1-\beta^2/2) - i\beta\boldsymbol{\pi}]\gamma^\nu\Big], \end{aligned} \tag{46}$$

and

$$\tfrac{1}{4}\sum_{\rm spin}|\mathcal{M}^t|^2=\tfrac{e^4\phi^8}{t^2}$$
$$\times{\rm Tr}\Big[[\not h_1+\mathbb{I}(1-\beta^2/2)-i\beta\boldsymbol{\pi}]\gamma_\mu$$
$$[\not g_1+\mathbb{I}(1-\beta^2/2)-i\beta\boldsymbol{\pi}]\gamma_\nu\Big]$$
$$\times{\rm Tr}\Big[[\not g_2-\mathbb{I}(1-\beta^2/2)+i\beta\boldsymbol{\pi}]\gamma^\mu$$
$$[\not h_2-\mathbb{I}(1-\beta^2/2)+i\beta\boldsymbol{\pi}]\gamma^\nu\Big], \tag{47}$$

with g and h the velocities associated with the momenta p and q respectively. It is easy to check that QFT results are recovered if we normalize $\phi^2=m$ with $p=mg$ and $q=mh$ with $\beta=0$. Calculating the traces shows that, up to a second-order correction, all β terms disappear and one is left with

$$\frac{1}{4}\sum_{\rm spin}|\mathcal{M}^s|^2=\frac{8e^4\phi^8}{s^2}\Big[(g_2\cdot h_1)(g_1\cdot h_2)$$
$$+(g_2\cdot h_2)(g_1\cdot h_1)+(g_1\cdot g_2)+(h_1\cdot h_2)+2\Big], \tag{48}$$

and

$$\frac{1}{4}\sum_{\rm spin}|\mathcal{M}^t|^2=\frac{8e^4\phi^8}{t^2}\Big[(g_2\cdot h_1)(g_1\cdot h_2)$$
$$+(g_2\cdot h_2)(g_1\cdot h_1)-(h_1\cdot g_1)-(h_2\cdot g_2)+2\Big], \tag{49}$$

showing no difference with respect to the result of standard QFT. We have also explicitly checked that this remains true for the interference term.

B. Compton scattering

We now move to the Compton scattering. This process is more complicated because it involves the evaluation of traces that contain the propagator of the fermion which, in our case, are given by intricate expressions. The generalization appears through corrections in the Yvon-Takabayashi angle. We consider an incident photon with momentum k^a and an electron in a hydrogen potentiel with momentum p^a given by (32). The final particles are a photon with k'^a and an electron with p'^a.

We still consider the two usual main Feynman diagrams. The matrix element in the s-channel is given by

$$\tfrac{1}{4}\textstyle\sum_{\rm spin}|\mathcal{M}^s|^2=\tfrac{e^4}{4}{\rm Tr}\Big[S(p')\gamma^\nu G(q)\gamma^\mu S(p)\gamma_\mu\overline{G(q)}\gamma_\nu\Big] \tag{50}$$

as it is well known with $q=p+k$.

For the spin-sums we take first-order corrections

$$S(p)=\phi^2\Big(\not g+\mathbb{I}-i\beta\boldsymbol{\pi}\Big), \tag{51}$$

and

$$S(p')=\phi'^2\Big(\not g'+\mathbb{I}-i\beta'\boldsymbol{\pi}\Big)=m\not g'+m\mathbb{I} \tag{52}$$

since β' is the Yvon-Takabayashi angle of the scattered electron, which can be considered as free. For β, one has to consider the Yvon-Takabayashi angle of the electron orbiting the nucleus, which is given in spherical coordinates by

$$\beta=-\arctan\Big(\frac{\alpha}{\Gamma}\cos\theta\Big), \tag{53}$$

with α the fine-structure constant and $\Gamma=\sqrt{1-\alpha^2}$ for hydrogen-like atoms. The values of the modules are given by $\phi'^2=m$ and

$$\phi=\sqrt{m}r^{\Gamma-1}e^{-\alpha mr}/\sqrt{\Delta} \tag{54}$$

with $\Delta(\theta)=(1-|\alpha\sin\theta|^2)^{-\frac{1}{2}}$ a function of the elevation angle, as it has been found in reference [6]. It is quite an interesting fact that β, $\ln\phi$ and their derivatives are of the same order than the fine-structure constant.

The propagators are given by (35) and the first-order truncation leads to

$$G(q)\approx(q^2-m^2+4q\cdot xi)^{-1}$$
$$\times\Big[W\mathbb{I}+X_a\boldsymbol{\gamma}^a+Y_a\boldsymbol{\gamma}^a\boldsymbol{\pi}+Z_{ab}\boldsymbol{\sigma}^{ab}\boldsymbol{\pi}\Big], \tag{55}$$

with

$$W=m+\frac{2im(x\cdot q)}{q^2-m^2}, \tag{56}$$
$$X_a=q_a+ix_a+\frac{2i(x\cdot q)}{q^2-m^2}q_a, \tag{57}$$
$$Y_a=\frac{1}{q^2-m^2}[-(q^2+m^2)y_a+2(y\cdot q)q_a], \tag{58}$$
$$Z_{ab}=\frac{4m}{q^2-m^2}y_aq_b. \tag{59}$$

It is worth noticing that starting from our general expressions and taking the first-order perturbative expansion, we obtain the imaginary term $4q\cdot xi$ in the denominator of the scalar factor without the necessity to postulate it as done in QFT. This term is needed to remove the poles and it is naturally present in the most general formalism used here.

At first-order in x, y, and β we have

$$W(q)W^*(q)=m^2, \tag{60}$$
$$X(q)X^*(q)=q^2, \tag{61}$$
$$W(q)X_a^*(q)+W^*(q)X_a(q)=2mq_a, \tag{62}$$
$$W(q)X_a^*(q)-W^*(q)X_a(q)=-2imx_a, \tag{63}$$

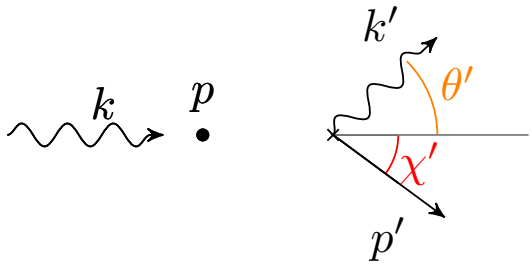

Figure 1: Compton scattering in the lab frame.

so that

$$\frac{1}{4}\sum_{\text{spin}}|\mathcal{M}^s|^2 = \frac{4\phi^2 m e^4}{(q^2-m^2)^2} \times\Big[4m^2+4q^2-4m(g\cdot q)-q^2(g\cdot g') -4m(g'\cdot q)+m^2(g\cdot g')+2(g\cdot q)(g'\cdot q)\Big] \quad (64)$$

for the s-channel.

For the u-channel, calculations are analogous and give

$$\frac{1}{4}\sum_{\text{spin}}|\mathcal{M}^u|^2 = \frac{4\phi^2 m e^4}{(f^2-m^2)^2} \times\Big[4m^2+4f^2-4m(g\cdot f)-f^2(g\cdot g') -4m(g'\cdot f)+m^2(g\cdot g')+2(g\cdot f)(g'\cdot f)\Big], \quad (65)$$

as it is easy to check, with $f = p - k'$.

For the interference term, we obtain

$$\frac{1}{4}\sum_{\text{spin}}\Re(\mathcal{M}^s\overline{\mathcal{M}^u}) = \frac{4\phi^2 m e^4}{(f^2-m^2)}\frac{1}{(q^2-m^2)} \times\Big[-2m^2+m^2(g\cdot g')+ +m(q+f)\cdot(g+g')+(q\cdot f)(1-2(g\cdot g'))\Big].$$

At this order, it should be noticed that the physical changes are not due to the new propagator but to the presence of the hydrogen potential, which is naturally accounted for in this framework.

To compute the cross section we pick the lab frame as in Fig. 1. The photon has momentum $k^a = (\omega, 0, 0, \omega)$ and the electron is such that, in Lorentz indices, it reads

$$\begin{pmatrix} p^0 \\ p^1 \\ p^2 \\ p^3 \end{pmatrix} = \begin{pmatrix} m+\frac{\alpha}{r} \\ -\sin\varphi/(2r\sin\theta) \\ \cos\ \varphi/(2r\sin\theta) \\ 0 \end{pmatrix}. \quad (66)$$

To recover the free case, as in QFT, one should consider $\alpha \to 0$ and $r \to +\infty$. At first order in α, we have $p^2 = m^2 + 2m\alpha/r - 1/(2r\sin\theta)^2$. The term $2m\alpha/r$ is due to the potential energy of the hydrogen atom, while the term $1/(2r\sin\theta)^2$ is due to the kinetic energy generated by the interaction with the hydrogen nucleus.

For the outgoing particles, the photon momentum is $k'^a = (\omega', \omega'\sin\theta', 0, \omega'\cos\theta')$ and a free electron has $p'^2 = m^2$.

The cross section is

$$d\sigma = \frac{1}{2\omega}\frac{1}{2(m+\alpha/r)}d\Phi_2|M(\{k,p\}\to\{k',p'\}|^2, \quad (67)$$

as easily shown by textbook calculations [10].

The explicit expression of $d\Phi_2$ is obtained using

$$\begin{aligned}\int\frac{d^3p'}{2E_p} &= \int d^3p'dp'_0\delta(p_0'^2-E_p^2)\Theta(p'_0)\\ &= \int d^3p'dp'_0\delta(p_0'^2-p'^2-\vec{p'}^2)\Theta(p'_0)\\ &= \int d^3p'dp'_0\delta(p'_ap'^a-p'^2)\Theta(p'_0), \end{aligned} \quad (68)$$

so that

$$\begin{aligned}\int d\Phi_2 =& \frac{1}{(2\pi)^2}\int\frac{d^3p'}{2E_{p'}}\frac{d^3k'}{2\omega'}\delta^{(4)}(k'+p'-k-p) && (69)\\ =& \frac{1}{(2\pi)^2}\int\frac{d^3k'}{2\omega'}\delta((p+k-k')^2-m^2) && (70)\\ & \Theta(\omega+E_p-\omega')\\ =& \frac{1}{2(2\pi)^2}\int\omega'd\omega'd\Omega\delta\Big(2m\alpha/r\\ & -1/(2r\sin\theta)^2+2\omega(m+\alpha/r)\\ & -\omega'[2(m+\alpha/r)+2(1-\cos\theta')\omega\\ & +\frac{\sin\varphi\sin\theta'}{r\sin\theta}]\Big)\\ =& \frac{1}{4\pi}\int d\cos\theta' && (71)\\ & \times\frac{\omega'^2}{2m\alpha/r-1/(2r\sin\theta)^2+2\omega(m+\alpha/r)}, \end{aligned}$$

and eventually

$$\frac{d\sigma}{d\cos\theta'} = \frac{1}{2\omega}\frac{1}{2(m+\alpha/r)}\mid M(\{k,p\}\to\{k',p'\})\mid^2 \times\frac{1}{4\pi}\frac{\omega'^2}{2m\alpha/r-1/(2r\sin\theta)^2+2\omega(m+\alpha/r)}, \quad (72)$$

where $|M|$ is the only unknown.

To evaluate $|M|$, the scalar products have to be explicitly performed. In [6], the velocity of the initial electron

is given in Lorentz indices. As we keep only the first order in α we have,

$$\begin{pmatrix} g^0 \\ g^1 \\ g^2 \\ g^3 \end{pmatrix} = \begin{pmatrix} 1 \\ -\alpha \sin\theta \sin\varphi \\ \alpha \sin\theta \cos\varphi \\ 0 \end{pmatrix}. \tag{73}$$

The total momentum $q^a = p^a + k^a$ is

$$\begin{pmatrix} q^0 \\ q^1 \\ q^2 \\ q^3 \end{pmatrix} = \begin{pmatrix} m + \frac{\alpha}{2r} + \omega \\ -\sin\varphi/(2r\sin\theta) \\ \cos\ \varphi/(2r\sin\theta) \\ \omega \end{pmatrix}. \tag{74}$$

Defining $Y \equiv \cos\theta'$ and considering the limit $r \to \infty$, we obtain:

$$\begin{aligned} \frac{d\sigma}{dY} = \frac{\pi\alpha^2}{m\omega(m+\omega-Y\omega)^3}\Big[& m^2(1+Y^2)\omega \\ & -m(Y-1)(1+Y^2)\omega^2 + (Y-1)^2\omega^3 \\ & +\sqrt{1-Y^2}\alpha\sin\theta\sin\varphi \\ \times\Big(& m^3 + m^2(3-2Y)\omega + m(Y-1)^2\omega^2\Big)\Big]. \end{aligned} \tag{75}$$

When α tends to zero, we find back the usual QFT result. However, in general, the result is different, as a consequence of the interaction. That is, individually, if one photon hits an electron within the hydrogen potential, the probability of diffusion depends on where the electron is (through the θ and φ dependance). In an hydrogen-like potential, β is indeed non-vanishing and describes an internal dynamics between the left and the right parts of the electron. This breaks down the spherical symmetry. If, however, we assume a statistical phenomenon – as implicitly done here –, the situation is different. For example, the spin-sum relationships that were used in (19) are statistical in nature. In this case, one needs to average the cross section (75) over θ and φ. The interaction term then cancels which, quite hopefully, leads to the usual result. Statistically, there is therefore no correction term at the first order in α that appears because of the electron-proton interaction.

V. CONCLUSION

The first result of this study is the derivation of the expression of the propagator for a fermion. The expression obtained is more general than the one of QFT. It is interesting to notice that, in this generalized approach, a "small" imaginary term elegantly appears in the denominator. In QFT, one has to put it by hand to carry out the calculations. Then, we have seen that in the Bhabha scattering case, the transition amplitude terms appear to be the same than in ordinary QFT. Even if some β^2 terms are cnosidered, they do compensate each other. In the case of the Compton scattering, considering only the first order, we observe that the cross section is modified by the derivative of the amplitude and the phase shift of the spinor. There are some corrections at first order in α, the fine structure constant. It is worth underlining that, considering the most general description of a spinor with ϕ, β and their derivatives, the α-correction appears even when considering only the lowest order in Feynman diagrams. This is different from the standard QFT corrections in α that are present in the g-factor once loops are added to the diagrams. However, the α corrections we get, due to the interaction, do cancel under the averaging procedure. It is important to mention that in this more general formalism, one can in principle describe fields in interaction, which is not possible in QFT as the plane wave approximation suppresses β, x and y. As a result, we have shown that the non-zero β of the initial electron breaks down the symmetry. Consequently, the diffusion probability for a single event in principle depends on the electron localisation in the hydrogen potential. However, statistically, the interaction term cancels and one finds back the QFT result. In a way, this provide an explanation of the reason why considering free fields is such a good approximation. One could possibly investigate if this results should lead to a widening of the experimentally measured distributions but this remains beyond the scope of this work.

[1] R.F.Streater, A.S.Wightman, "PCT, Spin and Statistics, and All That", Princeton (2014).
[2] R.Haag, "On quantum field theories", *Mat. Fys. Med.* **29**, 12 (1995).
[3] L.Fabbri, "A generally-relativistic gauge classification of the Dirac fields", *Int.J.Geom.Meth.Mod.Phys.***13**,1650078(2016).
[4] L.Fabbri, "General Dynamics of Spinors", *Adv. Appl. Clifford Algebras* **27**, 2901 (2017).
[5] L.Fabbri, "Torsion Gravity for Dirac Fields", *Int.J.Geom.Meth.Mod.Phys.***14**,1750037(2017).
[6] L.Fabbri, "Covariant inertial forces for spinors", *Eur.J.Phys.C***78**, 783 (2018).
[7] L. Fabbri, F. Moulin, A. Barrau, "Non-trivial effects of sourceless forces for spinors: toward an Aharonov-Bohm gravitational effect?", *Eur.Phys.J.C***79**, 875 (2019).
[8] L.Fabbri, "Geometry, Zitterbewegung, Quantization", *Int.J.Geom.Meth.Mod.Phys.***16**, 1950146 (2019).

[9] L.Fabbri, R.da Rocha, "Non-existence of rest-frame spin-eigenstate spinors in their own electrodynamics", *Eur.Phys.J.C***78**, 363 (2018).

[10] M.E.Peskin, D.V.Schroeder, "An introduction to quantum field theory" (Perseus Books).

4.5 Conclusion sur le formalisme polaire

La mécanique quantique révèle la dualité onde-corpuscule des particules. En pratique, dans le cadre de la TQC, l'aspect ondulatoire est décrit par l'approximation de l'onde plane et l'aspect corpusculaire par l'approximation de la particule ponctuelle. En réalité, nous savons que l'onde n'est pas délocalisée jusqu'à l'infini spatial et qu'à partir d'une certaine distance la particule ne peut pas être considérée comme un point. Le formalisme polaire permet de décrire les particules sans utiliser ces deux approximations. En effet, on pu voir dans la section 4.3, que pour des potentiels de Coulomb et d'oscillateur harmonique, il existe des solutions à l'équation de Dirac décrites par une amplitude non constante. L'amplitude diminue avec r et, pour l'oscillateur harmonique, on a également une brisure de symétrie sphérique. Ainsi le gradient $\nabla_r \phi$ permet de décrire une particule qui n'est pas étalée sur l'infini spatial mais localisée. De plus, une particule n'est pas ponctuelle et possède une structure interne. Grâce au formalisme polaire on a pu décrire la dynamique interne des spineurs. En effet, à l'intérieur du spineur, il y a une interaction entre ses parties droite et gauche qui est décrite par l'angle β. Cette dynamique diminue lorsqu'on s'éloigne du centre de la particule. Pour conclure, ce formalisme offre une excellente description des spineurs en utilisant pour unique hypothèse la validité de l'équation de Dirac.

Conclusion

La gravité quantique a longtemps été considérée comme une chimère qui ne pourrait pas être sondée par des expériences. Il existe différents modèles pour décrire la gravité quantique. Les travaux théoriques actuels sont assez élaborés pour permettre d'ores et déjà d'étudier certains aspects phénoménologiques associés à la gravité quantique. Dans ce manuscrit nous avons étudié principalement la LQG et ses propriétés associées à la cosmologie et aux trous noirs.

En LQC, nous avons vu que l'univers en contraction permet de prédire une distribution de probabilité sur la durée de l'inflation. Cette distribution réduit considérablement la fenêtre sur le nombre d'e-folds. Cette dernière est piquée aux alentours de 145 e-folds et se trouve donc proche mais au dessus de la limite minimale qui est de 60 e-folds. La perspective d'un univers en contraction avant le rebond ouvre également la possibilité de détecter des signaux pré-rebond. Nous avons étudié le comportement de la distance de luminosité dans un univers en contraction. Il est intéressant de noter que, en fonction du contenu en matière, la luminosité d'un signal peut augmenter avec l'intervalle de temps entre l'émission et la réception. Ainsi, malgré une amplitude fortement diminuée par l'expansion de l'univers actuel, des ondes gravitationnelles pré-rebond pourraient tout de même avoir des amplitudes raisonnables. Enfin, nous avons pu observer que la LQC prédit des spectres de puissances différents de ceux du modèle standard de la cosmologie. Dans le cadre de la LQC, la façon de choisir les conditions initiales est plus ambigüe car plusieurs instants peuvent être approximés par un vide de Bunch-Davies. Cependant, on a pu voir que, pour les perturbations scalaires, les différents instants impliquent des spectres de puissance similaires.

Nous avons étudié différents aspects associés aux trous noirs. Lorsqu'on prend en compte les effets quantiques, un trou noir qui atteint une densité importante pourrait transiter vers un état de trou blanc, par effet tunnel. Le signal émis par ces derniers dépend du contenu, de quand et comment ils ont été formés. Étant donné que le temps de rebond est long, nous nous sommes intéressés aux trous noirs primordiaux. Pour différents spectres de masse initiaux, nous avons pu voir comment le flux varie avec l'énergie. On observe que dans certains cas, un signal est émis dans l'échelle d'énergie des sursauts radio rapides et ce signal se distingue des autres sources possibles de part sa dépendance en redshift. Un autre article concerne la sections efficace associée au rayonnement de Hawking. On a considéré un modèle de trou noir qui s'inspire des travaux de la LQG. Ce modèle décrit un trou noir proche de celui Schwarzschild, qui prend en compte la discrétisation de l'espace et l'existence d'une aire minimale. L'échelle de discrétisation tend à diminuer la section efficace. Les effets sont d'autant plus grand que la discrétisation est ressentie à plus grande échelle. Ensuite, j'ai étudié la propriétés d'isospectralité. Les perturbations des trous noirs classiques (Schwarzschild, Reissner-Nordström, Kerr) sont isospectrales. Pour d'autres types de trous noirs, des travaux numériques ont été effectués. J'ai repris la preuve analytique de Chandrasekhar pour voir si l'isospectralité pouvait s'appliquer

à des cas plus généraux. Il se trouve que pour des trous noirs sans charge ni moment cinétique, la preuve s'étend aux trous noirs de Schwarzschild-de Sitter et Schwarzschild-Anti de Sitter. Par la suite, j'ai étudié comment la valeur de QNMs varie en fonction des différents modèles au delà de la RG. Leurs valeurs a été calculées pour les modèles de gravité massive, de gravité scalaire-tenseur-vecteur, de gravité de Hořava-Lifshitz, un modèle avec une correction en $\hbar$ et un modèle de trous noirs type LQG. En comparant ces valeurs à celles d'un trou noir de Schwarzschild on observe la prédiction de fréquences plus élévées ou plus faibles en fonction du modèle considéré. Cela ouvre une fenêtre vers la discrimination de certaines théories lorsqu'expérimentalement les QNMs seront mesurés avec plus de précision. Nous avons étudié un modèle jouet plus particulièrement. Ce dernier tente de dépeindre les effets quantiques qui pourraient apparaître en dehors de l'horizon, après une accumulation dans le temps. La différence relative par rapport aux trous noirs de Schwarzschild est d'autant plus élevée lorsque les effets quantiques se trouvent proche de la sphère de photon. Ces effets quantiques pourraient être observés pour des trous noirs de masse bien plus élevée que celle de Planck. Enfin, nous avons investigué la possibilité que les origines de la matière noire actuelle soient des reliques de trous noirs microscopiques, formés par la collision de particules trans-Planckiennes. Si l'échelle d'énergie de l'inflation est suffisamment élevée, la densité de reliques peut rendre compte de la quantité de matière noire.

Enfin j'ai étudié le formalisme polaire qui permet de décrire la dynamique des spineurs. En utilisant les six dégrées de liberté associés aux transformations de Lorentz, nous pouvons décrire les spineurs dans un référentiel où seulement deux dégrées résiduels persistent. Ce sont leur vrais degrés de liberté car ce sont des scalaires et ils ne peuvent pas être effacés par des transformations. On a alors l'amplitude ϕ et l'angle d'Yvon-Takabayashi β ainsi que leur dérivée. Nous avons étudié le cas des spineurs de Dirac et montré que sous un potentiel de Coulomb ou d'oscillateur harmonique, ϕ n'est pas constant et β n'est pas nul contrairement aux hypothèse de la TQC. Certains coefficients de la connexion tensorielle $R_{ij\mu}$ sont également non nuls et cela permet de décrire l'effet Aharonov-Bohm gravitationnel. Nous avons également utilisé ce formalisme pour décrire la section efficace Compton dans le cadre d'un électron en interaction avec un proton. On a pu observer, que contrairement à la TQC, ce formalisme était apte à décrire des sections efficaces pour des champs non libres. Le calcul de l'expression du propagateur fermionique permet de montrer que l'astuce mathématique de TQC qui consiste à ajouter un terme imaginaire au dénominateur apparaît ici naturellement. L'angle β qui traduit un déphasage entre la partie droite et gauche du spineur décrit une dynamique interne. Du fait de cette dernière, la probabilité d'interaction avec un électron sous un potentiel de Coulomb dépend de sa position, la symétrie sphérique est brisée. Cependant d'un point de vue statistique, la section efficace sera la même que celle calculée en TQC.

Perspectives

Un des points importants pour l'étude des perturbations primordiales en cosmologie concerne la durée de l'inflation. En effet le spectre de puissance est très différents en fonction de la fenêtre du nombre d'onde considérée. L'étude qu'on a effectué sur la LQC apporte une prédiction probabiliste sur sa durée et l'étude de la distance de luminosité ouvre la perspective d'observer des traces de la période pré-rebond. Cependant dans les deux cas nous avons négligé les conséquences dues au rebond où les effets de gravité quantique sont les plus importants. Le rebond pourrait complètement changer les grandeurs physiques qui le traversent et l'approximation de coller deux solutions classiques

pourrait être une mauvaise approximation. Cependant, à ce jour les connaissances sur la gravité quantique ne sont pas apte à décrire le rebond de façon rigoureuse. D'un point de vue expérimental, beaucoup d'espoir se portent vers la mesures des spectres de puissance. La connaissances du spectre des perturbations tensorielle pourrait clairement réduire le nombre de théories plausible. Cette mesure pourrait être effectuée dans les prochaines décennies. Pour l'étude des perturbations il serait intéressant de prendre en compte des relation de dispersion modifiées pour les effets transplanckiens.

Les études sur la phénoménologie des trous noirs en rebond restent préliminaires. En effet, le temps de rebond proportionnel à la masse au carré du trous noirs a été déterminé par analyse dimensionnelle et plus tard, des articles ont argumenté que le trou blanc pourrait émettre des signaux par oscillations sur des période proportionnelles à la masse. Il serait intéressant de faire une étude prenant en compte les différents paramètres du modèle : le temps de vie, le facteur de proportionnalité de ce dernier ainsi que les rebonds à grandes distances. De plus, le modèle de trou noir en rebond admis actuellement possède au contraire une probabilité de transition en $\exp\left(-M^2\right)$, ainsi il serait intéressant d'étudier la phénoménologie associée à ce modèle. Pour l'étude de la section efficace des trous noirs quantiques à boucles, on pourrait étudier d'autres modèles provenant de la théorie mère. Il serait également intéressant d'étudier la propagation des champs électromagnétiques. Concernant l'étude des QNMs, l'isospectralité incluse, la prochaine étape sera d'étudier le cas des trous noirs en rotation.

Dans le cadre du formalisme polaire, les termes de la connexion tensorielle manquent encore d'interprétation. Certains impliqueraient la localisation de la particule. Nous avons pu voir aussi que d'autres seraient responsables de l'effet Aharonov-Bohm gravitationnel. Il serait pertinent de calculer la section efficace d'autres processus que la diffusion Bhabha et Compton. Nous pourrions également aller plus loin en étudiant le cas des corrections quantiques avec une ou plusieurs boucles. Un autre point qu'il serait important d'étudier serait de considérer la probabilité de diffusion dans le cas d'un unique évènement. Comme nous l'avons vu des différences entre la TQC et le formalisme polaire pourraient apparaître. Cependant dans notre étude nous avons considéré un moyennage sur les spins ainsi, il serait intéressant de ne pas utiliser cette hypothèse statistique dans le calcul des sections efficaces.

Bibliographie

[1] Michele Maggiore. *A Modern introduction to quantum field theory*. 9 2005.

[2] Jean-Nouchs. An introduction to symmetries and quantum field theory, 2017.

[3] Robert M. Wald. *General Relativity*. Chicago Univ. Pr., Chicago, USA, 1984.

[4] S. Chandrasekhar. The mathematical theory of black holes. 1998.

[5] Rodilofo Gambini and Jorge Pullin. *A First Course in Loop Quantum Gravity*. 2011. ISBN-10 :0199590753.

[6] Michael E. Peskin and Daniel V. Schroeder. *An Introduction to quantum field theory*. Addison-Wesley, Reading, USA, 1995.

[7] Jme Martin, Christophe Ringeval, Roberto Trotta, and Vincent Vennin. The Best Inflationary Models After Planck. *JCAP*, 03 :039, 2014.

[8] C Rovelli and P Martin-Dussaud. Interior metric and ray-tracing map in the firework black-to-white hole transition. *Classical and Quantum Gravity*, 35(14) :147002, jun 2018.

[9] W.G. Unruh. Notes on black hole evaporation. *Phys. Rev. D*, 14 :870, 1976.

[10] S.W. Hawking. Particle Creation by Black Holes. *Commun. Math. Phys.*, 43 :199–220, 1975. [Erratum : Commun.Math.Phys. 46, 206 (1976)].

[11] Carlo Rovelli and Francesca Vidotto. *Covariant Loop Quantum Gravity*. Cambridge University Press, 2014. ISBN :9781107069626.

[12] Ivan Agullo and Alejandro Corichi. *Loop Quantum Cosmology*, pages 809–839. 2014.

[13] Ivan Agullo and Parampreet Singh. *Loop Quantum Cosmology*, pages 183–240. WSP, 2017.

[14] Martin Bojowald. *Canonical Gravity and ApplicationsCosmology, Black Holes, and Quantum Gravity*. Cambridge University Press, 12 2010.

[15] Abhay Ashtekar, Alejandro Corichi, and Parampreet Singh. Robustness of key features of loop quantum cosmology. *Phys. Rev. D*, 77 :024046, 2008.

[16] Peter Diener, Brajesh Gupt, and Parampreet Singh. Numerical simulations of a loop quantum cosmos : robustness of the quantum bounce and the validity of effective dynamics. *Class. Quant. Grav.*, 31 :105015, 2014.

[17] D. Langlois. Lectures on inflation and cosmological perturbations. *Lect. Notes Phys.*, 800 :1–57, 2010.

[18] G. W. Gibbons and Neil Turok. The Measure Problem in Cosmology. *Phys. Rev.*, D77 :063516, 2008.

[19] Linda Linsefors and Aurelien Barrau. Duration of inflation and conditions at the bounce as a prediction of effective isotropic loop quantum cosmology. *Phys. Rev. D*, 87 :123509, Jun 2013.

[20] Linda Linsefors and Aurelien Barrau. Exhaustive investigation of the duration of inflation in effective anisotropic loop quantum cosmology. *Classical and Quantum Gravity*, 32(3) :035010, jan 2015.

[21] Boris Bolliet, Auren Barrau, Killian Martineau, and Flora Moulin. Some Clarifications on the Duration of Inflation in Loop Quantum Cosmology. *Class. Quant. Grav.*, 34(14) :145003, 2017.

[22] James M. Bardeen. Gauge-invariant cosmological perturbations. *Phys. Rev. D*, 22 :1882–1905, Oct 1980.

[23] Ivan Agullo, Abhay Ashtekar, and William Nelson. A Quantum Gravity Extension of the Inflationary Scenario. *Phys. Rev. Lett.*, 109 :251301, 2012.

[24] Ivan Agullo, Abhay Ashtekar, and William Nelson. The pre-inflationary dynamics of loop quantum cosmology : Confronting quantum gravity with observations. *Class. Quant. Grav.*, 30 :085014, 2013.

[25] Ivan Agullo, Abhay Ashtekar, and William Nelson. Extension of the quantum theory of cosmological perturbations to the planck era. *Phys. Rev. D*, 87 :043507, Feb 2013.

[26] Martin Bojowald. Non-covariance of the dressed-metric approach in loop quantum cosmology. 2 2020.

[27] Martin Bojowald, Hector H. Hernandez, Mikhail Kagan, Parampreet Singh, and Aureliano Skirzewski. Hamiltonian cosmological perturbation theory with loop quantum gravity corrections. *Phys. Rev. D*, 74 :123512, 2006.

[28] Martin Bojowald, Golam Mortuza Hossain, Mikhail Kagan, and S. Shankaranarayanan. Anomaly freedom in perturbative loop quantum gravity. *Phys. Rev. D*, 78 :063547, Sep 2008.

[29] Martin Bojowald, Golam Mortuza Hossain, Mikhail Kagan, and S. Shankaranarayanan. Gauge invariant cosmological perturbation equations with corrections from loop quantum gravity. *Phys. Rev. D*, 79 :043505, Feb 2009.

[30] Thomas Cailleteau and Aurelien Barrau. Gauge invariance in Loop Quantum Cosmology : Hamilton-Jacobi and Mukhanov-Sasaki equations for scalar perturbations. *Phys. Rev. D*, 85 :123534, 2012.

[31] Thomas Cailleteau, Jakub Mielczarek, Aurelien Barrau, and Julien Grain. Anomaly-free scalar perturbations with holonomy corrections in loop quantum cosmology. *Class. Quant. Grav.*, 29 :095010, 2012.

[32] Thomas Cailleteau, Aurelien Barrau, Julien Grain, and Francesca Vidotto. Consistency of holonomy-corrected scalar, vector and tensor perturbations in Loop Quantum Cosmology. *Phys. Rev. D*, 86 :087301, 2012.

[33] Thomas Cailleteau, Linda Linsefors, and Aurelien Barrau. Anomaly-free perturbations with inverse-volume and holonomy corrections in Loop Quantum Cosmology. *Class. Quant. Grav.*, 31 :125011, 2014.

[34] Martin Bojowald and Jakub Mielczarek. Some implications of signature-change in cosmological models of loop quantum gravity. *Journal of Cosmology and Astroparticle Physics*, 2015(08) :052–052, aug 2015.

[35] Auren Barrau, Pierre Jamet, Killian Martineau, and Flora Moulin. Scalar spectra of primordial perturbations in loop quantum cosmology. *Phys. Rev. D*, 98(8) :086003, 2018.

[36] Roger Penrose. The basic ideas of conformal cyclic cosmology. *AIP Conf. Proc.*, 1446(1) :233–243, 2012.

[37] Robert H. Brandenberger. The Matter Bounce Alternative to Inflationary Cosmology. 6 2012.

[38] Auren Barrau, Killian Martineau, and Flora Moulin. Seeing through the cosmological bounce : Footprints of the contracting phase and luminosity distance in bouncing models. *Phys. Rev. D*, 96(12) :123520, 2017.

[39] Carlo Rovelli and Francesca Vidotto. Planck stars. *Int. J. Mod. Phys.*, D23(12) :1442026, 2014.

[40] Tommaso De Lorenzo, Costantino Pacilio, Carlo Rovelli, and Simone Speziale. On the Effective Metric of a Planck Star. *Gen. Rel. Grav.*, 47(4) :41, 2015.

[41] Hal M. Haggard and Carlo Rovelli. Quantum-gravity effects outside the horizon spark black to white hole tunneling. *Phys. Rev.*, D92(10) :104020, 2015.

[42] Tommaso De Lorenzo and Alejandro Perez. Improved Black Hole Fireworks : Asymmetric Black-Hole-to-White-Hole Tunneling Scenario. 2015.

[43] Marios Christodoulou, Carlo Rovelli, Simone Speziale, and Ilya Vilensky. Planck star tunneling time : An astrophysically relevant observable from background-free quantum gravity. *Phys. Rev. D*, 94(8) :084035, 2016.

[44] Aurélien Barrau and Carlo Rovelli. Planck star phenomenology. *Phys. Lett.*, B739 :405–409, 2014.

[45] Aurélien Barrau, Carlo Rovelli, and Francesca Vidotto. Fast Radio Bursts and White Hole Signals. *Phys. Rev.*, D90(12) :127503, 2014.

[46] Aurélien Barrau, Boris Bolliet, Francesca Vidotto, and Celine Weimer. Phenomenology of bouncing black holes in quantum gravity : a closer look. *JCAP*, 1602(02) :022, 2016.

[47] Bernard Carr, Kazunori Kohri, Yuuiti Sendouda, and Jun'ichi Yokoyama. Constraints on Primordial Black Holes. 2 2020.

[48] Auren Barrau, Boris Bolliet, Marrit Schutten, and Francesca Vidotto. Bouncing black holes in quantum gravity and the Fermi gamma-ray excess. *Phys. Lett. B*, 772 :58–62, 2017.

[49] Auren Barrau, Flora Moulin, and Killian Martineau. Fast radio bursts and the stochastic lifetime of black holes in quantum gravity. *Phys. Rev. D*, 97(6) :066019, 2018.

[50] Ted Jacobson. Introduction to quantum fields in curved space-time and the Hawking effect. In *School on Quantum Gravity*, pages 39–89, 8 2003.

[51] W. G. Unruh. Origin of the particles in black-hole evaporation. *Phys. Rev. D*, 15 :365–369, Jan 1977.

[52] Leonardo Modesto. Semiclassical loop quantum black hole. *Int. J. Theor. Phys.*, 49 :1649–1683, 2010.

[53] Emanuele Alesci and Leonardo Modesto. Particle Creation by Loop Black Holes. *Gen. Rel. Grav.*, 46 :1656, 2014.

[54] Flora Moulin, Killian Martineau, Julien Grain, and Auren Barrau. Quantum fields in the background spacetime of a polymeric loop black hole. *Class. Quant. Grav.*, 36(12) :125003, 2019.

[55] Kostas D. Kokkotas and Bernd G. Schmidt. Quasinormal modes of stars and black holes. *Living Rev. Rel.*, 2 :2, 1999.

[56] R.A. Konoplya and A. Zhidenko. Quasinormal modes of black holes : From astrophysics to string theory. *Rev. Mod. Phys.*, 83 :793–836, 2011.

[57] Carl M. Bender and Steven A. Orszag. *Advanced Mathematical Methods for Scientists and Engineers*. Springer, 1 1999.

[58] Bernard F. Schutz and Clifford M. Will. BLACK HOLE NORMAL MODES : A SEMIANALYTIC APPROACH. *Astrophys. J. Lett.*, 291 :L33–L36, 1985.

[59] Sai Iyer and Clifford M. Will. Black Hole Normal Modes : A WKB Approach. 1. Foundations and Application of a Higher Order WKB Analysis of Potential Barrier Scattering. *Phys. Rev. D*, 35 :3621, 1987.

[60] Sai Iyer. BLACK HOLE NORMAL MODES : A WKB APPROACH. 2. SCHWARZSCHILD BLACK HOLES. *Phys. Rev. D*, 35 :3632, 1987.

[61] R. A. Konoplya. Quasinormal behavior of the d-dimensional schwarzschild black hole and the higher order wkb approach. *Phys. Rev. D*, 68 :024018, Jul 2003.

[62] Carl M. Bender and Steven A. Orszag. *Advanced Mathematical Methods for Scientists and Engineers*. Springer, 1999.

[63] Maximiliano Isi, Matthew Giesler, Will M. Farr, Mark A. Scheel, and Saul A. Teukolsky. Testing the no-hair theorem with GW150914. *Phys. Rev. Lett.*, 123(11) :111102, 2019.

[64] Cecilia Chirenti. Black hole quasinormal modes in the era of LIGO. *Braz. J. Phys.*, 48(1) :102–109, 2018.

[65] S. Chandrasekhar. On the Equations Governing the Perturbations of the Schwarzschild Black Hole. *Proc. Roy. Soc. Lond. A*, A343 :289–298, 1975.

[66] S. Chandrasekhar and Xanthopoulos B. C. On the Metric Perturbations of the Reissner-Nordstrm Black Hole. *Proc. Roy. Soc. Lond. A*, 367(1728) :1–14, 1979.

[67] S. Chandrasekhar and Detweiler S. Equations governing gravitational perturbations of the Kerr black-hole. *Proc. Roy. Soc. Lond. A*, A350 :165–174, 1976.

[68] Flora Moulin and Aurélien Barrau. Analytical proof of the isospectrality of quasinormal modes for Schwarzschild-de Sitter and Schwarzschild-Anti de Sitter spacetimes. *Gen Relativ Gravit.*, 52(82), 2020.

[69] J.W. Moffat. Scalar-tensor-vector gravity theory. *JCAP*, 03 :004, 2006.

[70] J.W. Moffat. Black Holes in Modified Gravity (MOG). *Eur. Phys. J. C*, 75(4) :175, 2015.

[71] Thomas P. Sotiriou. Horava-Lifshitz gravity : a status report. *J. Phys. Conf. Ser.*, 283 :012034, 2011.

[72] Alex Kehagias and Konstadinos Sfetsos. The Black hole and FRW geometries of non-relativistic gravity. *Phys. Lett. B*, 678 :123–126, 2009.

[73] P. Bargue. Bravo Medina, M. Nowakowski, and D. Batic. Quantum Mechanical Corrections to the Schwarzschild Black Hole Metric. *EPL*, 117(6) :60006, 2017.

[74] H.W. Hamber and S. Liu. On the quantum corrections to the Newtonian potential. *Phys. Lett. B*, 357 :51–56, 1995.

[75] Flora Moulin, Auren Barrau, and Killian Martineau. An overview of quasinormal modes in modified and extended gravity. *Universe*, 5(9) :202, 2019.

[76] Hal M. Haggard and Carlo Rovelli. Quantum Gravity Effects around Sagittarius A*. *Int. J. Mod. Phys. D*, 25(12) :1644021, 2016.

[77] Auren Barrau, Killian Martineau, Jeremy Martinon, and Flora Moulin. Quasinormal modes of black holes in a toy-model for cumulative quantum gravity. *Phys. Lett. B*, 795 :346–350, 2019.

[78] Alexandre Feller and Etera R. Livine. Surface state decoherence in loop quantum gravity, a first toy model. *Class. Quant. Grav.*, 34(4) :045004, 2017.

[79] Auren Barrau, Killian Martineau, and Flora Moulin. A status report on the phenomenology of black holes in loop quantum gravity : Evaporation, tunneling to white holes, dark matter and gravitational waves. *Universe*, 4(10) :102, 2018.

[80] Katherine Freese. Review of Observational Evidence for Dark Matter in the Universe and in upcoming searches for Dark Stars. *EAS Publ. Ser.*, 36 :113–126, 2009.

[81] Pisin Chen, Yen Chin Ong, and Dong-han Yeom. Black Hole Remnants and the Information Loss Paradox. *Phys. Rept.*, 603 :1–45, 2015.

[82] Lars Husdal. On Effective Degrees of Freedom in the Early Universe. *Galaxies*, 4(4) :78, 2016.

[83] Auren Barrau, Killian Martineau, Flora Moulin, and Jean-Frric Ngono. Dark matter as Planck relics without too exotic hypotheses. *Phys. Rev. D*, 100(12) :123505, 2019.

[84] Marcos Moshinsky and Yuri F. Smirnov. *The Harmonic Oscillator In Modern Physics*. Harwood Academic Publishers, 1996.

[85] Luca Fabbri. The Tensorial Connections. *Eur. Phys. J. C*, 80(5) :385, 2020.

[86] Luca Fabbri. Covariant inertial forces for spinors. *Eur. Phys. J. C*, 78(9) :783, 2018.

[87] Luca Fabbri. Polar solutions with tensorial connection of the spinor equation. *Eur. Phys. J. C*, 79(3) :188, 2019.

[88] Luca Fabbri. Spinors in Polar Form. 3 2020.

[89] Doron M. Ludwin. The Gravitational analog of the Aharonov-Bohm electric effect. 12 2010.

[90] Raymond Y. Chiao, Robert Haun, Nader Inan, Bong-Soo Kang, Luis A. Martinez, Stephen J. Minter, Gerardo Munoz, and Douglas Singleton. A Gravitational Aharonov-Bohm Effect, and its Connection to Parametric Oscillators and Gravitational Radiation. pages 213–246, 1 2013.

[91] Luca Fabbri, Flora Moulin, and Auren Barrau. Non-trivial effects of sourceless forces for spinors : toward an Aharonov–Bohm gravitational effect ? *Eur. Phys. J. C*, 79(10) :875, 2019.

[92] Eugenio Bianchi, Marios Christodoulou, Fabio D'Ambrosio, Hal M. Haggard, and Carlo Rovelli. White Holes as Remnants : A Surprising Scenario for the End of a Black Hole. *Class. Quant. Grav.*, 35(22) :225003, 2018.